UNIVERSITY OF READING

Department of Meteorology

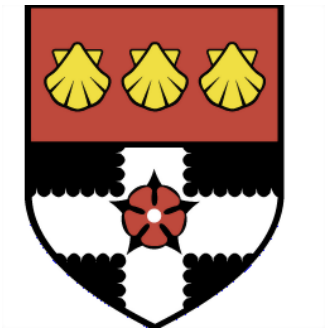

The Impact of Arctic Sea Ice Change on Midlatitude Climate

Caroline Ruth Holmes

A thesis submitted for the degree of Doctor of Philosophy

2015

Declaration

I confirm that this is my own work and the use of all material from other sources has been properly and fully acknowledged.

Caroline Holmes

Abstract

Arctic sea ice loss is a robust feature of observations and of climate model projections. Amplified winter lower tropospheric warming in the Arctic relative to the global mean is associated with this ice loss. Many recent studies have addressed the possible effects of these changes on the midlatitude atmospheric circulation, particularly in the North Atlantic. These studies suggest responses including an equatorward jet shift, a negative annular mode response and changes in Rossby wave behaviour. However, there is disagreement on the magnitude, significance and even sign of these responses.

Previous studies have shown the advantages of model hierarchies for understanding the atmosphere. In this thesis, experiments are conducted in HadGAM1 with simplified lower boundary conditions. Two sets of experiments are conducted, one in a zonally symmetric aquaplanet and the other in a configuration with representative northern hemisphere land masses. A wide range of sea ice profiles are imposed.

The dominant response to ice removal in an aquaplanet is an equatorward jet shift, consistent with previous work. This response is moderate in magnitude for ice which does not exceed 65° latitude, but strongly nonlinear for greater ice extents. The zonal mean response is qualitatively similar in the asymmetric configuration, but the nature of the asymmetric response shows sensitivity to the exact ice edge location. These results have implications for understanding the impact of sea ice anomalies in past as well as present climates.

Changes in surface temperature gradients, including from Arctic amplification, could affect midlatitude climate even if circulation changes are small. In particular, changes in thermal advection could alter midlatitude temperature variability and extremes. In this thesis a multiple regression model is used to investigate projected monthly temperature variance changes in a recent single model ensemble. Many robust changes, including reduced winter temperature variance in Europe, are consistent with the effect of changes in the seasonal mean temperature gradient alone.

Acknowledgements

I wish to extend special thanks to my supervisors, Tim Woollings, David Brayshaw and Len Shaffrey, for their support over the duration of this project. Their insight, guidance, wisdom and encouragement has been invaluable.

The Reading Meteorology department has been a brilliant place to work, and there are too many people within it who have provided either practical or moral support to mention. However, particular thanks must go to 'IT@met' for fixing things and answering questions, to the CMS computing team for their assistance setting up the Unified Model on HECToR, and to my thesis committee Maarten Ambaum and Mike Blackburn for providing feedback and support. I am also particularly indebted to office '2U0Cake' for providing much laughter in addition to copious cake, and to Brodie Pearson, who was a source of laughter, conversation and free donuts throughout my second and third years.

Three other people are deserving of special mention; Chrissy, for chocolate and words of wisdom; Lizzy, for perspective; and Lizzie, for evidence that there is light at the end of the PhD tunnel. I am grateful to my parents and sisters for their support and understanding, as well as for bringing me up to be interested in the maths and physics of the wonderful world that we live in. Finally, tremendous thanks to James, whose endless supply of love and patience, despite having his own thesis to write, helped me through my PhD and the last year in particular.

Contents

List of Figures

Chapter 1

Introduction

Arctic sea ice decline is one of the most visible markers of climate change. Robust negative trends in Arctic sea ice extent (SIE) are observed and projected to continue through the 21st century (Stroeve *et al.*, 2012b). Evidence points towards greenhouse gas forcing as the dominant cause of this trend in the recent past (Kay *et al.*, 2011) and future, although high internal variability partially accounts for recent dramatic events. Long-term downward trends in sea ice cover are evident year-round but greatest in summer.

The dramatic loss of sea ice is associated with Arctic Amplification (Screen and Simmonds, 2010), whereby the near-surface warming over the northern polar region exceeds that for the earth as a whole. This feature is present throughout the extended winter season and strongest in early winter. As a result, the large-scale meridional temperature gradient is weakened.

This thesis is concerned with the effects of Arctic sea ice loss and associated warming on midlatitude circulation and climate, and explores this through two mechanisms.

The first mechanism will be referred to hereafter as the thermal advection mechanism; surface temperatures in any given location are partially determined by advection of air masses (as well as by local processes). Therefore temperature variability is affected by temperatures in source regions and in particular by the temperature gradient of the underlying surface. Changes in the temperature gradients such as that induced by Arctic amplification are therefore related to changes in temperature variability, contributing to our understanding of temperature extremes.

The second mechanism relates to changes in the thermal structure of the atmosphere. A decreased meridional temperature gradient must be accompanied by a decreased vertical shear in the zonal wind, through thermal wind balance, suggesting that sea ice loss would contribute to a decelerated jet stream. Reductions in temperature gradient also decrease the baroclinic instability of the atmosphere, with the potential for changes in the eddy-driven jet through eddy feedbacks from midlatitude synoptic eddies (extratropical

storms). Changes in jet structure may also affect the critical latitudes at which waves break and so alter momentum transports into the jet by eddies, thus providing a possible feedback onto the jet due to wave-mean flow interaction.

The behaviour of the atmospheric jet streams is crucial for the weather and climate of midlatitudes, including the UK. While the southern hemisphere jet is robustly projected to shift poleward under climate change, there is much less certainty in the northern hemisphere and in particular in the North Atlantic.

In recent years, possible links between reductions in sea ice cover and changes in the jet stream have been an active area of research. Some observational studies have suggested a resulting relationship with changing weather extremes (e.g. Francis and Vavrus, 2012), but such studies may be limited by the short data record and high natural variability (Barnes, 2013). Many modelling studies investigating the response to sea ice loss have found a negative-NAO-like response (e.g. Magnusdottir *et al.*, 2004; Seierstad and Bader, 2009) or negative-AO-response (Liu *et al.*, 2012). However, the scientific literature is not completely in consensus regarding the response; for example, two single-model ensembles in Screen *et al.* (2013a) produce either NAO positive or no NAO-like signal in response to historical sea ice trends, in contrast to the above studies. Arctic sea ice change and related processes such as Arctic Amplification may therefore be one of the factors contributing to uncertainty in projections for circulation changes over the 21st century (e.g. Harvey *et al.*, 2013), because both the timescales of 21st century Arctic sea ice decline and the impact of sea ice on atmospheric processes are uncertain (Stroeve *et al.*, 2012b; Bader *et al.*, 2011).

Due in part to these uncertainties, and to biases in GCM representations of jet streams, it is beneficial to complement studies in fully coupled GCMs with experiments in different modelling frameworks, in order to improve our fundamental understanding of how the atmosphere is affected by sea ice extent. Experiments in simplified models have been used in the past to investigate the atmospheric response to idealised heating such as Arctic amplification (e.g. Butler *et al.*, 2010). However, experiments whose complexity fits in between the two extremes are valuable to bridge between understanding and simulation (Held, 2005). One such approach is the use of aquaplanet models (Neale and Hoskins, 2000b). Brayshaw *et al.* (2009) added idealised land masses to an aquaplanet model to investigate the driving mechanisms behind the North Atlantic storm track. This project

builds on this modelling setup, developing it to investigate the response to a climate change-like thermal forcing, in this case sea ice change. The model used is HadGAM1, an atmosphere-only configuration of the Met Office Unified Model, with simplified lower boundary forcings and perpetual equinox conditions.

The following questions are investigated:-

1. To what extent does thermal advection contribute to projections of 21st century temperature variability in coupled climate models? As discussed above, thermal advection will be affected by changing temperature gradients, such as that introduced by amplified polar warming.

2. What is the atmospheric response to sea ice removal? In particular what is the response of the eddy driven jet, including its mean, variability and spatial heterogeneity?

3. What sets the nature and magnitude of the jet response to sea ice forcing; is there nonlinearity in the response?

This thesis is organised as follows. Chapter 2 gives further details on Arctic sea ice loss and Arctic Amplification, discusses the dynamics of the jet and storm track, and outlines the current understanding of sea ice impacts on the atmospheric circulation, and chapter 3 introduces the models and data used. The thermal advection mechanism for temperature variability change is explored in chapter 4 using data from a single-model ensemble and the CMIP5 archives. Chapter 5 gives the experimental design for investigations into the response of the circulation to sea ice removal in an aquaplanet and presents the results from these experiments, and chapter 6 does similarly for experiments with idealised land masses.

Chapter 2

Scientific Background

This chapter introduces the scientific literature underlying this thesis, including:-

- The recent and projected state of Arctic sea ice and key related processes
- Heterogeneous distribution of warming under anthropogenic forcing
- The dynamics of the jet and storm track, in particular wave-mean flow interaction
- The response of the jet and storm track to surface asymmetries and temperature anomalies
- The atmospheric response to recent and projected sea ice reduction, and the outstanding questions in this field

2.1 Sea Ice

This section gives an overview of the current state of Arctic sea ice and recent and projected trends in key sea ice variables. In addition the processes through which the sea ice, atmosphere and to a lesser extent ocean interact are discussed.

Antarctic sea ice extent has increased slightly during the satellite era (e.g. Parkinson and Cavalieri, 2012)[1]. The Antarctic is not the focus of this thesis so Antarctic sea ice is not discussed in this section. A brief discussion of modelled impacts of Antarctic sea ice on the atmosphere is given in section 2.4.2, since the results are relevant to the experiments in this thesis.

[1]The reasons for the recent increase in Antarctic sea ice are the subject of current research. There are strong regional variations in the trends, and it is unclear whether the trends are consistent with internal variability (Bindoff *et al.*, 2013).

2.1.1 Arctic sea ice in the satellite era

2.1.1.1 Concentration, area and extent

Since 1979, satellite observation systems have enabled sea ice concentration (SIC) in the Arctic to be quantified far more extensively than before (Vaughan *et al.*, 2013). The brightness temperature of a given pixel is measured, and is assumed to be a linear combination of the brightness temperature of open ocean and sea ice (e.g. Comiso and Nishio, 2008) depending on their relative concentrations within the pixel. Therefore the ice concentration can be retrieved if these two brightness temperatures are known. Whilst the instrument used for brightness measurements has changed during the satellite recording period, suitable corrections for the earlier instruments enable the existence of a consistent record from 1978 to the present (Comiso and Nishio, 2008)[2].

The most frequently used large scale sea ice variable is sea ice extent (SIE), the area of ocean covered by sea ice of at least 15% concentration[3]. Arctic SIE has a strong seasonal cycle, with a minimum in September and maximum in February or March. During this cycle Arctic sea ice covers 1.7–3.9% of the Earth's ocean area (approximately 6×10^6–15×10^6 km^2, Vaughan *et al.*, 2013). Sea ice retreat has been evident in recent years, with a record minimum SIE of 3.44×10^6 km^2 in 2012; this is significantly lower than the climatology just mentioned. Figure 2.1 demonstrates the strong seasonal cycle and the 2012 record minimum. As shown in these figures, sea ice at minimum extent is typically contained poleward of 70°N, but at maximum extends locally to around 50°N, for example in the marginal seas along the west of the Pacific and Atlantic basins.

Recent trends in SIE can be accurately evaluated using satellite based records such as that in Comiso and Nishio (2008), which was extended to cover the period to 2012 in Vaughan *et al.*, 2013. Northern hemisphere SIE trends for all monthly anomalies in the period 1978–2006 are -3.4% per decade (ice area trends are -4% per decade; Comiso and Nishio, 2008). Trends in the annual minimum extent are larger, as suggested by Figure 2.1. As well as strong seasonal variations in the trends in SIC, the pattern of sea ice retreat is spatially complex (Vaughan *et al.*, 2013, Figure 4.2).

[2]The instruments used are the SMMR (Scanning Multichannel Microwave Radiometer, 1978–Aug 1987), the SSM/I (Special Scanning Microwave Imager, Jul 1987–present), and the AMSR-E (Advanced Microwave Scanning Radiometer, Jun 2002–Oct 2011)(Comiso and Nishio, 2008).

[3]Sea ice area (SIA), the sum over all grid boxes of concentration multiplied by grid box area, is also sometimes used.

(a) Regions of Arctic Ocean

(b) MAR SIE, 2012 (white) and 1981–2010 climatology (pink)

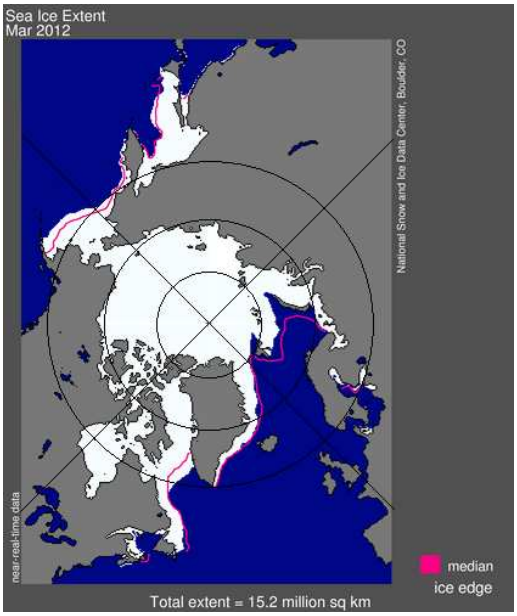

(c) SEP SIE, 2012 (white) and 1981–2010 climatology (pink)

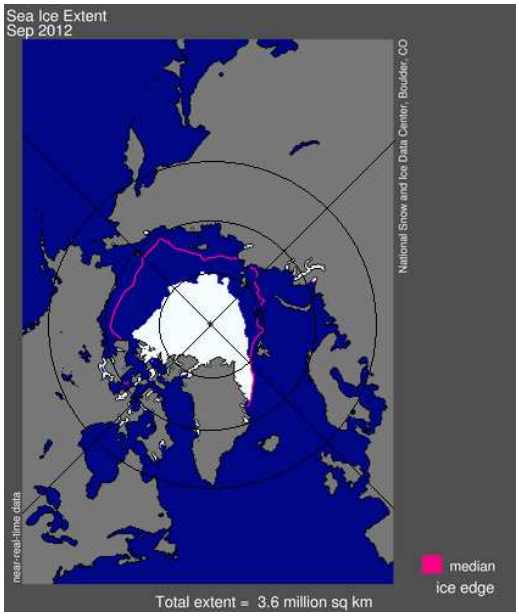

Figure 2.1: The Arctic ocean. a) Regions of the Arctic ocean; b) March 2012 sea ice cover (white) and 1981–2010 median ice edge (pink). (Sea ice cover is defined as where sea ice concentration >15% , and the ice edge as the edge of this region). c) as b) but for September 2012 and climatology. Selected lines of longitude and latitude are shown at 60, 70 and 80°N and 0, 90, 180 and 270°E. Figures amended from The National Snow and Ice Data Centre (NSIDC), Boulder, Colorado. Sea ice concentration is derived from the same datasets as mentioned in the text but using a different algorithm, developed at NASA. It is available as the NSIDC sea ice index (Fetterer *et al.*, 2002).

2.1.1.2 Thickness

Relative to SIC, it is harder to obtain accurate volume or thickness measurements, and the record for these latter variables is shorter. Analysis is largely restricted to two methods:-

- Recent satellite missions use satellite altimetry to calculate sea ice freeboard, which is the height above local sea level. Assumptions about snow depth and ice and snow density must then be made to deduce the depth and therefore volume of sea ice (Kwok, 2010). Such records include those from ERS-1 (1993–2001), Envisat (2002–present), ICESat (2003–2009) and CryoSAT-2 (2010-2012). The first two of these records, however, have coverage only south of 81.5°N and therefore are of limited use.
- PIOMAS (Panarctic Ice Ocean Modelling and Assimilation System) uses a coupled sea ice-ocean model to calculate sea ice thickness and volume (Zhang and Rothrock, 2003). This model assimilates SIC fields obtained from satellite data and is forced at the surface with NCEP-NCAR analysis data.

New measurements from CryoSat-2 enable quantification of ice thickness and volume for the winters 2010/11 and 2011/12 (Laxon *et al.*, 2013). Comparing this record to earlier data from the IceSAT mission for 2003–2008, Laxon *et al.* (2013) found a decline in autumn (Nov/Dec) volume (4291 km^3 or 36%) and winter (Feb/Mar) volume (1479 km^3 or 9%) between the two periods. This decline was greater in autumn and weaker in winter than in PIOMAS modelled estimates. Therefore, while sea ice volume as well as extent is decreasing, there is uncertainty over the magnitude of this decrease.

2.1.2 Arctic sea ice before the satellite era

HadISST1 (Hadley centre sea ice and sea surface temperature data set; Rayner *et al.*, 2003) provides sea ice concentrations and extent dating back to 1871 using data from sea ice charts based on sources such as ships' records. However this longer data set is less reliable than the shorter satellite record. This is due to lack of winter observations in the first part of the period, data sparsity in time and space, possible inconsistencies or biases dependent on those recording the data, and the necessity of making assumptions about the concentration of ice within the ice pack. Indeed, in the southern hemisphere, HadISST1 provides seasonal climatologies only (i.e., no interannual variability) until 1973.

HadISST1 and the datasets which contributed to it suggest that sea ice concentration was relatively constant, at much higher values than found in recent decades, between 1870 and 1950 (e.g. Figure 4.3 of Vaughan *et al.*, 2013). However uncertainties in the earlier record as outlined above mean that quantification of trends for this period is difficult. Reconstructions of Arctic-wide sea ice using land proxy data (predominantly ice cores, but also tree rings, lake sediments and documentation) provide some skill since the sixth century AD (Kinnard *et al.*, 2011). These provide evidence that the recent decline of Arctic sea ice is unprecedented in the period since the sixth century AD.

2.1.3 Causes of 20th century sea ice trends

Notz and Marotzke (2012) in a purely observational study discounted internal variability or self-acceleration as an explanation for the observed negative trend in SIE in the satellite era. Instead, they found it was well described by a linear trend which was correlated with, and physically consistent with, increasing atmospheric carbon dioxide (CO_2) and the resulting increases in downwelling longwave radiation. They therefore concluded that the increasing CO_2 was the most likely cause of the SIE reduction. Attribution studies in climate models have similarly reached this conclusion (e.g. Min *et al.*, 2008; Kay *et al.*, 2011), leading the Intergovernmental Panel on Climate Change (IPCC) to conclude that 'Anthropogenic forcings are *very likely* (>90% probability) to have contributed to Arctic sea ice loss since 1979'[4]. Kay *et al.* (2011) found that approximately half of the recent decline is anthropogenically forced, and the other half is due to internal variability.

Arctic warming, which is intrinsically linked to sea ice reductions (Section 2.2.1) was also found to be 'very unlikely' due to internal forcing in the CMIP5 detection and attribution study of Fyfe *et al.* (2013).

2.1.4 21st century projections

Climate models are used to project 21st century changes in sea ice concentration under assumptions of anthropogenic external forcing (greenhouse gas emissions, aerosol emissions, and land use change). Recently, coupled climate models contributing to CMIP5

[4]Detection and attribution studies are a very active area of current climate research. Detection refers to the identification of a statistically significant change in some aspect of the climate system, while attribution is quantifying the role of possible causes, such as greenhouse gas increases, in forcing the identified change (Bindoff *et al.*, 2013)

(Coupled Model Intercomparison Project phase 5) have been a major source of information for such projections, replacing the previous phase CMIP3.

One goal, given the observed downward trend, is to determine the year by which the Arctic will be 'nearly' sea ice free in September, i.e. have SIE of less than 1.0×10^6 km^2 (e.g. Wang and Overland, 2012). It is difficult to obtain a small time window for such an event, because as well as the large model uncertainty, there is uncertainty in the greenhouse gas forcing applied to 21^{st} century model runs. Stroeve *et al.* (2012b), using CMIP5 models forced with RCP4.5[5], found that there is considerable uncertainty in this date even under this single forcing scenario. Some members of the multi model ensemble become ice free as early as 2020, and 32% of the members are ice free by 2100.

One approach for reducing this uncertainty is to restrict the ensemble to models which can adequately represent the observed climatology and seasonal cycle. This assumes that these models might give the most reliable projections due to better representation of physical processes relevant to sea ice. An accurate downward trend over the past 30 years might also be seen as a necessary condition for a model to be deemed reliable, but this assumes that the observed trend is indeed a forced trend rather than a consequence of internal variability. The above paper by Stroeve *et al.* (2012b) did not perform such a restriction, and noted that most models do not capture the rate of decline over recent years. Wang and Overland (2012) did use such a restriction; in seven models which accurately reproduced the climatology and seasonal cycle they found a projected ice free date between 2040 and 2060. However, they postulated that since even these models were unable to capture the rapid observed decline after 2007, the Arctic may be 'ice free' as early as the mid 2030s.

In summary, models point to a continued reduction in Arctic sea ice thickness and area in the coming century, and the IPCC assigned a >90% probability to 'continued shrinking and thinning [of Arctic sea ice] year-round in the course of the 21st century' (Collins *et al.*, 2013).

[5]The RCPs (Representative Concentration Pathways) are the forcing scenarios used for the CMIP5 models (van Vuuren *et al.*, 2011). RCP4.5 refers to the fact that under this forcing scenario, radiative forcing reaches 4.5 Wm^{-2} by 2100. The RCPs are described in more detail in Section 3.1.

2.1.5 The sea ice - ocean - atmosphere coupled system

Here a brief overview is given of processes driving sea ice variability on seasonal to multi-decadal timsecales and the processes via which it directly affects the atmosphere. Understanding the role of sea ice in the climate system is key for interpreting experimental results in the light of observations.

2.1.5.1 Drivers of sea ice variability

The seasonal cycle of sea ice is dominated by thermodynamics, as ice melt and growth are determined primarily by the cycle of solar insolation (http://nsidc.org/cryosphere/seaice/processes/circulation.html). In summer (between March and September) melting dominates and ice extent decreases, and in winter the opposite occurs. However, interannual variations in this seasonal cycle are driven by processes such as ice export due to anomalous atmospheric circulation and ice melt driven by anomalous warm air advection or ocean heat content.

The effect of large scale variability in the atmosphere and ocean on sea ice throughout the year has been investigated by numerous authors (e.g. Deser *et al.*, 2000; Day *et al.*, 2012; Zhang *et al.*, 2000; Rigor *et al.*, 2002). This variability includes the Arctic Oscillation (AO; Thompson and Wallace, 2000) and North Atlantic Oscillation (NAO; Hurrell *et al.*, 2003) in the atmosphere (Section 2.3.5.1) and the Atlantic Multidecadal Oscillation (AMO) and variability associated with the Atlantic Meridional Overturning Circulation (AMOC) in the ocean (Day *et al.*, 2012). Many such studies have focused on changes in very localised regions of the Arctic; the discussion here is restricted to drivers of large-scale sea ice changes.

Deser *et al.* (2000) identified a north-south sea level pressure (SLP) dipole in the North Atlantic associated with the leading pattern of sea ice variability, based on winter observations between 1958 and 1997. The SLP dipole resembled the NAO, and the positive-NAO-like pattern (positive anomalies centred on 40°N and negative anomalies north of Iceland) was associated with more ice in the Labrador sea and less to the east of Greenland. Correlations between the SLP index and sea ice were highest with the SLP pattern leading by 2–6 weeks. The authors claimed that the associated sea ice anomalies were qualitatively consistent with dynamic and thermodynamic forcing by the anoma-

lous geostrophic winds; for example, that anomalous southerly winds east of Greenland would contribute to dynamic ice retreat and would also be anomalously warm, contributing to ice melt. However, the paper did not quantify the effects of these mechanisms, and in winter melt is less important than growth which is heavily moderated by ocean as well as atmospheric temperature. This suggests that the thermodynamic component may be more complicated than the simple picture of atmospheric warm advection causing melt.

Later, Rigor *et al.* (2002) found evidence that the AO had a large effect on observed sea ice in the period 1979–1998. Regressions suggested that during a positive AO winter, there was increased ice divergence in the eastern Arctic. Consistent with this divergence there was more open ocean, allowing for more growth of thin sea ice and associated strong heat fluxes to the atmosphere. These in turn provided a preconditioning for less sea ice in the following summer. However the interpretation of such results is challenging due to the short record and to the strong trends in the AO, SIC, and temperature. The divergence and growth effect was also found in the coupled sea ice–ocean model used by Zhang *et al.* (2000), who highlighted the role of coupling between dynamic and thermodynamic processes (e.g. ice advection exposing the warm, low albedo ocean surface). Day *et al.* (2012) estimated, based on relationships obtained in long climate model simulations, that the AMO could explain approximately 30% of the 1979–2010 negative SIE trend. However, they found no relationship with the AO.

All the above studies deal with recent (1950–2010 or a shorter period) variability and trends. However, Strong and Magnusdottir (2010a) found that in long climate change simulations in two AOGCMs the relative importance of the sea ice dipole related to NAO variability decreased over time; the dipole was dominant in the early 20th century but in the 21st century the emergent dominant mode of variability was a widespread ice reduction. This is consistent with the discussion in Section 2.1.3 about the emerging role of external forcing in driving recent and future sea ice reductions.

Statistical relationships have been found with the tropics (Henderson *et al.*, 2014), although data is limited and physical mechanisms for such a connection are unclear in some cases. Causal linkages between waves from the tropics and Arctic warming have been proposed and are discussed in Section 2.2.1.

In summary, wind-driven variability in sea ice motion appears to be important for interannual variability of sea ice extent, in particular a sea ice dipole between the Labrador

and Greenland seas. However, the strength of relationships with patterns such as the NAO may not be robust on long (>30 year) timescales and in particular may be dwarfed by external forcing causing a widespread sea ice decline (Strong and Magnusdottir, 2010a). Ocean memory processes are relevant for relationships between winter atmospheric circulation and summer sea ice decline. Oceanic heat transport is also important for sea ice variability on interdecadal timescales.

2.1.5.2 Case Studies

As discussed above (section 2.1.3), recent downward trends in sea ice have been attributed to anthropogenic forcing, but this forced trend is superimposed on high variability. This combination of factors and examples of the processes described above can be seen in the two record years, 2007 and 2012.

Observational and reanalysis data for 2007 showed accelerated decline in June and July, linked to anomalously southerly winds (Comiso *et al.*, 2008). A thinner, more vulnerable ice cover than in earlier years, wind anomalies driving both warm advection and ice export, and clear skies, were all suggested as causes in Stroeve *et al.* (2008). Modelling studies in PIOMAS provided evidence for the role of preconditioning and wind anomalies (Lindsay *et al.* (2009) and Zhang *et al.* (2008)) but did not find evidence for clear skies having a role (Schweiger *et al.*, 2008).

In 2012, an exceptional cyclone in early August (Simmonds and Rudeva, 2012) was linked to rapid sea ice loss. Reanalysis and satellite datasets show a large region of ice break up and melt consistent with the wind forcing (Parkinson and Comiso, 2013). Furthermore, simulations in PIOMAS show fast ice loss directly linked to bottom melt from ocean heat transport linked to the cyclone (Zhang *et al.*, 2013). However, both studies find that the sea ice was preconditioned to a low state; Parkinson and Comiso (2013) demonstrate rapid ice loss in June linked to an already thin ice cover while Zhang *et al.* (2013) show using sensitivity simulations that a record but weakened minimum would have occured, later in the season, even without the storm.

2.1.5.3 Sea ice impacts on the atmosphere

The above discussion has focused on how sea ice is affected by oceanic and atmospheric processes. However, fundamental to the questions addressed in this thesis, sea ice affects the ocean-atmosphere system through its modification of the surface energy budget (e.g. Serreze and Barry, 2005).

The proportion of solar shortwave radiation reflected by a surface is quantified by its albedo. The albedo of sea ice is between 0.3 and 0.6 for thick first year ice and may be as high as 0.75 for multiyear ice or still higher for snow on sea ice (Serreze and Barry, 2005, chapter 5). This compares to albedo of less than 0.1 for open ocean. Therefore, an area of sea ice reflects more incoming solar radiation than open ocean would. One consequence is the albedo feedback effect (Sellers, 1969). Namely, an increase in surface temperature can increase melt and decrease freeze, leading to a reduction in sea ice. There is therefore a decrease in surface albedo so more solar radiation is absorbed at the surface, increasing its temperature further. This is a positive feedback, enhancing the initial temperature anomalies. The snow and ice albedo feedback has been considered in the literature for many years, including early papers by Sellers (1969) and Manabe and Wetherald (1975). There are subtleties in this process, since high latitudes only receive significant solar radiation in the summer months. The albedo effect is therefore key for spring ice melt (e.g. Schröder *et al.*, 2014) , but also winter refreeze due to heat stored in the ocean as a result of earlier melt (Screen and Simmonds, 2010). In addition, sea ice (especially when snow-covered) provides an insulating layer between the ocean and atmosphere; in winter, this acts to reduce latent and sensible heat fluxes (Serreze and Barry, 2005, chapter 5).

In addition, the boundary between open ocean and sea ice constitutes a sharp surface temperature front. It is known that the ice edge is associated with storm activity in both present and past climates (e.g. Deser *et al.*, 2000; Kageyama *et al.*, 1999). This can be related to extensive literature considering the effect of sea surface temperature fronts on the atmosphere, which is discussed in Section 2.3.4.4 along with the relevant mechanisms.

2.2 Global Temperature Change

Global average surface temperatures increase in climate models in response to anthropogenic forcing. The geographical pattern of this warming is highly heterogenous. Two

key features of the surface heterogeneity are Arctic amplification (AA; increased warming in high northern latitudes relative to the global average) and greater warming over land than ocean, both seen in the CMIP5 ensemble (Figure 2.2). Heterogeneities of the upper-tropospheric temperature are also large, but different in structure from those at the surface.

2.2.1 Arctic Amplification

2.2.1.1 Features

Arctic amplification (AA) refers to an enhanced warming signal in the Arctic region. It is typically expressed as the temperature trend or anomaly over the Arctic relative to that for the Earth as a whole. An AA signal is emerging in observations, and is produced in

(a) Surface warming for the median CMIP5 model under RCP4.5, 2046–2065 relative to 1986–2005: DJF (left) and JJA (right).

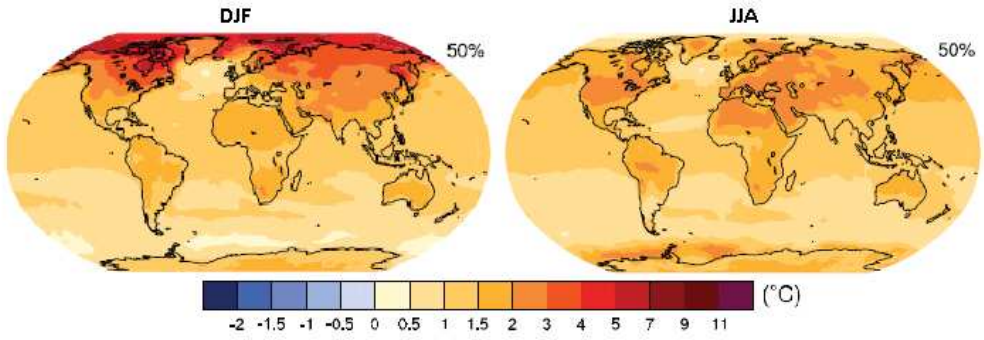

(b) Multi-model mean, zonal, annual mean warming for 2081–2100 relative to 1986–2005, for three scenarios

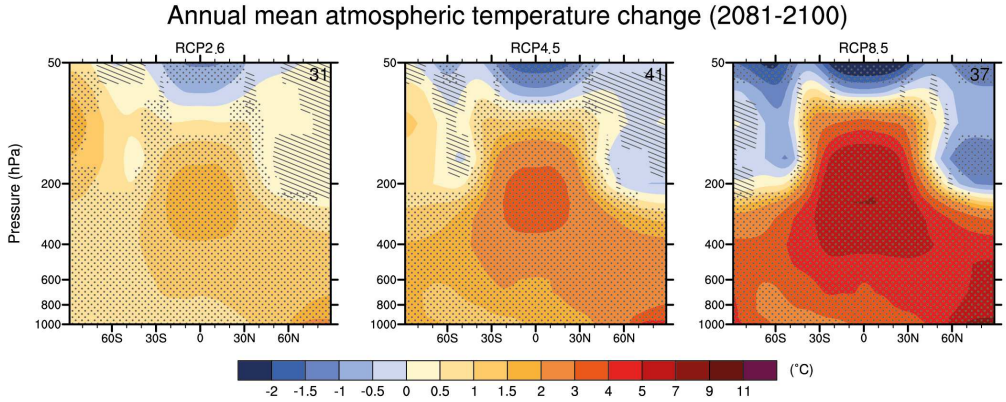

Figure 2.2: Projected temperature increase in CMIP5 models. Full details in sub-captions. Adapted from van Oldenborgh *et al.* (IPCC AR5 WG1 Annex 1; 2013) figures A1.4 and A1.5 and Collins *et al.* (IPCC AR5 Chapter 12; 2013) Figure 12.12.

climate model simulations forced with increased greenhouse gases.

Observational evidence of AA has traditionally been hard to obtain due to sparse observations in the Arctic region (Serreze and Barry, 2011). However, data based both only on surface observations and on satellite measurements are now providing a consensus on surface AA. For example, the GISS (Goddard Institute for Space Studies) surface temperature analysis (Hansen *et al.*, 2010) shows that surface temperature anomalies in the Arctic for the 2000s relative to 1951-1980 exceed those for the rest of the globe by more than a factor of three (Hansen *et al.*, 2010). Arctic warming between these two periods is over 1.5°C.

Observed AA is strongest in autumn and winter, and not manifest in the summer (Serreze and Francis (2006); Screen and Simmonds (2010); Figure 2.2). Possible reasons for this seasonal variation are addressed in Section 2.2.1.2. It is largely a near-surface phenomenon, strongest below 850 hPa. Data from the ERA-Interim reanalysis for 1989–2008 shows that the warming decreases with height in all seasons except summer, and displays an AA-type signal above 700 hPa only in winter (Screen and Simmonds, 2010).

Conclusions about recent AA rely on the use of short timeseries and limited spatial data coverage (Serreze and Francis, 2006). However, climate models forced with different forcings (anthropogenic only, all forcing, or natural forcing only) have shown that the 21st century Arctic temperature record cannot be explained by internal variability alone (Fyfe *et al.*, 2013). The IPCC AR5 (Bindoff *et al.*, 2013) concluded that it is *likely* that Arctic warming in the last 50 years has been influenced by anthropogenic forcing.

AA has been a feature of increasing CO_2 experiments throughout their history; the early study of Manabe and Wetherald (1975) highlighted enhanced lower tropospheric (below 500 hPa) warming in high latitudes as a feature of their $2xCO_2$ experiments. The most recent climate model simulations give a very coherent picture of strong AA increasing through the 21st century (Collins *et al.*, 2013). In the CMIP5 multi-model ensemble under RCP4.5 forcing, mean surface warming north of 67.5°N for the period 2081–2100 relative to 1986–2005 exceeds global mean warming by more than a factor of four (Collins *et al.*, 2013). As found in the observational record, model projections show that Arctic warming is greatest near the surface (Collins *et al.*, 2013).

2.2.1.2 Mechanisms

The mechanisms for AA are broadly debated (e.g. the comprehensive review by Serreze and Barry, 2011), and the coupled ice-atmosphere-ocean processes contributing in the Arctic make it hard to isolate individual mechanisms. Proposed mechanisms include:-

- Sea ice, via the sea ice albedo feedback or changes in summer oceanic heat uptake (Serreze *et al.*, 2009; Screen and Simmonds, 2010; Screen *et al.*, 2012)
- Cloud feedbacks, whereby changes in cloud cover affect the longwave and shortwave energy budgets (Bengtsson *et al.*, 2013)
- The lapse rate feedback/stability (Pithan and Mauritsen, 2014)
- The Planck feedback (e.g Pithan and Mauritsen, 2014; Lesins *et al.*, 2012)
- Changes in poleward heat transport by the ocean (Graham and Vellinga, 2013) and atmosphere (Lee *et al.*, 2011; Ding *et al.*, 2014)

These can be separated into local processes (sea ice, clouds, and lapse rate and Planck feedbacks) and remote influences (poleward heat transport).

Serreze *et al.* (2009), Screen and Simmonds (2010) and Screen *et al.* (2012) all highlighted sea ice loss as the key factor leading to observed near surface warming. Screen and Simmonds (2010) linearly regressed ERA-Interim temperatures onto Arctic-wide sea ice and found that the temperature trend linked to sea ice alone captured much of the magnitude and structure. They argued that decreased sea ice cover in the summer months causes increased ocean heat uptake, resulting in increased ocean-to-atmosphere heat fluxes in autumn and winter. This is consistent with the results of model runs under increasing CO_2 performed by Graham and Vellinga (2013) who found increased heat flux from the ocean to the atmosphere in regions of sea ice loss. Screen *et al.* (2012) conducted AGCM experiments for the 20th century and highlighted sea ice as causing warming below 700 hPa, but suggested that remote SSTs and their effect on poleward heat transports were important for upper levels.

Amplified high latitude warming was also linked to the surface albedo feedback (from both snow and ice) in earlier 2xCO_2 experiments (Hall, 2004; Manabe and Wetherald, 1975). The configuration in Manabe and Wetherald (1975) was simple, such that high

latitudes were specified as land, and here the snow albedo feedback was discussed as a driver of AA.

Bengtsson *et al.* (2013) found increased poleward moisture transport into the northern polar region in the 21st century in a climate model simulation. The resulting increase in net downward longwave radiation combined with an increased net shortwave radiation at the surface (consistent with reduced sea ice) contributed to an increased net surface flux into the ocean in summer. The release of this extra heat in winter contributed to winter Arctic warming, implying that both local sea ice processes and poleward heat and moisture transports contributed.

Regarding recent Arctic warming, dynamical links from the tropics have been studied. Lee *et al.* (2011) analysed the processes leading to the increase in winter Arctic surface temperature between 1958–1977 and 1982–2011 in reanalysis data. They found that poleward heat flux by stationary eddies and adiabatic descent, rather than local feedback processes, were dominant for warming over ice (although longwave fluxes were found to be dominant over open water). Further, they found that the associated extratropical circulation changes were linked with an increase in positive phases of the Pacific/North American pattern, which in turn was lag-correlated with increased tropical convection in the West Pacific on short timescales. They therefore hypothesised that Rossby waves triggered by anomalous tropical convection may contribute to Arctic warming.

Ding *et al.* (2014) specifically investigated causes of observed annual-mean warming throughout the troposphere in East Canada and Greenland. Evidence from reanalysis data suggested that SST anomalies in the tropical Pacific triggered a Rossby wave train, affecting the NAO and East Canada/Greenland temperatures. Based on a single-model ensemble forced with observed tropical SSTs, they hypothesised that while half of the observed warming was likely linked to externally-forced Arctic-wide warming, the other half could be linked to Rossby waves emanating from the central tropical Pacific. However, the wave trains in the model and observations have notable differences. The focus of Ding *et al.* (2014)- a deep, local, annual mean warming- is somewhat different from the characteristic near-surface, Arctic-wide, winter amplification discussed in most studies. It does however provide evidence that Arctic warming is affected by remote changes. Also finding evidence of remote influence, Sato *et al.* (2014) found that in reanalysis data, an anomalously warm Barents Sea in December is associated with a Rossby wave train

triggered by a poleward shifted Gulf Stream.

Pithan and Mauritsen (2014) investigated the causes of AA in 4xCO_2 CMIP5 runs. They found that temperature feedbacks were dominant, followed by the albedo feedback related to sea ice loss. The first of these temperature feedbacks was the nonlinear dependence of radiation on temperature; black body radiation scales as T^4 according to Planck's law, so a colder body will need to increase its temperature more to balance a given radiative forcing. The second was the difference in lapse rate feedbacks between the stable Arctic environment and the convective tropical environment. However, it is not clear whether the mechanisms would have the same relative importance under smaller radiative forcings (such as that in the satellite era, or the 21st century).

In summary, feedbacks associated with ice cover are one of the key components in AA (Serreze and Barry, 2011), but longwave feedbacks also play a dominant role (Pithan and Mauritsen, 2014). However, changes in poleward heat transport, either throughout the Arctic due to externally forced change (Bengtsson *et al.*, 2013) or tropical convection (Lee *et al.*, 2011), or locally due to Rossby wave propagation from lower latitudes (Ding *et al.*, 2014; Sato *et al.*, 2014), can also affect Arctic temperatures.

2.2.2 Land/sea warming contrast

Globally, land areas warm more than ocean areas (e.g. Boer, 2011). The ratio of land to ocean warming has been found to be relatively constant over time (Joshi *et al.*, 2013). It is therefore likely to be attributable to processes other than thermal inertia (Collins *et al.*, 2013) and has been linked to differing lapse rate feedbacks over land and ocean (e.g. Joshi *et al.*, 2008) and cloud feedbacks.

The idea of disparate warming also arises in the Cold Ocean-Warm Land (COWL) pattern (Randall *et al.*, 2007). This describes the phenomenon that when the Northern Hemisphere is anomalously warm, land areas north of 40°N warm more than the oceans. The COWL pattern is a signature of natural climate variability. However, the structure of the forced trend in surface temperatures bears many similarities to the COWL pattern, and a trend in COWL was observed in the second half of the twentieth century (Broccoli *et al.*, 1998).

2.2.3 Upper tropospheric warming pattern

In the upper troposphere, a rather different pattern of mean warming emerges; in GCM projections of 21st century warming, there is enhanced warming in the tropical upper troposphere (approximately 400 hPa to the tropopause; Collins *et al.* (2013) Figure 12.12.) Under RCP4.5, for the period 2081–2100, the upper-level warming maximum exceeds the surface warming by approximately a factor of 2 (Figure 2.2b).

This feature was also present in earlier multi-model ensembles, such as that used in IPCC AR4, and has a robust physical basis. A saturated parcel raised through the atmosphere cools, and as it does so the water within it condenses out, releasing heat and offsetting the cooling. It therefore cools at the moist adiabatic lapse rate, which is less than the dry adiabatic lapse rate. The Clausius-Clapeyron relationship (e.g. Ambaum, 2010b) implies that a warmer parcel becomes saturated at a higher water content and therefore 'contains more water'; therefore it is able to offset more of the cooling. Therefore there is a reduction in the moist adiabatic lapse rate in a warmer environment. This results in a decreased temperature gradient between the surface and upper levels, i.e., relatively more warming aloft.

While models suggest enhanced tropical upper tropospheric warming should already be evident in observations, the observed tropospheric warming is much lower than model estimates in both CMIP3 and CMIP5 (Flato *et al.*, 2013). Part of the model overestimate is due to overestimations in the model SST trend, but there are also large observational uncertainties in upper tropospheric temperatures (Flato *et al.*, 2013). Therefore it is challenging to ascertain to what extent model simulations of tropical tropospheric warming are consistent with recent change.

2.2.4 Lower stratospheric warming pattern

Finally, there was an observed cooling in the southern hemisphere polar lower stratosphere between 1960 and 2000 (e.g. Wilcox *et al.*, 2012). This was caused by both stratospheric ozone depletion and greenhouse gas increases. In simulations of the 21st century, CMIP5 models show a lower stratospheric warming in the period 2000–2050, when the warming effect of ozone recovery and cooling effect of greenhouse gas increases compete; for later decades, a lower stratospheric cooling is projected (Wilcox *et al.*, 2012).

This feature of the warming pattern is not central to this thesis, as it is at upper levels and restricted to the southern hemisphere. It is mentioned here because it is important for understanding observed and projected changes in the southern hemisphere jet stream which are discussed briefly below to provide context.

2.3 The Atmospheric Jet Streams

2.3.1 Observed characteristics

The jet streams are one of the characterising features of the Earth's atmospheric circulation (Holton, 2004). There are two types of jet found in the midlatitudes, the subtropical and eddy-driven jets. The subtropical jet found at the boundary of the Hadley cell arises due to angular momentum conservation of air in the upper branches of the Hadley cell (Held and Hou, 1980) and is characterised by a strong vertical wind shear. The eddy-driven jet is found further poleward and takes its name from the eddies which grow in the baroclinic region which in turn produce momentum fluxes which drive the jet (e.g. Li and Wettstein, 2012). It has a deeper structure and is associated with a near-surface wind maximum. There is often only one jet stream, combining these processes (Lee and Kim, 2003), but it can be useful to discuss the mechanisms separately.

The climatological zonal mean circulation in each hemisphere displays a single jet, evident as a localised region of high wind speeds (Figure 2.3 a and b), combining subtropical and eddy-driven features. (There is some evidence of a split jet in southern hemisphere winter.) The mean zonal wind in winter has a maximum of approximately $40\,ms^{-1}$ at around 30° latitude and 200 hPa, corresponding to the top of the troposphere and the edge of the tropics. In summer, the jet is weaker and its maximum is found further poleward.

The northern hemisphere in particular contains large zonal asymmetries so the jet stream is localised (Figure 2.3 c). In Figure 2.3 d, the zonal averaging is performed only over the Atlantic sector (300 to 360° E) and the separation of the subtropical and eddy driven jet is evident.

2.3.2 Mechanisms: subtropical jet

The subtropical jet (STJ) exists because of angular momentum conservation in the Hadley cell. The Hadley cell [6] is the bouyancy driven overturning circulation in the tropical atmosphere, associated with ascent near the equator in the summer hemisphere and descent in the subtropics (e.g. James, 1995).

Held and Hou (1980) presented an analytical model for the width and strength of the Hadley cell and hence also the position and strength of the STJ. This assumes a dry, hemispherically symmetric and axisymmetric atmosphere with no friction in the upper atmosphere. It is assumed that the flow is driven by relaxation to a specified radiative equilibrium profile. Secondly, the zonal wind is assumed to be near-zero at the equator, and the assumption of angular momentum conservation as air moves poleward gives an upper-level latitudinal zonal wind profile. This zonal wind must be in thermal wind balance with meridional temperature gradients, so, assuming that wind is zero at the sur-

[6] The Hadley cell is named after George Hadley who proposed it as the mechanism leading to the observed equatorward direction of the trade winds near the surface, although Edmund Halley had earlier proposed the existence of an overturning motion (James, 1995)

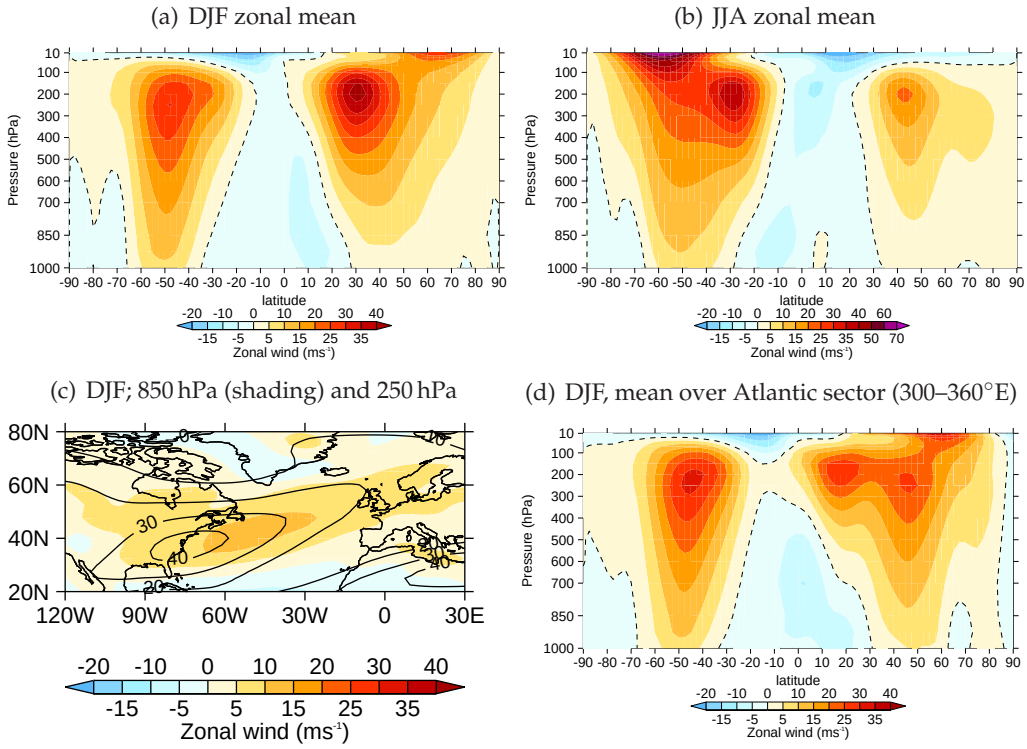

Figure 2.3: Climatological zonal wind (ms^{-1}) for 1981–2010; a) DJF zonal mean; b) JJA zonal mean; c) DJF at upper (250 hPa, contours) and lower (850 hPa, shading) levels; d) DJF zonal mean in Atlantic sector. Data from the NCEP/NCAR reanalysis (Kalnay *et al.*, 1996).

face due to friction, a second temperature profile is obtained. However, this temperature profile is cooler at the equator and warmer in the subtropics than the equilibrium profile specified previously (Held and Hou, 1980, Figure 4), consistent with the thermally direct circulation acting to transport warmth polewards. This same comparison leads to determination of the width of such a circulation, since the model assumptions must break down at the latitude poleward of which further net radiative heating is implied. The subtropical jet strength in this analytical model is given by the zonal wind at this latitude.

These arguments lead to an estimated Hadley cell which is slightly too narrow with respect to observations, and a jet which is too strong and has a wind discontinuity at the boundary. However, allowing frictional dissipation in the atmosphere reduces the wind speed and relaxes the discontinuity (James, 1995). Moisture considerations improve the representation of the Hadley cell structure, localising the region of heating and ascent and broadening the region of descent (James, 1995).

A slightly different interpretation of what sets the Hadley Cell terminus comes from assessing the latitude at which the circulation implied by the above arguments becomes baroclinically unstable to perturbations (e.g. Frierson *et al.*, 2007; Korty and Schneider, 2008). In particular, this onset of baroclinic instability may occur at a lower latitude than that of the predicted Hadley Cell terminus under the Held Hou model. Frierson *et al.* (2007) found that a scaling built on this argument, using a critical value of wind shear for the onset of baroclinic instability, predicted the Hadley Cell width well in both simple and complex GCMs except for very warm or cold conditions. However, Korty and Schneider (2008) argued that while the concept of baroclinic instability onset is crucial, arguments using critical wind shear to predict this onset did not agree with experimental results in a dry GCM. Both studies found a measure of the tropical static stability to be key in predicting the width of the Hadley Cell, and O'Gorman (2011) incorporated the effect of moist processes into the estimation of this static stability.

2.3.3 Mechanisms: eddy-driven jet

The second driving mechanism for the jets is eddy momentum forcing by transient eddies. The midlatitudes are regions of strong temperature gradients, or equivalently (by thermal wind balance) vertical wind shear. They are therefore highly baro-

clinic; density and pressure surfaces are not parallel. Such regions can be baroclinically unstable, i.e., unstable to disturbances which generate vorticity through baroclinic processes (Holton, 2004). Such disturbances are variously referred to as baroclinic waves/modes/disturbances, storms, cyclones, or transient eddies, and the regions of maximum storm activity known as the storm tracks. Their growth is characterised by baroclinic processes which convert available potential energy into eddy (zonally asymmetric) kinetic energy (Simmons and Hoskins, 1978). Their decay is characterised by barotropic processes which convert this eddy kinetic energy into zonal kinetic energy (Simmons and Hoskins, 1978). Through these processes, westerly momentum is transported into the region (Held, 1975; Hoskins *et al.*, 1983), as discussed in the following paragraphs. These processes, whereby the mean flow determines the growth and propagation of disturbances which in turn modulate the flow, are referred to as wave-mean flow interaction.

2.3.3.1 Disturbance growth and lifecycle

The growth of such midlatitude disturbances was investigated by Eady (1949) under the assumption of adiabatic, frictionless motion and convective stability. The analysis reveals that in a simple case of flow between rigid boundaries and under certain assumptions, the growth rate of eddies is determined by the parameter

$$\sigma_{BI} = \frac{bf}{N}\frac{\partial \overline{U}}{\partial z} \tag{2.1}$$

The maximum value of b at which growth occurs is shown in Eady (1949)[7] to be b=0.3098, therefore with this value of b the equation identifies the regions most unstable to baroclinic disturbances. This can be used to approximate the location of the atmospheric storm tracks (Hoskins and Valdes, 1990).

The behaviour of the arising eddies or storms has been examined extensively in lifecycle experiments. In particular, Simmons and Hoskins (1978) introduced normal mode disturbances of wavenumber 6 to a baroclinically unstable jet, analysing the eddy fluxes, energy conversions, and modifications to the basic flow. Their results confirm the general picture of baroclinic growth and barotropic decay as discussed above. The relative

[7] b was denoted β in Eady, 1949 but is given different notation here to avoid confusion with $\beta = \frac{df}{dy}$).

importance of momentum fluxes $\overline{u'v'}$ to heat fluxes $\overline{v'T'}$ increases through the disturbance, such that the heat fluxes are more associated with the growth and the momentum fluxes with decay. Such fluxes, then, provide another description of the storm tracks. In the zonally localised North Atlantic storm track, the heat flux maximum is concentrated upstream while the momentum flux maximum is concentrated downstream, consistent with the lifecycle discussed above (Chang *et al.*, 2002; Novak *et al.*, 2015).

2.3.3.2 Wave-mean flow interaction

Eliassen-Palm Flux

The merit of considering heat and momentum fluxes extends beyond visualising the storm tracks. These fluxes describe the transport of heat and momentum by the eddies which act to accelerate the mean flow and a mathematical formalism can be developed in which their structure determines the effect of the eddies/waves on the mean flow.

This formalism introduces the Eliassen-Palm (EP) flux **F** (Edmon *et al.*, 1980), expressed in the y-p co-ordinate system as

$$\mathbf{F} = (F_y, F_p) = (-[u^*v^*], f\frac{[v^*\theta^*]}{\theta_p}) \tag{2.2}$$

where the subscript p with no brackets denotes differentation with respect to p (Edmon *et al.*, 1980). The divergence of the EP flux is a powerful diagnostic, describing the acceleration of the mean zonal flow by the eddies.

Physically understood, the meridional momentum fluxes (horizonal component) transfer momentum into the region from other latitudes and correspond to a barotropic acceleration of the flow (e.g. Holton, 2004). The meridional heat fluxes (vertical component) mix the horizontal temperature gradients which led to the disturbance. In decreasing the meridional temperature gradient they also reduce the vertical wind shear, by thermal wind balance, and therefore drive a transfer of momentum down through the atmospheric column.

Eddy feedbacks on the 3 dimensional flow: the E-vector

A three dimensional extension to the EP flux is given by the E-vector **E** (Hoskins *et al.*,

1983), given in pressure co-ordinates by the expression

$$\mathbf{E} = (\overline{v'^2 - u'^2}, -\overline{u'v'}, f_0 \frac{\overline{v'\theta'}}{\theta_p}) \tag{2.3}$$

This is formulated with respect to deviations from the time mean rather than zonal mean flow, such that it is appropriate to three dimensions. In analogy to the EP fluxes, the divergence of the E-vector quantifies the westerly acceleration of the flow by transient eddies. The two horizontal terms were shown in Hoskins *et al.* (1983) to represent the eddy anisotropy. Therefore there is a physical link between these terms and the deformation of eddies, or alternatively breaking of waves.

Hoskins *et al.* (1983) also noted that the magnitude of the low-level poleward heat flux (e.g., at 700 hPa) and the direction of the upper tropospheric horizontal E-vector provide a good insight into a complete picture of the eddy structure and the effect on the mean flow.

Rossby wave breaking

Rossby waves are wave solutions in the atmosphere arising for example as solutions to the quasi-geostrophic vorticity equation (James, 1995). The dispersion relationship for barotropic Rossby waves is given by $\omega = \overline{u}k - \frac{\beta k}{K^2}$ (where k is zonal wavenumber, $K = \sqrt{k^2 + l^2}$ is total wavenumber, and β is the meridional gradient of planetary vorticity). The zonal phase speed c_p is given by $c_p = \frac{\omega}{k} = \overline{u} - \frac{\beta}{K^2}$, so Rossby waves always propagate westward relative to the mean flow. The wave properties are dependent on the background flow. In particular, waves break at their critical latitude where $c_p = \overline{u}$ and are reflected meridionally at the turning latitude at which k=K. As discussed above, Rossby wave breaking is associated with dynamical feedbacks on the jet, as discussed in the previous section.

The Rossby wave group velocity is $\{c_{gx}, c_{gy}\} = \{\frac{\partial\omega}{\partial k}, \frac{\partial\omega}{\partial l}\} = \{\overline{u} - \frac{\beta(l^2-k^2)}{(k^2+l^2)^2}, \frac{\beta kl}{(k^2+l^2)^2}\}$. Since energy or information travels at the group velocity, it is these expressions which are related to the EP flux. For example, it can be shown that convergent meridional momentum fluxes (horizontal EP flux divergence) arise when wave energy flux is divergent; equivalently when c_{gy} is divergent such that waves are propagating meridionally out of a region (e.g. Holton, 2004).

2.3.4 Asymmetries: theory and modelling

The observed time-mean atmospheric flow is not axisymmetric, but displays notable zonal variations (e.g. Figure 2.3c). This section describes theoretical arguments for the origins of this asymmetry, in particular asymmetries in land, orography and SST, and linear 'stationary wave model' results. The following section (2.3.4.3) discusses GCM studies which have examined the relative importance of these factors, particularly in the North Atlantic.

2.3.4.1 Stationary Rossby wave theory

Stationary Rossby wave theory is a key tool for understanding the time-mean zonal variations in the observed atmospheric flow. Stationary Rossby waves have phase speed $c_p = 0$, such that the total stationary wave number is given by (rearranging the relationship above) $K = \sqrt{\frac{\beta}{\bar{u}}}$. Thermal and mechanical forcings which cause a vorticity perturbation lead to such features.

Hoskins and Karoly (1981) investigated the response to thermal and orographic forcing asymmetries, including such Rossby waves, in a linear, steady, five-layer baroclinic model. The model was linearised around the northern hemisphere winter flow. For a midlatitude low level heat source, the heating is balanced by horizontal advection, and a surface trough develops downstream. For an orographic source, the (upper level) response is of a ridge on the upslope and a trough on the downslope, and two downstream wavetrains propagating roughly East and South-East. Later authors examined in more detail the extent to which such linear theory explained the full winter flow; in particular, Held *et al.* (2002) discussed the successes and limitations of this linear stationary wave modelling framework. They demonstrated that the linear response to orography and observed heat sources and transient heat fluxes reproduces many elements of the main stationary wave peaks and troughs in the northern hemisphere January circulation. However, there are notable differences between the linear and nonlinear responses.

2.3.4.2 Linear versus nonlinear response to heating

As discussed in the previous section, the linear response to zonally localised extratropical heating is the direct thermodynamic response, whereby a local heating is balanced by

horizontal advection (Hoskins and Karoly, 1981). It is baroclinic, with a surface (warm) low and a high in the mid troposphere. Kushnir *et al.* (2002) discussed the extent to which this response (termed variously as the 'direct' or 'thermodynamic', linear baroclinic response) extends to the nonlinear case. In the full nonlinear response, there is a modification in the local storm track as a result of the local heating anomalies. These changes in the transient eddies interact with the mean flow, leading to the nonlinear 'indirect' eddy mediated response which may be fundamentally different in character to the linear response. For example many GCM studies produce an equivalent barotropic high pressure in response to a positive SST anomaly. Moreover, linear models forced with the transient eddy response to an SST heating are able to recreate the full nonlinear response (Kushnir *et al.*, 2002).

2.3.4.3 GCM studies

Several studies have sought to understand the Northern Hemisphere winter circulation, and the relative importance of different boundary asymmetries, using GCMs forced with simplified lower boundary conditions. Forcings have included SST anomalies of fixed wavenumber in the tropics or extratropics (Inatsu *et al.*, 2000, 2002b, 2003; Brayshaw *et al.*, 2008) and simplified land and orography (Inatsu *et al.*, 2002a; Cash *et al.*, 2005; Wilson *et al.*, 2009; Chang, 2009; Brayshaw *et al.*, 2009; Saulière *et al.*, 2012; Kaspi and Schneider, 2013). Here, attention is restricted mainly to extratropical forcing.

Aquaplanet Modelling

Many of the following studies refer to aquaplanet AGCMs. These are AGCMs in which the Earth surface is assumed to be entirely ocean. In general, SSTs are specified (although some aquaplanet studies such as Kaspi and Schneider (2013) couple the atmospheric model to a slab ocean, which has no dynamics but does have a specified local energy balance). Neale and Hoskins (2000b) proposed a framework in which atmospheric models are evaluated and compared according to their simulation of climate in an aquaplanet with zonally symmetric fixed SSTs. In this way, complexities associated with different treatment of land surface and orographies are not considered. However, the full complexity of the atmospheric model is retained, including the dynamical core, moist processes, and physical parametisations of unresolved processes.

Aquaplanet models have been exploited extensively to investigate the atmospheric response to zonally symmetric SST anomalies (e.g. Caballero and Langen, 2005; Brayshaw *et al.*, 2008) and asymmetric SST anomalies (e.g. Inatsu *et al.*, 2000; Brayshaw *et al.*, 2008).

The series of papers by Inatsu *et al.* investigated the responses to several asymmetries in a GCM at T42 resolution under perpetual January conditions. Inatsu *et al.* (2002b) found that in an aquaplanet, tropical SST asymmetries were dominant in setting up stationary waves, while a zonal wavenumber-1 extratropical SST anomaly dipole around 40°N had a weaker effect on stationary waves but produced a deep asymmetric storm track. Furthermore, the study of Inatsu *et al.* (2003) showed that the response to wavenumber-1 extratropical SST asymmetries was sensitive to the latitude of the imposed anomaly, and was stronger when the anomaly was centred at 30°N or 40°N than at 50°N. They found competing effects of $\frac{\partial T}{\partial y}$ and vertical stability to be a cause of the sensitivity. Brayshaw *et al.* (2008) also found that the storm track response to zonal wavenumber-1 extratropical SST perturbations was very sensitive to the latitude of the surface temperature gradient anomaly.[8]

Inatsu *et al.* (2002a) investigated the relative responses to tropical SST monopoles, extratropical land-sea contrast, and a broad mountain (of zonal extent 180°). The land had a limited effect on the stationary eddies, consistent with the earlier finding by the same authors (Inatsu *et al.*, 2000) that tropical SST anomalies rather than extratropical land-sea contrast were dominant in localising the upper level subtropical jet. Inatsu *et al.* (2002a) also found that orography created stationary eddies. However, the zonal extent of the mountain is not particularly representative of anything observed in reality.

Gerber and Vallis (2009) investigated possible drivers of North Atlantic circulation features in a dry GCM. They introduced a zonally localised mountain of 1000–3000 m in height and a zonal cooling/warming dipole to simulate the effect of the North American/North Atlantic coast. The orographic feature introduced a standing wave pattern, characterised locally by an upstream ridge (to the north-west) and downstream trough (to the south and east). Such a feature was also found in response to orography in the study of Cash *et al.* (2005) and is similar to the linear response discussed in Hoskins and Karoly (1981).

[8]The response to SST anomalies, in particular the role of surface fronts, is discussed later in the chapter.

Wilson *et al.* (2009) considered the effect of ocean dynamics and orography on northern hemisphere storm tracks by removing these elements from an otherwise realistic model. The localisation of atmospheric transient heat fluxes is retained when the land distribution is retained but neither orography nor ocean dynamics is included. However, orography was required to introduce damping of storm tracks over land, and the ocean dynamics and their effect on SST in order to give a realistic latitude of the storm tracks. Chang (2009) investigated the relative importance of diabatic forcing (tropical and extratropical asymmetric heating distributions) and orographic forcing (Tibet and the Rockies) in a dry GCM. Again, different components were found to be important for different fields: orographic forcing was crucial for producing asymmetry in the upper-level streamfunction, while both heating and orography contributed to low-level asymmetries. The extratropical heating, however, was key for the storm tracks.

Three papers by Brayshaw *et al.* built on many of the above ideas by investigating the effect of more tailored boundary forcings. Brayshaw *et al.* (2009) found a weak localisation of storm tracks from idealised extratropical land surfaces (Eurasia and North America) alone, with storm tracks weakened over land. This was associated with reduced moisture availability and frictional damping, although strong baroclinicity over land associated with differential heating and frictional restoration of vertical wind shear acted in the opposite direction. Moreover they found a downstream effect of continents with enhanced baroclinicity 'advected' over the oceanic moisture source seeding storm growth. The addition of 'Rocky mountains' enhanced this effect due to the existence of a cold pool in the lee of the mountain, interacting constructively with gradients associated with the tilted American coast to produce strong storm tracks. The Rockies were also fundamental in producing stationary waves in the northern hemisphere.

Brayshaw *et al.* (2011) investigated the response to tightened midlatitude SST gradients associated with the Gulf Stream and slackened midlatitude SST gradients associated with North Atlantic drift. They found that the change in baroclinicity associated with these gradients, rather than diabatic effects associated with the temperature anomaly, dominated the response of the storm tracks and therefore the jet. Finally, Saulière *et al.* (2012) added Tibetan orography, a tilted Eurasian coastline and the Kuroshio current, all features expected to be key to the Pacific storm track. They found Pacific responses consistent with many of the results in Brayshaw *et al.* (2009, 2011) as well as a remote re-

sponse in the Atlantic. This could be associated with either interacting stationary waves from the orographic features, or with changes in the response to the Rockies given reduced incident flow associated with orographic drag.

The above results (e.g. Wilson *et al.*, 2009) suggest that frictional damping downstream is required to terminate a storm track. In contrast, experiments by Kaspi and Schneider (2013) where a simplified GCM was coupled to a slab ocean with specified local heat flux convergence contained zonally localised storm tracks despite no such damping. The length of the storm track in these experiments was set by the length scale of the stationary eddy triggered by the forcing.

In summary, orographic features such as the Rocky mountains and Tibet have generally been found to be crucial for creating the characteristic stationary waves in the Northern Hemisphere, as well as localising the storm tracks due to enhanced baroclinicity downstream of the orography. On the other hand, asymmetric heating distibutions associated with SST asymmetries and the land-ocean contrast are more fundamental for asymmetries in the storm track. However, these studies typically contain an isothermal cap in the polar regions. No study has used such a framework to investigate the atmospheric response to sea ice loss or, more fundamentally, assessed the effect of sea ice on these large scale atmospheric responses to midlatitude lower boundary asymmetries; most have treated the polar surface as an isothermal cap.

2.3.4.4 Response to extratropical local SST anomalies

The previous section has discussed the role of various asymmetric forcings on the atmospheric mean state, including the role of SSTs in time-mean atmospheric asymmetries. There is also a substantial body of literature on the effect of local SST anomalies on the atmosphere. Two themes from both bodies of literature are discussed here; first, the hypothesis that it is local SST fronts rather than the anomaly themselves which are dynamically important, and secondly that the response to an anomaly is sensitive to season. Both themes are particularly relevant for the understanding of the impact of sea ice anomalies on the atmosphere.

SST fronts

Reanalysis data has been used to demonstrate that the SST front associated with the Gulf Stream has a strong influence particularly on local climate (Minobe *et al.*, 2008). This

occurs through triggering of a surface pressure adjustment by the SST front, causing wind convergence and consequently vertical motion. This in turn is associated with precipitation over the front. A similar response was found in the modelling study of Brayshaw *et al.* (2011).

In addition, Brayshaw *et al.* (2008) highlighted the importance in their studies of the latitude of the surface temperature gradient anomaly, and therefore the baroclinicity anomaly, for determining the storm track response to extratropical SST anomalies. This finding implies the importance of eddy feedbacks, rather than the linear response (Section 2.3.4.2), for the response to an SST anomaly, as well as the importance of the surface front itself.

Response sensitivity to season and location

Another key theme highlighted in the review of Kushnir *et al.* (2002) was the sensitivity of the atmospheric response to the background state (which varies for example with season) and to the location of the forcing relative to the background state. For example, Ting and Peng (1995) investigated the response to a North Atlantic SST anomaly at 50°N 40°W for January and November insolation and SST in an AGCM, and further in a linear baroclinic model. The response is sensitive to the mean flow, being cyclonic in January but anticyclonic in November.

In addition as already discussed the exact location of the forcing affects the response (Brayshaw *et al.*, 2008; Inatsu *et al.*, 2003). Other sensitivities may also be important- even in linear theory, the response is sensitive to the details (spatial extent, depth and latitude) of the heating (Hoskins and Karoly, 1981).

2.3.5 Variability and impacts

2.3.5.1 Modes of variability: definition

The jet stream and its variability is intimately related to atmospheric modes of variability, which describe spatially coherent patterns of geopotential height or atmospheric pressure (and therefore winds) in a sector or hemisphere. They include, but are not restricted to, the Southern Annular Mode (SAM) in the southern hemisphere (Thompson and Wallace, 2000), the Arctic Oscillation (AO) in the northern hemisphere (Thompson and Wallace, 2000) and the North Atlantic Oscillation (NAO) for the North Atlantic and western Eu-

rope (Hurrell *et al.*, 2003). These modes are relevant on timescales of several days to decades.

One of the most common methods for defining these modes is Empirical Orthogonal Function (EOF) analysis (also called Principal Component Analysis). This is a statistical analysis of a timeseries of spatial data which isolates the patterns which describe most of the variance in the timeseries (Wilks, 2005). The principal component (PC) timeseries is the timeseries of the projection of the anomaly field onto this EOF pattern.

Following this methodology, one common index of the NAO (the leading pattern of atmospheric variability in the North Atlantic) is the first PC of SLP in the domain 20–80°N, 90°W–40°E (Hurrell, 2015). This index defines over 40% of variance in DJF, or over 30% annually. The AO and SAM are defined as the leading modes of variability in winter near-surface geopotential height poleward of 20°(Thompson and Wallace, 2000). The AO describes 20% of the variance in SLP and 45% of the variance in zonal-mean geopotential height in the NH, while the SAM in the SH explains slightly higher percentages of the variance.

An alternative method is to construct teleconnection maps displaying for each point the maximum correlation with any other point. The main 'centres of action' can then be isolated from these maps; the index is taken to be the pressure difference between the two main centres of action. The pressure difference may instead be taken between two locations with long historic SLP records which are known to vary in phase; for the NAO such locations are Lisbon (or the Azores) and Reykjavik (Hurrell *et al.*, 2003). This method allows construction of long timeseries, and is non-data-intensive. However, it is a simple measure, and differences in the location of the centres of action will not be captured (Hurrell *et al.*, 2003). Despite this, an index based on this 'station difference' is typically highly correlated with a PC index ($r>0.9$ for winter and annual indices; Hurrell, 2015). Results are therefore unlikely to be highly sensitive to the methodological detail.

2.3.5.2 Modes of variability: relationships with the jet

These modes of variability (NAO, SAM, AO) essentially represent jet variability (e.g. Woollings *et al.*, 2010). The sign convention is that the positive phase refers to anomalously low pressure/geopotential in the poleward centre of action and anomalously high pressure/geopotential in the equatorward centre of action. Therefore, the positive phase

describes an anomalously strong gradient of geopotential, and, simply understood, an anomalously strong and poleward jet stream.

However, there are arguments that this is an over simplification. As demonstrated by Monahan and Fyfe (2006), EOFs cannot truly separate physical variability- shifts, pulses and width alterations- since these physical structures are not orthogonal. Therefore care is required when interpreting the physical meaning of an EOF. Woollings *et al.* (2010) investigated the relationship of the NAO and EA (East Atlantic) patterns with an index of jet latitude and strength in the ERA-40 reanalysis. Here, the NAO and EA were defined as the first and second EOFs of monthly mean 500 hPa geopotential heights in the North Atlantic and Western Europe. It was found that, while negative NAO corresponded to a southerly jet stream, knowing the state of one of the PCs is in general insufficient to determine the jet position and strength. Equivalently, the EOFs again combine changes in jet position and strength, rather than isolating one or the other.

Another possible simplification is that the AO and SAM are often referred to as 'annular modes'. However, this interpretation has been questioned; Ambaum *et al.* (2001) demonstrated that EOFs do not necessarily represent physical structures in the underlying data. In particular, they found that:-

- the AO based on reanalysis SLP has equally-signed centres in the North Pacific and Atlantic but this does not correspond to correlations in SLP between these sectors

- regionally-defined EOFs of different variables were dynamically consistent with one another but hemispherically-defined EOFs were not.

These results suggest that the NAO is a physically more meaningful construct than the annular modes. Cash *et al.* (2002) found that while EOFs defined in an aquaplanet were zonally symmetric, individual events associated with high PC index were localised at different longitudes. The EOF structure represented the average of these equally likely events, rather than a tendency for the whole hemisphere to vary in phase. This argument is consistent with that of Ambaum *et al.* (2001).

Both these findings- the lack of a direct physical interpretation of an EOF structure and the difference between regional and annular modes- demonstrate that care must be taken when interpreting the physical meaning of an EOF structure or EOF-like anomaly.

2.3.5.3 Impacts

The jet stream and storm tracks play a crucial role in the weather and climate of mid-latitudes. This is particularly true for the northern hemisphere midlatitude continents and can be seen both in climatological relationships and in case studies. These impacts can often be well described by relationships between the variables in question and the dominant regional mode of variability.

The review by Hurrell *et al.* (2003) provides a valuable summary of the impacts of the NAO as observed in the second half of the twentieth century. During this period, positive NAO winters were associated with a poleward shift of the storm track, increased precipitation–minus–evaporation (P-E) in the north east Atlantic (Iceland, the UK and Scandinavia) and south west Atlantic and reduced P-E elsewhere. Anomalously warm temperatures in northern Europe and Eurasia are also associated with positive NAO. The possible impacts of the NAO and AO on sea ice have already been described (Section 2.1.5.3). Other documented variability associated with the NAO includes variability in wave height (Hurrell *et al.*, 2003) and wind speeds (Ely *et al.*, 2013). However, not all winters are well described by the NAO.

The storm tracks are also important for extreme weather events; it has been estimated that between 60–80% of short timescale precipitation extremes in the densely populated areas of North Europe, Japan, and North East America, are associated with cyclones (Pfahl and Wernli, 2012b).

The winter of 2013/14 provides an excellent recent example of the impacts of these large scale circulation patterns. In January 2014, eastern North America experienced strongly anomalous cold temperatures while the UK experienced warm and stormy conditions (Slingo *et al.*, 2014). The cold temperatures in America were caused by a particularly strong deflection of the jet northward at the west coast of America and resulting cold advection southwards from Canada in the downstream jet stream. Meanwhile a particularly strong Atlantic jet (related in part to this anomalously cold air causing stronger-than-normal temperature gradients in the West Atlantic) was associated with the passage of storms over the UK, heavy precipitation and high storm surges (Slingo *et al.*, 2014).

2.3.6 GCM representation

As mentioned above (e.g. section 2.3.4), the broad characteristics of atmospheric jets and stationary waves can be reproduced by relatively simple configurations. Depending on the problem studied, the atmosphere might be assumed to be dry, barotropic, linear, or have very simple parameterisations of friction. However, these are obvious simplifications of the real climate system. The best tools available to the climate community for accurately simulating the Earth's atmosphere are fully coupled GCMs, containing a dynamic ocean and coupled components for land and sea ice, land surface, and vegetation. Such models are used for climate projection, for example in the experiments contributing to the IPCC process (Flato *et al.*, 2013).

However, even these coupled GCMs have biases in their representation of the jet streams. The CMIP5 ensemble (Barnes and Polvani, 2013) typically simulates annual-mean low level zonal wind maxima (representing the eddy-driven jet) which are too far equatorward in both the North Atlantic and Southern Hemisphere. An equatorward bias is also evident in the summer southern hemisphere in the mid troposphere in CMIP5 (Wilcox *et al.*, 2012), and at lower levels in the southern hemisphere (Kidston and Gerber, 2010) and the North Atlantic (Woollings and Blackburn, 2012) in CMIP3. Woollings and Blackburn (2012) also documented insufficient tilt and a too-strong bias in the North Atlantic jet stream. The CMIP ensembles in both phases also display significant inter model variability (Kidston and Gerber, 2010; Woollings and Blackburn, 2012; Barnes and Polvani, 2013).

As expected from the above discussions, jet biases are accompanied by biases in the storm track position. Low-level winter storm tracks in the North Atlantic in many CMIP5 models are too zonal or too equatorward, although there is a general improvement since CMIP3 (Zappa *et al.*, 2013b). An upper level winter bias was reported in Chang *et al.* (2012) but this did not separate the northern hemisphere ocean basins. For summer, both studies found that the storm track latitude was generally well represented, while Zappa *et al.* (2013b) reported a negative strength bias.

Therefore, model representation of the jet and storm track in particular in the North Atlantic is improving but biases remain. This is of concern when using climate models to simulate future change. Therefore it is essential to use methods other than future climate projections in GCMs in order to obtain the best possible understanding of the future, for

example experiments with simplified forcings which build understanding of processes.

2.3.7 Observed and projected changes

Due to their impacts on the weather and climate of midlatitudes, it is important to establish what changes in the jet and associated features might be expected as a result of anthropogenic forcing. It is also of interest to establish what, if any, observed variability can be attributed to human behaviour.

The jet streams and associated features are highly variable systems, displaying inter-decadal variability (Woollings *et al.*, 2014). Therefore, even seemingly 'large' trends, as recently observed, may not be a signature of any external forcing but only a manifestation of internal variability. For example the NAO displayed positive trends between 1960 and 1990 but this trend has appeared to reverse since (Hartmann *et al.*, 2013). It is therefore challenging to draw conclusions about the robustness and cause of changes for which data is available only since the late 1970s, when satellite observations became commonplace. However, there is some evidence of a poleward shift in observations of the North Atlantic storm track (Hartmann *et al.*, 2013).

In GCM simulations of future change, Woollings and Blackburn (2012) found a projected poleward shift in the EDJ in the North Atlantic in CMIP3, but the response was robust only in summer. This is in contrast to the southern hemisphere, where Kidston and Gerber (2010) found a robust projected poleward EDJ shift in all seasons except summer. They suggested that the summer discrepancies between models were due to differing stratospheric ozone, the effects of which are largest in summer. In the southern hemisphere, the response was correlated with the 20^{th} century equatorward bias (equatorward jets shift further; Kidston and Gerber, 2010) while there is no evidence of this relationship in the North Atlantic. Woollings and Blackburn (2012) found no robust jet speed responses in the North Atlantic.

The newer CMIP5 models do not provide a radically different view. Barnes and Polvani (2013) found, in the CMIP5 models, a projected poleward shift of the EDJ in the North Atlantic as well as in the North Pacific and Southern Hemisphere. They also found a strengthening in the Southern Hemisphere. However, they found that the variability of the jets changes, such that projections onto annular modes are not sufficient to capture the response.

To first order, the storm track response to anthropogenic forcing in the 21st century is often seen as a poleward shift (Yin, 2005). This is seen in Yin (2005) as a robust upward and poleward intensification of the transient eddy kinetic energy in CMIP3 models in SH summer and winter and NH winter; it is related to upward intensification of the baroclinicity, dominated by the temperature gradient contribution rather than static stability. However, Ulbrich *et al.* (2008) found that the response of the North Atlantic storm track is instead described by a downstream extension into Europe. The CMIP5 multi-model ensemble provides further evidence for this conclusion; the multi-model mean response in SLP variance in the North Atlantic is relatively small and does not correspond to a poleward shift (Harvey *et al.*, 2012). Zappa *et al.* (2013a) found an eastward extension of the winter Atlantic jet and storm density field, although there is evidence of the poleward shift in both measures in summer. The results of Chang *et al.* (2012) are largely restricted to the zonal mean, and while they show a poleward shift in some variables in winter, this is dependent on the variable and on the level analysed. Finally there is not a clear relationship between the control period bias and the projected winter change in CMIP3 models (Ulbrich *et al.*, 2008), or in CMIP5 models for the North Atlantic (Zappa *et al.*, 2013a). Asymmetries in the North Atlantic in particular (Section 2.3.4.3) are one possible reason why the response here may be less robust, since the forcing is interacting with pre-existing stationary waves.

The above discussion highlights that there is complexity and uncertainty in the response of the jets and other features of the atmospheric circulation to external forcing. The response is dependent on the variable, season, level and location considered, and, for the storm tracks, even robust responses are generally small in the Northern Hemisphere. While the 'poleward shift' of the jet and storm track system is a recurrent theme, this response is generally not robust or dominant in projections for the winter North Atlantic; rather, there is substantial evidence that the long-term response of this storm track in this region is a downstream extension into Europe.

The causes of these uncertainties have not yet been discussed in this chapter. Broadly opposite circulation responses can be found in regional model responses for at least the next fifty years due to internal variability alone, dwarfing the forced response (Deser *et al.*, 2012, 2014). However, the range of projections can also be related to the mechanisms of change. This is discussed in Section 2.3.7.1.

2.3.7.1 Thermal drivers of circulation change under greenhouse gas forcing

Held (1993) discussed two possible pathways by which global warming might cause changes in the jet stream. These are the increase in upper-tropospheric temperature gradient (Section 2.2.3) and the decrease in lower-tropospheric temperature gradient (Section 2.2.1). Because geostrophic winds are related to the horizontal temperature gradient via thermal wind balance

$$p\frac{\partial \mathbf{u}_g}{\partial p} = -\frac{R}{f}\mathbf{k} \times \nabla T \tag{2.4}$$

a strengthened meridional temperature gradient must be balanced by an increased vertical wind shear, and vice versa. That the upper and lower level gradient responses conflict thus has opposing impacts on thermal wind balance as well as on baroclinicity and so on eddy behaviour. In the southern hemisphere recent stratospheric ozone depletion and projected recovery, causing lower stratospheric cooling and warming respectively, cause a further thermal forcing which is seen to affect the jet (Section 2.2.4; Wilcox *et al.*, 2012)

Butler *et al.* (2010) investigated the response to these three different climate-change-like thermal forcings in a simple dry GCM. Both polar stratospheric cooling and tropical tropospheric warming (although not designed to have realistic magnitudes) contributed to increased westerly wind shear at upper levels and a poleward shift in eddy measures of the storm tracks. In contrast, polar surface warming gave an equatorward shift in the storm track. These responses were broadly robust to details of location and spatial scale. The tropospheric wind response was nonlinear; the response to a sum of forcings was weaker than the sum of responses to individual forcings. They also found qualitative similarity between the wintertime and equinox response, although the winter response was shifted in latitude and strengthened. Chen *et al.* (2010) also found that 'high latitude' warming (beginning at 30°) caused an equatorward jet shift in an aquaplanet GCM. Lorenz and DeWeaver (2007) investigated the causes of jet shifts in CMIP3 and a simple GCM, and found that the raising of the tropopause is key in causing zonal wind changes. They further found that while high latitude (poleward of 50°) heating causes an equatorward jet shift, low latitude heating (equatorward of 30°) has the opposite effect. In between these latitudes, stratospheric or low level warming causes an equatorward shift while mid tropospheric warming causes a poleward shift. Further discussion of studies investigating the response to SST and sea ice anomalies is found in Sections 2.3.7.2 and

2.4.2.

As discussed in Section 2.3.7, there is a spread in model responses of the jet and storm tracks to anthropogenic forcings, particularly in the North Atlantic. Such model spread can provide insight into the role of different mechanisms in model changes. Barnes and Polvani (2015) found that the CMIP5 models with stronger AA by the end of the 21st century tend to have weaker poleward shifts of the winter jet. Harvey *et al.* (2013) performed a cross-model regression in the CMIP5 archive between the responses of the temperature gradient (upper and lower level) and the storm track. Again, they found correlations such that a weakening of the gradient acted to reduce the storm tracks, suggesting that sea ice loss is a key factor in inter model spread in atmospheric responses. Cattiaux and Cassou (2013) found that CMIP3 has a more poleward jet shift in the North Atlantic, but less ice loss, than CMIP5. This is consistent with the argument that greater sea ice loss acts to favour an equatorward shift, so masking any poleward shift in CMIP5. Therefore, sea ice begins to emerge as at least a moderating influence on future jet changes.

However, the warming and thermal wind balance in itself does not provide a dynamical mechanism for changes; such a response must be maintained by the circulation, and eddy feedbacks may modulate the response. One possible mechanism for changes in the jet calls on changes in wavebreaking on the polar flank of the jet due to the change in jet structure (Barnes and Polvani, 2013), causing changes in the eddy feedbacks. Rivière (2011) also link changes in wavebreaking, due to changes in the upper troposphere, to poleward jet shifts under global warming. Another possible mechanism assumes that global warming changes the length scale of dominant eddies (Kidston *et al.*, 2011a); therefore the speed of wave propagation, and as a result the region of dissipation, changes. As a result the regions which are net sources of eddy activity shift polewards, as do the jets (Section 2.3.3.2).

2.3.7.2 Responses to zonal mean SST

Various authors have investigated the atmospheric response to zonal mean SST changes in an aquaplanet (responses to SST asymmetries were discussed earlier in the chapter). Such studies provide further insight on the large scale response to thermal forcing.

Caballero and Langen (2005) investigated the response of poleward heat transport to changes in global mean and equator-to-pole SST, and with ice fixed where T$<0°$C. Sampe

et al. (2010) investigated the atmospheric response to changes in the midlatitude SST front against different strengths of subtropical jet as forced by different tropical SSTs. They showed the importance, in an aquaplanet, of midlatitude SST fronts for the formation of a deep eddy driven jet and storm track. Lu *et al.* (2010) adjusted global mean SST (T_m) in the range 0–35°C and the equator-to-pole difference ($\triangle T$) in the range 0–60°C. They found a poleward shift of the jet with increasing T_m and, above a given threshold, with increasing $\triangle T$.

Graff and LaCasce (2011) prescribed SST anomalies of 2 K in different latitudinal bands in an AGCM with otherwise realistic lower boundary conditions. The response of the storm track (bandpass filtered geopotential height variance) depended on the latitude of heating, with intensification on the equatorward side for high latitude heating and the poleward side for low latitude heating. They concluded that SST changes could be contributing to observed storm track changes.

2.3.7.3 Projection onto modes of variability

Responses to forcing of the atmosphere are often framed as projections onto the modes of variability of the system (see e.g. Section 2.4.2). There are two perspectives on such a problem. First, the response of a nonlinear system with inherent regimes would be expected to manifest in changes of frequency of occurrence, rather than structure, of these regimes (Palmer, 1999). As such the response would look like these regimes (Palmer, 1999; Branstator and Selten, 2009). However, there is some evidence from GCMs that the structure of the states themselves may also change under anthropogenic forcing (Barnes and Polvani, 2013). The alternative perspective suggests that the response should look like the internal variability because the modes of variability are favourably forced on quasi-stationary timescales (Branstator and Selten, 2009).

Ring and Plumb (2007 and 2008) investigated the annular mode response, in a simplified GCM, to mechanical and thermal forcings. Ring and Plumb (2007) found the response to mechanical forcing to be dependent both on the location of the forcing relative to the modes of variability and on the season of integration. (Ring and Plumb, 2008) investigated the response to thermal forcing. Of specific interest to the questions within this thesis, they found that while the response is not always annular mode like, it is so for thermal forcings restricted to high latitudes (above 45°), and that the eddy feedback was

crucial for the annular mode nature of the response. Moreover, (Ring and Plumb, 2008) discussed the applicability of the Fluctuation-Dissipation theorem, which states that the response of a system to forcing can be described by a linear operator dependent on the system's unperturbed state. In many cases, for example when a system's variability is Gaussian, this linear operator is simply a function of the system's timescales. Therefore this provides another argument regarding the importance of a system's timescales to the response to forcing, as discussed in the previous paragraph.

2.4 Jet stream responses to sea ice

This section will discuss the observational and model evidence for jet stream responses to sea ice on a range of timescales. As discussed in Section 2.3.7.1 in the context of 21st century change, sea ice is only one of the possible drivers of changes in the jet stream.

2.4.1 Observational studies

Since substantial sea ice decline has already occurred, observational and reanalysis data have been probed to investigate relationships between sea ice trends or anomalies and the atmospheric circulation.

Liu *et al.* (2012) investigated the relationship between autumn ice extent and winter snow and atmospheric fields in the period 1979–2010 through the use of linear regression. The SLP associated with low sea ice had a positive anomaly over the Arctic and a negative anomaly in midlatitudes. This slightly resembled the negative AO (Section 2.3.5.1) but had more zonal variations than this pattern. The associated wind change was a reduction in westerlies and more meandering flow. They also found an increase in snow cover over high latitudes, associated with both increased precipitation and colder temperatures due to weakened westerlies and therefore reduced warm advection.

The proposed responses to declining sea ice cover implied by the observational analysis of Liu *et al.* (2012) - a negative phase of the mode of variability, increased snow cover, and more 'meandering' flow - have all been discussed at length in the literature (see below). A further hypothesis, of possible planetary wave propagation from regions of anomalous heating over retreated sea ice, has also arisen (Honda *et al.*, 2009).

Jaiser *et al.* (2012) examined the differences in autumn and winter atmospheric circu-

lation between the periods 1990–2000 and 2001–2010 in ERA-interim, these periods representing high and low autumn (September and October) ice conditions respectively. In winter, they found a barotropic positive anomaly over the pole and a low over the Pacific and Atlantic, again slightly resembling negative AO. In contrast, the autumn response was baroclinic. They suggested a mechanism where baroclinic processes in autumn set up the winter barotropic anomaly, and also found evidence of a planetary wave response in winter.

The relationship between sea ice and winter precipitation was examined by Li and Wang (2013). Specifically, they found negative correlations between SIC in the Kara-Laptev sea in autumn and winter SLP anomalies over northern Eurasia, such that a SIC reduction was associated with positive SLP anomalies. Both the increase in specific humidity and the changes in circulation associated with the sea ice anomaly then favoured increased winter precipitation in this region (Li and Wang, 2013). However, while they examined data since 1950, this relationship only emerged after 1982. Also interested in the Eurasian region, Honda *et al.* (2009) found relationships between reduced Siberian sea ice in September and cold events in Japan (in December) and in Eurasia and China (in February), which they linked to the Siberian high and negative NAO respectively. They postulated a mechanism whereby heating in the Barents sea excites a stationary Rossby wave train in November. However, Sato *et al.* (2014) questioned the causality of such a mechanism, suggesting that both warming in the Barents sea and December cold anomalies over Eurasia were associated with a wave train from the Gulf Stream. This highlights the difficulty of establishing causality in observational data and the importance of modelling studies and physical understanding of the mechanisms.

Francis and Vavrus (2012) related AA in reanalysis data to Rossby wave behaviour. They argued that decreased thickness gradients are associated with slower jet speeds and so slower wave propagation, and also that this is associated with higher wave amplitudes. They secondly argued that the differential increase in geopotential height at 500 hPa (Z500) contributes to higher ridges. However, Barnes (2013) investigated this hypothesis further in three reanalyses. It was found that trends in meridional wave extent, phase speeds and blocking are either not significant or sensitive to methodology, and that relationships between these variables are not simple, where they exist. Screen and Simmonds (2013) also responded, analysing wave amplitudes in the ERA-Interim reanal-

ysis using two measures of amplitude; the spatial displacement of a given Z500 isoline as well as the Z500 anomaly at a fixed latitude. They found no more significant trends than would be expected by chance, in any season. They also questioned the relationship of changes at 500 hPa to sea ice induced AA, which is primarily shallow.

Hassanzadeh *et al.* (2014) investigated the Francis and Vavrus (2012) hypothesis in a dry GCM. They found that a reduction in meridional temperature gradient reduced the geopotential height gradient at 500 hPa and decreased the westerlies, particularly on the poleward flank of the jet. However, this resulted in a decrease in blocked area and in wave amplitude, in contrast to the hypothesis of Francis and Vavrus (2012). They demonstrated that a chain of reasoning which takes into account only reductions in the geopotential height gradient, and not in the variance of geopotential heights, would lead to expecting an increase in blocking and wave amplitude under a reduced gradient. Other complexities in evaluating the response of blocking or wave amplitude include a range of models and of definitions of blocking, such that it is challenging to interpret the many differing results.

A related hypothesis (i.e., regarding amplification of certain circulation patterns) was proposed by Petoukhov *et al.* (2013), although they investigated summer and were not directly interested in the effect of Arctic change. They associated recent Northern Hemisphere summer extremes, in particular heat waves in Europe, North America and Russia since 2000, with amplification of waves at zonal wavenumber 6–8. Following barotropic theory, they proposed a mechanism whereby free waves of zonal wavenumber 6–8 can become trapped in a wave guide, resulting in increased magnitudes and persistence on monthly timescales as was observed during these extremes. Furthermore they demonstrated that such a waveguide requires a particular zonal jet structure. They then hypothesised that such a structure may be favoured by recent AA. However, AA is not observed in summer, and it is unclear if or to what extent this mechanism is relevant in winter, when AA chiefly occurs and when the jet has a very different structure.

Remote impacts on the Atlantic from Pacific sea ice anomalies have been hypothesised: Mesquita *et al.* (2011) found through feature-tracking of storms in reanalysis data that sea-ice anomalies in the Sea of Okhotsk have a bigger influence on Atlantic storms than anomalies in the Atlantic, and also an effect on the NAO.

The short observational record and high internal variability of the atmosphere mean

it is challenging to interpret the relationships found in observational data. Moreover, causality cannot be conclusively established from observations of a coupled system. Therefore GCM studies are frequently used to analyse the response to sea ice anomalies.

2.4.2 Sea ice anomalies in GCMs

There is a substantial body of literature investigating atmospheric responses to sea ice anomalies in GCMs. Much of this addresses some of the hypotheses arising from the observational studies (see above), and tailored experiments provide the opportunity to address issues of causality and lack of robustness due to high internal variability. Experiments are generally conducted in atmosphere only models, with prescribed sea ice concentration anomalies and SSTs. Experiments considering the response to ice thickness anomalies are rare, and in the following discussion, models are forced only with SIC unless specified. The fields used as lower boundary conditions in these experiments have included SIC from modelled or observed 'high' and 'low' sea ice years (e.g. Liptak and Strong, 2014), SIC based on trends (e.g. Magnusdottir *et al.*, 2004), and idealised sea ice fields (e.g Kidston *et al.*, 2011b). SSTs are fixed either to climatology or to anomalies coherent with the sea ice forcings.

2.4.2.1 Energy Budget response

The direct effect of sea ice anomalies is to impact the surface energy budget and thereby the Arctic boundary layer (Cohen *et al.*, 2014). Deser *et al.* (2010) forced an AGCM with projected reductions in SIC and thickness. They found that the maximum response in the surface energy budget was dominated by change in turbulent heat fluxes and was largest in winter, lagging the maximum SIC reduction by two months. This is consistent with the results of Peings and Magnusdottir (2013) who found that the maximum anomalous energy transfer to the atmosphere also occurred in late Autumn and early winter in response to both current and future SIC anomalies. Semmler *et al.* (2012) focused on the effect on the Arctic energy budget of ice reduction and removal in an AGCM such that the ice reduction experiment resulted in an ice-free summer Arctic. However, Deser *et al.* (2010), Peings and Magnusdottir (2013) and Screen *et al.* (2013b) (who investigated the response to recent ice loss) all commented on possible exaggeration of the surface energy budget response, or unrealistic features away from the ice edge (Peings and Magnusdot-

tir, 2013) due to the lack of a coupled ocean.

2.4.2.2 Evidence for and against an NAO response

Magnusdottir *et al.* (2004) and companion papers (Deser *et al.*, 2004, 2007; Strong and Magnusdottir, 2010b) forced the CCM3 climate model with SIC and/or extratropical SST anomalies based on, but exaggerated from, the observed 1954–1994 trend. The response resembled NAO negative and since the anomalies were representative of NAO positive (Strong and Magnusdottir, 2010b) this may be seen as a negative feedback. However, issues around causality and the robustness of the link from NAO to sea ice remain (Section 2.1.5.1).

This idea that the response to negative sea ice anomalies projects onto the negative phase of the NAO (or sometimes NAM or AO) recurs frequently in the literature (Budikova, 2009) and is consistent with certain theoretical arguments (Section 2.3.7.3). While the projection is sometimes quantified, the evidence given is generally the existence of a correctly signed north-south pressure dipole in pressure or geopotential height. Moreover, as discussed in Section 2.3.5.1, it is not possible to directly deduce changes in physical structures such as the jet stream from NAO information only.

In addition, the location and magnitude of the sea ice forcing may be crucial for determining the response (e.g. Strong and Magnusdottir, 2010b) rather than the overall anomaly. For example, in Alexander *et al.* (2004) the response to forcing by SIE anomalies which are generally positive but negative in the GIN (Greenland, Iceland and Norwegian) seas (see map in Figure 2.1) resembles the negative NAO/AO in that a north-south dipole in pressure is found between Greenland and the mid Atlantic. Therefore the NAO/AO response in this case appears to be determined by the local rather than hemispheric sea ice anomaly.

Honda *et al.* (2009) found a negative NAO-like response in February in response to September-December sea ice anomalies representative of recent ice loss in the Siberian sea. This response was further associated with late winter cold anomalies in China and Eurasia associated with reduced September SIE. Examples of cases where an NAO negative response have been found in an AGCM forced with projected sea ice changes are as follows:-

- In March, and to a lesser extent in DJF, in response to a projected late-21st century seasonal cycle of SIC (Seierstad and Bader, 2009).

- In February, but not earlier in winter, in response to a projected, late-21st century seasonal cycle of SIC and SIT (Deser *et al.*, 2010)

- Peings and Magnusdottir (2013) found a negative winter NAM response to imposed current and projected sea ice and SST anomalies in the free troposphere, although there were differences between the Atlantic and Pacific responses in the vertical. The response, however, was significant only for forcings representing 2090 conditions, and not for 2010 conditions.

Other studies considering recent Arctic sea ice anomalies have also found results consistent with NAO or AO negative; Liu *et al.* (2012) found a positive SLP response over the pole and negative SLP response in midlatitudes in DJF, and Semmler *et al.* (2012) found a dipole of the zonal wind response around 50°N, with reductions to the north.

However, other studies provide conflicting evidence. One reason is that internal variability in the winter atmospheric circulation is high and care must be taken interpreting the response to forcings. Screen *et al.* (2013b) forced small model ensembles of 5 and 8 members with annually repeating cycles representing observed sea ice loss. The response of the surface energy balance and temperature was strong and largely confined below 700 hPa. They found some evidence of an NAO negative response in early winter, but it was weak and not robust across other seasons. This was conducted using an index based on SLP differencing rather than EOFs which may bring out different features of the circulation (see Section 2.3.5.1). Screen *et al.* (2013a) used large model ensembles of 100 and 60 members to investigate the strength of these responses relative to internal atmospheric variability. The response in this case was a shallow heat low, and either an NAO–positive response or a response which is not NAO–like. Finally, Liptak and Strong (2014) found a negative NAO-like response to both anomalously 'high' and anomalously 'low' sea ice.

Possible mechanisms for an NAO response are examined in Deser *et al.* (2004), Deser *et al.* (2007) and Strong and Magnusdottir (2010b). The response was separated into an 'indirect' or 'modal' NAO-like equivalent barotropic response and a baroclinic 'direct' residual response (see also Section 2.3.4.2). They suggested that the direct response sets up the NAO response. This hypothesis was supported in transient experiments (Deser

et al., 2007), in which the direct response is the fast response (reaching a maximum after 5–10 days) and the 'modal' response is triggered later and maintained by anomalous vorticity and heat fluxes. Strong and Magnusdottir (2010b) further found that the fast response caused changes in Rossby wave breaking (RWB) via changes in the critical lines at which wavebreaking occurs (Section 2.3.3.2). Resulting reductions in anticyclonic RWB at around 55°N and increases in anticyclonic RWB around 30°N corresponded to acceleration of zonal winds south of 55°N and north of 30°N, explaining most of the zonal wind anomalies.

2.4.2.3 Seasonal Dependence

As is evident from the bullet points in the previous section, the response to sea ice anomalies appears to vary through the winter season (here considered to be DJFM).

Strong and Magnusdottir (2010b) found the greatest response to sea ice anomalies, and strongest projection onto the internal mode of variability, in late winter (March), although this was not the time of strongest forcing. Unlike many studies, Semmler *et al.* (2012) investigated all seasons, and found that the response is greatest in winter (DJF) followed by Spring (MAM). The different combinations of months analysed means it is not possible to conclusively determine whether the results of Strong and Magnusdottir (2010b) and Semmler *et al.* (2012) are in disagreement.

Seierstad and Bader (2009), investigating the modelled response to a projected future seasonal cycle of ice anomalies, also found the greatest response and the strongest projection onto the mode of variability in March. Given the weaker surface forcing than in earlier winter, they suggested that this may be due to different background circulation in March, consistent with evidence from studies investigating the response to midlatitude SSTs (Section 2.3.4.4). Deser *et al.* (2010), also investigating the response to future, seasonally varying ice anomalies, also found a seasonal dependence, with a baroclinic response to the heating anomaly in early winter and a barotropic, NAO-like response in late winter. This may therefore suggest that the NAO response is set up by the baroclinic response, as discussed above (Section 2.4.2.2, Deser *et al.*, 2007).

Liptak and Strong (2014) forced an atmospheric model with 'high' and 'low' daily varying DJF sea ice concentrations (obtained from a long control run of the ice model). In both cases, the atmospheric response (relative to a run forced with sea ice climatol-

ogy) matures from a local response in December to a north–south dipole in atmospheric pressure in February. Therefore both the 'high' and 'low' sea ice forcings produce an NAO negative like response, but the longitude of the maximum response differs greatly depending on the forcing.

2.4.2.4 Planetary wave and Precipitation responses

As noted in Section 2.4.2.4, two other hypotheses regarding winter effects of sea ice anomalies are, first, excitation of planetary Rossby waves and, second, precipitation and snow anomalies particularly in Eurasia.

The setup of a Rossby wave train response by anomalous heating over sea ice anomalies has been proposed by Alexander *et al.* (2004) for anomalies in the Sea of Okhotsk and by Honda *et al.* (2009) for November anomalies in the Barents-Kara Sea. The latter is used to explain an observed relationship between Autumn (September) Siberian sea ice anomalies and Far East cold anomalies in December. Mori *et al.* (2014) also conducted modelling studies into the relationship between recent negative sea ice anomalies and cold Eurasian winters. Their results suggested that the recent very cold winters are a combined result of sea ice anomalies and internal, unforced variability associated with the AO. Interestingly, they did not find a statistical link between the AO and ice anomalies. Finally, the modelling study of Peings and Magnusdottir (2013) further suggested the role of the stratosphere in setting the timescale of the remote circulation anomaly.

In terms of snow, both Liu *et al.* (2012) and Li and Wang (2013) found increased winter snowfall in response to reductions in sea ice in reanalysis data and models forced with recent sea ice anomalies. This relationship has also been found in future projections; Deser *et al.* (2010) found an increase in winter accumulated precipitation and March snow cover over Northern Eurasia and North America in response to projected 2080–2099 sea ice concentration and thickness anomalies.

2.4.2.5 Thickness Anomalies

Sea ice thickness anomalies cause weaker heat flux anomalies per unit area, but the anomalies are geographically more widespread (Gerdes, 2006). There are few studies addressing the response to thickness anomalies. However, in a model forced with up-

per and lower extremes of ice thickness derived from a hindcast model for 1948–1998, the response to thickness and concentration anomalies is quite different to the response to concentration-only anomalies (Gerdes, 2006). Negative thickness anomalies force a dipole of reduced Arctic SLP and increased Pacific SLP, while the NCEP reanalysis suggests increased SLP in the Atlantic rather than the Pacific.

2.4.2.6 Coupled and unforced models

The literature discussed so far in this section has mostly focused on experiments with prescribed SSTs and sea ice distributions. However, there are limitations of such a technique. As discussed in Section 2.1.5.1, the atmosphere drives sea ice variability both dynamically and thermodynamically. It also drives SSTs at lags of up to one month (e.g. Kushnir *et al.*, 2002). The implications of this have been noted in several studies. For example, Peings and Magnusdottir (2013) noted unrealistic surface heat flux anomalies to the south of the sea ice anomaly in atmosphere-only experiments. This is a result of the ocean's inability to adjust to the increased atmospheric temperatures by warming, and therefore damping the anomaly. Attempts at understanding the response of the coupled system are therefore of particular interest, although harder to implement and interpret.

Sedlàček *et al.* (2012) approached the problem by reducing the albedo of ice and snow on ice in a fully coupled model. They ran an eight member ensemble for one year for both 'equilibrium' and 'transient' CO_2 forcing. The location of the atmospheric response differed between these two setups, probably due to the precise location of the SIC anomalies. However, an albedo approach can only produce realistic sea ice anomalies in the summer months (Deser *et al.*, 2015). Deser *et al.* (2015) instead prescribed longwave nudging to the sea ice field, creating sea ice fields which closely resembled the CCSM4 20th century and 21st century simulations under historical and RCP8.5 conditions. The zonal mean response resembled a negative NAM in both coupled and uncoupled experiments. However, coupled experiments produced a larger and more global response, with the response differing between the two south of 30°N.

Taking a different approach, Sokolova *et al.* (2007) examined the atmospheric circulation associated with ice cover anomalies using 7-year periods of 'high' and 'low' DJF sea ice from a long, coupled, unforced simulation. Again, the 'high'-'low' difference is indicative of AO positive, but the projection is not quantified. Moreover, it is difficult to

conclude the direction of causality in such an uncoupled simulation, particularly since sea ice and atmospheric fields are analysed in the same season.

Finally, there is also evidence from statistical models and climate models that the feedback strength between sea ice (specifically in the Barents Sea) and the NAO impacts the variance of both components (Strong and Magnusdottir, 2011). Increased sensitivity of the sea ice to the atmosphere, as expected from thinner ice, decreases the variance of the NAO and increases the variance of sea ice.

2.4.3 Antarctic sea ice

Antarctic sea ice covers between 0.8 and 5.2% of the Earth's ocean area (3×10^6–$18\times10^6\,km^2$; Vaughan *et al.*, 2013). Antarctic sea ice cover is thus more seasonal than that in the Arctic, and so has a higher proportion of first year ice with lower thicknesses and different thermal and salinity properties. Unlike sea ice in the Arctic, it is not in a bounded ocean; in comparison to the Arctic it is generally more zonally symmetric, and typically extends to lower latitudes (55 to 65° in winter, depending on longitude [Kidston *et al.*, 2011b]).

Trends in sea ice extent and area in the Antarctic are positive over the satellite era (e.g. Parkinson and Cavalieri, 2012). Even the newest coupled models (CMIP5) are unable to capture this positive trend; most display a negative trend in response to historical forcing (e.g. Turner *et al.*, 2013). Projections for the end of the 21st century suggest widespread ice loss (Collins *et al.*, 2013). However there is considerable uncertainty in these projections due to the inability of models to recreate past trends (Collins *et al.*, 2013). This apparent failure of the models to represent past Antarctic sea ice trends could be due to internal variability, or missing processes in the representation of Antarctic sea ice, for example in its response to atmospheric circulation anomalies (Turner *et al.*, 2013).

Nevertheless, the possible effects of Antarctic sea ice loss on the atmosphere has received some attention. This has been motivated either by understanding shorter timescale influences for seasonal forecasting, or by the potential for impact on the atmospheric circulation should large trends occur in future. These studies are discussed briefly below, since they will inform discussion of the Northern Hemisphere and shed light on behaviour in idealised zonally symmetric models such as will be used in this thesis.

Menendez *et al.* (1999) found that the strongest response to removing all Antarctic sea ice occurred in winter (note that the forcing due to removal of all ice would be strongest in this season), with an equatorward shift of the storm tracks and weakened transient eddies. This study is however relatively low resolution by modern standards with resolution of 3.75° longitude by 3° latitude at 60°S, so the relevant mechanisms such as eddy heat and momentum fluxes are unlikely to be accurately represented. The model was run for only ten years, so internal variability may still be playing a large role. More recently, Kidston *et al.* (2011b) forced a GCM with synthetic changes in sea ice. In response to increased sea ice in the cold season, anomalies in the upper level jet stream are as large as 4 ms^{-1}, at approximately 60°S. They form a dipole about the control period jet maximum and thus represent a 'shift' in the jet. However, the response to reduced sea ice is small. Finally, Bader *et al.* (2013) found a negative SAM response in a model ensemble forced with projected late 21st century sea ice loss. The projection is strongest in September (late winter), but this is not the time at which Eady growth rate changes are greatest. Two themes emerge from these papers; sensitivity to the season investigated or equivalently the latitude of the forcing, consistent with results in the SST literature (see earlier in this chaper) and an equatorward jet shift in winter in response to reduced sea ice.

2.4.4 Palaeoclimate

The atmospheric state in a colder climate such as that at the Last Glacial Maximum (LGM) 21,000 years before present may also provide insights into the atmospheric circulation response to ice changes. Increased sea ice relative to the present day was one feature of this period.

New proxies support equatorward shifts of the jet of up to 10° in the LGM (Toggweiler *et al.*, 2006). Toggweiler *et al.* (2006) discussed possible positive feedbacks between poleward-shifting midlatitude westerlies and atmospheric CO_2 primarily due to Southern Ocean processes. This is consistent with a poleward shift in warm climates and vice versa. However, sea ice is not directly implicated in any of the mechanisms. Toggweiler and Russell (2008) argued that stronger westerlies should be expected in the colder climate of the LGM. Toggweiler (2009) suggested a mechanism whereby northern hemisphere cooling and southern hemisphere warming at the end of the LGM caused a restoration of the inter-tropical convergence zone (ITCZ) to the equator and a southward

and poleward shift in the southern hemisphere westerlies. This was also associated with a small shift in the Northern hemisphere, with the jet shifts being asymmetric between the hemispheres due to the hemispheric asymmetry of the warming.

The results in the previous paragraph suggest an equatorward jet shift in cold past periods such as the LGM. Model experiments have further investigated this hypothesis. Model simulations of the LGM with specified SST (either from reconstructions or from model runs) create storm tracks which are very much aligned along the zonal ice edge on the North Atlantic (Kageyama *et al.*, 1999; Dong and Valdes, 2000). Dong and Valdes (1998) also attributed part of the response in LGM experiments with fixed SSTs versus those with a slab ocean to the change in sea ice. Pausata *et al.* (2011) forced a coupled climate model with isolated components of LGM forcing (greenhouse gases, ice sheet albedo and ice sheet topography). The response to topography, in particular the Laurentide ice sheet over the North American continent, dominated the response in mean SLP, the leading mode of SLP variability, and the North Atlantic jet stream. This suggests that it is the mechanical forcing from topography driving the downstream response, rather than local surface temperatures. This contrasts with the conclusions of Kageyama *et al.* (1999) andDong and Valdes (2000); however, the runs in Pausata *et al.* (2011) did have less sea ice than the atmosphere only models of these two earlier studies. The dominance of the Laurentide ice sheet in driving the LGM stationary wave patterns and Atlantic eddy driven jet was also found in the atmosphere- and land- only simulations of Merz *et al.* (2015).

2.5 Concluding Remarks

This chapter has demonstrated that there is a substantial theoretical and modelling basis for the possible effects of thermal and mechanical forcings, in particular surface SST anomalies, on the extratropical atmosphere. Sea ice constitutes a thermal and to a lesser extent mechanical forcing on the atmosphere, and is in decline. However, extracting the impacts of sea ice on the atmospheric circulation is challenging, due in particular to high internal variability and the short observational record available for attribution studies. As a result, there is some controversy over the observed impacts of sea ice.

Model experiments have also produced conflicting results regarding the response of

the atmosphere to sea ice anomalies. Key outstanding questions relate to:-

- the dependence of the response to sea ice anomalies on the season investigated (also found in studies of the response to SST anomalies)
- the possibility for remote impacts via teleconnections and triggering of wave trains
- the causality of observed relationships
- the extent to which it is helpful to frame the response as a projection onto modes of variability.

Regarding this last, there is evidence both from previous studies of the response to sea ice and from general considerations regarding the nature of annular modes, and their response to forcing, that examination of results should not focus only on these modes.

The progress made by previous authors in using a hierarchy of models, for example GCMs with simplified boundary conditions, to understand the atmospheric response to surface forcing suggests that such an approach would help to address these outstanding questions. Therefore, the following two questions (restated from Chapter 1) will be considered in this thesis using modelling experiments with simplified boundary conditions:-

- What is the atmospheric response to sea ice removal? In particular what is the response of the eddy driven jet, including its mean, variability and spatial heterogeneity?
- What sets the nature and magnitude of the jet response to sea ice forcing?

A separate question, regarding a slightly different hypothesis considering the impacts of near-surface warming heterogeneities such as Arctic amplification on midlatitude temperature variability, is expanded upon in Chapter 4.

Chapter 3

Models and Datasets

Three models, or groups of models, are used in this thesis. In brief:

- Data from experiments conducted as part of CMIP5 are used to examine future changes in surface temperature variance, and its robustness across models
- Data from the ESSENCE single model ensemble is used to further explore these changes, and in particular to test the role of the thermal advection mechanism
- Idealised model experiments are conducted using HadGAM1, a configuration of the Met Office Unified Model, to investigate the effect of sea ice removal on the atmosphere

This chapter describes the details of the two datasets (CMIP5 and ESSENCE) and the configuration of HadGAM1. Further details of the experimental design employed in HadGAM1 to answer the questions in this thesis are given later, in chapters 5 and 6. This chapter also gives details of analysis methodologies (including tests for statistical significance) used in Chapters 5 and 6, and the reanalysis data sets mentioned in this thesis.

3.1 CMIP5

The fifth phase of the Coupled Model Intercomparison Project (CMIP5) provides a framework for co-ordinated experiments using climate models (Taylor *et al.*, 2011). These were designed to address a range of goals including decadal prediction and understanding of past climates (palaeoclimates). However the main goal relevant to this thesis was to evaluate recent ('historical') climate simulations and to produce projections of future climate to aid understanding of the range of possible responses to anthropogenic forcing, including increased greenhouse gases. The resulting multi-model ensemble is a valuable

tool for assessing how robust projected changes are. Data was available from 2011 onwards and was a key component of evidence for the Intergovernmental Panel on Climate Change fifth assessment report (IPCC AR5), published in 2013 (IPCC, 2013).

The experiments which will be mainly considered are those using 'historical' forcing of atmospheric composition and land use in the period 1850–2005 and representative concentration pathway 4.5 (RCP4.5) in the period 2006–2100 (van Vuuren *et al.*, 2011). There are four such pathways- RCP2.6, RCP4.5, RCP6.0 and RCP8.5. These were developed for IPCC AR5, based on existing scenarios in the literature and named according to their radiative forcing in 2100, i.e. RCP4.5 has a radiative forcing of $4.5\,\mathrm{Wm}^2$ in 2100. RCP4.5 is likely to correspond to implementation of climate policy. It is chosen because, as well as representing a middle-of-the-road scenario, it is the forcing pathway for one of the two core projection experiments in CMIP5 (the other uses RCP8.5; Taylor *et al.*, 2011); therefore the multi-model ensemble is larger than for RCP2.6 and RCP6. The RCPs prescribe greenhouse gases and other forcing agents; in particular, the CO_2 concentration in 2100 under RCP4.5 is approximately 525 ppm (Taylor *et al.*, 2011, Fig.9). Since modelling groups could either specify time-varying ozone from a provided dataset or calculate ozone using interactive chemistry, there are some inter-model differences in ozone concentrations. Relative to the SRES (Special Report on Emissions Scenarios) forcings, RCP4.5 is approximately comparable to SRES B1 (Taylor *et al.*, 2011). The two sets of scenarios (RCP and SRES) also differ in that the RCPs specify concentrations (rather than emissions), and that the RCPs specify reductions in aerosol concentrations in the 21^{st} century.

The models used are listed in Table 3.1. They have a range of atmospheric spatial resolutions from 0.5° to 4° (Taylor *et al.*, 2012). However, all data is interpolated onto a common grid for the purposes of this thesis and only multi-model statistics are shown. Therefore the individual models are not discussed further.

3.2 ESSENCE

Sources of uncertainty in climate projections are three-fold; forcing uncertainty, internal variability, and model uncertainty (Hawkins and Sutton, 2012). While multi-model ensembles, such as that above, predominately address the issue of model and scenario

uncertainty, large ensembles of a single model are useful to evaluate the significance of a signal (e.g Deser *et al.*, 2012), particularly in higher order statistics such as the variance.

The ESSENCE single model ensemble (Ensemble SimulationS of Extreme weather events under Nonlinear Climate change; Sterl *et al.*, 2008) is a seventeen member single-model ensemble of the ECHAM5/MPI-OM coupled model. The ensemble is generated through perturbation of the initial atmospheric conditions only, and can be expected to effectively sample the internal variability in the climate system. The model is forced with observations for 1950–2000 and with the SRES A1B emission scenario for 2001–2100. This scenario has rapid economic growth, a peak in global populations at around 2050, and a mix of fossil fuel and other sources for energy (Nakicenovic and Swart, 2000).

3.2.1 The ECHAM5/MPI-OM model

The atmospheric component of ECHAM5/MPI-OM is described in detail in Roeckner *et al.* (2003). The model represents divergence, temperature, vorticity and the logarithm of surface pressure with truncated series of spectral harmonics in the horizontal, with a semi-implicit time differencing scheme, and a hybrid sigma-pressure vertical coordinate. In ESSENCE the model was run at T63 with 31 levels in the vertical, extending to 10 hPa (Sterl *et al.*, 2008). (T63 denotes that total wavenumbers up to 63 are retained, corresponding to a resolution of 1.875° at the equator.) The ocean component is described in Marsland *et al.* (2003). It is a primitive equation z-coordinate model with variable horizontal resolution.

The ECHAM5/MPI-OM coupled model was shown to produce a good representation of observed global SLP patterns over the 20th century (van Ulden and van Oldenborgh, 2006). Relative to other CMIP3 models, it has relatively modest surface temperature biases over well-observed regions (Randall *et al.*, 2007, Figure S8.1b) although it shares a cold bias in the North Atlantic and large biases over south west Greenland and much of Antarctica. Under greenhouse gas forcing, it has a relatively high transient climate response (the temperature increase at time of doubled CO_2 in a 1% yr^{-1} CO_2 increase run) but an equilibrium sensitivity of 3.4°C, close to the CMIP3 model mean (Randall *et al.*, 2007, Table 8.2).

3.3 HadGAM1

3.3.1 Atmospheric component

Experiments investigating the effect of sea ice on the atmospheric circulation are run using HadGAM1, the atmospheric component of HadGEM1 (The Hadley Centre Global Environmental Model; Martin *et al.*, 2006). HadGAM1 differs profoundly from earlier model versions, employing a non-hydrostatic semi-Lagrangian dynamical core and advanced model physics. The justification behind the model configuration, its formulation and the discretized equations solved in the model are presented in Davies *et al.* (2005). Key features are described in the following paragraphs.

The dynamical core was that used in operational numerical weather prediction from 2002 and climate studies from 2004. It uses the deep atmosphere, fully compressible, non-hydrostatic equations. Semi-Lagrangian advection is applied to all prognostic variables except density, i.e., Eulerian treatment of the continuity equation is applied, which ensures that dry mass is conserved in the model. Tracers, and moisture, are also conserved, using moisture correction (Martin *et al.*, 2006). The typical resolution of the model is N96 (1.25° latitude by 1.875° longitude) with 38 levels in the vertical, double that used as standard in HadAM3. Notably the semi-Lagrangian, semi-implicit scheme allows stability at a longer timestep than an Eulerian explicit scheme would. An 1800 s time step (30 minutes) is appropriate for global climate runs. The model is run on an Arakawa C-grid and uses a terrain following height-based vertical co-ordinate.

HadGAM1 featured significant changes to many physical parametisation schemes, discussed in the following sections.

3.3.1.1 Clouds and microphysics

Cloud water and liquid cloud amount are diagnosed from the grid box moisture and potential temperature, to give the cloud cover fraction within each gridbox (Martin *et al.*, 2006).

3.3.1.2 Radiation

Radiation is modelled by splitting the frequency spectrum of atmospheric radiation into a limited number of spectral bands which capture the radiative properties of the different constituent components of the atmosphere. Radiation is separated into shortwave and longwave radiation and into two streams in the vertical, upward and downwards flux. Horizontal radiative flux is not considered. The Edwards and Slingo (1996) radiation code is used, as in HadCM3, but with minor adjustments, for example updated absorption spectra. There are six shortwave and nine longwave bands, and the effects of water, carbon dioxide, ozone, oxygen, nitrous oxide, methane and CFCs are included (Martin *et al.*, 2006).

3.3.1.3 Aerosols

In HadGAM1, there is the capability for a new interactive treatment of aerosols including black carbon, sea salt, sulphate, and biomass-burning aerosols. The model also includes the 'direct' scattering and absorption aerosol effect, the 'semi-direct' affect of aerosol absorption properties on cloud and temperature. For aerosols other than black carbon, the first indirect effect (whereby aerosols affect cloud albedo) and second indirect effect (whereby they effect cloud precipitation efficiency) are also included.

3.3.1.4 Orographic drag

A new scheme was used in HadGAM1 relative to that used in previous versions of the UM (Webster *et al.*, 2003). Whereas the old scheme assigned the orographic drag entirely to perturbations of the flow over orography, i.e., to gravity wave drag, the new scheme also allows for drag due to flow around orography. Therefore the drag is dissipated both at the height of the orography and in the lower stratosphere. This scheme greatly improved the model's skill in the troposphere (Webster *et al.*, 2003).

Representation of orography requires both the mean gridscale orography and the subgrid scale orography, including the horizontal gradients of and standard deviation of orographic height within the gridbox. The Webster *et al.* (2003) scheme uses a newer, higher resolution raw dataset for these orographic fields than the scheme in earlier versions of HadAM3. The dataset of mean and subgrid scale orography is also filtered in space to

avoid gridscale features which may cause numerical instabilities.

3.3.1.5 Boundary layer and convection

It is key to the realism of atmospheric models that they are able to account for turbulence in the atmospheric boundary layer. HadGAM1 uses the boundary layer scheme presented in Lock *et al.* (2000). The scheme works by identifying the boundary layer type, of which there are six. The type is identified by considering the motion of a lifted parcel with adiabatically conserved properties identified at the surface. The mixing and entrainment are then parameterized according to the type identified.

3.3.2 Land surface model

HadGAM1 uses the Meteorological Office Surface Exchange Scheme MOSES version 2.2 (MOSES-II; Cox *et al.*, 1999; Essery *et al.*, 2001) land surface model to calculate surface energy and moisture fluxes.

The main new feature in MOSES-II is the introduction of a tiling scheme (Essery *et al.*, 2001) to account for subgridscale surface heterogeneity. There are nine surface tiles corresponding to nine surface types; five plant functional types as well as bare soil, inland water, urban surface and (land) ice. At each grid point, the fraction of each land surface type is specified to the model, and fluxes are calculated for each tile separately. This representation of subgridscale surface heterogeneity allows for more accurate calculation of surface fluxes than earlier schemes.

There are four soil levels with thicknesses, in order of depth, of 0.1, 0.25, 0.65 and 2 m (such that the deepest level extends to 3 m below the ground; Cox *et al.*, 1999). Moisture content and temperature, allowing for moisture phase change in the soil, are modelled on these soil layers.

Snow is ascribed a constant density of ρ_{snow}=250 kg m^{-3}. Lying snow alters the surface friction, albedo, and thermal conductivity.

3.3.3 Model performance

Before conducting idealised experiments (i.e., with simplified lower boundary conditions) it is important to know the model's ability to simulate key processes and features

of the global climate system. This section discusses key improvements from the previous model version HadAM3 before focussing on the biases in the extratropical circulation, which are particularly relevant to this thesis. It draws heavily on the validation papers by Martin *et al.* (2006) and Ringer *et al.* (2006) but, for readability, these citations are not repeatedly mentioned. Validation in these papers was performed against the ERA-40 and ERA-15 reanalyses.

In comparison with HadAM3 (at N48), the largest improvement in HadGAM1 (at N96)[1] is in the representation of temperature and relative humidity in the upper troposphere and lower stratosphere (Martin *et al.*, 2006). However, a cold bias of -5 K remains around the southern hemisphere polar tropopause. The improvement is attributed to improved vertical resolution around the tropopause, a more accurate advection scheme, and more efficient conversion of water to ice. The second notable improvement is of representation of transient eddy fields (eddy kinetic energy EKE and transient eddy heat and moisture fluxes). The improvement comes from an increase in for example EKE (Ringer *et al.*, 2006, Figure 1), reducing the negative bias. However, semi-Lagrangian cores have been found to decrease EKE relative to Eulerian cores at the same resolution; therefore the increase and improvement can be attributed to increased horizontal resolution (Ringer *et al.*, 2006). Other variables are similar between the two configurations or slightly deteriorated in HadGAM1.

There is generally a small positive zonal wind bias, of less than $2\,\mathrm{ms}^{-1}$, in midlatitudes (Figure 3.1d). This bias is present at around 40–60°N throughout the depth of the troposphere in both hemispheres in the zonal mean. In the northern hemisphere it is evident in both ocean basins at approximately these latitudes. The jets have generally shifted poleward since earlier models, an effect of increased horizontal resolution also found in earlier model versions, which contributes to this, a poleward bias. However representation is generally good, and the extratropical and polar stratosphere is greatly improved since HadAM3 (Figure 3.1d vs c).

Positive MSLP biases poleward of 70°N are greatly improved relative to HadAM3. This can be attributed to the semi-Lagrangian scheme which performs better near the poles, and to improved eddies resulting from increased horizontal resolution. In the eastern North Atlantic, there is a meridional dipole of MSLP biases with negative biases

[1]These resolutions are the standard resolutions of the respective models. Comparing HadAM3 and HadGAM1 at N48 shows deterioration in certain fields in HadGAM1

(a) Zonal wind

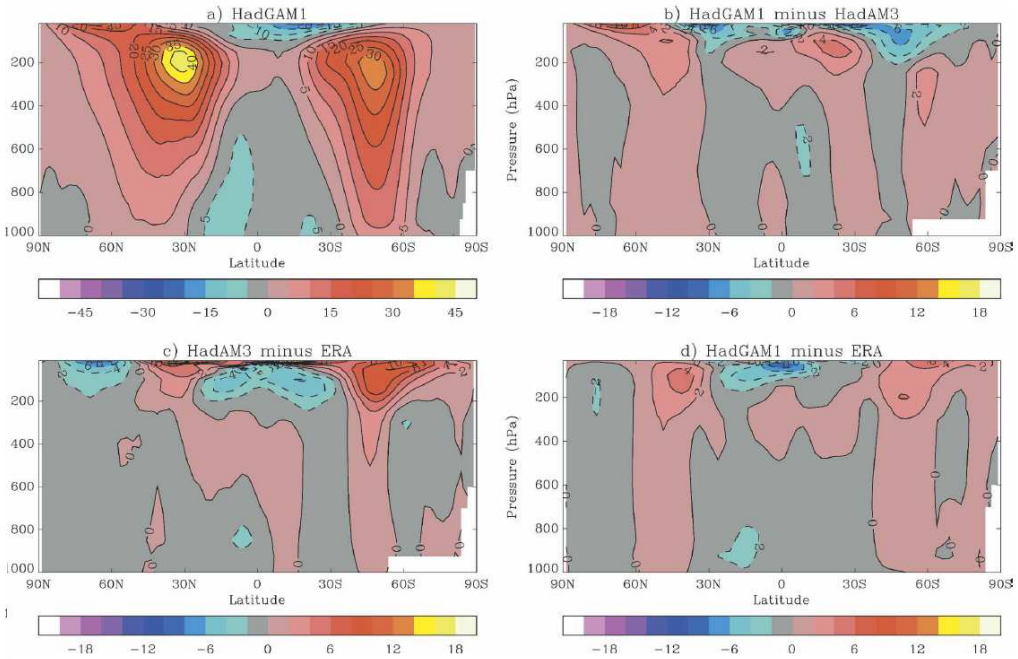

Figure 3.1: Zonal mean zonal winds (ms^{-1}) in HadGAM1 relative to HadAM3 and the ERA reanalysis. The north pole is at the left of the plot and the grey/pink divide is $0\,ms^{-1}$. This figure is Figure 4 of Martin *et al.* (2006).

in the region 50–70°N and positive biases to the south, while the high in the East Pacific is too strong. These biases contributes to positive 850 hPa wind bias in the north Atlantic and northeast Pacific, also affecting continental temperatures. The previous model version had opposite signed biases.

As already mentioned for the zonal mean, the representation of transient eddy fields is greatly improved in HadGAM1 relative to HadAM3 (Ringer *et al.*, 2006). For various measures of the northern hemisphere storm tracks, the extension into Europe is underestimated (Ringer *et al.*, 2006; Greeves *et al.*, 2007) but the tracks are generally well represented.

The NAO in the coupled model has a similar structure to that in observations, although the southern centre of action is displaced to the west (Ringer *et al.*, 2006, ; only the coupled model is shown). The model pattern explains 44% of the interannual variability in Atlantic surface pressure, which is similar to the value of 48% in observations, and its power spectra has the observed peaks at approximately 3 and 5 years and retains power in long timescales (Ringer *et al.*, 2006).

To summarise, in a fully realistic configuration, HadGAM1 at N96L38 resolution gives

a good representation of the mean circulation and of features such as the NAO and northern hemisphere storm tracks (Martin *et al.*, 2006; Ringer *et al.*, 2006). Although the newer model is not universally an improvement on the older HadAM3, components key to this project such as the storm tracks are represented better, as are the upper troposphere and lower stratosphere (Martin *et al.*, 2006; Ringer *et al.*, 2006). The use of HadGAM1 also allows some comparison with earlier experiments performed in the same model (Saulière *et al.*, 2012).

3.3.4 Sea Ice component

The sea ice component in HadGEM1 (the coupled version of the above model) is described in detail in McLaren *et al.* (2006). It incorporates several elements of CICE: The Los Alamos Sea Ice Model (Hunke *et al.*, 2010), and produces an improved representation of for example the annual cycle of sea ice (McLaren *et al.*, 2006) relative to the sea ice model used in HadCM3. However, the sea ice model components are split between the ocean and atmosphere models; in particular, the ocean component determines growth and melt and ice dynamics. The atmospheric component, used in this project, solves for the radiative and heat fluxes between the ice and atmosphere, the diffusive heat flux through the ice, and the ice surface temperature.

The temperature of the ocean-ice interface (the bottom of the sea ice) is set at the freezing temperature of salt water, -1.8°C. The surface temperature is then solved for; its evolution in time is calculated according to the zero-layer thermodynamics model of Semtner Jr (1976). This evolution depends only on the difference between the downward heat flux into the ice, calculated as a residual from the surface energy balance, and the downward diffusive heat flux through the ice which is dependent on the sea ice temperature and depth. In addition to the Semtner model, an effective surface heat capacity is included. The surface temperature is constrained never to rise above the melting temperature of fresh water (0°C).

The albedo of sea ice is a function of surface temperature, such that albedo is lower at higher temperatures, to allow for the effect of melt ponds (McLaren *et al.*, 2006). The configuration used here has no snow depth dependency[2]. For $T > T_{melt}$-10 K, albedo is

[2]In fact, there is no snow on sea ice. Although 'snow on sea ice' was not specified as a diagnostic, a comparison of monthly mean surface temperature T with monthly mean heat flux F_i through the ice verifies that the two are linearly related. The relationship is that specified in McLaren *et al.* (2006) equation 3, $F_i =$

a linear function of temperature, while for lower temperatures, albedo is capped at a maximum value of 0.8 (McLaren *et al.*, 2006).

3.4 Analysis Methods

3.4.1 Empirical orthogonal functions

In chapters 5 and 6, empirical orthogonal function (EOF) analysis is used to extract the modes of variability in a system. At the core of EOF analysis is the fact that, since atmospheric fields are highly spatially correlated, the behaviour of a field **x** can be captured by the projections of the field at each time onto a smaller set of eigenvectors **e** of the covariance matrix of the field (Wilks, 2005). Following the notation of Wilks (2005), the key components of EOF analysis for spatial fields are:-

- The normalised eigenvectors (EOFs) $\mathbf{e_m}$ of the covariance matrix. Here, m=1,2,..K where K is the number of spatial data points; see below for the restriction to fewer eigenvectors. The normalisation gives $||\mathbf{e_m}||$=1 for each $\mathbf{e_m}$.
- Their corresponding eigenvalues λ_m. The percentage of the variance in the underlying fields explained by $\mathbf{e_m}$ is given by $\frac{100\lambda_m}{\sum_{k=1}^{K}\lambda_k}$.
- Their corresponding principal component (PC) time series $\mathbf{u}_m$(t), defined as the projection at each point in time of **x**(t) onto $\mathbf{e_m}$ (equivalently, the inner product of **x**(t) and $\mathbf{e_m}$)

A further consideration is that appropriate weighting must be applied to gridded data in order to account for the variation of gridbox area with latitude. In addition, in the case of EOFs in the vertical, the variation of mass with height must be taken into account. Therefore data is weighted by $\sqrt{cos(\phi)}$ and $\sqrt{\rho}$ before calculating the EOFs (Butler *et al.*, 2010).

Typically only the few EOFs which explain the most variance are considered. This is sufficient to capture the majority of the variability in the system, and sampling issues at some point become a problem for calculating further eigenvalues. North *et al.* (1982) presented a 'rule of thumb' for the independence of two eigenvalues; given an eigenvalue

$\kappa_i \frac{T-T_f}{h_e}$, for constant effective depth h_e=2, therefore confirming that there cannot be snow present, or h_e would vary

λ_1, the difference between it and another eigenvalue λ_2 should be greater than the sampling error $d\lambda_1$ associated with the eigenvalue. $d\lambda_1$ can be approximated by $\lambda_1(\sqrt{2/N})$, where N is the effective number of independent samples (i.e. the number of samples reduced by some factor to allow for temporal autocorrelation).

Since an EOF has unit norm, the values associated with it do not have physical meaning. To give the EOF physical meaning, the PC timeseries is first normalised by its standard deviation. The timeseries of the original, unweighted data anomaly field **x** is then regressed upon the normalised PC timeseries, giving the anomalies associated with an anomaly of one standard deviation.

Finally, for a particular anomaly field of a variable **x** (for example, the response to an external forcing) the projection onto a given EOF can be established. The projection is calculated as the scalar product of the response with the EOF anomalies defined in the paragraph above (normalised such that $|EOF| = 1$) multiplied by the EOF anomaly pattern. Finally, the projection strength is this scalar product, converted into units of σ, where σ is the standard deviation of the original PC timeseries associated with this EOF.

3.4.2 Jet latitude index

The jet latitude index (JLI) is a simple geometrical index of the jet stream which can provide insights into its behaviour (Woollings *et al.*, 2010). JLI is calculated as follows:-

- The timeseries of daily-mean zonal wind u is averaged over the required longitudes and pressure levels

- At each timestep, the maximum of the resulting zonal wind profile and the latitude at which it occurs are stored as the jet speed u_{jet} and jet latitude ϕ_{jet} on that day

- A 10 day low-pass filter is applied to both time series. The Lanczos filter (Duchon, 1979) is used with 61 weights, i.e. 61 days of data are used to calculate the filtered field at each time.

Statistics of u_{jet} and ϕ_{jet} can then be examined.

3.4.3 Transient fluxes

Transient heat fluxes $\overline{v'T'}$, momentum fluxes $\overline{u'v'}$, and geopotential height variance $\overline{z'z'}$ are calculated from 6 hourly instantaneous fields. A 2–6 day band pass Lanczos filter (Duchon, 1979) with 121 weights (31 days of data) is applied to the raw fields; these time scales capture the synoptic scale eddies or 'storms' (Blackmon, 1976).

3.4.4 EP fluxes and E-vectors

The Eliassen-Palm (EP) flux vector **F**, and the three dimensional E-vector **E** are used in chapters 5 and 6. The expressions for both the EP flux and the E-vector were introduced in Section 2.3.3.2 together with the key elements of the theory.

As discussed in Section 2.3.3.2, the EP flux is formulated with respect to the zonal mean. Here, it is calculated from daily mean data. Again, a 2–6 day band pass Lanczos filter with 61 weights is applied, such that the flux particularly shows the effect of synoptic frequency transient eddies on the flow. The necessary extensions to spherical geometry, and an appropriate scaling for plotting of the EP flux vectors, are developed in (Edmon *et al.*, 1980) and are used in this thesis.

Following Hoskins *et al.* (1983), **E** is summarised by plots of low level thermal activity ($\overline{v'T'}$ at 850 hPa) and upper level horizontal divergence, i.e. the divergence of $\mathbf{E_h} = (\overline{v'^2 - u'^2}, -\overline{u'v'})$ at 250 hPa.

Table 3.1: List of CMIP5 models used

Model name	Institution
ACCESS1-0	CSIRO (Commonwealth Scientific and Industrial Research Organisation, Australia), and BOM (Bureau of Meteorology, Australia)
ACCESS1-3	CSIRO (Commonwealth Scientific and Industrial Research Organisation, Australia), and BOM (Bureau of Meteorology, Australia)
bcc-csm1-1	Beijing Climate Center, China Meteorological Administration
bcc-csm1-1-m	Beijing Climate Center, China Meteorological Administration
BNU-ESM	College of Global Change and Earth System Science, Beijing Normal University
CanESM2	Canadian Centre for Climate Modelling and Analysis
CCSM4	National Center for Atmospheric Research (NCAR)
CESM1-BGC	National Science Foundation, Department of Energy, NCAR
CESM1-CAM5	National Science Foundation, Department of Energy, NCAR
CMCC-CM	Centro Euro-Mediterraneo per I Cambiamenti Climatici
CMCC-CMS	Centro Euro-Mediterraneo per I Cambiamenti Climatici
CNRM-CM5	Centre National de Recherches Meteorologiques / Centre Europeen de Recherche et Formation Avancees en Calcul Scientifique
CSIRO-Mk3-6-0	CSIRO in collaboration with the Queensland Climate Change Centre of Excellence
EC-Earth23	EC-EARTH consortium
FGOALS-g2	LASG, Institute of Atmospheric Physics, Chinese Academy of Sciences; and CESS, Tsinghua University
FIO-ESM	The First Institute of Oceanography, SOA, China
GFDL-CM3	Geophysical Fluid Dynamics Laboratory (GFDL)
GFDL-ESM2G	Geophysical Fluid Dynamics Laboratory
GFDL-ESM2M	Geophysical Fluid Dynamics Laboratory
GISS-E2-H-CC	NASA Goddard Institute for Space Studies
GISS-E2-H	NASA Goddard Institute for Space Studies
GISS-E2-Hp2	NASA Goddard Institute for Space Studies
GISS-E2-Hp3	NASA Goddard Institute for Space Studies
GISS-E2-R-CC	NASA Goddard Institute for Space Studies
GISS-E2-R	NASA Goddard Institute for Space Studies
GISS-E2-Rp2	NASA Goddard Institute for Space Studies
GISS-E2-Rp3	NASA Goddard Institute for Space Studies
HadGEM2-AO	National Institute of Meteorological Research/Korea Meteorological Administration
HadGEM2-CC	Met Office Hadley Centre
HadGEM2-ES	Met Office Hadley Centre
INM-CM4	Institute for Numerical Mathematics
IPSL-CM5A-LR	Institut Pierre-Simon Laplace
IPSL-CM5A-MR	Institut Pierre-Simon Laplace
IPSL-CM5B-MR	Institut Pierre-Simon Laplace
MIROC-ESM	Atmosphere and Ocean Research Institute (The University of Tokyo), National Institute for Environmental Studies, and Japan Agency for Marine-Earth Science and Technology
MIROC-ESM-CHEM	Atmosphere and Ocean Research Institute (The University of Tokyo), National Institute for Environmental Studies, and Japan Agency for Marine-Earth Science and Technology
MIROC5	Atmosphere and Ocean Research Institute (The University of Tokyo), National Institute for Environmental Studies, and Japan Agency for Marine-Earth Science and Technology
MPI-ESM-LR	Max Planck Institute for Meteorology (MPI-M)
MPI-ESM-MR	Max Planck Institute for Meteorology (MPI-M)
MRI-CGCM3	Meteorological Research Institute
NorESM1-M	Norwegian Climate Centre
NorESM1-ME	Norwegian Climate Centre

3.5 Significance Testing

This thesis uses the common method of p-values to assess statistical significance. The p-value is the probability that the result, for example a difference in means, occured if the null hypothesis (in this case the means being the same) is true. As demonstrated by Ambaum (2010a), this in itself does not give a probability of the hypothesis that the mean is different being true, and Bayesian concepts of prior odds would be required to assess this different question. This note is included to clarify that statements about significance in this thesis are exactly statements about the p-values; i.e. '95% significance' is precisely 'p-value less than 0.05'.

3.5.1 Temperature, zonal wind and geopotential height fields

The temperature, zonal wind and geopotential height anomaly significance fields are evaluated using a two-tailed Student's t-test for equivalance of means. The number of degrees of freedom is modified on a gridpoint basis to allow for autocorrelation, using the adjustment $n_{eff} = n\frac{1-\rho}{1+\rho}$ where ρ is the lag-one autocorrelation.

3.5.2 Transient fluxes

The timeseries $\overline{v'T'}$, $\overline{u'v'}$ and $\overline{z'z'}$ have strongly non-Gaussian distributions. In order to estimate the significance of responses in these fields, a Wilcoxon-Mann-Whitley rank-sum test (Wilks, 2005) is performed on the time-filtered (co)variances. This is a non parametric test, which takes the null hypothesis of equivalence of location, specifically median, of the two samples.

In order to ensure that the data are uncorrelated, they are subsampled before applying the test. The autocorrelation function at various lags was evaluated in order to establish a suitable subsample lenght. An interval of 24 time points, therefore 6 days, was found to be appropriate; this was chosen to be a lag at which all points in the northern midlatitudes had autocorrelations of less than 0.1. Since some points will have shorter intrinsic timescales this is a conservative estimate.

3.6 Reanalyses

Two reanalysis datasets are mentioned in this thesis; the NCEP-NCAR reanalysis (Kalnay *et al.*, 1996) is used in order to compare the circulation in modelling experiments to the climatology from recent decades. The ERA-40 dataset (Uppala *et al.*, 2005) is not used directly but has been mentioned above as the validation dataset for HadGEM1. Since the results in this thesis are not dependent on the reanalysis product, reanalyses are discussed only briefly.

The concept of a reanalysis is the combination of historical observations and numerical models in order to produce a physically consistent gridded historical dataset of the state of the atmosphere or ocean. A numerical forecast model is run and at each time, available observations are incorporated into the model to produce a best estimate of the state of the system. This process is known as data assimilation and allows for error in both the forecast model and the observations.

Reanalyses are therefore sensitive to both the model used, the assimilation scheme, and the observations. This thesis only presents zonal wind fields from the reanalysis and is primarily interested in tropospheric winds. Since these are well constrained by observations (Kalnay *et al.*, 1996) there is relatively little difference between different reanalyses (Pope and Stratton, 2002), therefore the choice of dataset is of relatively low importance in the context of this thesis.

Reanalysis data (monthly and seasonal climate composites) are provided by the NOAA/ESRL Physical Sciences Division, Boulder Colorado, and were downloaded from their website at http://www.esrl.noaa.gov/psd.

Chapter 4

The Impacts of Heterogeneous Surface Warming on Midlatitude Temperature Variability

4.1 Introduction

The work in this chapter has been published, Holmes et al. *(2016), Journal of Climate 29 (6), "Robust Future Changes in Temperature Variability under Greenhouse Gas Forcing and the Relationship with Thermal Advection". This appears here with minimal edits, although changes are made in particular to the Introduction and Data sections to avoid repetition and improve consistency with other chapters.*

As discussed in section 2.2, robust regional and seasonal heterogeneities exist in the observed and projected mean surface warming under increased greenhouse gases (van Oldenborgh *et al.*, 2013; Hartmann *et al.*, 2013). These include winter Arctic amplification, which is directly linked to the focus of the rest of this thesis, as well as enhanced warming over land (e.g. Boer, 2011), and enhanced warming in the winter hemisphere. However, for useful impacts assessment the mean temperature is not necessarily the most important parameter. Recent extreme temperature events have highlighted the urgency of assessing whether the likelihood of such events changes in an anthropogenically forced world. Two examples are the 2003 European heat wave (Stott *et al.*, 2004) and the very cold winter of 2010 across Europe (Cattiaux *et al.*, 2010). For the European region, research into the mechanisms for changes in extreme hot days (Fischer and Schär, 2009) and cold spells (de Vries *et al.*, 2012; Peings *et al.*, 2012) is ongoing. Changes in variability may be more important for temperature extremes than the well documented changes in the mean, as suggested both by considerations from extreme value theory (Katz and

Brown, 1992) and climate model analysis (Schär *et al.*, 2004).

Therefore a review of the projected global changes in temperature variability is timely. The aims of the paper which forms this chapter are

- To assess the robustness of projected changes in variability in coupled climate models
- To quantify the relationship between these changes in variability and the heterogeneity of the warming pattern to answer the first question posed in the introduction; to what extent does thermal advection contribute to projections of 21st century temperature variability in coupled climate models?

The existing literature on this subject, and the proposed mechanism, is discussed below.

4.1.1 Review of changes in temperature variability

Some common features of changing variability have emerged in the literature. On interannual timescales there is evidence of decreasing variability of winter mean temperatures and increasing variability of summer mean temperatures in Europe (Rowell, 2005; Scherrer *et al.*, 2005). Gregory and Mitchell (1995) found that daily temperature variability in Europe also decreased in winter but increased in summer under doubling of CO_2 in an atmosphere and slab ocean configuration of the UK Met Office Hadley Centre model. Whilst this model at the time showed strong mean state biases, recent studies using state of the art climate models and 21^{st} century forcing scenarios have concluded similarly for Europe; de Vries *et al.* (2012) found decreased winter daily temperature variability in a 17-member ensemble of ECHAM5/MPI-OM and Fischer and Schär (2009) found increasing variability of summer daily temperatures in a multi-model ensemble of regional climate models. Ylhäisi and Räisänen (2014) found similar results for Europe, and decreases for the northern hemisphere mid latitudes as a whole, in daily temperature variability.

However, the picture is not so robust everywhere (Ylhäisi and Räisänen, 2014). For example, the Arctic response tends to be characterised by variability changes of the same sign as those in midlatitudes in early models with simple sea ice treatment (Stouffer and Wetherald, 2007); in contrast, later models with ice dynamics and features such as sea ice leads show increasing variability in winter and decreasing variability in summer.

It is also important to note that models differ considerably in their representation of 20^{th} century interannual temperature variability (Hawkins and Sutton, 2012).

4.1.2 Mechanisms for changing temperature variability

The dominant mechanisms driving temperature variability and its projected changes differ by region and season. In summer, radiative and land surface processes are thought to dominate. In particular, changes in surface heat balance (Gregory and Mitchell, 1995) related to reduced soil moisture availability have been shown in several studies (Fischer and Schär, 2009; Fischer *et al.*, 2012; Seneviratne *et al.*, 2006; Lenderink *et al.*, 2007; Vidale *et al.*, 2007) to be important in central Europe. Changes in the radiative balance associated with cloud cover (Pfahl and Wernli, 2012a; Lenderink *et al.*, 2007) have also been discussed. For autumn and winter changes in thermal advection, specifically from changes in time-mean surface temperature gradients, have been proposed as a dominant mechanism (Gregory and Mitchell, 1995; van Ulden and van Oldenborgh, 2006; de Vries *et al.*, 2012; Screen, 2014). This has also been mentioned as a less important driver in summer (van Ulden and van Oldenborgh, 2006; Lenderink *et al.*, 2007). It is this mechanism that forms the focus of this study, and it is discussed further below.

Circulation patterns such as the North Atlantic Oscillation and synoptic patterns such as blocking have a strong influence on regional temperatures largely through thermal advection. For example, a winter blocking system over Europe brings cold air from the Arctic or the cold continental interior (e.g. Goubanova *et al.*, 2010). In the UK, this is manifest as a relationship between Central England Temperature (Parker *et al.*, 1992) and synoptic variability as characterised by either air source or geostrophic flow direction and strength (Parker, 2009; Osborn *et al.*, 1999). It may therefore be expected that changes in either circulation patterns or surface temperature gradients, together contributing to thermal advection, may contribute to changing variability.

This mechanism is potentially valid anywhere on the globe; land areas are generally warmer than ocean areas in summer and colder in winter [Figure 4.1a,b; Kang *et al.* (2015)]. Land areas also warm faster in response to external forcing than ocean areas in both seasons, especially summer (Figure 4.1c,d). Thus the heterogeneity of the warming pattern is such that the land-ocean temperature gradient strengthens in summer and weakens in winter (Figure 4.1, lower panels). On the other hand, the Arctic is colder than

the tropics year round, so that northern polar amplification of surface warming (predominantly in the winter) weakens the time mean meridional temperature gradient at 2 m, $\frac{\partial \bar{T}}{\partial y}$ (Figure 4.1g). The figure shows the change in the absolute values of $\frac{\partial \bar{T}}{\partial y}$ and $\frac{\partial \bar{T}}{\partial x}$ such that negative (blue) is a weakening and positive (red) is a strengthening. Therefore, even unchanged wind patterns blowing across projected mean temperature gradients would cause widespread decreased variability in winter, and increased variability in summer in or near coastal areas.

Thus, in Europe for example, the changes in surface temperature gradient (Figure 4.1) are consistent with increases in summer variability (strengthening gradients) and decreases in winter variability (weakening gradients). Indeed, Gregory and Mitchell (1995) proposed that the changing land-sea temperature contrast was the key mechanism for simulated changes in winter variability and de Vries *et al.* (2012) used a cross-member regression in a single-model ensemble to show the role of zonal temperature gradients in projected winter changes in Central Europe. Projected changes in the summer land-sea temperature difference over Australia have been shown to drive thermal advection changes contributing to enhanced temperature extremes (Watterson *et al.*, 2008). Most recently, Arctic amplification and the reduction of the northern hemisphere meridional temperature gradient have been linked to reduced severity of cold days, and so to reduction of daily temperature variance (Screen, 2014).

Changes in mean gradients and their impact on thermal advection therefore provide a possible physical mechanism behind changing temperature variability (de Vries *et al.*, 2012; van Ulden and van Oldenborgh, 2006). Circulation changes projected by global climate models would also impact thermal advection but there is more uncertainty as to the direction and causes of such changes than in the case of mean temperature gradients (as discussed in the Introduction and in Chapters 5 and 6).

This chapter addresses the aims stated above through the use of two datasets, the ESSENCE single model ensemble and the CMIP5 multi-model archive, both introduced in Chapter 3. The effect of thermal advection on 20^{th} century temperature anomalies is investigated in ESSENCE through the use of multiple linear regression (section 4.4). This regression is then used to investigate what proportion of ESSENCE projected changes in variability can be attributed to thermal advection. This study considers both winter and summer and has a particular focus on midlatitude continents.

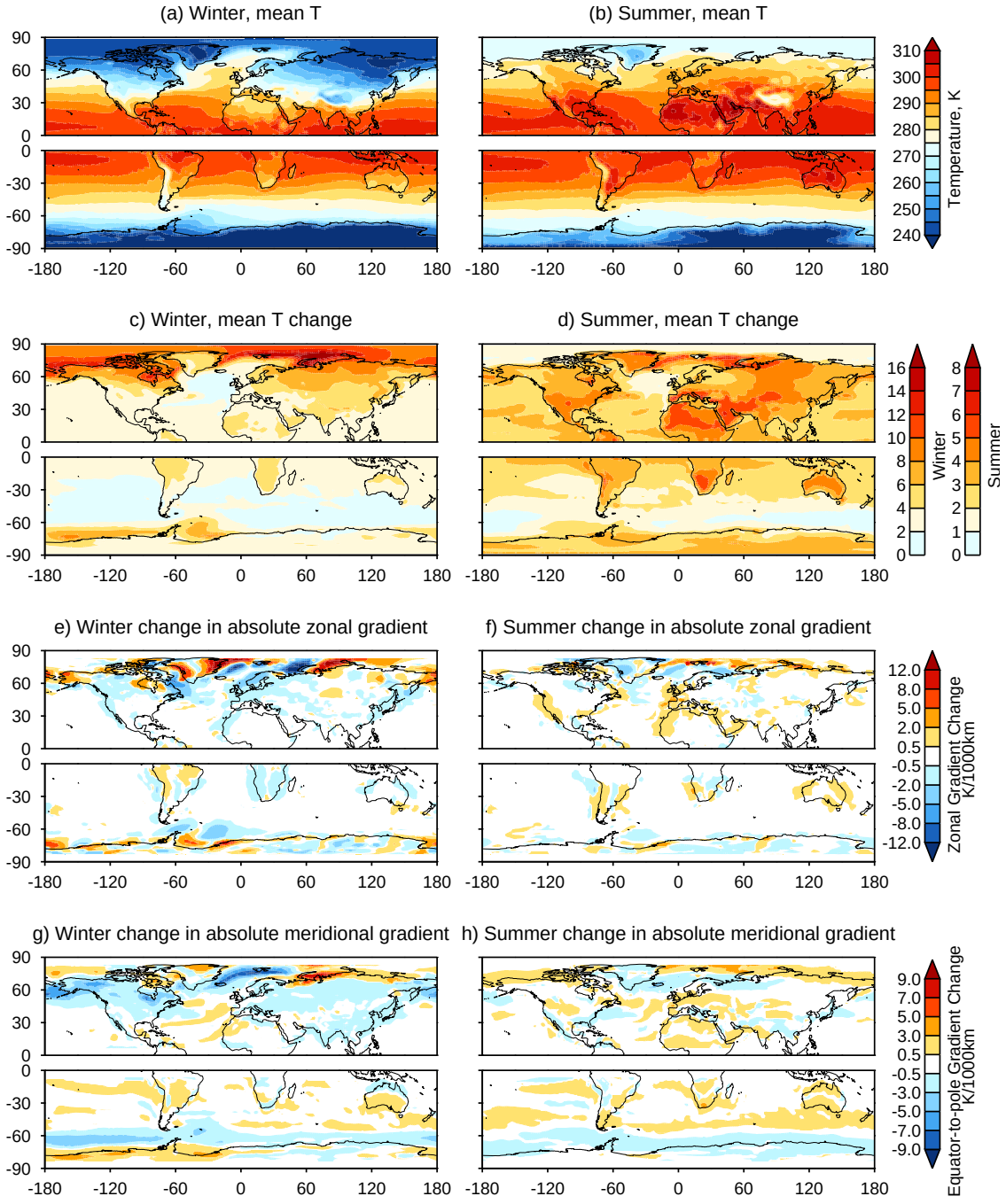

Figure 4.1: Top panel: ESSENCE seasonal-mean, ensemble-mean 2 m air temperature ($\bar{T}$) for a) winter and b) summer. Second panel; the projected change FUT-C20 in ESSENCE seasonal-mean, ensemble-mean $\bar{T}$ for c) winter and d) summer. Third panel; as above, but for absolute zonal gradient $mod(\frac{\partial \bar{T}}{\partial x})$, calculated over 18.75° longitude. Bottom panel; as above, for absolute meridional gradient $mod(\frac{\partial \bar{T}}{\partial y})$, calculated over 11.25° latitude. Gradients in K/1000km.

4.2 Data

4.2.1 The ESSENCE ensemble

The majority of the analysis in this chapter uses data from the ESSENCE ensemble, described in Section 3.2.

Two periods are isolated for comparison; a twentieth century control period C20 (Dec 1950–Jul 1990) and a future period FUT (Dec 2060–Jul 2100). DJF (December, January and February) and JJA (June, July and August) are considered. Due to the seasonality discussed in the introduction, the periods discussed hereafter are winter (northern hemisphere DJF and southern hemisphere JJA) and summer (vice versa).

The data used are daily mean fields of 2m air temperature T and sea level pressure SLP, computed into monthly averages where required, and monthly mean sea ice concentration SIC (as fraction of sea area in the grid box) and snow depth (m). All data are global and on an N48 Gaussian grid (1.875° longitude by 1.865° latitude).

4.2.2 CMIP5

CMIP5 multi-model ensemble data (from the models in Table 3.1) is interpolated to a regular 2.5° grid prior to analysis, and only monthly-mean near-surface air temperature TAS is utilized. As discussed in Chapter 3, RCP4.5 is comparable to SRES B1 (Taylor *et al.*, 2011) and therefore the forcing for the CMIP5 models considered is weaker than SRES A1B which is used in ESSENCE. Despite this difference in forcing scenarios, identifying the changes which are both robust across the CMIP5 ensemble and consistent between the CMIP5 and ESSENCE ensembles gives confidence in the qualitative nature of the changes seen, since they are found in the response to different levels of forcing, in different models, and with different initial conditions. The C20 and FUT periods are used as previously defined.

4.2.3 Processing

An underlying trend in a data series serves to inflate its true intrinsic variability (Scherrer *et al.*, 2005). Therefore such trends should be removed prior to conducting variance analysis, particularly for variables such as surface air temperature where strong trends

exist. In this study, the 40 year linear trend in ensemble-mean, seasonal-mean grid point temperature is removed for each period, thus discarding year-to-year temperature variability arising from the linear warming trend but retaining that which may result from persistent circulation anomalies.

In addition, the choice is made to discard changes in variability brought about by changes in the seasonal cycle alone, so that the changes are not dominated by for example different seasonality of snow and ice in a future climate. Therefore the gridpoint period-mean for each calendar month is removed from each data point in the monthly time series after detrending. For CMIP5, each ensemble member has its own trend and seasonal cycle removed, rather than the CMIP5 ensemble mean trend and seasonal cycle.

4.3 Temperature Variability and Projected Changes

4.3.1 Control period variability in ESSENCE

Much of the variability in circulation acts on sub-monthly timescales, so that thermal advection influences might be expected to be strongest at short timescales. However daily data is very noisy and other processes also modify the temperature variability. Moreover, it is persistent anomalies which can have the strongest impacts on health and agriculture, as well as possibly contributing to climate feedbacks. Therefore, it is of merit to look at longer timescales, and so the analysis which follows will focus on monthly data. Using monthly data has the added benefit of allowing direct comparison with CMIP5 data.

The global map of monthly temperature variability in ESSENCE in the C20 period is presented in the top panels of Figure 4.2, for winter (a) and summer (b). Variability is quantified by $\sigma(T'_{C20})$, the standard deviation of all monthly temperature anomalies taken across the full ensemble after removing the trend and seasonal cycle. Winter daily temperature variability in Europe was shown in de Vries *et al.* (2012) to compare very well with ERA-40 reanalysis data even though Europe is a particularly hard area to model. However, different climate models show very varied 20^{th} century interannual TAS variability (Hawkins and Sutton, 2012) which must be borne in mind when interpreting studies such as this.

Temperature variability is highest in the winter, especially in mid to high latitude land areas in the northern hemisphere. It is also higher over sea ice covered areas such

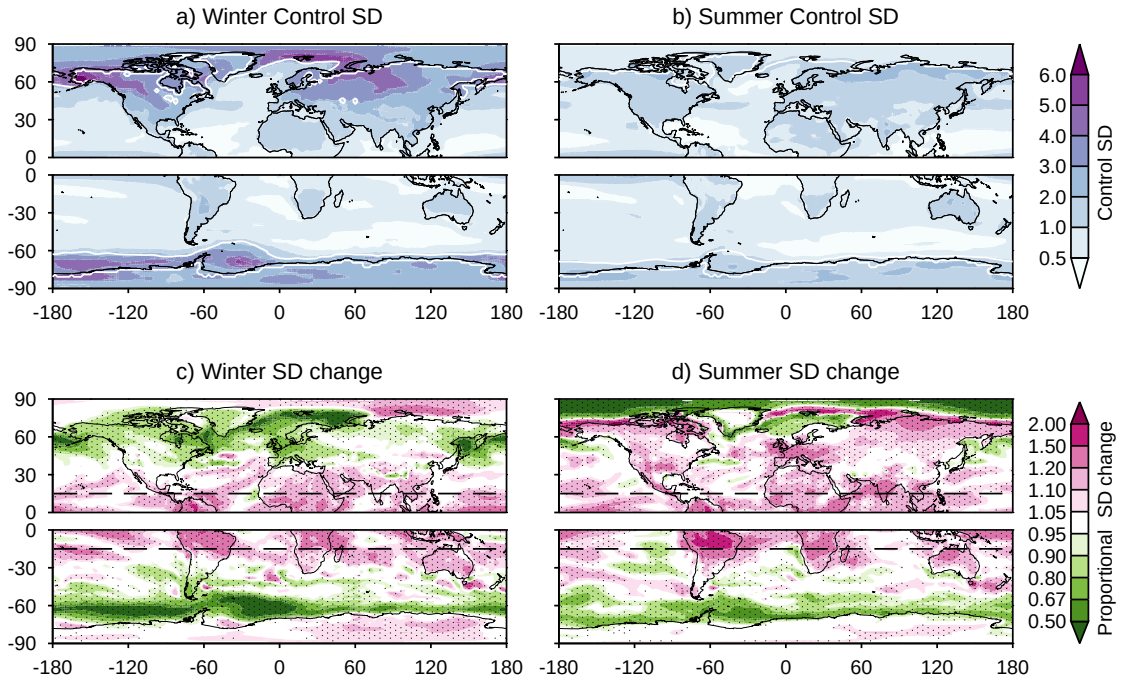

Figure 4.2: Top panel: $\sigma(T'_{C20})$, the standard deviation of ESSENCE monthly temperatures in C20 (shading) and ESSENCE climatological ice edge (15% concentration contour) in the relevant season (white contour). Bottom panel: Projected 21st century change in variability quantified by the ratio $\frac{\sigma(T'_{FUT})}{\sigma(T'_{C20})}$. Stippling where 12 ensemble members ($>$ 67% of ensemble) agree with ensemble-mean on sign of change.

as east of the Antarctic peninsula and large regions of the Arctic Ocean than over open ocean (Stouffer and Wetherald, 2007) as seen by the location of the seasonal-mean ice edge (15% contour of seasonal mean ice cover; white contour in Figure 4.2).

4.3.2 Change in temperature variability in ESSENCE

The change in temperature variability, quantified as the ratio $\frac{\sigma(T'_{FUT})}{\sigma(T'_{C20})}$, is presented in the second panel of Figure 4.2. Proportional changes are presented due to their relationship to the F-test for statistical significance of changes in variability (Barlow, 1989). In the northern hemisphere extratropics there is a notable seasonality to the response; variability generally decreases in winter and increases in summer. In the Arctic Ocean the opposite is broadly true, although local behaviour varies. Elsewhere this seasonality is not evident; the standard deviation increases in the tropics and decreases in the southern ocean in both seasons. Regions where twelve members (67% of the ensemble) agree on the sign of change are stippled in Figure 4.2 (c) and (d); this constitutes 75% of gridpoints

where the given sign of variability change is 'likely' in IPCC terminology. When the condition enforced is that 90% of the ensemble must agree (IPCC 'very likely'), 30% of all gridpoints show ensemble agreement.

Due to the large spatial scales of changes of a given sign, it is reasonable to consider the regional average standard deviation over the full 151 year period of ESSENCE to give insight into how the signal develops and how it is related to the ensemble spread. Figure 4.3 displays time series of 40 year running σ averaged over three representative regions: Europe, the Arctic Ocean, and the Southern Ocean. These time series reinforce some points from Figure 4.2; firstly, the seasonal dependence of both initial variability and response in variability is evident in all three regions. In Europe, the ensemble members unanimously agree on a summer increase in variability, and on a winter decrease. The timeseries demonstrate the large spread in the ensemble representation of variability demonstrating the need for use of a large ensemble or long periods for analysis. Note that even in the summer Arctic, where the signal is strongest, it does not 'emerge' from the ensemble noise until the middle of the 21^{st} century.

4.3.3 Comparison with CMIP5

Figure 4.4 displays $\sigma(TAS_{C20})$and $\frac{\sigma(TAS_{FUT})}{\sigma(TAS_{C20})}$for the CMIP5 models; σ is calculated as the median of the model standard deviations at each gridpoint, after removing the linear trend in seasonal mean temperature and the seasonal cycle for each model. Globally, ESSENCE variability in the control period is well representative of that in the CMIP5 ensemble (compare with Figure 4.2). This is true despite the coarser grid in the CMIP5 data which might lead to the measured variability being lower (Hawkins and Sutton, 2012). ESSENCE variability is slightly higher than that in the CMIP5 median model over the tropical Pacific and other regions of the tropics in both seasons, a difference likely due to differences in ENSO representation. There are also differences in the Barents sea and Southern Ocean, likely related to sea ice representation. Finally, while in the time processed data shown (time and seasonal cycle removed) the two datasets generally agree over Antarctica, this was not the case for the raw data; in summer the standard deviation of temperatures in ESSENCE was approxiately half that in the CMIP5 median model. This discrepancy was found largely to result from different representations of the seasonal cycle across the CMIP5 ensemble. However, Antarctica is not a key region of inter-

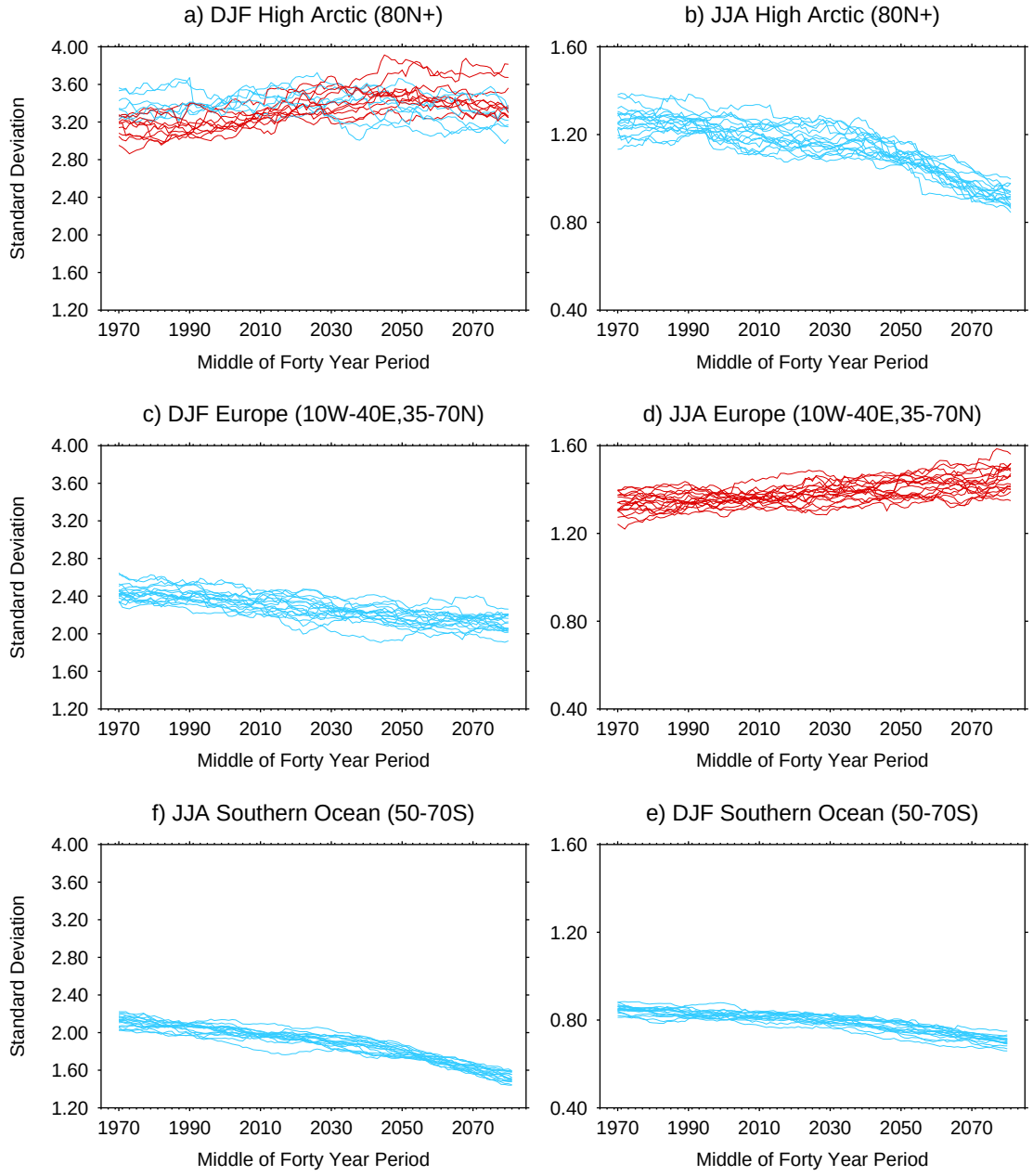

Figure 4.3: The emergence of the variability signal in the 17 ensemble members of ESSENCE in winter (left) and summer (right). Each line resembles an ensemble member; red indicates an increase, blue indicates a decrease. The time series is the square root of the regional mean of the variance of monthly mean temperatures, for the 40 year period centred on the given year. The trend and seasonal cycle of the ensemble mean is removed prior to analysis (see text).

est for this study, so is not discussed further.

The direction of change is robust between the two datatsets except for two regions, as seen by again comparing Figures 4.4 and 4.2. The first region is the equatorial Pacific, in both seasons, which is again likely to be due to disagreement on ENSO processes

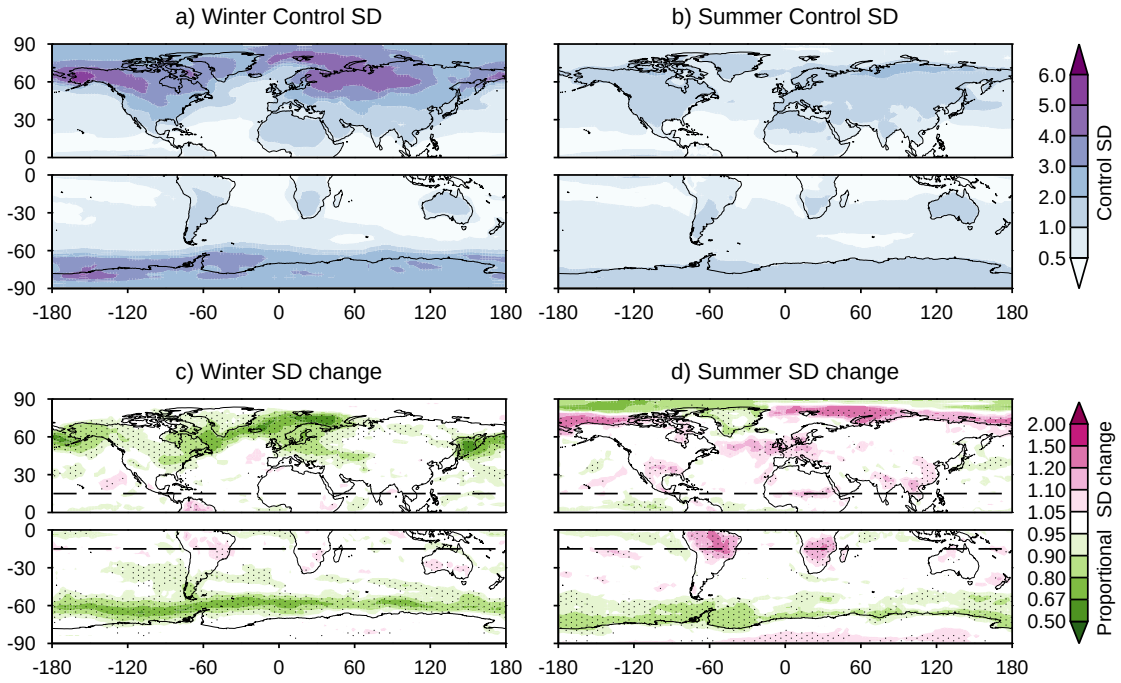

Figure 4.4: Top panel: standard deviation of CMIP5 monthly temperatures in the control period. Bottom panel: Projected 21st century change in variability quantified by the ratio $\frac{\sigma(TAS_{FUT})}{\sigma(TAS_{C20})}$. The grid point trend and seasonal cycle is removed for each model prior to analysis. The data shown is the median of the values in the multi-model ensemble; the median is calculated at separately each grid point. Stippling shows where $> 67\%$ of multi model ensemble agrees on sign of change.

between the models. The other region is the marginal ice zone in the Barents sea in summer, which is likely to be due to differences in sea ice processes and melt. Overall, projected changes in ESSENCE are stronger and more robust than in the CMIP5 ensemble median, particularly in the tropics. This is perhaps unsurprising, but points to the role of model uncertainty increasing the CMIP5 model spread.

When the emergence analysis is conducted on the CMIP5 models (not shown), there is strong evidence of the effect of removing the seasonal cycle and trend. For five of the models, leaving in the seasonal cycle produces dramatic increases in DJF variability at the end of the 21^{st} century, while leaving in the trends produces similar increases mid-century. Changing seasonality is therefore a cause of changes in monthly variability and of intermodel differences.

For the regions of particular interest in this study, namely midlatitude continents, the two datasets show strong agreement on the magnitude of control period variability

and on the sign of change, with the exception of the Eurasian continental interior, where CMIP5 has no robust trend. This suggests that it is appropriate to conduct further analysis in ESSENCE only, as it is consistent with the multi-model ensemble.

4.3.4 Qualitative relationship with temperature gradients

The changes in variability found in response to greenhouse gas forcing (outlined above) are consistent with a relationship with temperature gradients, as follows.

In the northern hemisphere in winter, the dominant and most spatially coherent signal is a widespread decrease in $mod(\frac{\partial \bar{T}}{\partial y})$, i.e., a weakening of the meridional temperature gradient between 35 and 80° N (Figure 4.1g). There is also a widespread weakening of the zonal gradients across the coasts due to changes in the land-sea contrast. It should be noted that on the west coasts of Europe and North America, the land-sea contrast effect spreads some way inland (Figure 4.1c and e), for example in Europe (10W-30E), probably due to the moderating oceanic influence on Western European climate. In general therefore, advection-driven variability would be expected to decrease, consistent with the overall changes found above.

In the northern hemisphere in summer, land-sea contrasts increase (gradients strengthen) and additionally in southern and central Europe there is a strengthening of the meridional gradient due to the enhanced warming over Spain and the Mediterranean coast (Figure 4.1f and h). Advection-driven variability would therefore be expected to increase.

In the southern hemisphere, there are no large zonally extending continents in the midlatitudes so the land-sea contrast is evident only locally. The meridional gradient signal is a weakening over ocean poleward of 60° S and a strengthening equatorward of here. The decrease in variability in the high latitude ocean in both seasons is consistent with decreasing temperature gradients, although this could also be directly attributable to Antarctic sea ice which is projected by the ESSENCE ensemble to decrease.

4.4 Reconstruction of Temperature Variability

4.4.1 Multiple regression model

To quantify the relationship between variability and thermal advection, and to investigate what portion of the changes discussed above can be attributed to changing temperature gradients and circulation patterns, we construct a multiple regression model. The variables considered are monthly mean temperature anomalies T' (processing as described above), climatological mean temperature gradients $\frac{\partial \bar{T}}{\partial y}$ and $\frac{\partial \bar{T}}{\partial x}$, and geostrophic wind anomalies u'_g and v'_g. Use of geostrophic winds follows van Ulden and van Oldenborgh (2006) and de Vries *et al.* (2012); the components are calculated from ESSENCE SLP poleward of 15° latitude (equatorward of here geostrophic balance is not a valid approximation), assuming constant density of 1.2kg m^{-3} and Coriolis parameter f calculated by latitude. Use of geostrophic winds is designed to capture the large-scale flow; however, in regions where geostrophic winds deviate significantly from the near-surface wind speed, this can be expected to limit the utility of the model. Regions where this is observed include the Tibetan plateau, Greenland and the Andes (not shown).

Gradients in both SLP and T are calculated over 11 gridpoints in the x-direction (18.75° longitude) and 7 gridpoints in the y-direction (11.25° latitude). These spatial scales are similar to those in van Ulden and van Oldenborgh (2006) and de Vries *et al.* (2012). A simple point difference is used such that, for example,

$$\left(\frac{\partial T}{\partial x}\right)_{i,j} = \frac{T_{i+5,j} - T_{i-5,j}}{x_{i+5,j} - x_{i-5,j}} \tag{4.1}$$

where the subscripts i and j are gridpoint indices in the zonal and meridional directions.

The variables are related using the multiple regression model

$$T' = (A{u_g}'\frac{\partial \bar{T}}{\partial x} + B{v_g}'\frac{\partial \bar{T}}{\partial y}) + \epsilon \equiv T'_{lin} + \epsilon \tag{4.2}$$

at each gridpoint, where ϵ is the residual. The regression is applied in the C20 period to obtain the regression coefficients A and B at each gridpoint.

More advanced methods in the calculation of the temperature gradient (such as averaging over a domain) were found not to affect the results. Likewise, a sensitivity test using geostrophic height at 850 hPa to calculate the winds reduced the fraction of vari-

Table 4.1: The notation for temperature anomalies in the linear model discussion

T'_{C20}	ESSENCE temperatures, C20 period
T'_{FUT}	ESSENCE temperatures, FUT period
T'_{lin}	Linear fit to T'_{C20}
ϵ	Residual T'_{C20}-T'_{lin}
$T2'_{u\nabla T}$	Reconstructed FUT timeseries; both $\mathbf{u_g}$ and ∇T replaced with FUT values
$T2'_{\nabla T}$	Reconstructed FUT timeseries; ∇T only replaced with FUT values
$T2'_{u}$	Reconstructed FUT timeseries; $\mathbf{u_g}$ only replaced with FUT values
$T3'_{u\nabla T}$	$T2'_{u\nabla T} + \epsilon$
$T3'_{\nabla T}$	$T2'_{\nabla T} + \epsilon$
$T3'_{u}$	$T2'_{u} + \epsilon$

ance explained by the regression model in general. Therefore SLP was used.

4.4.2 Fraction of variance explained

The correlation coefficient can be viewed as an indicator of the goodness of fit of the regression. The regression model above equates a temperature anomaly with selected terms from the tendency equation for temperature, so neglecting temporal variability in temperature gradients as well as thermodynamic effects (as discussed in the Introduction). Thus the correlation coefficient quantifies the ability of thermal advection acting across mean temperature gradients to explain temperature anomalies. Figure 4.5a and b show the correlation coefficient in both seasons. Correlations are generally higher in winter, particularly in the northern hemisphere. Correlations in winter exceed 0.7 in regions such as Western Europe, Alaska, and the eastern seaboard of North America- equivalently, 50% of monthly temperature variance in these regions can be explained by variability in circulation on monthly timescales. In summer, high correlations are restricted to much smaller geographical areas, in particular on the west coast of Europe, northern Africa, North America and Australia, and the Arctic coast. Even in these regions, the variance explained generally does not exceed 40%.

There are various reasons for the spatial and seasonal variation in the fraction of variance explained. Firstly, in regions of high orography (for example the Rocky Mountains, Tibetan plateau and the Andes) geostrophic balance based on SLP is not a good approximation. Indeed, the wind components u'_g and v'_g are very poorly correlated with the

ESSENCE 10m wind speed in these regions.

Secondly, the regression model may not capture the main drivers of variability. For example, in the high Arctic temperatures are strongly moderated by the radiative budget, and the temperature gradient is very variable such that using the mean temperature gradient is not a good approximation.

The difference between the summer and winter correlations is particularly striking. This can in many places be linked to summer having either weaker geostrophic winds (for example in Western Europe) or weaker temperature gradients (in the North American interior and across the coasts of North America, Norway, and East Asia; implicit from temperature fields, Figure 4.1a and b). The dominant driving mechanism for summer variability therefore appears to be something other than thermal advection, for example the radiative and land surface drivers discussed in Section 4.1.2.

4.4.3 Use of the simple model to simulate future change: methodology

The multiple regression model can be used to investigate what portion of the change in variability discussed in section 4.3.1 can be attributed to changes in thermal advection. A new time series of temperature anomalies is constructed for the future period using the linear model with coefficients A and B retained from the C20 regression and winds and/or temperature gradients calculated from the FUT period of ESSENCE. This is denoted e.g. $T2'_{u\nabla T}$ with the subscripts denoting whether winds, temperature gradients or both are changed. To retain a comparable level of noise, the control period timeseries of ϵ is then added to create a modelled timeseries of future temperature anomalies $T3'_{u\nabla T}$. (See Table 4.1 for a full explanation of notation. $T2'_{u\nabla T}$ is not discussed further.)

The standard deviation of this time series can be compared to $\sigma(T'_{FUT})$ (temperature anomalies computed directly from ESSENCE). It is then possible to estimate how much of the projected change in temperature variability in ESSENCE is a direct consequence of thermal advection. By retaining either control period temperature gradients or winds, the contribution to changing temperature variability from wind anomalies and temperature gradients can be partitioned.

This methodology applied directly produces many points at which a nonphysical change in variability is produced (i.e. an increase of greater than double the maximum seen in the ESSENCE data, or a decrease of less than half the minimum). These points are

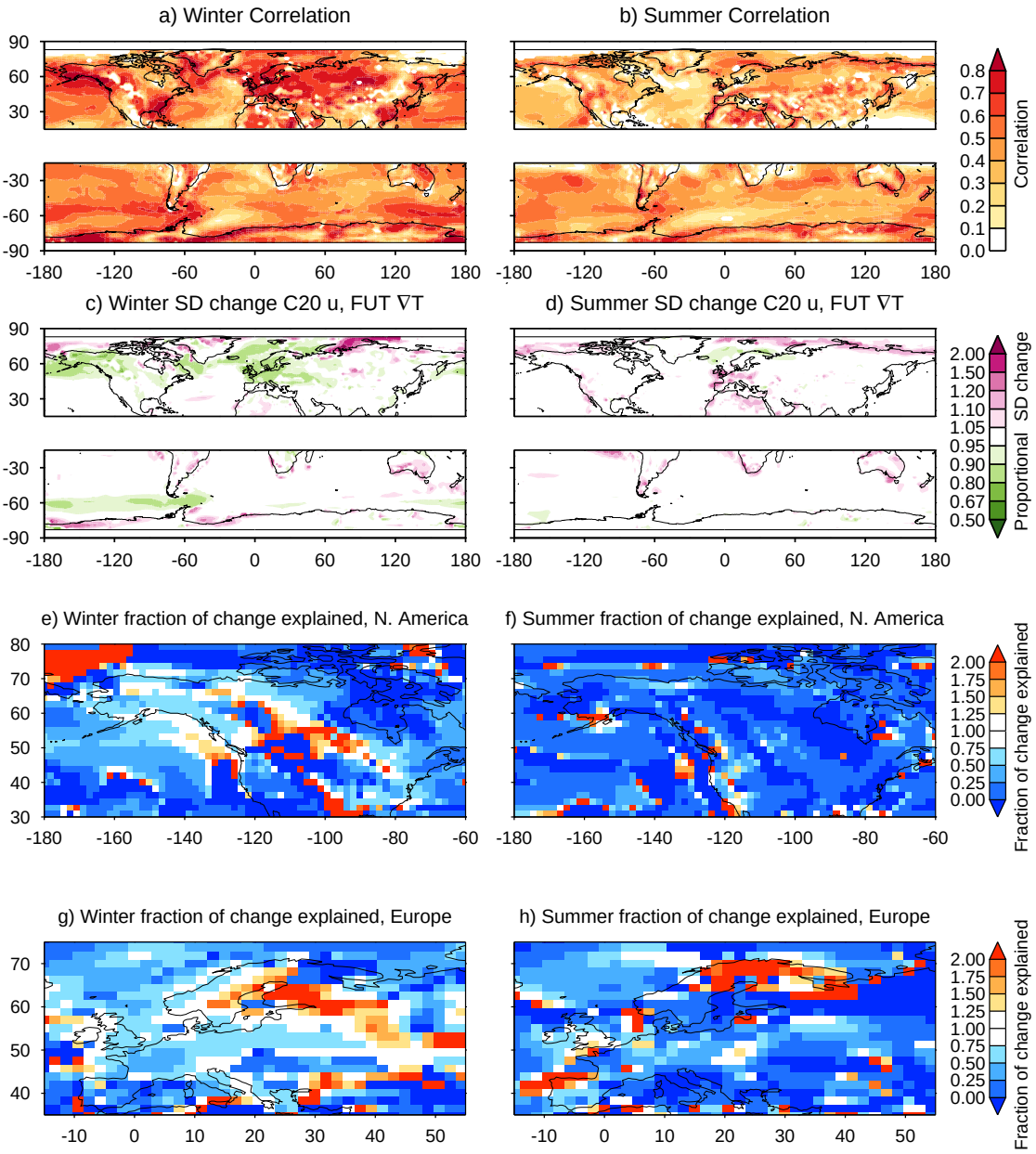

Figure 4.5: a) and b): The correlation of T'_{C20} with T'_{lin} for winter and summer. c) and d) The change of standard deviation in the regression model quantified as $\frac{\sigma(T3'_{\nabla T})}{\sigma(T'_{C20})}$. All data is monthly. e)–h); The fraction of change captured by the linear model; $\frac{\sigma(T3'_{\nabla T})-\sigma(T'_{C20})}{\sigma(T3'_{FUT})-\sigma(T'_{C20})}$. Here and in subsequent figures, data is not available for very high latitudes, where the tight grid spacing is deemed to make the scales of the zonal gradient calculation inappropriate, or the tropics, where the geostrophic assumption is invalid. Therefore these areas are excluded from the plots.

generally those in which the mean control or future temperature gradient is very small (of order $1 \times 10^{-3} Kkm^{-1}$ or less). Therefore any small shift in mean temperature patterns

produces an increase of order several hundred in the regression and consequently in the reconstructed time series, because temperature anomalies are modelled as a linear function of the gradient components. For this reason any temperature gradient component which is less than $1 \times 10^{-3} Kkm^{-1}$ in either period is not included in the regression.

Figures 4.5c and 4.5d display the change in temperature variability produced by the linear model in the case when only temperature gradients are replaced with their 21^{st} century values (i.e., wind components are retained from the C20 period). Evidently, there are large regions where this is not a good model. In particular, these include the tropics and low to mid latitude oceans in both seasons, regions of high orography, and the midlatitude continental interiors especially in summer. These regions can be linked back to those where correlation is small in the C20 period (section 4.4.2), or where temperature gradient changes are small (section 4.3.4). Over southern hemisphere midlatitude oceans, the Indian Ocean and southern Eurasia in winter, and over northern China and Eurasia in summer, the model does not even recreate the sign of change correctly. These regions are therefore not considered further.

Panel 4.5c shows the results from the linear model for winter. By changing temperature gradients alone, the decrease in winter variability is qualitatively recreated in Alaska and Western Canada, the subpolar North Atlantic and much of Europe, the ACC region west of the Drake Passage, and south Australia. Of these regions, it is of interest to focus on the quantitative agreement for two regions where there is particularly widespread agreement in the sign of change, namely, Europe and North America. Panels 4.5e and g show this agreement for winter. The agreement is quantified by $\frac{\sigma(T3'_{\nabla T}) - \sigma(T'_{C20})}{\sigma(T3'_{FUT}) - \sigma(T'_{C20})}$. A value less than 0 (dark blue) implies the linear model sign of change is incorrect, and a value of 1 (white) implies the linear model recreates the exact magnitude of change. Over much of Europe and large regions of North America, over 50% of the projected change in variability can be reproduced solely using the change in mean temperature gradient.

Over the ocean there are regions where the linear model future variability is over a factor of two greater than that simulated in ESSENCE. These are regions of decreasing variability; therefore the discrepancy implies that much of the decrease is caused by processes not accounted for in the linear model. Comparison with Figure 4.2 shows that these regions are those just inside the control period sea ice zone. This is discussed in the next section.

In summer (Figure 4.5d), the linear model induces the largest changes at the coasts (excluding that of Antarctica) and in high latitudes of the northern hemisphere (70–80°N). There is also a strong signal inland in northern Africa and over much of Europe. The linear model correctly reproduces increasing variability in Australia, Europe and northern Africa, India and South America, and off the Arctic coast. There is also scattered agreement elsewhere, but often in regions where the change simulated by ESSENCE is small. In subpolar regions (poleward of 60°) the linear model again underestimates the projected changes. Increasing variability in other areas is generally underestimated by the linear model, in particular in India and South America, off the Arctic coast, and to a small extent in parts of Europe. Panels 4.5f and h show the agreement between the linear model and ESSENCE for summer. Evidently the linear model is less skilful in summer than winter, but there are still areas, including southern England, southern Spain and central Europe, where the change in temperature gradient reproduces 50% of the future change in variability. Thermal advection does not appear to be an important process in changing variability in North America in summer.

Circulation changes may also contribute to changes in advection. ECHAM5 (the atmospheric model in ESSENCE) shares many features of circulation change with other models. These include a poleward shift of the westerlies in the southern hemisphere in both seasons and in the Pacific in winter and a downstream extension of the Atlantic storm track (not shown; e.g. Pinto *et al.*, 2007). Figure 4.6 shows which of the variability changes described above are reproduced when circulation $\mathbf{u_g}$ is changed in addition to or instead of temperature gradients. The change induced by circulation changes and temperature gradients together (Figure 4.6, top) is in the opposite sense to that in the full simulation across much of the subtropical southern hemisphere ocean. The change induced by circulation changes only is very small (Figure 4.6, bottom), so we conclude that temperature gradients are more important for explaining future changes in variability.

As the Arctic is a region of distinctive changes in temperature variability which are qualitatively but not quantitatively recreated by the simple linear model, and due to the role of Arctic Amplification in changing temperature gradients, we now discuss the Arctic region in more detail.

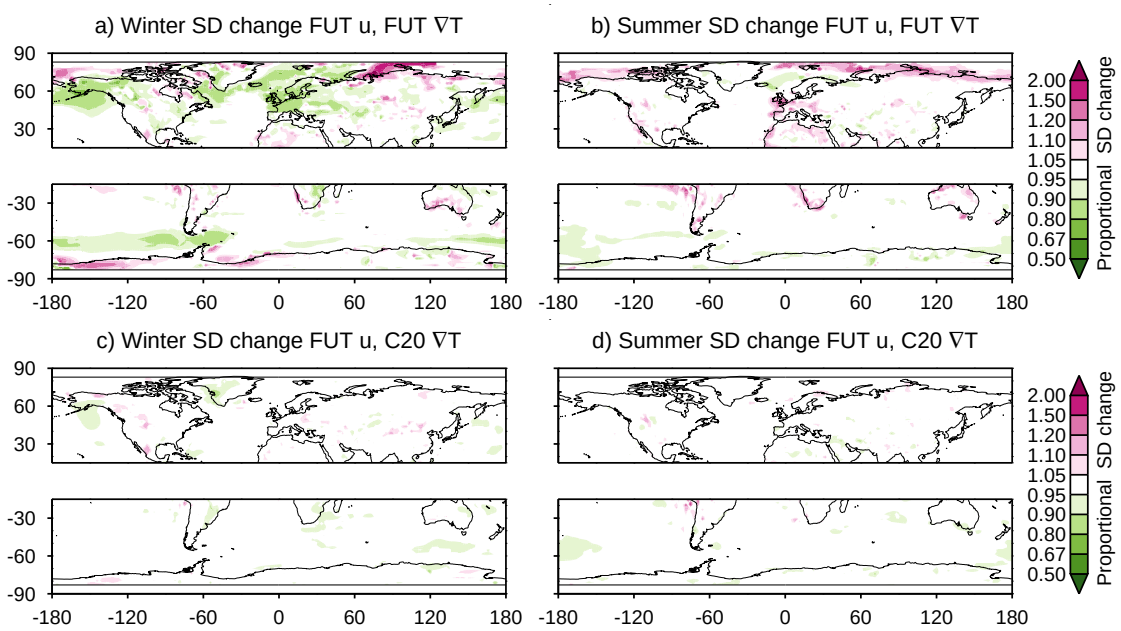

Figure 4.6: As for Figure 4.5c) and d) but (top) with $\frac{\sigma(T3'_{u\nabla T})}{\sigma(T'_{C20})}$ and (bottom) $\frac{\sigma(T3'_{u})}{\sigma(T'_{C20})}$.

4.4.4 Arctic regions

The low correlations in the Arctic (Figure 4.5, panels a and b) suggest that circulation variability is not a key driver of surface temperature variability here. As is the case anywhere, this could be due either to dynamical terms neglected in the regression which include variability in ∇T or to thermodynamic effects. High temperature gradients across the ice edge and the intraseasonal movement of this edge causes high variability in gradients themselves, and so if dynamics are the cause it could be expected that including $\nabla T'$ in the regression would increase correlations and the ability of the regression to reproduce future change. This can be done either within the regression components (so that e.g. $u'_g \frac{\partial \bar{T}}{\partial x}$ becomes $u'_g \frac{\partial T}{\partial x}$) or by fitting the model separately to u'_g and $\frac{\partial T'}{\partial x}$. However, sensitivity tests (not shown) confirmed that neither method notably improves correlations in the Arctic region, except between 30° W and 60° E, a region where the simpler description of thermal advection variability was already producing good results.

This is consistent with temperatures (and temperature variability) in the Atlantic sector in winter being dominated by thermal advection but elsewhere across Arctic being dominated by the longwave radiation budget (Serreze and Barry, 2005). The longwave radiation budget is affected by the extent and depth of sea ice cover as well as the amount

and type of cloud cover.

4.4.5 Daily variability

A preliminary analysis of variability, its changes, and the 20^{th} century relationship with thermal advection was also conducted for ESSENCE daily data. These results are summarised below (not shown).

As expected, the C20 standard deviations of daily data are larger than monthly values. The seasonal and spatial structure is similar, with greater variability in winter, and at high latitudes or over sea ice, snow, land, and the western boundary currents in the ocean. Some features differ; for example, the local maximum in monthly variability in the equatorial Pacific, which can be linked to ENSO, is not as prominent in daily data. The changes are also consistent with the findings in monthly data, although changes in daily variability are weaker in the Arctic and stronger over Eurasia than in the the monthly data.

Finally, the correlations between geostrophic winds and temperature are lower on daily timescales than on monthly timescales; in daily data, while correlations still exceed 0.6 in some regions, summer correlations in the northern hemisphere are particularly low ($<$0.4 everywhere). Therefore, the relative importance of different processes for daily variability is, as may be expected, somewhat different than for monthly variability. A detailed analysis of processes acting on daily timescales is left for future work.

4.5 Discussion and Conclusion

This chapter has presented a global assessment of the climatological variability of monthly and to a lesser extent daily temperatures in the two solstitial seasons, projected changes, and the role of the thermal advection mechanism. The key findings may be summarised as:-

- There is a clear spatial pattern and seasonality in the projected changes of the standard deviation σ of monthly surface air temperature variability. This is robust across a single model initial condition ensemble (Figure 4.2). Many of these changes are also robust across the CMIP5 multi-model ensemble (Figure 4.4).

- The time series of σ averaged over a large region (Figure 4.3) is noisy, showing the importance of good sampling, such that the use of a large ensemble as is done in this paper is essential.
- Emergence of the signal is not expected until at least the middle of the 21^{st} century.
- A simple metric of atmospheric thermal advection explains over 50% of 20^{th} century monthly temperature variability in widespread areas in winter (Figure 4.5c).
- A relatively simple regression model, taking account only of changes in mean temperature gradients, is able to reproduce many aspects of the spatial pattern of change in temperature variability. Over large regions of Europe and North America in winter the advection could account for over half of the projected change in temperature variability. The contribution is weaker in summer but still amounts to several tens of percent over large regions (Figure 4.5e–h). This suggests that the thermal advection mechanism, whereby anomalous winds (relative to the time mean) blowing across a region of temperature gradation cause anomalous temperatures downstream, provides a physical explanation for many of the projected changes in temperature variability.

Regarding the variability changes themselves, preliminary analysis found similar results for daily variability. Robust signals of change in the large ESSENCE ensemble thus add weight to recent papers by Ylhäisi and Räisänen (2014), Screen (2014) and Schneider *et al.* (2015) demonstrating changes in daily variability.

Considering the difference between ESSENCE and CMIP5, regions where results are robust in ESSENCE but not in CMIP5 point to the role of structural differences between models, rather than internal variability, in the uncertainty.

For winter, our findings on the role of thermal advection are consistent with the link between variability and zonal gradients proposed by de Vries *et al.* (2012), and between variability and Arctic amplification as shown by Screen (2014) and Schneider *et al.* (2015). All these papers look at a specific domain (Europe or the northern hemisphere) and at a specific temperature gradient direction, whereas our model is successful over a large spread of geographic regions and covers both directions. Moreover, we explicitly recreate future changes in variability using changed temperature gradients, which no previous study has done. Thermal advection is found to be important for projected changes in

Alaska, Western Canada, Europe, south Australia, and subpolar oceans in winter.

In summer, local radiative and land surface processes are more often invoked to explain changes in variability, with some exceptions; Watterson *et al.* (2008) showed that projected changes in summer temperature extremes in south central Australia can be understood in terms of thermal advection from the hot continental interior, using a simple model with some similarities to ours. They concluded that it is the increasing temperature gradient, and not changes in wind variability, which dominate the response. Our results also show a role of the temperature gradient and thermal advection for Australia in summer, but in the south east (Figure 4.5d). We also find other regions where the effect of temperature gradients can be seen in summer, for example in Europe, subtropical land areas, and off the Arctic coast. However, the change induced by the thermal advection mechanism is, in most areas, less than 50% of the whole, with the local radiative and land surface processes discussed previously playing a more dominant role.

The regression model is deliberately simple, and yet is able to capture a large proportion of projected changes in temperature variability. It is to be expected that some of the choices made may have moderate effects on the findings; for example, the influence of the land-sea contrast on variability near coasts may extend further inland were a different lengthscale used. In addition, there are limitations to using the geostrophic wind, in particular that calculated from SLP, since it itself may be affected by temperature anomalies. However, the winds calculated in this way did provide a good representation of the near-surface wind speeds in the regions of interest (as discussed in Section 4.4.1), and use of geostrophic winds has precedent in previous studies of this nature (van Ulden and van Oldenborgh, 2006; de Vries *et al.*, 2012).

The thermal advection mechanism discussed in this chapter would manifest as changes in the relationships between circulation and temperature anomalies, as found in Goubanova *et al.* (2010) and Masato *et al.* (2014). For example, the familiar temperature impacts of given circulation regimes such as the cold weather found in northern Europe in the negative phase of the North Atlantic Oscillation may become less severe in winter due to reduced temperature gradients (Cattiaux *et al.*, 2010; Osborn, 2011; Masato *et al.*, 2014; Dong *et al.*, 2011). Cattiaux *et al.* (2012) found that in each season, circulation changes (assuming the same relationship between circulation and temperature) are not the dominant driver of future warming and of increases in interannual variability. This

is consistent with the findings above that temperature gradient changes are more important than circulation changes. These results therefore have important implications for understanding the impacts of circulation patterns in the future, as well as contributing to the ongoing discussion about extremes in a more statistical sense. Crucially, changes predicted by the thermal advection mechanism as outlined in this study can be treated with added confidence due to the physical understanding underlying heterogenous changes in mean surface temperature.

Chapter 5

The Response to Sea Ice in an Aquaplanet Configuration of HadGAM1

As discussed in the Introduction, one of the key goals of this thesis is to examine the atmospheric response to sea ice forcing in simplified configurations. In this chapter, modelling experiments are performed in an aquaplanet configuration of HadGAM1. Aquaplanet experiments are a useful tool for examining the purely dynamical behaviour of any given GCM (Neale and Hoskins, 2000b), and have previously been used for the examination of the effect of both symmetric and asymmetric SST perturbations in the tropics and midlatitudes (e.g. Caballero and Langen, 2005; Neale and Hoskins, 2000b; Inatsu *et al.*, 2002b; Brayshaw *et al.*, 2008). Here, atmosphere-only aquaplanet modelling is extended to investigate the effect of zonally symmetric sea ice perturbations.

In using an AGCM, aquaplanet modelling is a step up in complexity from simpler techniques previously used to study the impacts of sea ice loss (e.g. Butler *et al.*, 2010). On the other hand, since the lower boundary forcings are zonally symmetric, it represents a notable simplification from most studies into the effects of sea ice (as discussed at length in chapter 2). Therefore it provides a unique opportunity to investigate the mechanisms which contribute to modelled responses to changing sea ice conditions.

The key questions investigated in this chapter are-

- What is the response of the jet stream to sea ice change?
- What mechanisms are fundamental to this response?
- At what latitudes, if any, is the atmosphere particularly sensitive to forcing?
- How is the response to a given sea ice forcing sensitive to the background atmo-

spheric state?

This chapter is structured as follows; the experimental design, in particular the SST and sea ice forcings, are introduced in section 5.1. The model state in a case with no sea ice is described in section 5.2. The main body of the chapter examines the response of the time mean circulation, and its variability, to ice addition (section 5.3). Finally, section 5.4 investigates which aspects of this response are robust and which are sensitive to the control run circulation; this is achieved through experiments with a different SST profile.

5.1 Experimental Design

In this chapter, zonally symmetric, time invariant sea ice and SST profiles are specified as forcing in an aquaplanet configuration of HadGAM1 (described in Section 3.3). It is run at N69L38 resolution, corresponding to 1.875° x 1.25° in the horizontal. There are 38 vertical levels extending to 39.3 km (Martin *et al.* (2006)). The other details of this configuration are specified below.

5.1.1 Solar, Atmospheric and Aerosol Forcings

Emissions of aerosol, CO_2, soot and black carbon are turned off, and ozone is specified at northern hemisphere annual mean (derived from the standard, late 20^{th} century ozone climatology for HadGAM). The insolation is specified at perpetual equinox conditions so that the insolation is both time invariant (excepting the diurnal cycle) and symmetric around the equator. Equinox conditions are chosen rather than solstice conditions so that that there is some insolation at high latitudes, otherwise the pole may become unrealistically cold[1].

5.1.2 SST forcing

Figure 5.1 shows three SST profiles. Two of these, denoted SST1 and SST2, are used in this chapter. The third, QOBSWIDE (on which SST1 and SST2 are based) was used in Brayshaw *et al.* (2009) where it was described as representing Northern Hemisphere

[1]Perpetual equinox is achieved by setting both the Earth's obliquity (the axial tilt relative to the plane of orbit) and the eccentricity of its orbit to 0.

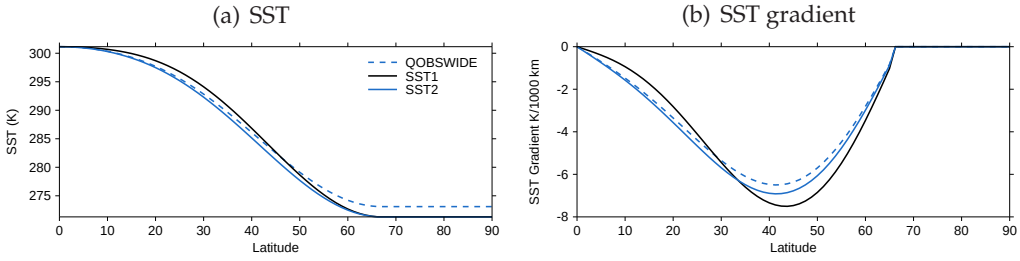

Figure 5.1: SST profiles specified for HadGAM1 experiments. a) SST profiles 'SST1' (black), 'SST2' (blue), and QOBSWIDE (Brayshaw *et al.*, 2009) (blue dashed). b) As a) but for SST gradient.

winter SSTs[2].

The profiles as a function of latitude ϕ take the form:-

$$T(\phi; T_0, T_{\phi_c}, r, \phi_c) = \begin{cases} (T_0 - T_{\phi_c})(1 - rsin^2(90\frac{\phi}{\phi_c}) - (1-r)sin^4(90\frac{\phi}{\phi_c})) + T_{\phi_c} & \text{if } |\phi| \leq \phi_c \\ T_{\phi_c} & \text{if } |\phi| > \phi_c \end{cases} \tag{5.1}$$

The parameters are: T_0, the temperature at the equator; $0 < r < 1$, describing the relative weighting of sin^2 and sin^4 terms; and ϕ_c, the critical latitude poleward of which SST is set to the constant T_{ϕ_c}.

For both SST1 and SST2, ϕ_c=67°, T_0=301.15 K (28°C), and T_{ϕ_c} is the freezing temperature of salt water (below which sea ice would be expected to exist) 271.35 K (-1.8°C). For SST1, r=0.25, and for SST2, r=0.5. With these values, SST2 is the same as QOBSWIDE except that the polar cap temperature is lower. In SST1 the curvature is reduced in the tropics but increased in mid-latitudes relative to QOBSWIDE or SST2. The SST gradient in SST1 is therefore increased close to the region where sea ice and the associated surface temperature front is to be imposed.

5.1.3 Sea Ice Forcing

A control run is conducted with no sea ice[3]. This is denoted 'NOICE'. In all other cases, ice of concentration 100% and thickness 2 m is imposed from the pole to a specified latitude ϕ_1. Thickness and concentation decrease linearly over 5° latitude to zero at ϕ_2. These experiments are denoted 'INN', where $NN = \phi_2$ (as shown in Table 5.1). These

[2]QOBSWIDE was in turn a warmer, broader version of QOBS (e.g. Neale and Hoskins (2000b) and Brayshaw *et al.* (2008)).

[3]For computational reasons both polar points are still specified at SIC=100% in this run

sea ice profiles were chosen to provide a simplified forcing in keeping with the style of the experiment. SST in all grid boxes containing sea ice is set to 271.35 K (-1.8°C).

Since the control run contains no ice, all the perturbed runs (with ice added) are in the opposite sense to the majority of previous studies, which examine the response to sea ice removal. The ice addition approach enables a constant benchmark in a way that arbitrarily picking a control ice extent at high or midlatitudes would not. In addition, it enables comparison of the control run to previous aquaplanet studies.

Since the focus of this thesis is the North Atlantic, ice thickness is set to 2 m, for the following reasons:-

- This is the default thickness in the Northern Hemisphere in UM atmosphere-only integrations (Jones, 1993)[4].
- Where previous studies have stated the thickness used, this is the most common value (Seierstad and Bader, 2009; Blüthgen *et al.*, 2012; Screen *et al.*, 2013b).
- While sea ice thickness is very heterogeneous, and multi-year ice may have thick-

[4]Southern hemisphere ice is typically thinner, and the default thickness there is 1 m (Jones, 1993).

Experiment	Lowest Latitude with c=100% (ϕ_1)	Highest Latitude with c=0% (ϕ_2)	Ice Extent	Ice Area
NOICE			0.02	0.02
I80	85	80	3.41	2.26
I75	80	75	7.98	6.12
I70	75	70	14.44	11.87
I65	70	65	22.73	19.48
I60	65	60	32.79	28.88
I55	60	55	44.53	40.00
I50	55	50	57.89	52.75
I45	50	45	72.73	67.05

Region and Period	Ice Extent	Ice Area
NH climatology Sep (month of minimum)	6.5	4.4
NH climatology Mar (month of maximum)	15.5	13.7
SH climatology Feb (month of minimum)	3.0	1.9
SH climatology Sep (month of maximum)	18.8	14.5
NH 2012 Sep mean (month of record minimum)	3.6	2.36

Table 5.1: Top: The sea ice extent and area (10^6 km^2) in each hemisphere for all experiments. NOICE has a non-zero area due to polar sea ice point. Bottom: Sea ice climatology for 1981–2010 for both Northern Hemisphere (NH) and Southern Hemisphere (SH), derived from the NSIDC Sea Ice Index (Fetterer *et al.*, 2002) (Section 2.1.1). Observed NH areas are a lower bound on the true values as there is a small polar area of 0.31–1.19 10^6 km^2, depending on the year, which is outside the range of the satellites.

nesses of 5 m or more, 2 m is close to the average depth of first-year Arctic ice in late winter (Kwok *et al.*, 2009), and there is a growing proportion of first-year ice in the Arctic.

The extents and areas in the different experiments are presented in Table 5.1 for comparison with observed values. While ice in the Northern Hemisphere is observed as far south as 45° (Serreze and Barry, 2005), this is only in highly localised regions in marginal seas, and at maximum extent. The climatological maximum and minimum extents are closest to the experiments I70 and I75, respectively, while the record minimum observed in September 2012 is most similar to I80 (Table 5.1). Some of the forcings presented here are therefore large in the context of 21^{st} century northern hemisphere sea ice. Large expanses of the Eurasian and North American land masses north of 45°N have surface temperatures below freezing in winter (Figure 4.1a) so there are cold surface temperatures at these latitudes. Moreover, the cases with most ice may have particular relevance to past climates and to the southern hemisphere, where sea ice surrounding Antarctica extends to between 55°S and 65°S in winter (e.g. Kidston *et al.*, 2011b).

5.1.4 Spinup, Run Length, and Data Processing

The aquaplanet simulations are run for five years. The time evolution of area-mean surface temperature, lower tropospheric temperature and lower tropospheric zonal wind suggests that the ice-atmosphere system is spun up by 5–6 months into the integration (not shown), whether the averages are taken globally or only poleward of 45°. The first year of simulation is therefore discarded to ensure that the atmosphere is spun up.

The hemispheres can be assumed to be independent and so within this chapter, all analysis uses data from both hemispheres. For example, time mean plots show the average over both hemispheres for years 2–5. The overbar denoting time mean is in general dropped for ease of presentation, and a time mean should be assumed unless noted otherwise. Moreover, in all axis labels, 'latitude' refers to 'absolute latitude'.

In the model output, when the surface pressure is below 1000 hPa, variables on pressure levels are not extrapolated to the 1000 hPa surface. Rather, the data appears as zero. Variables are therefore only presented for 925 hPa and above. However, in three of the experiments (I55, I50 and I45) the surface pressure response is strongly negative over the pole, such that there is often also missing data at 925 hPa. Therefore, variables presented

at 925 hPa (temperature and zonal wind) are only averaged over valid time points, determined by evaluating the 6 hourly data. This generally affects results polewards of 70° latitude.

5.2 The Control Run: 'NOICE'

This section introduces the basic structure of the atmospheric circulation in the NOICE run (forced with SST1).

The time-mean zonal-mean zonal wind $[\bar{u}]$ is shown in Figure 5.2a. The maximum of $[\bar{u}]$ in the control run is 35 ms^{-1} at approximately 200 hPa and 47° (Figure 5.2a). The maximum at 850 hPa is 16 ms^{-1} and is at the same latitude on the model grid. A stratospheric polar vortex is evident poleward of 55° and above 50 hPa.

Direct comparisons with observations are difficult since these experiments are not designed to exactly simulate any one season; nor is a symmetric planet with an isothermal cap a very accurate description of either hemisphere. Nevertheless, the zonal wind structure can be compared to early winter (December and January) in the North Atlantic (Figure 5.2b); the eddy driven jet is of comparable magnitude to the subtropical jet, and the winter polar vortex is apparent. The structure is also very similar to that in Brayshaw *et al.* (2009) using QOBSWIDE, although SST1 produces a slightly stronger and poleward shifted eddy driven jet than QOBSWIDE. This is consistent with the poleward shift of the maximum surface temperature gradient and the increased pole-to-equator temperature

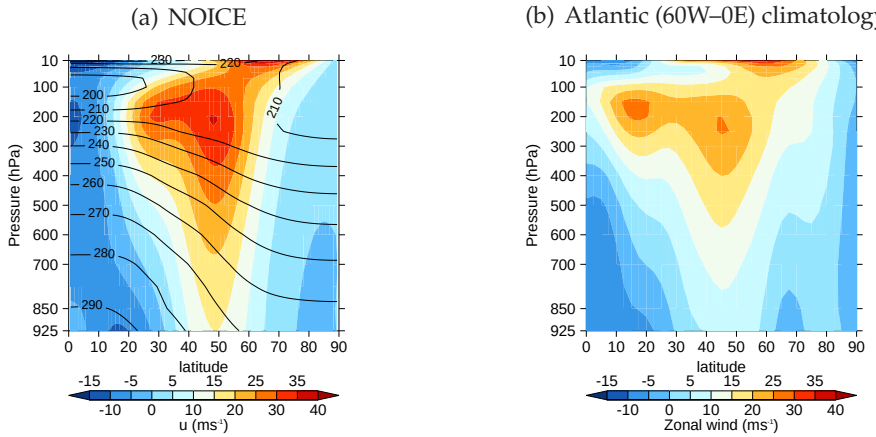

Figure 5.2: a) Zonal-mean zonal wind (shading) and temperature (contours) in the NOICE experiment. b) December 1981–2010 zonal-mean zonal wind over the Atlantic basin, 60W–0E, in NCEP/NCAR reanalysis (Kalnay *et al.*, 1996).

difference in SST1 relative to QOBSWIDE (Figure 5.1).

Figure 5.3 shows the precipitation P, meridional mass streamfunction ψ, Eady growth rate σ_{BI}, and band-pass filtered covariances $\overline{u'v'}$ and $\overline{v'T'}$. P (Figure 5.3a) has a maximum at 10° and a secondary maximum around 40°. The primary maximum is almost exclusively convective precipitation, and its offset from the equator is suggestive of a double ITCZ, which is also found in other aquaplanet models (Neale and Hoskins, 2000a), including HadAM3. The meridional mass streamfunction (Figure 5.2(b)) indicates a Hadley cell extending to just poleward of 30°, with a maximum strength of 10×10^{10} kg s^{-1}.

The secondary precipitation maximum is dominated by large-scale precipitation (Figure 5.3a) with a secondary contribution from convective precipitation. This secondary precipitation maximum is approximately co-located with the lower-level zonal wind maximum near 50°, consistent with its having a strong contribution from cyclone precipitation in the storm track associated with the EDJ.

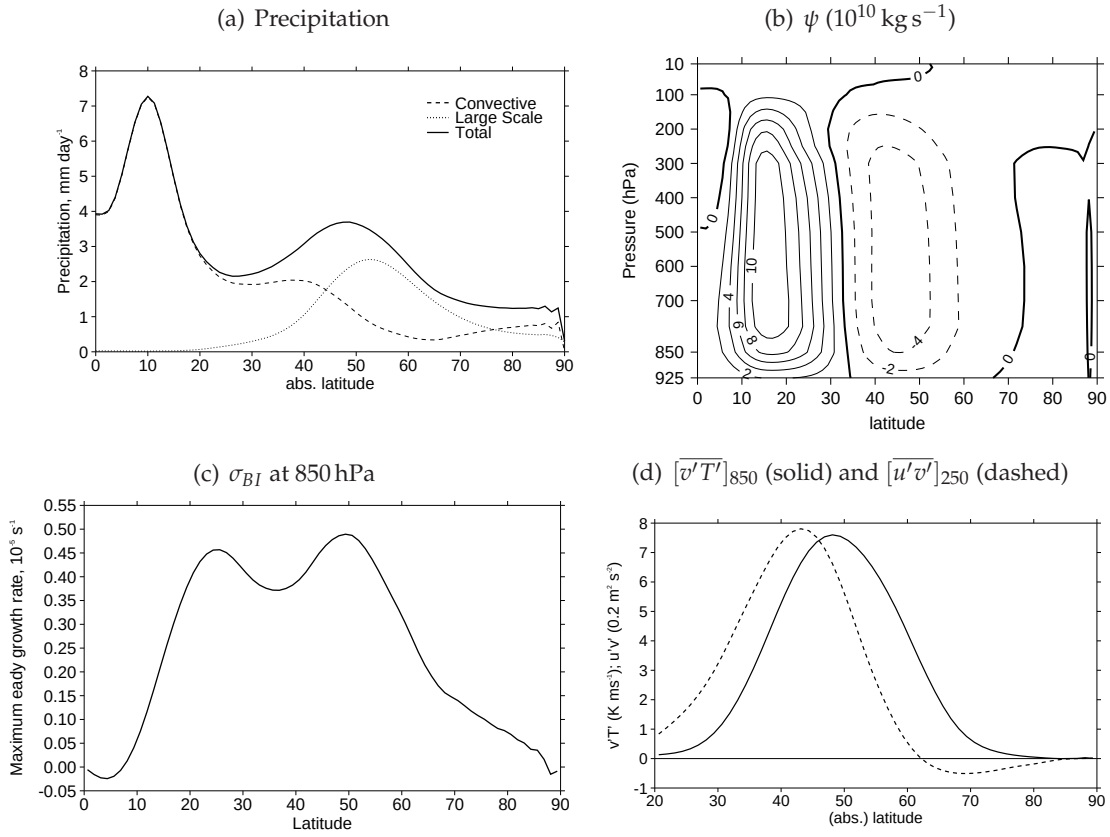

Figure 5.3: Features of the atmospheric circulation in NOICE: (a) Precipitation and the contribution from convective and large scale precipitation. (b) Meridional mass streamfunction. (c) Eady growth rate at 850 hPa. (d) Covariance measures of the storm track.

The low-level baroclinicity (Figure 5.3c) has two maxima, at 26° and 49°. Both these maxima are co-located with local maxima in the temperature gradient at 850 hPa (see later, Figure 5.5d), suggesting that this component largely determines the structure with static stability playing a weaker role. The peak in temperature gradient (and baroclinicity) at 49° can be linked to the maximum in the surface temperature gradient, and the peak at 26° to the edge of the tropics. The low level poleward heat flux by transient eddies, $\overline{v'T'}$ (Figure 5.3d, solid line) has a single maximum at 48°. This is co-located with the poleward of the two peaks in the baroclinicity, and with the low level zonal wind maximum. Finally, $\overline{u'v'}$ at 250 hPa has a maximum at 42° (Figure 5.3d, dashed line). This is consistent with convergence of westerly momentum into the core upper-level jet region at 48° by transient eddies (2–6 days, capturing the role of synoptic storms which grow as a result of the baroclinicity) providing the driving mechanism for the eddy driven jet.

5.3 The Response to Ice Addition (SST1)

5.3.1 The time-mean response

5.3.1.1 Temperature

The zonal mean temperature response to ice addition is shown in Figure 5.4. The dominant signal in all cases is of statistically significant low-level cooling above the added ice. This cooling further extends at least 10° equatorward of the imposed ice edge. The surface temperature response is shown in Figure 5.5a. In I70, a 'real-world-like' extent, the surface temperature drops to 250 K at the pole (-23°C, anomaly -25°C) and in the most extreme case considered I45 it reaches 233 K (-40°C, anomaly -42°C).

The realism of such temperatures can be evaluated by comparison with March surface air temperature in reanalysis, since March is the month of maximum extent and therefore most comparable. Over the period 1981–2010 average March temperatures reach approximately -30°C north over the thick ice north of Greenland and are below -25°C across the central Arctic ocean (NCEP/NCAR reanalysis, not shown). Therefore, despite the simple aquaplanet configuration in these experiments, the temperatures being simulated over sea ice in these experiments appear broadly consistent with what would be expected in more realistic settings.

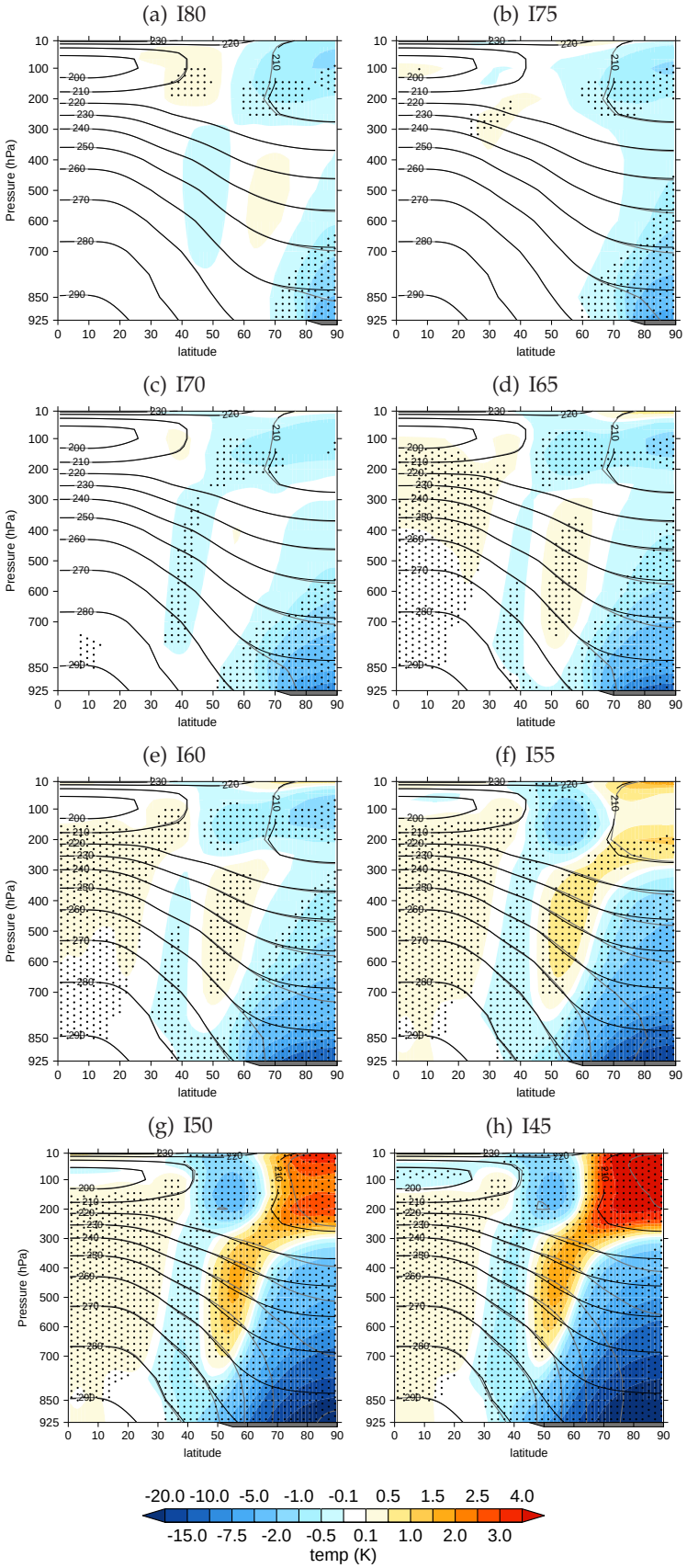

Figure 5.4: The zonal mean temperature response to ice addition. The shading depicts the anomaly from NOICE, the black contours the NOICE simulation and the grey contours the perturbed simulation (both black and grey contour interval 10 K). Stippling indicates significance at the 95% level in a two tailed student's t-test. The wedge on the x-axis indicates the latitudinal extent of sea ice.

That ice addition induces a surface cooling can be understood from the surface energy budget. Sea ice acts to insulate the warm ocean surface and the associated moisture source from the atmosphere, and so decreases the sensible and latent heat fluxes from the ocean to the atmosphere. At high latitudes, in this model, the direction of the surfaceheat flux reverses when ice is added (not shown). In addition, sea ice has a high albedo α (in the range $0.5 < \alpha < 0.8$, dependent on surface temperature; Section 3.3.4) and so the net down shortwave flux at the surface is significantly decreased when ice cover is increased. It is noted that, due to the fixed SSTs in the NOICE simulation and at low latitudes in all simulations, the lower boundary in the model is not able to equilibrate to the radiative conditions, so the model is not in radiative balance.

The cooling weakens strongly with height (Figure 5.4). From I65 onwards there is a secondary feature of mid-tropospheric warming centred on 50° and cooling centred on 40°. There is also a polar stratospheric response, of cooling in cases I80–I60 and warming for I55, I50 and I45.

5.3.1.2 Temperature gradient

Figure 5.5b, d and f show $\left|\frac{d[T]}{dy}\right|$, the absolute value of the meridional temperature gradient, at the surface, 850 hPa and 500 hPa for each experiment. The absolute value is plotted so that a positive anomaly implies a strengthening of the gradient.

The surface temperature response is very tightly tied to the ice forcing, as discussed in the previous section. In the perturbation experiments, there is a very sharp spike in the surface gradient over the five degree zone where SIC is increasing from 0 to 100%. Further poleward, where SIC=100%, the temperature gradient has a smooth profile (Figure 5.5b).

On the other hand the temperature response in the free troposphere, shown at 850 hPa and 500 hPa (Figure 5.5d and f) is mediated to a greater extent by the response of the atmospheric circulation, for example through heat transports and latent heating (discussed later). At these levels, the response differs between the strongest forcing cases (I45, I50 and to some extent I55; purple/grey lines) and the rest.

In the case of weaker forcing (I60–I80) there is a local maximum in the absolute gradient at 850 hPa directly over the transition from open water to sea ice (Figure 5.5d). For I65 and I60, the gradient at 500 hPa (Figure 5.5f) is perturbed everywhere poleward of 25°

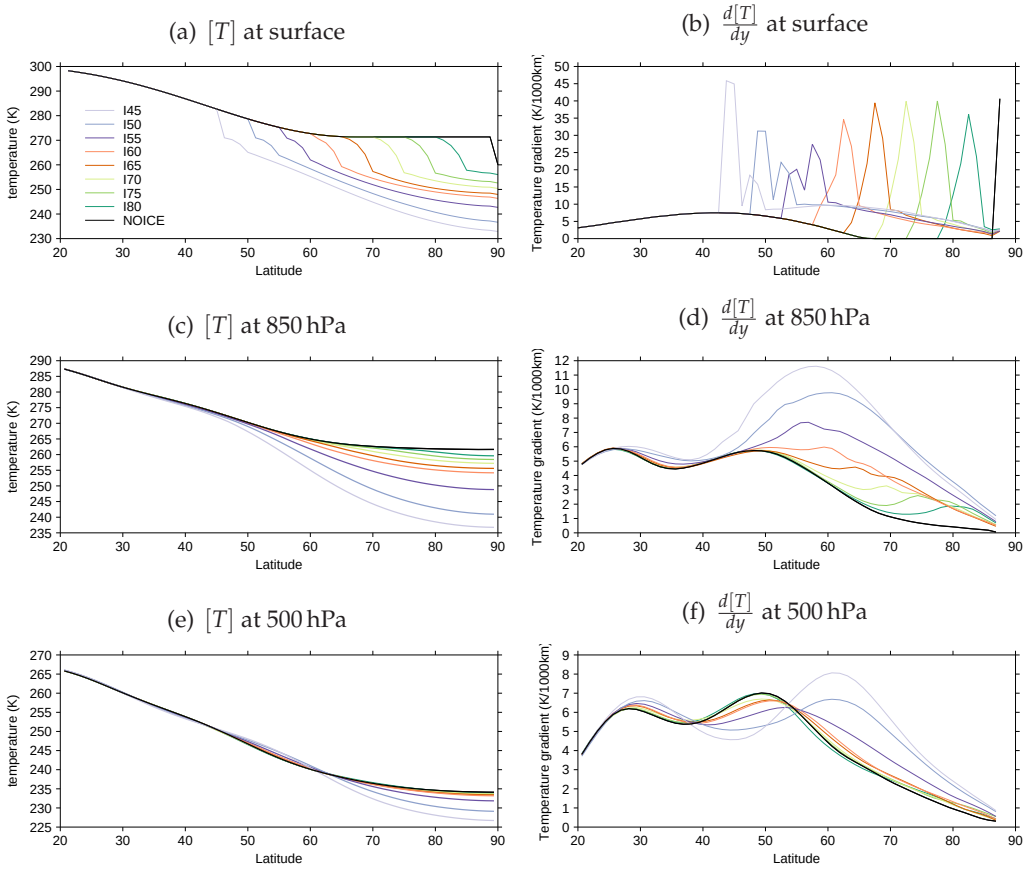

Figure 5.5: The temperature response to ice addition: temperature and the equator-to-pole temperature gradient at the surface, 850 hPa and 500 hPa.

although Figure 5.4 suggests that this may not be significant everywhere. There is a small poleward shift of the two maxima, with the maximum near 50° reducing in importance relative to that at 30°.

In the strongly perturbed experiments I50 and I45, the gradient at 850 hPa is strengthened everywhere poleward of 25° (Figure 5.5d), particularly poleward of 50°. The local extrema shift poleward and the maximum, now between 55 and 60°, strengthens; in I45 its magnitude doubles. In these two experiments the structure at 500 hPa is also changed by a large amount (Figure 5.5f); the midlatitude maximum, previously at 50°, moves over 10° poleward. I55 is a transition case, with behaviour at 500 hPa that is in between that of I60 and that of I45 or I50. These two types of behaviour (or three, if I60/I65 are also viewed as different from I70/I75/I80) are discussed further in Section 5.3.1.4.

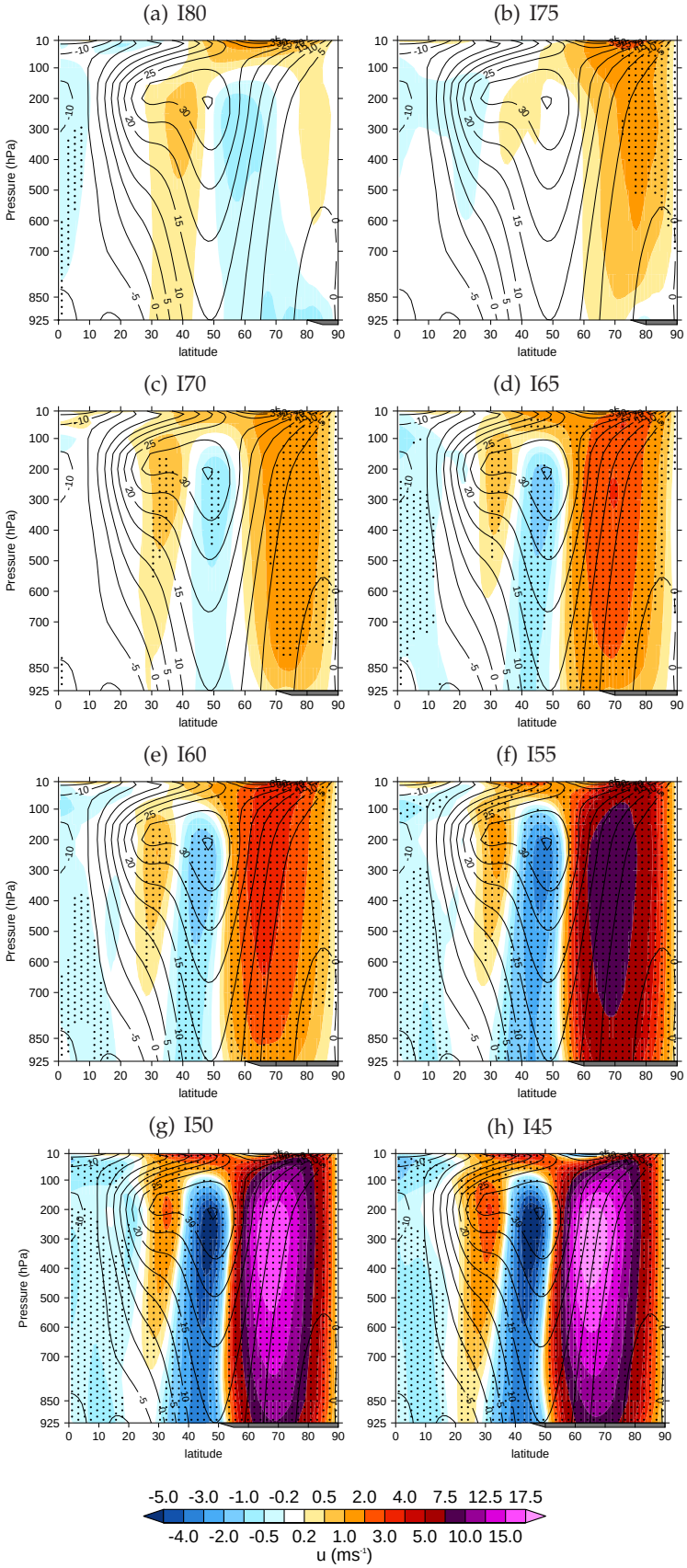

Figure 5.6: The zonal mean zonal wind response to ice addition. The shading depicts the anomaly from NOICE, and the black contours the NOICE simulation (contour interval 5 ms^{-1}). Other details as Figure 5.4.

5.3.1.3 Zonal wind

The zonal-mean zonal wind response is shown in Figure 5.6, overlaid with the NOICE wind contours. Ice addition forces an intensification on the poleward flank of the jet, a reduction in or near the jet core, and an intensification of the subtropical flank of the jet. This structure is robust in all experiments except the weakest forcing cases I80 (where the response is non-significant) and to a lesser extent I75. The anomalies increase nonlinearly with the ice edge latitude (note nonlinear colour bar in Figure 5.6).

Figure 5.7 shows zonal wind integrated over 850–500 hPa, a measure of the eddy-driven jet, and at 250 hPa which captures both the subtropical and eddy driven components of the jet. For the weaker forcings (I60–I80, oranges and greens), the anomalies (discussed above) do not change the latitude of the jet maximum, only affecting the poleward flank. In contrast, the strongest forcings (I55, I50 and I45, purples/greys) force a more sizable change in the jet structure. In I55 the EDJ at low levels is shifted poleward and broadened, but its maximum is reduced (Figure 5.7a). In I50 and I45 the EDJ is again shifted poleward and broadened, but its maximum is also increased (Figure 5.7a). The upper level jet anomalies actually constitute a weakening of the EDJ maximum in all cases except I45 (Figure 5.7b), although the zonal wind increases locally on the poleward flank.

The zonal wind adjustments must be locally consistent with the temperature anomalies via thermal wind balance. Therefore, the strengthening of low level temperature gradient (Figure 5.5d) is linked to the increase in vertical wind shear in the lower troposphere (Figure 5.6). The temperature gradient weakens at middle latitudes (40–55°) and pressures (700 – 300 hPa; Figure 5.4), consistent with the reductions in vertical wind shear here.

5.3.1.4 Response clustering

In examination of the temperature and zonal wind response, there has been a clear separation between the response of the strongest forcings (I45, I50 and to a lesser extent I55) and the rest. Furthermore, the strength of the zonal wind response (Figure 5.7) suggests a possible further separation between the weakest cases (I80, I75 and I70) and the moderate cases (I65 and I60), although this is a somewhat more subjective distinction; I70 could be

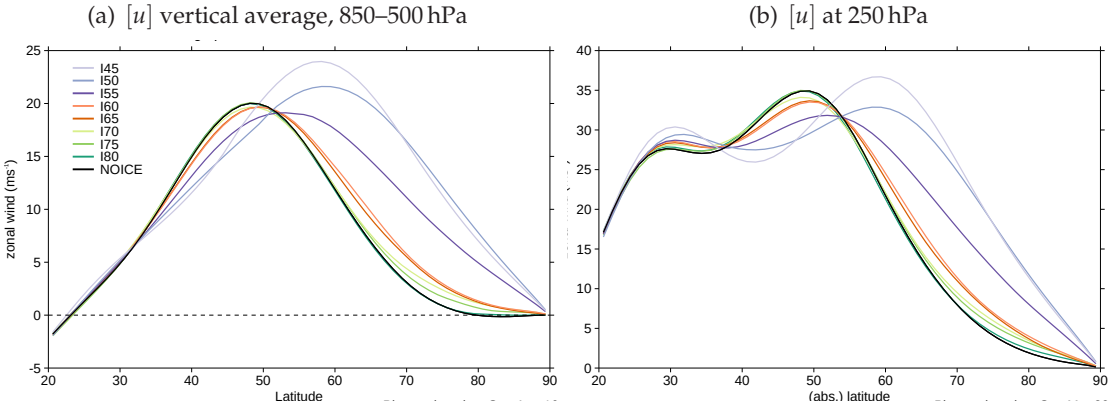

Figure 5.7: The time-mean, zonal-mean zonal wind response to ice addition. (a) Vertical average over 850–500 hPa. (b) At 250 hPa.

grouped rather with I65 and I60. The discussion hereafter will be simplified by grouping the forcings into clusters: 'WEAK' (I80, I75 and I70), 'MODERATE' (I65 and I60), and 'STRONG' (I55, I50 and I45), and only a subset of the experiments will be presented. The responses in the 'WEAK' forcing cases are small, but of interest because these ice extents are closest to those observed in the real world (Table 5.1).

Figure 5.8 shows the potential temperature response (c.f. the temperature response in Figure 5.4) for cases representing each cluster. This will be helpful in the following discussion, but also helpfully summarises the temperature responses; all cases have a dome of cooling over the pole, and MODERATE and STRONG additionally have a mid tropospheric midlatitude warming. WEAK and MODERATE cases have polar stratospheric cooling while STRONG cases have polar stratospheric warming.

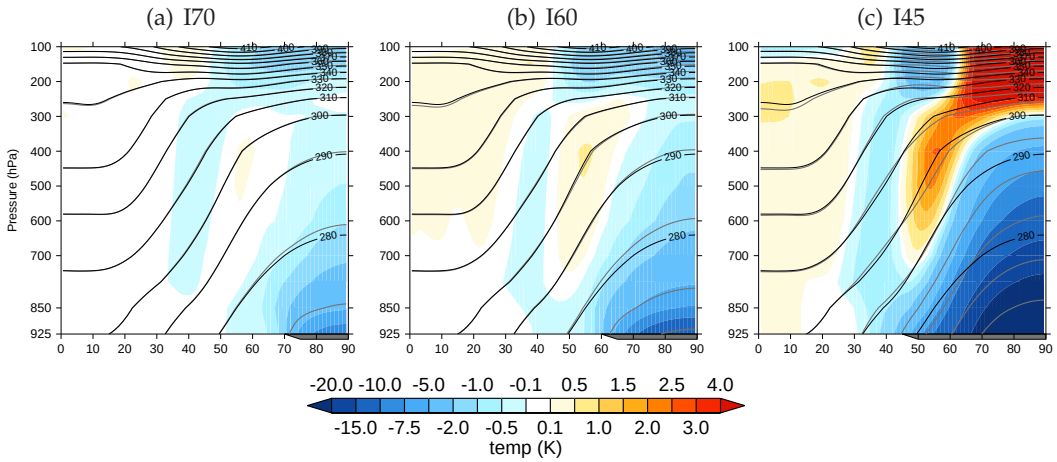

Figure 5.8: The zonal mean potential temperature response to ice addition. The shading depicts the anomaly from NOICE, the black contours the NOICE simulation and the grey contours the perturbed simulation (both black and grey contour interval 10 K). The wedge on the x-axis indicates the latitudinal extent of sea ice.

5.3.1.5 Dynamics of the response

WEAK and MODERATE cases

This section considers the WEAK and MODERATE cases only, depicted by green and orange lines in Figure 5.9.

Figures 5.9a and b show the Eady growth rate σ_{BI} at in the lower troposphere (850 hPa) and mid troposphere (500 hPa). The low level Eady growth rate change for these cases is dominated by an increase at high latitudes and a peak over the ice edge. This is similar to the changes in meridional temperature gradient (Figure 5.5d), suggesting that the changing temperature gradient plays a dominant role. However, the growth rate is also a function of static stability N^2. The contributions of the two components are quantified in Figure 5.9c for the I60 case; the NOICE eady growth rate at each latitude is multipled separately by the proportional change in $\frac{du}{dz}$ and in $\frac{1}{\sqrt{N^2}}$. This shows that the change in meridional gradient does indeed dominate the change in growth rate, but that its effect is partially offset at high latitudes by the increasing static stability. This increasing static stability is a result of a stronger increase of potential temperature with height over ice (Figure 5.8). In the mid-troposphere (500 hPa), the much smaller change is almost entirely determined by the meridional gradient change (not shown).

The combination of the two effects, at 850 hPa, is that in the WEAK forcing cases there is little change to the main baroclinic zone at 49°, while in the MODERATE case this zone extends poleward (Figure 5.9a). The response of the stormtracks can be seen in the transient fluxes of heat and momentum, $\overline{v'T'}$ and $\overline{u'v'}$. Figure 5.9c shows $\overline{v'T'}$ at 850 hPa; this is sufficiently close to the surface that large shallow positive anomalies can be seen, which are associated with the strong temperature gradient across the ice edge and with the peak in baroclinicity. The response of $\overline{u'v'}$ at 250 hPa (Figure 5.9d) is confined to the poleward flank and is small.

Anomalies in the EP flux and its divergence for transient eddies (2–6 days) are shown in Figure 5.10b for representative case I60 (MODERATE). Anomalous divergence (red shading) of the EP flux signifies that anomalous transient eddy fluxes are acting to accelerate the jet. In the WEAK (not shown) and MODERATE forcing cases, the EP flux anomalies are dominated by anomalous vertical convergence of $\overline{v'T'}$ in the lower troposphere (850–600 hPa) over the imposed ice edge. This anomalous convergence is very shallow. The dominant effect then, is of a local and shallow response.

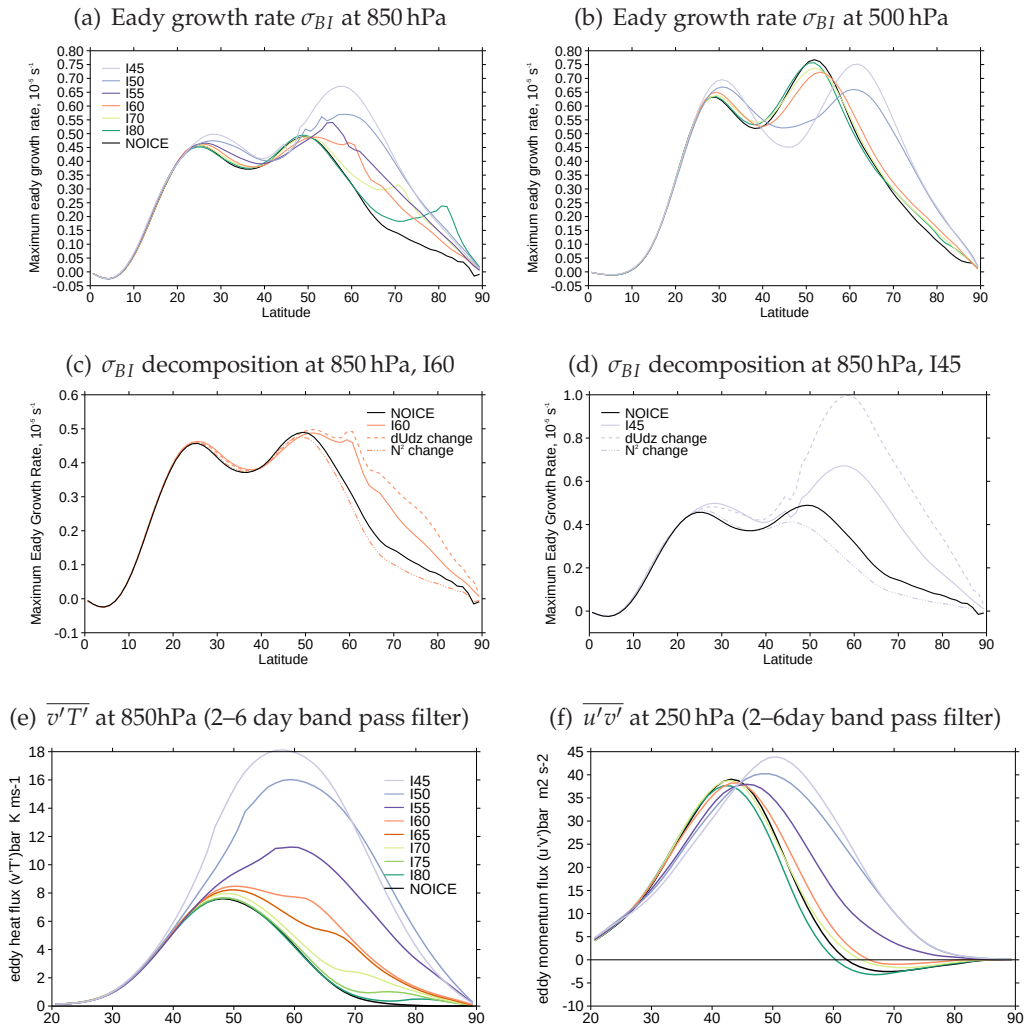

Figure 5.9: Storm track response to ice addition. (a) Eady growth rate at 850 hPa; (b) As a) but at 500 hPa. (c) Eady growth rate at 850 hPa, decomposition into contributions from vertical wind shear and static stability, I60. (d) as c) but for I60. (e) Transient heat flux $\overline{v'T'}$ at 850 hPa. (f) Transient momentum flux $\overline{u'v'}$ at 250 hPa. Both $\overline{v'T'}$ and $\overline{u'v'}$ are band pass filtered here and in subsequent plots, as described in Section 3.4.3.

The precipitation (Figure 5.11) reinforces this view. When ice is added, precipitation increases between its NOICE maximum at 50° and the ice edge and decreases polewards of the ice edge. Partitioning this response (Figure 5.11b, for I60 as a representative case), large scale precipitation increases at all latitudes poleward of 50°, consistent with the storm track response. However, over the ice, a decrease in convective precipitation (consistent with a reduced moisture source and increased static stability) dominates, leading to a decrease in total precipitation.

STRONG cases

Under STRONG forcing there is a poleward shift and strengthening of the baroclinic

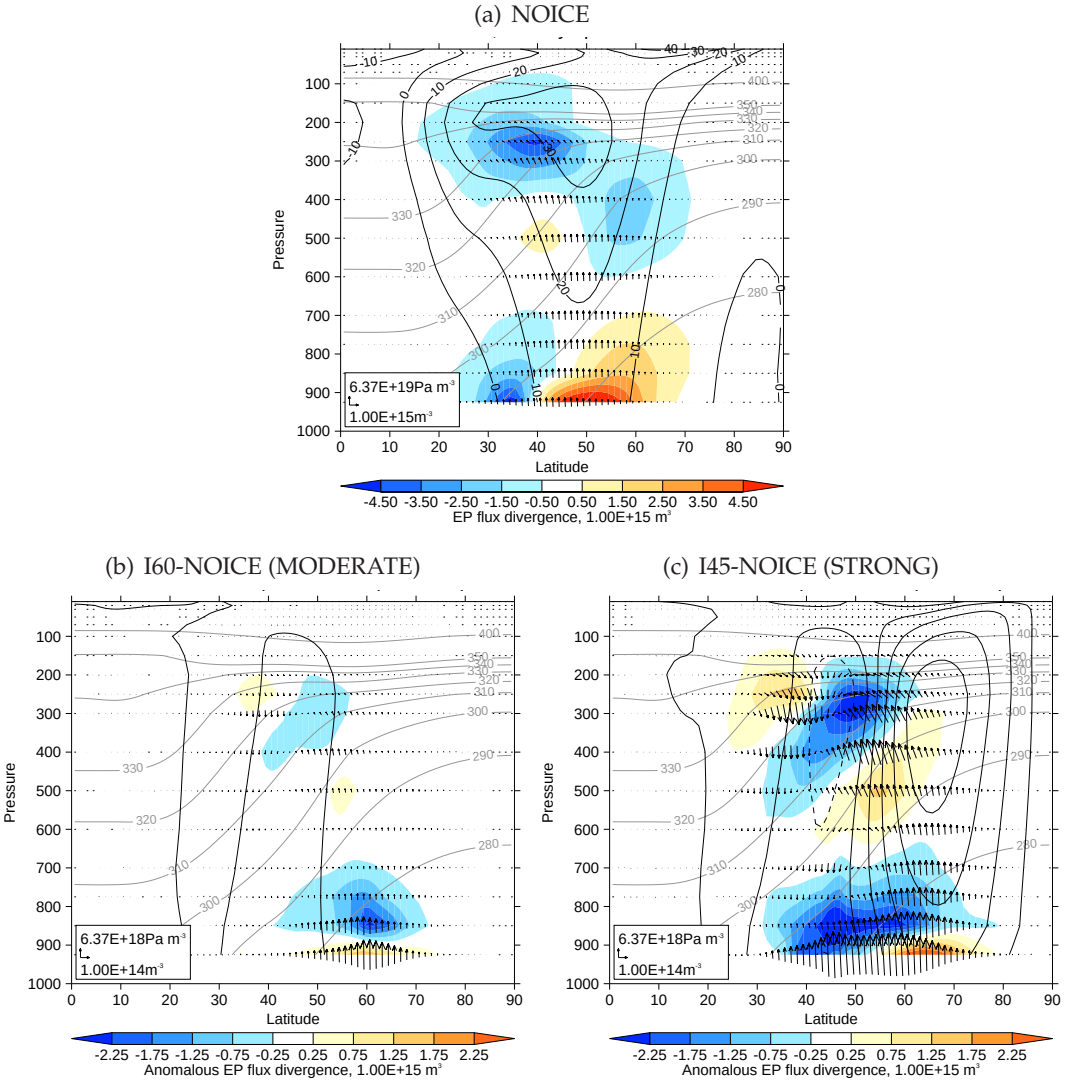

Figure 5.10: EP flux for transient eddies (2–6 days), and its divergence, in selected experiments. a) EP flux (arrows) and its divergence (shading), zonal mean zonal wind (black contours) and potential temperature (grey contours, to 350 K only). b) The anomalous EP flux (arrows), EP flux divergence (shading), and zonal mean zonal wind (black contours, interval 4 ms^{-1}) in I60 relative to NOICE, and the potential temperature in NOICE (grey contours, to 350 K only). Scalings follow Edmon *et al.* (1980).

zone at 850 hPa, and a poleward shift of the baroclinic zone at 500 hPa (Figure 5.9a and b, purple/grey lines). Again, the change at 850 hPa is dominated by an increase in the temperature gradient or equivalently vertical wind shear, with static stability moderating the increase (Figure 5.9d). There is a poleward shift and an increase in the low-level heat flux $\overline{v'T'}$ (Figure 5.9c). This is qualitatively similar to the response in the baroclinicity, which is physically consistent as it is the baroclinicity which leads to the disturbances in which the heat flux occurs. However, the heat flux increase is larger; in I45 its maximum increases by more than a factor of two relative to NOICE. $\overline{u'v'}$ at 250 hPa also responds

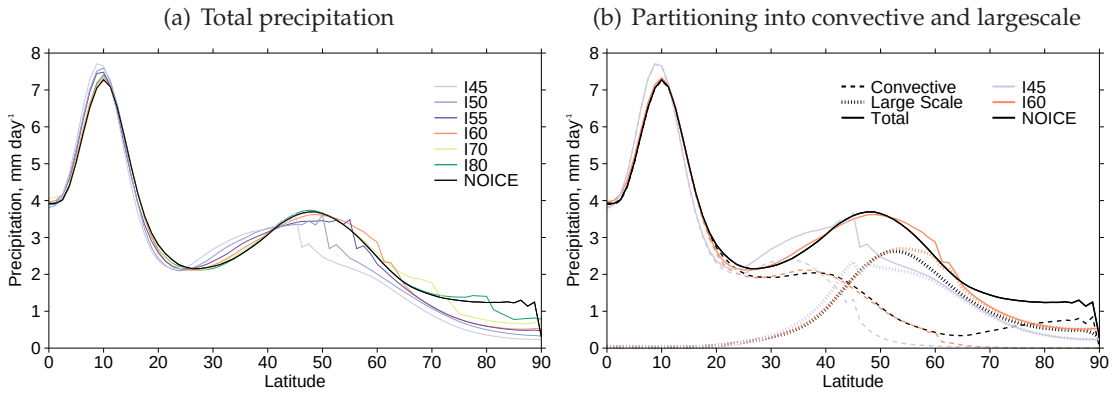

Figure 5.11: Precipitation response to ice addition a) the total precipitation for a wide range of ice extents and b) convective and large-scale contributions to precipitation, I45, I60 and NOICE.

strongly to STRONG forcing (Figure 5.9d). There is a poleward shift of the maximum (from 43° to 51°), and additionally in I50 and I45 a slight increase of the maximum. Positive anomalies extend to the pole such that $\overline{u'v'}$ is now positive everywhere poleward of the maximum. The decrease in momentum flux out of the subtropics is consistent with the increase in the subtropical jet maximum (Figure 5.7b), while the shift in the momentum flux convergence region ($\frac{d\overline{u'v'}}{dy} < 0$) is consistent with the poleward shift of the eddy driven jet maximum. Again, the EP fluxes, shown for I45 (Figure 5.10d), reinforce this view. The anomalies in the divergence now extend to the upper troposphere, and have a stronger contribution from $\overline{u'v'}$ than in the WEAK and MODERATE forcings. When only the horizontal component ($\overline{u'v'}$) is plotted, the anomalies are very closely associated with the zonal wind anomalies (not shown).

The STRONG forcings therefore result in a much larger response, and, while the anomalies are in a similar location to those in the WEAK and MODERATE cases, they cause a fundamental shift in the atmospheric state. Moreover the response is no longer locally confined. This can also be seen from the precipitation (Figure 5.11a and b). As in the weaker cases, large scale precipitation in the STRONG case (I45 is shown in Figure 5.11b) increases over open ocean poleward of 30°. Over the ice the large scale precipitation response varies; it is a decrease in I45 (Figure 5.11b, dotted lines) and an increase in I50 and I55 (not shown). Convective precipitation (CV; dashed lines in Figure 5.11b) decreases over the ice and as far equatorward as 40° (again this is the same as in the weaker case). However, there is now also a response in CV in low latitudes; equatorward of 40°, the CV structure shifts equatorward and its maxima increase. This convective precipitation response is the leading contributor to the changes in total precipitation at these

latitudes (Figure 5.11b).

Temperature response

Having examined the dynamics of the response, the tropospheric temperature response structure which was shown in Figure 5.4 can be better understood. The features of interest are

- The deep cooling over the ice and in particular its vertical structure, which is relevant to the debate over the causes of Arctic amplification in the real atmosphere;
- The mid-tropospheric mid-latitude warming in the MODERATE and STRONG cases (at 50°) and the cooling equatorward of here;
- The different response in the polar stratosphere in the STRONG case from that in the WEAK and MODERATE cases.

These features are now discussed in turn.

As discussed in section 5.3.1.1, the polar surface cooling is an expected consequence of the addition of sea ice. The deep and dome-like structure of the polar tropospheric warming however is of interest. As seen from the potential temperature response (Figure 5.8), the structure of the response over the pole is very similar to the structure of the full field in the ice addition experiment- the anomaly contours roughly follow the isentropes. This suggests that the minimum latitude of the surface temperature anomaly sets, to first order, the vertical structure of cooling, consistent with strong mixing along isentropic layers. However, the change in gradient of the isentropic slopes (comparing grey and black contours, Figure 5.8) suggests that this is not the full story and that other diabatic processes are also acting to modify the structure, as discussed in the following paragraph.

Firstly, at high latitudes, there is a large decrease in specific humidity (Figure 5.12). The percentage change is approximately constant in isentropic layers. Therefore, there is less LW radiation absorption by the atmosphere, contributing to cooling, lifting the isentropes. Secondly, the combined effect of the decrease in specific humidity and decrease in temperature is to increase relative humidity, so cloud increases (not shown). This further increases planetary albedo and further cools the surface. Finally, the decrease in precipitation over the poles (Figure 5.11) also contributes to a decrease in latent heating.

The midlatitude (45°–60°) mid-tropospheric warming, of up to 2 K, is inconsistent with the local effect of the precipitation decrease (Figure 5.11) which would cause latent

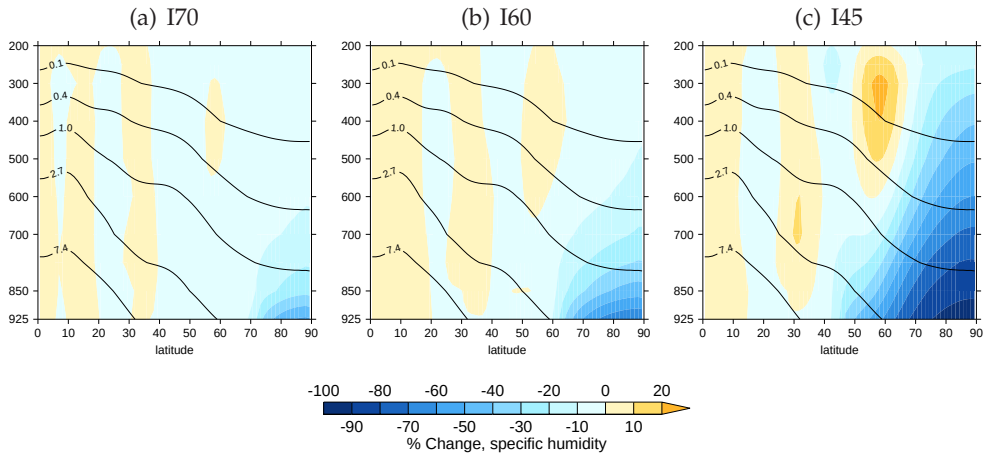

Figure 5.12: The zonal mean specific humidity response to ice addition. The shading depicts the percentage anomaly from NOICE, and the black contours the NOICE simulation. This figure uses a logarithmic scale for the specific humidity so that high latitude features can be seen. It is only plotted as far as 200 hPa, since only the troposphere is of interest (because the stratosphere is very dry).

cooling. An alternative explanation is found in the meridional overturning streamfunction. The change in the streamfunction (Figure 5.13a, comparing grey I45 contours with black NOICE contours) is consistent with strengthening of the Hadley cell, local ascent over the ice edge (a feature previously reported over surface SST fronts, e.g. Minobe *et al.* (2008)), and expansion of the Ferrel cell. This expansion is a manifestation of the poleward extension of the baroclinic zone and extratropical jet discussed earlier. In particular, I45 has descent as far poleward as 55°, where NOICE had ascent. Such descent would cause anomalous adiabatic warming.

As a step towards quantifying this effect, Figure 5.13b shows the expected anomalous heating/cooling rate in I45 relative to NOICE as a result of changed vertical motion across isentropes. This is calculated as $-\omega' \frac{\partial \bar{\theta}}{\partial p}$, where ω' is the I45-NOICE difference in time-mean vertical pressure velocity, and the potential temperature gradient is calculated in the NOICE experiment. The meridional extent of the midlatitude warming region (approximately 45 to 60°) is consistent with the meridional extent of the temperature anomaly, although the vertical structure is different. At the point of maximum tropospheric potential temperature anomaly (2.5 K at 400 hPa and 55°; Figure 5.8c), the magnitude of this anomaly reaches around 0.6 K/day, which given typical damping timescales in the troposphere of over 10 days would result in a larger anomaly than the 2.5 K. However, as discussed above this process is competing with others, such as latent cooling. Therefore this seems like a suitable candidate for explaining the anomalous warming

exists here.[5]

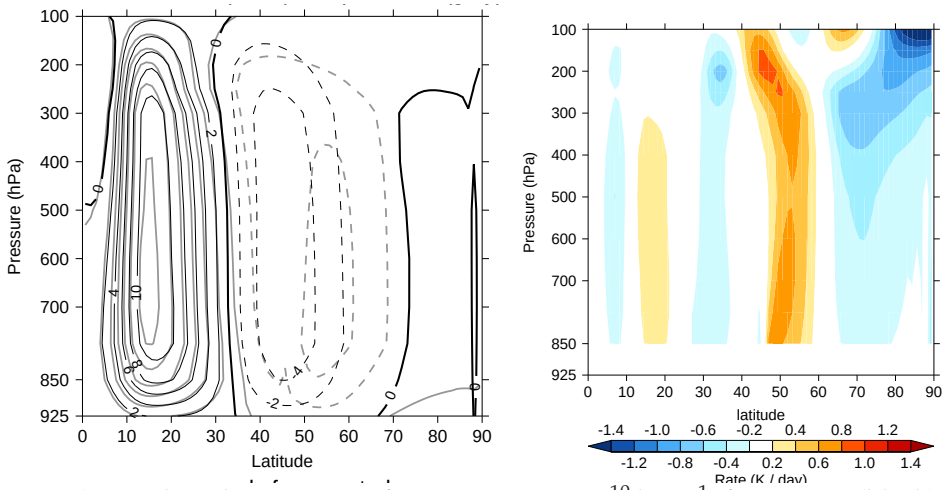

Figure 5.13: a) Meridional mass streamfunction ψ, units 10^{10} kg s^{-1}, for NOICE (black) and I45 (grey). Negative contours dashed. b) Anomalous heating rate in I45 relative to NOICE, units K/day, due to anomalous vertical motion across NOICE isentropes; see text.

The final element of interest is the change in the character of the polar stratospheric response (above 300 hPa) between the WEAK/MODERATE cases, where the stratosphere cools relative to NOICE, and the STRONG cases, where it warms. These are consistent with changes in $\overline{v'T'}$ (all timescales); in the lower stratosphere (250–150 hPa) there is an increase in the magnitude of these fluxes in mid-to-high latitudes (not shown, but see increase of the vertical component of EP flux in Figure 5.10). For I45, these changes cause the upper level heat flux maximum to move poleward, to between 60° and 70° depending on the pressure level considered, which could alter the stratospheric temperature. The effect of anomalous time-mean vertical motion in the polar stratosphere in I45 would appear to be a cooling one (Figure 5.13), so changes in the time-mean vertical circulation in the stratosphere do not explain the warming.

Summary

Following the above discussion, the response can be summarised as follows:-

- In the WEAK and MODERATE cases, there is cooling over the ice, largely confined to the lower troposphere. The tropospheric structure of this polar cooling is largely set by the isentropic surfaces intersected by the surface anomaly, reinforced by radiative and diabatic feedbacks. The increase in local surface and near-surface baroclinicity caused by the ice edge and ice induces a pertubation in the storm track,

[5]Tendencies due to different processes, including advection, were not returned as diagnostics from the simulations and so the roles of these processes can not be directly assessed.

but the perturbation is separated from the main baroclinic zone and storm track and the response remains shallow

- In the STRONG cases, the cooling over the ice extends to the mid troposphere. The ice edge perturbs the maximum surface baroclinic region, and there is also a perturbation to baroclinicity in the mid troposphere due to the deep cooling set by isentropic surface. Eddy activity persists into the upper troposphere, and there is a large scale change in the circulation, with a poleward expansion of the Ferrel cell and poleward shift of the eddy driven jet.

5.3.1.6 Projection onto control state EOF

As discussed in Section 2.4.2, responses to forcings and in particular sea ice removal are often described in terms of their projection onto atmospheric modes of variability. Such a framework can be a useful way of describing the general characteristics of a response. However, it may also mask information found by examining the full fields. In what follows, the response is split into that which projects onto the NOICE modes of variability and the residual which does not. The annular mode represents a self-consistent set of eddy-mean flow feedbacks acting to vary the jet, so such a separation aids understanding of the importance of the different mechanisms.

Here, the modes of variability are quantified as the first two EOFs (Empirical Orthogonal Function; Section 3.4.1) of daily-mean zonal-mean zonal wind, vertically averaged over 925–700 hPa. These pressure levels capture variability associated with the low-level eddy driven jet. Taking EOFs of the two dimensional (latitude-height) field did not add information relative to the one dimensional analysis. Vertically averaging over a different choice of pressure levels, or using the full 2D fields, produced PC timeseries that are correlated at $r>0.94$ with the PC timeseries obtained with the original choice.

EOF1 of the NOICE state is a dipole around 50°, which is close to the maximum of the time mean field (Figure 5.14). EOF2 has a primarily tripolar structure. Physical processes (shifts, pulses and broadenings) cannot necessarily be linked to EOF structures (monopoles, dipoles, or tripoles) (Monahan *et al.*, 2006). However, a dipole around the mean maximum position is a somewhat special case (Monahan *et al.*, 2006) and is primarily the result of a shift, i.e. change in position, of the jet. The latitude-height anomaly associated with EOF1 (Figure 5.14b) is also a dipole. This is immediately comparable in

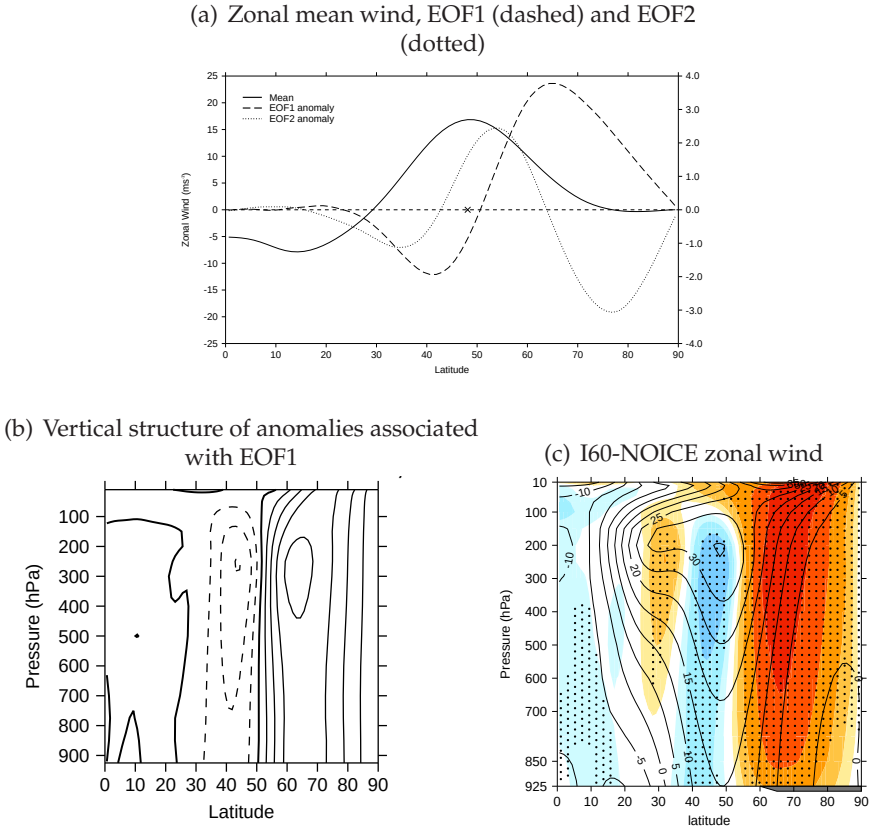

Figure 5.14: EOFs of vertically-integrated daily zonal wind in the NOICE experiment. a) The zonal wind anomalies associated with EOF1 (dashed) and EOF2 (dotted) (see text for details), and the mean zonal wind field (solid line). The cross denotes the latitude of maximum time-mean zonal wind. b) The zonal mean zonal wind anomalies associated with EOF1. c) The anomaly in response to ice addition, I60-NOICE (see Figure 5.6e)

structure to the wind anomalies observed in response to ice addition, in particular with respect to the latitude of the node (50°) shown for example for I60-NOICE (Figure 5.14c).

Figure 5.15 shows the projections of the zonal wind response onto NOICE EOF1 and EOF2. For MODERATE and STRONG forcings, the response is well described by a projection onto EOF1 (Figure 5.15). However this is not the case for the WEAK forcing experiments.

The residual response after removing the projection onto EOF1 is of positive anomalies south of the jet maximum and at high latitudes (yellow line), corresponding to a broadening of the jet. The structure of this residual bears some similarity to EOF2 (blue line).

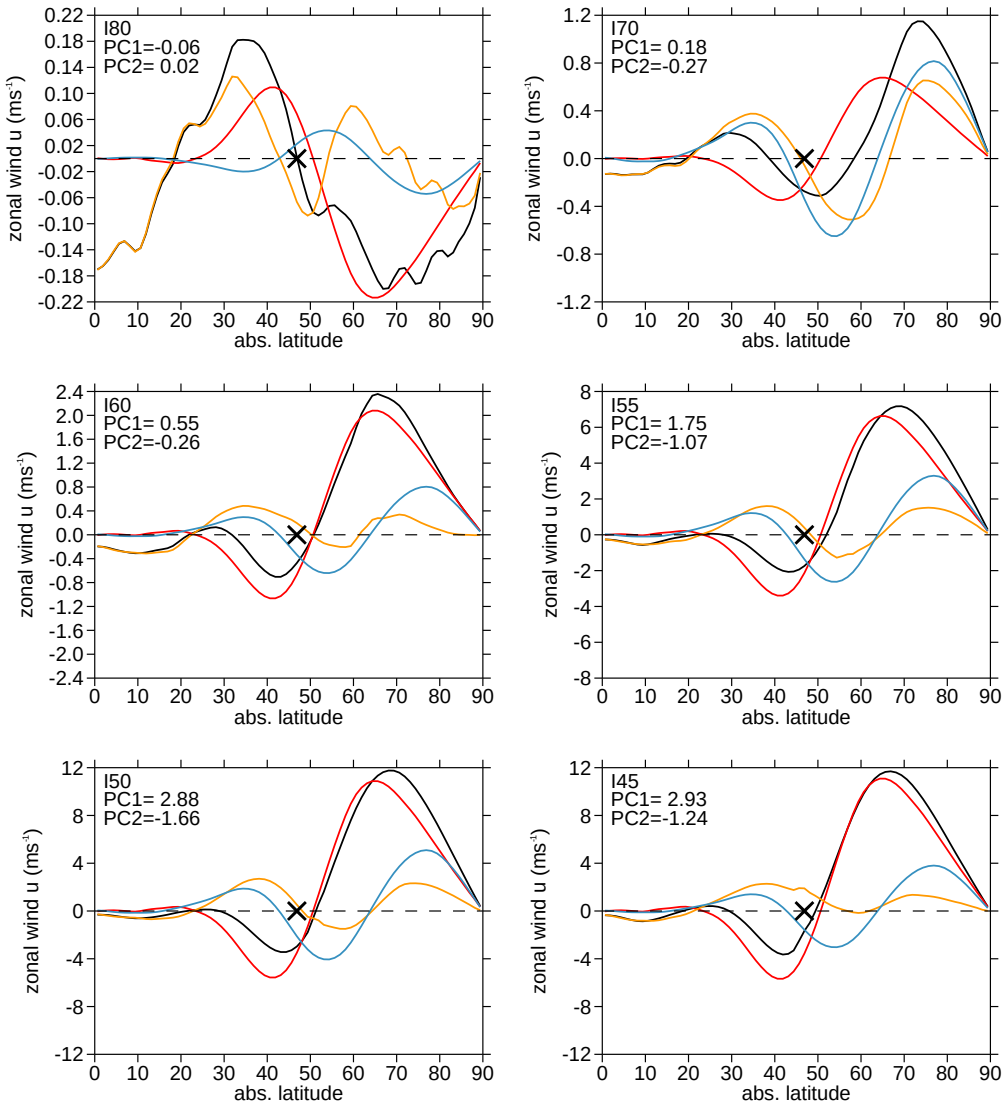

Figure 5.15: The $[\overline{u}]$ response associated with EOF 1 and 2. For each experiment: the anomaly (black), projection onto EOF1 (red), residual (yellow) and projection onto EOF2 (blue). Again $[\overline{u}]$ refers to the vertical integral over 925–700 hPa. The value PC1 and PC2 are the projection strengths onto EOF1 and EOF2 respectively.

5.3.2 Understanding jet variability: EOFs and the jet latitude index

The discussion thus far has focussed on understanding the response of the mean atmospheric circulation to the imposed forcing. However, the variability of features such as the jet has been the subject of many recent theories. Here, two simple metrics are analysed to examine this problem:

- EOF1 of zonal-mean zonal-wind

- The jet latitude index (JLI).

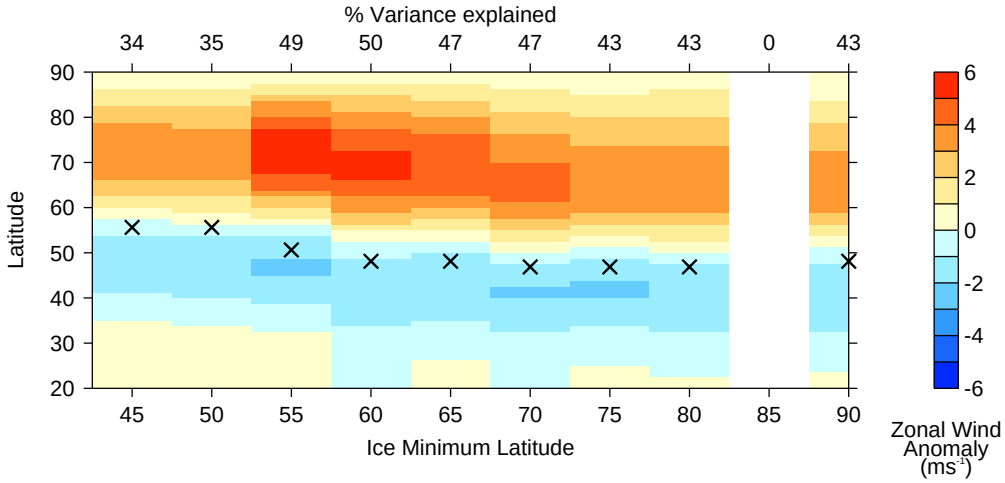

Figure 5.16: EOF1 structures for each experiment. The values on the upper x-axis give the percentage of variance explained by EOF1. The crosses give the latitude of the maximum time-mean, zonal-mean zonal wind.

EOFs are calculated as discussed in Section 5.3.1.6 for each experiment, and shown in Figure 5.16. For each experiment (abscissa), the shading displays the EOF1-associated anomaly at each latitude and the cross denotes the latitude of maximum time-mean zonal wind $[\bar{u}]$. Firstly, the shift of the mean jet can be seen in the movement of this cross to more poleward positions in the strong ice forcing experiments. When viewed across all experiments, the EOF moves with the westerlies.

Barnes and Polvani (2013) found evidence of an effective poleward limit on jet latitude in climate models, imposed by wavebreaking restrictions; in their experiments the EOFs of more poleward jets increasingly resembled a 'pulse' rather than 'shift', demonstrating a limit on the poleward extension of the EOF. There is some limited evidence of this in the present experiments, as between the MODERATE and STRONG experiments, the mean jet shifts poleward (from approximately 50 to 55°) while the poleward centre of action of the EOF does not move. However this only occurs across this subset of experiments. Moreover the EOF in this case is already much further poleward than that in Barnes and Polvani (2013).

The timescale of EOF1 (calculated as the e-folding autocorrelation of the PC time-series) is approximately 2.5 weeks for the NOICE case, increasing to 3.5 weeks for the I55 case. This timescale dramatically reduces to approximately one week for the I50 and I45 cases. For the cases with a favoured position, i.e., all except I55, this is consistent with

equatorward jets being more persistent (e.g. Barnes *et al.*, 2010).

The second measure considered is the jet latitude index (JLI; Section 3.4.2). The JLI calculation is performed on zonal-mean wind averaged between 925 and 700 hPa in order to capture the eddy driven jet variability. The statistical distributions of the jet speed u_{jet} and jet latitude ϕ_{jet} are examined below. This analysis allows the examination of jet variability and in particular the possibility of regime behaviour.

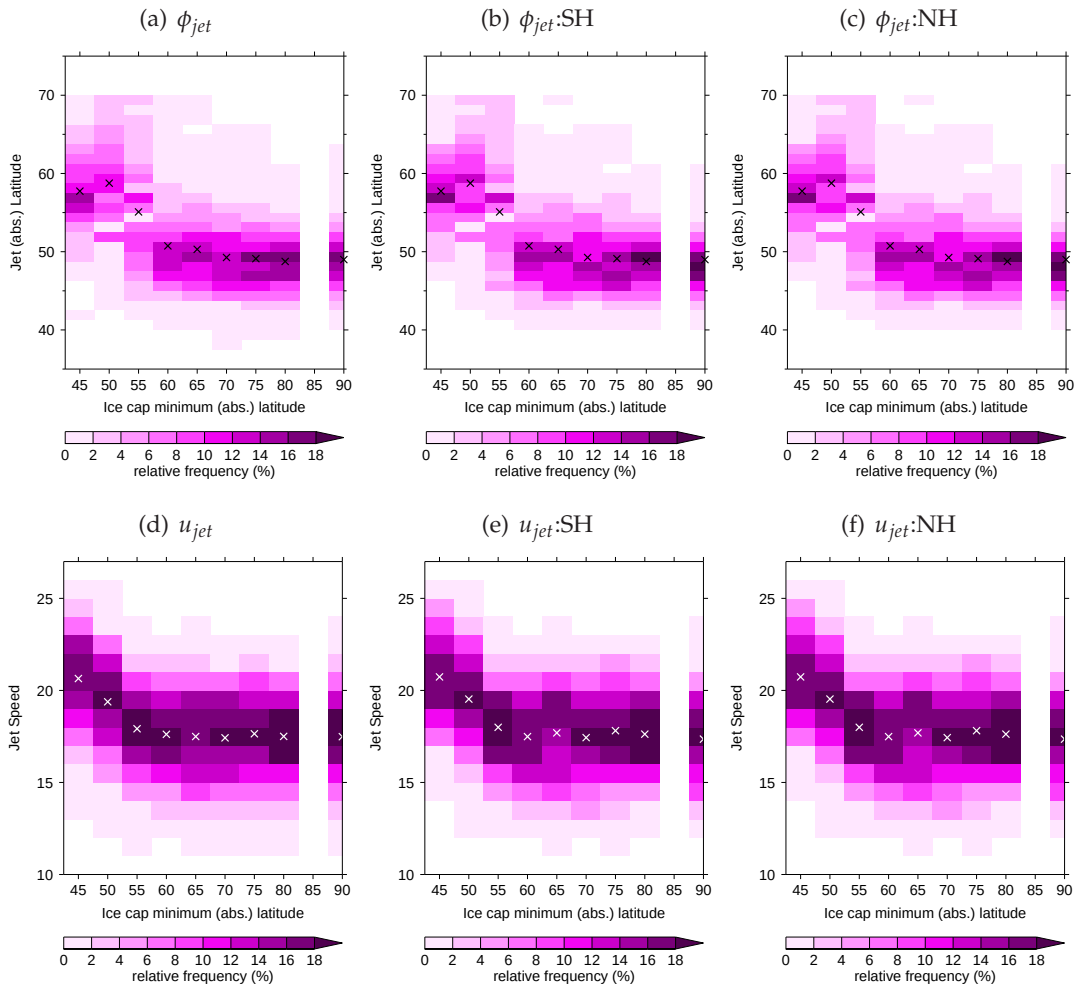

Figure 5.17: The PDF of jet latitude ϕ_{jet} (top) and speed u_{jet} (bottom), as derived from daily-mean $[u]$, vertically averaged over 925–700 hPa. Panels a) and d) show results for the full dataset; b) and e) for the 'Southern Hemisphere' only; and c) and f) for the 'Northern Hemisphere' only. Crosses denote mean ϕ_{jet} (a,b,c) and u_{jet} (d,e,f).

Figure 5.17 shows the PDF of both ϕ_{jet} (top) and u_{jet} (bottom) for all the ice forcing cases. Panels a and d show the results for the full dataset. The modal latitude of the jet (just equatorward of 50° in the NOICE case) is approximately equal to the latitude of the time-mean jet (compare to Figure 5.7a). The favoured position of the jet remains here until the STRONG forcings are applied, when it moves to 57°. In other words, the response remains small until the imposed ice reaches the latitude of the stormtracks. This response is consistent with the findings of Section 5.3.1.3. The other panels (b,c,e,f) show the results subsampled over each 'hemisphere', demonstrating that the behaviour is robust to subsampling.

Figure 5.17a also shows that the variability of the jet latitude changes considerably between the experiments. The distribution broadens, particularly on the poleward side, in the MODERATE and STRONG forcing cases, for ice up to I55. Again, this is consistent with the increased time-mean zonal wind at these latitudes (Figure 5.7). For I45 the variability (standard deviation) of jet latitude is reduced again to a level approximately equal with that in I60A (not shown), consistent with the jet being strictly confined at this new poleward latitude by the forcing in the I45 case.

The large poleward shift in the modal jet position in I50 and I45 relative to the other experiments gives further evidence that I50 and I45 are in a fundamentally different jet regime to the experiments with less ice. However, I55 is a transition case, with evidence of bimodality (two peaks in the distribution at 51° and 55°), or equivalently of regime behaviour. Given the reduced maximum in time-mean zonal wind in I55 compared to all other cases (Figure 5.7), the distribution of u_{jet} is of interest; it is possible that the jet in I55 is as fast as that in I50 and I45, but that the information is masked in the time-mean picture. Figure 5.17d shows the frequency distribution of u_{jet}. It reveals that I55 has similar time-mean u_{jet} to the weaker forcing cases, with the transition to higher speeds occuring only for I50 and I45. However, I55 u_{jet} is not decreased either, in contrast to the time mean zonal wind.

The two-dimensional PDF of jet latitude and speed in I55 (not shown) further confirms that the I55 jet is fluctuating between favoured latitudes, but that there is not a difference in speed between these two positions. Furthermore, while the two experiments with strongest eddy driven jets (I50 and I45) are also furthest poleward, there is no correlation in individual experiments between latitude and speed when all days are

considered. However, there is a positive correlation between latitude and strength when restricting to days when the jet is situated poleward of 50°.

The JLI therefore adds evidence that the system moves into a new regime under I50 and I45, and that I55 is a transition case. In addition, the states with more ice feature more variability in jet position for all but the very strongest case (I45).

5.3.2.1 Scaling of responses with forcing

The results in this chapter so far suggest that the magnitude of the atmospheric response to ice addition increases gradually as the ice edge moves equatorward, until the ice edge reaches around 55°. Beyond this latitude, the response (e.g. zonal wind anomalies) increase more strongly and the atmospheric circulation looks very different. This section seeks to formalise this distinction and in particular to establish whether this change in response is manifest as a change from a linear to nonlinear dependence of the response magnitude on the forcing magnitude. As well as providing a summary of the responses, it will then also be possible to test whether the same relationship holds for example with a different SST profile.

The first interesting relationship is that between the polar temperature response and the ice forcing, quantified by either ice area or the latitude of the ice edge. It will then be possible to ask

- Can the zonal wind response then be understood as a function of the forcing itself (ice) or the temperature response to it?
- Is the projection of the response onto the annular mode a function of the strength of the forcing (e.g. Ring and Plumb, 2008)?

Firstly, the surface temperature at the pole is found to be very highly correlated (r=0.98) with the minimum ice latitude (not shown). Secondly, the low level temperature averaged over the polar cap, denoted $[T_{850,\phi>70^\circ}]$, is correlated with both minimum ice latitude (not shown) and ice area (Figure 5.18a). The linear correlation with $[T_{850,\phi>70^\circ}]$ is higher for ice area than ice latitude, which may be expected because ice area is a nonlinear function of ice latitude. The linear correlation between ice area and $[T_{850,\phi>70^\circ}]$ is high suggesting that a linear relationship is a good approximation ($|r|$ =0.986). However, a linear relationship is a much better fit when restricting attention to the MODERATE cases

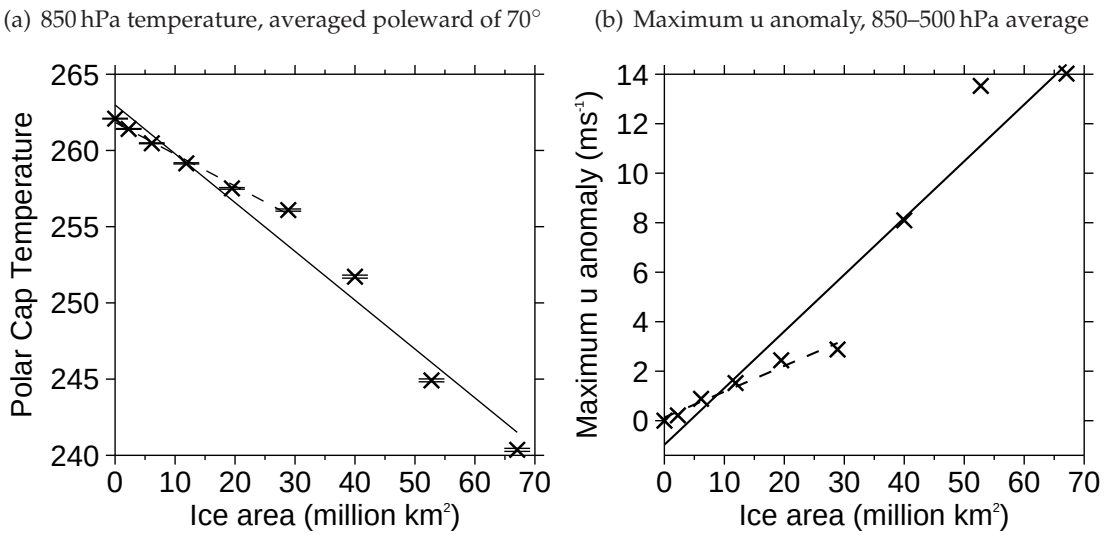

Figure 5.18: Relationship between atmospheric response and ice area. a) Relationship between 850 hPa temperature averaged poleward of 70° and ice area (SST1). Linear regression slopes including all experiments (solid line) and excluding STRONG experiments (dashed line). b) As a) but for maximum anomaly of the zonal wind averaged over 850–500 hPa. Error bars indicate 5–95 percentiles according to a bootstrap resampling.

only (Figure 5.18a, dashed line) than when considering all cases (Figure 5.18a, solid line). This is quantitative evidence of nonlinearity in the forcing magnitude for the STRONG forcing cases.

Figure 5.18b shows the relationship between the maximum zonal wind anomaly and ice area. Linear regressions against ice area provide evidence that for zonal wind, too, there is a linear scaling governing the WEAK and MODERATE cases (Figure 5.18b, dashed line) but nonlinearity for the STRONG cases. The STRONG anomalies are greater than suggested by the scaling obtained from the moderate cases. Excluding the STRONG cases, the zonal wind anomaly is approximately 0.1 ms^{-1} per million km^2. The behaviour of the EOF projection strength (not shown) is very similar, which is unsurprising since the maximum zonal wind anomaly is located around 70°N in all cases and dominates the EOF projection in all but the weakest case (Figure 5.15).

5.3.3 Impacts of friction

In the above discussion, the circulation response to sea ice addition is discussed in the light of changing temperature gradients. This, and to some extent the accompanying insulation of the moisture-rich ocean surface, is the focus of most previous studies and the clearest causal link between sea ice anomalies and the circulation. However, the extent to

(a) 10 m

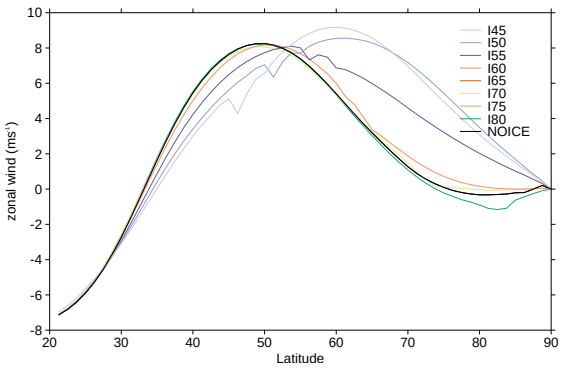

Figure 5.19: The time-mean, zonal-mean zonal wind at 10m

which the anomalous winds may be affected by surface friction is an important caveat to the above results.

The roughness length of sea ice is 5×10^{-4} m in HadGAM1 (McLaren *et al.*, 2006), while the roughness over the marginal ice zone is much higher (0.1 m). While roughness length was not output as a diagnostic in the symmetric simulations, a one month simulation run to examine roughness found zonal mean high latitude values over open ocean of between 1×10^{-4} m and 2×10^{-4} m. This decreased with decreasing latitude, consistent with the roughness length being a representation of wave height and therefore a function of wind speed. Together, these suggest that the frictional effect is likely to be significant over the marginal ice zone only.

The zonal wind at 10 m provides evidence for this hypothesis; in I45, I50 and I55, there is a sharp reduction in zonal wind over the marginal ice zone (Figure 5.19). However, at 925 hPa over the marginal ice zone the response has the sign found in the rest of the tropospheric column, which for cases I50 and I55 is an increase (Figure 5.7). This suggests that the response is not dominated by the surface effect.

Over the 100% ice zone, zonal winds at 10 m increase, and the qualitative response is similar to that at 850 hPa. Moreover, at a given latitude the shear $u_{850\,hPa}/u_{10m}$ is larger in an experiment with ice than one without. This is consistent with the expectations of both an increased temperature gradient and an increased surface roughness. On the other hand the wind at 10 m is also stronger over the ice than in an experiment where there is no ice present; this would be consistent with decreased surface roughness.

In summary, evidence suggests that surface roughness over ice is not a leading driver of the changes above although it is likely to be moderating the response in some way.

However, it is not possible to further separate these components without conducting sensitivity experiments.

5.4 Sensitivity to SST Profile

As discussed in the Introduction, previous experiments with surface thermal forcings have found that the response is sensitive to the season of integration. For example, Kidston *et al.* (2011b) found the amplitude of the response to sea ice forcing in the southern hemisphere to be dependent on season, with a significant response only to increased sea ice in the cold season. One possible reason is the proximity of the imposed forcing, here the ice edge, to the baroclinic zone of the unperturbed experiment; this is a theme which also arises in SST perturbation experiments (e.g Brayshaw *et al.*, 2008). While the experiments above with varying ice edge go some way to investigating this, applying the same forcing to a different state is useful to establish whether the response to the same sea ice anomaly may be different in different seasons.

Therefore, integrations were also performed with the SST2 profile (Section 5.1.2). This is shown again in Figure 5.20a[6]. SST2 (blue) imposes a stronger surface temperature gradient than SST1 (black) equatorward of 34° and a weaker gradient poleward of here. The SST2 profile is also colder than or the same temperature as SST1 everywhere. The strongest surface temperature gradient in SST2 is slightly weaker than, and equatorward of, that in SST1.

In the troposphere, NOICE_2 is warmer in the tropics (0–20°), colder in midlatitudes (20–60°) and not significantly changed in polar latitudes relative to NOICE (Figure 5.20e). NOICE_2 has a clear subtropical jet maximum at 200 hPa and 29° of 44.5 ms^{-1}, and near-surface zonal wind maximum at 43° of 15.5 ms^{-1} (Figure 5.20c). The subtropical (upper-level) jet maxima is much nearer the equator and stronger compared to SST1, while the eddy-driven component is slightly nearer the equator and weaker compared to SST1 (Figure 5.20d). Therefore, in SST2, the subtropical jet is more dominant. Likewise, the overturning circulation (Figure 5.20f) displays a contracted, strengthened Hadley cell and an equatorward shifted Ferrel cell. The resulting jet structure bears closer resemblence to the reanalysis for SH winter (JJAS) or NH late winter (FM), although the jet is stronger

[6] As discussed in Section 5.1.2, SST2is very similar to the QOBSWIDE profile of Brayshaw *et al.* (2008) but with the minimum temperature reduced to the freezing temperature of salt water.

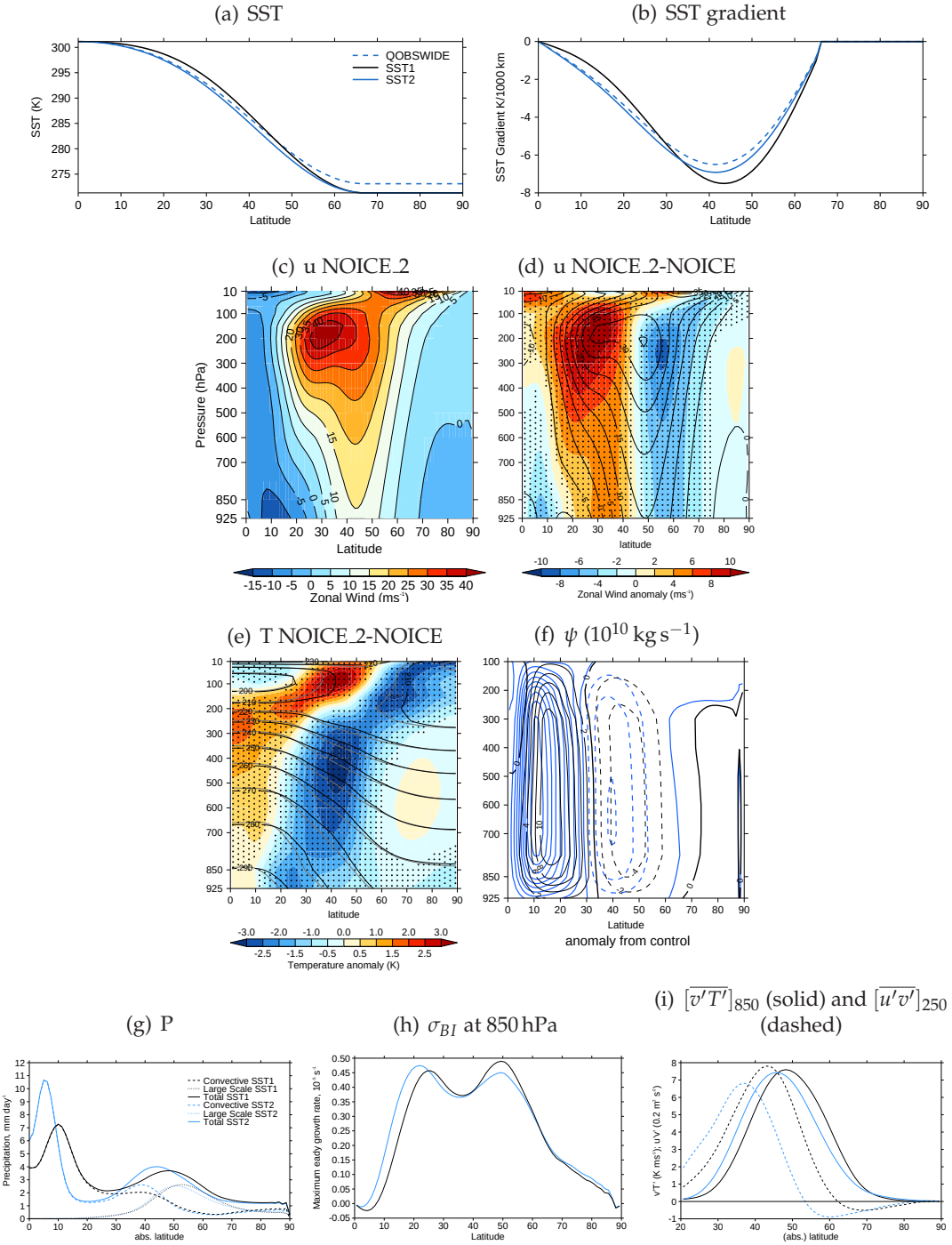

Figure 5.20: A comparison of the SST profiles and resulting atmospheric state between NOICE (black lines in (a), (b) and (d)–(i)) and NOICE_2 (blue lines). (a) The imposed SST profile in context. (b) The SST gradient. (c) NOICE_2 zonal wind. (d) NOICE_2 zonal wind as anomaly from NOICE (shading) and NOICE zonal wind (contours, contour interval 5 ms^{-1}. (e) NOICE_2 temperature (grey contours), as anomaly (shading) from NOICE (black contours). (f) meridional mass streamfunction ψ. (g) Precipitation and its partition into convective and large scale precipitation. (h) Eady growth rate at 850 hPa. (i) Covariance measures (with 2-6 day band pass filter) of the storm track.

than is found in either of these cases (not shown). This is probably a result of the lack of asymmetries and frictional land masses in the aquaplanet experiments.

Other measures support the conclusions of the previous paragraph (Figure 5.20); first, the stronger SST gradients in low latitudes are associated with a Hadley cell which is more intense and narrower than that in SST1, so the convective precipitation maximum is increased and shifted equatorward relative to SST1 (Figure 5.20g). Despite the shift in the maximum (absolute) surface temperature gradient, the midlatitude baroclinicity maximum does not shift but only weakens (Figure 5.20f), consistent with the 850 hPa temperature anomaly structure, which differs from that at the surface. The transient heat and momentum fluxes and eddy driven jet are weaker but also closer to the equator in SST2 (Figure 5.20i), as is the large scale precipitation maximum (Figure 5.20g), implying an equatorward shift of the storm track.

A hypothesis, therefore, is that due to the equatorward shifted storm track in SST2, a more equatorward ice edge may be required to perturb the storm track and to obtain the same magnitude of response as in the SST1 case. This hypothesis is tested using a subset of sea ice forcings, with the experiments denoted NOICE_2, I80_2, I70_2, I60_2 and I50_2, where '_2' refers to the use of SST2.

5.4.1 Evidence of sensitivity

In what follows, a subset of the analysis as performed in the SST1 case is presented in order to highlight the similarities and differences between the results.

The temperatures and temperature responses are summarised in Figure 5.21. At 850 hPa, the NOICE and NOICE_2 temperature structures are similar (Figure 5.21b vs a), and in particular the 850 hPa temperatures at the pole differ by under 1 K. However, in the SST2 case the low-latitude maximum in the 850 hPa temperature gradient is stronger relative to the mid-latitude maximum and is further equatorward (Figure 5.21d vs c). The mid-latitude maximum is less well defined than in SST1.

Regarding the response to ice addition, only for a strong forcing, here I50_2, does the midlatitude maximum temperature gradient intensify and shift; this is consistent with SST1. The cooling at the pole at 850 hPa in SST2 is weaker by up to 5 K than in SST1 (Figures 5.21a and b). At 500 hPa (Figure 5.21c), it is again (as in SST1) only for a relatively strong forcing that anomalies are notable (comparing Figures 5.21e and f), but at this level

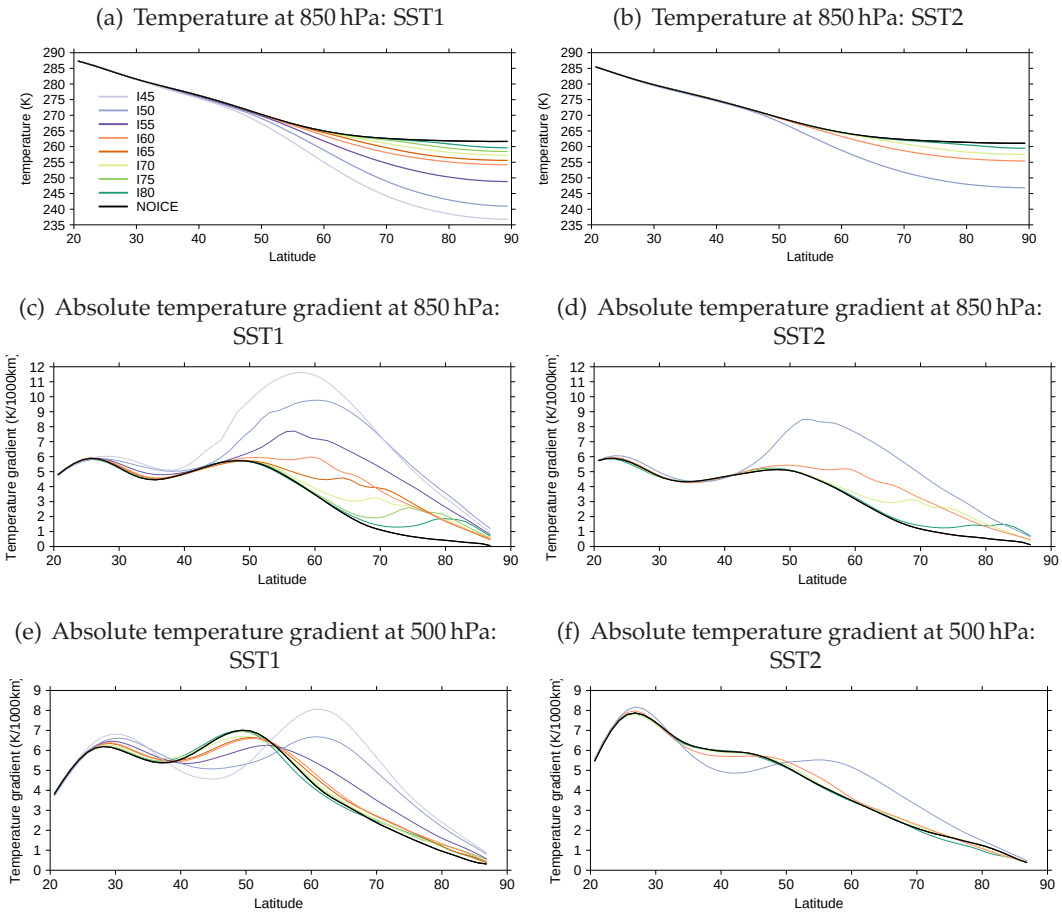

Figure 5.21: Zonal-mean temperature response to ice addition; a comparison of SST1 (left; a, c and e) and SST2 (right; b, d and f). a),b); Temperature at 850 hPa. c),d); Absolute temperature gradient at 850 hPa. e),f); Absolute temperature gradient at 500 hPa.

these anomalies are superimposed on a rather different initial state given the new SST profile.

As in SST1, I50_2, I60_2 and I70_2 impose an increase in time-mean zonal wind on the poleward flank of the low level eddy driven jet maximum (Figure 5.22d), and I50_2 causes a poleward shift of the maximum. The response in I80_2 is in the opposite sense, and opposite to I80-NOICE, but this response is not statistically significant at the 95% level. At upper levels, the reduction in the eddy driven jet core is seen again, as is the increase in the subtropical jet (Figure 5.22f). Comparing to SST1, the anomaly structure has therefore shifted with the jet, such that it again resembles a dipole roughly around the NOICE_2 eddy driven jet maximum (Figure 5.22a and b, for I60 and I60_2). The response of transient fluxes $\overline{v'T'}$ and $\overline{u'v'}$ (Figure 5.23) and precipitation (not shown) generally reinforce the picture given by the zonal wind and temperature plots that the response and its progression as more ice is added is qualitatively similar to the SST1 case.

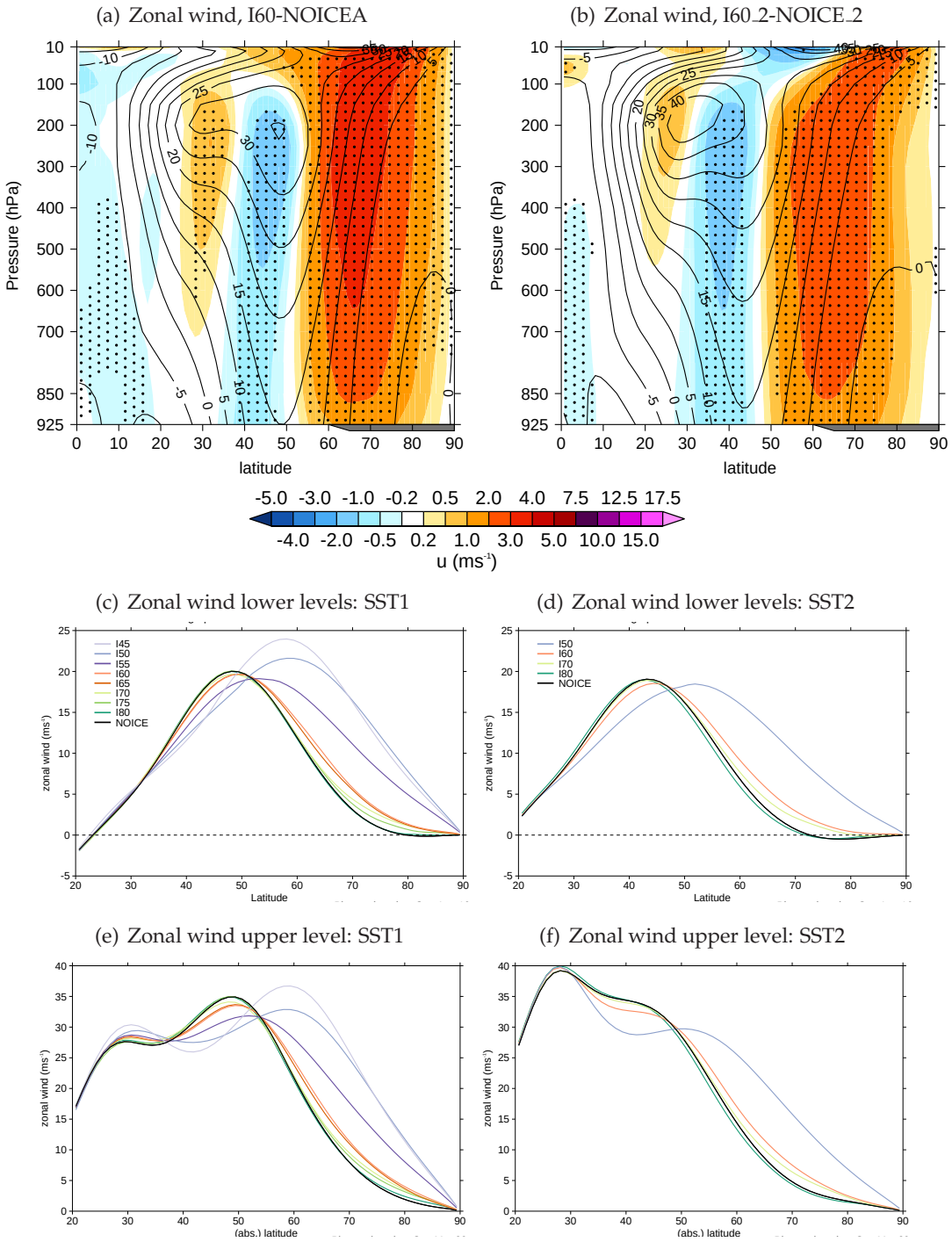

Figure 5.22: Zonal-mean zonal wind response to ice addition; a comparison of SST1 (left; a, c and e) and SST2 (right; b, d and f). a); I60-NOICE. b); I60_2-NOICE_2. c),d); zonal wind averaged over 850–500 hPa. e),f) zonal wind at 250 hPa.

However, key differences can be seen particularly in the I50_2 case. The response in both $\overline{v'T'}$ and $\overline{u'v'}$ is weaker than in SST1, such that it looks more similar to the I55 case than the I50 case (Figure 5.23c vs d, e vs f). It can also be argued that the I60_2 anomaly structure looks more similar to the I65 anomaly structure in $\overline{v'T'}$, with the anomaly well

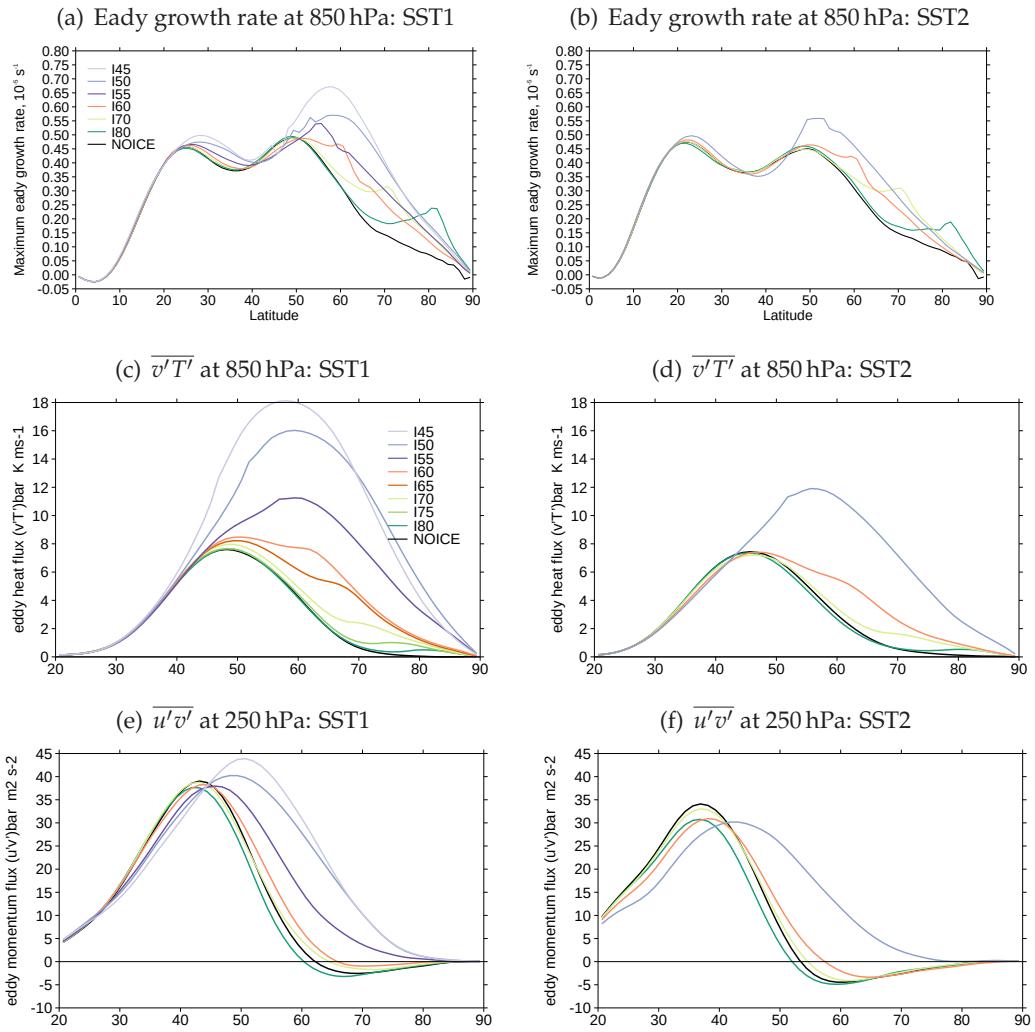

Figure 5.23: Storm track response to ice addition in the two SST profiles a) Eady growth rate at 850 hPa, SST1. b) as a) but SST2. c) Transient heat flux $\overline{v'T'}$ at 850 hPa, SST1. d) as c) but SST2. e) Transient momentum flux $\overline{u'v'}$ at 250 hPa, SST1. f) as e) but SST2

separated from the maximum. Therefore, there is some evidence for the hypothesis that the different structure of the baroclinic zone in SST1, with a weaker midlatitude maximum, affects the extent to which a sea ice anomaly near this zone is able to perturb the atmosphere.

The evidence above shows that the response is qualitatively similar for these two different SST profiles, with the anomalies shifting with the control jet. There is some evidence that there is a weaker response of several variables to sea ice anomalies in SST2 than in SST1, suggesting that the response to a given (sea ice) forcing may be weaker in SST2, but this argument is somewhat speculative thus far. To test the hypothesis, the regression of response against forcing has been calculated for SST2 (Figure 5.24). As found in SST1, the WEAK and MODERATE responses are well described by a linear

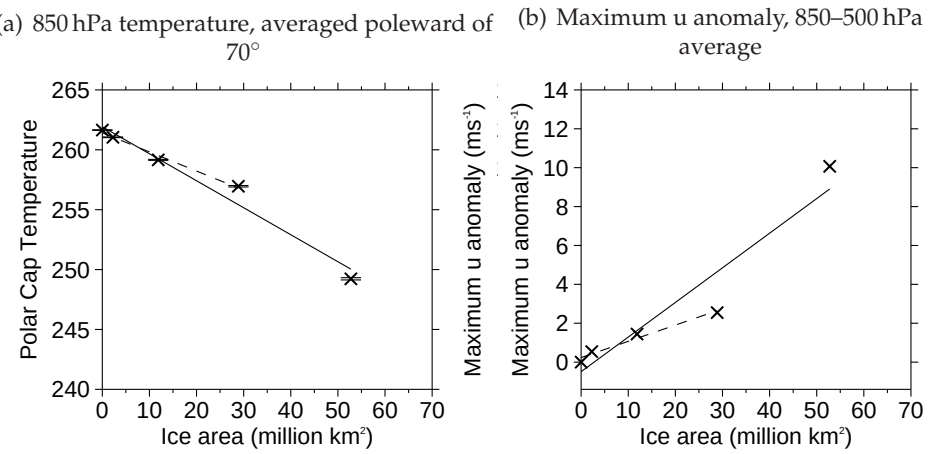

Figure 5.24: Relationship between atmospheric response and ice area; as Figure 5.18 but for SST2

scaling which appears not to hold for I50_2 or the STRONG cases in SST1 experiments. Table 5.2 demonstrates the key results from these regressions:

- The response (either the polar cap temperature anomaly or the maximum wind anomaly) from a given magnitude of forcing is significantly weaker (based on a bootstrap method) in SST2 than in SST1 (Table 5.2, second and fourth rows)

- The responses of I50_2 and I50 both deviate from the linear fit for weaker cases in their respective SST cases. For temperature, the response is approximate 50% stronger than this linear fit and for zonal wind it is over twice as strong.

- The anomaly I50_2-NOICE_2 is much smaller than the anomaly I50-NOICE (Table 5.2, third and fifth rows).

This provides strong evidence that the response to a given sea ice anomaly in the SST2 profile is weaker than for the same anomaly in the SST1 profile, notwithstanding the limited number of experiments performed in the SST2 case.

Finally, the JLI is examined to investigate whether regime behaviour is again evident. This is shown in Figure 5.25 (compare to Figure 5.17). The behaviour is similar to that shown for SST1: in NOICE_2 there is a modal jet position near the position of time-mean jet maximum. This remains relatively unchanged until a certain threshold is reached, when the modal latitude shifts about 10° poleward. The intermediate forcing cases (I60_2, I70_2 and I80_2) are associated with an increased probability of a poleward shifted jet stream.

Variable	SST1	SST2
Control EDJ latitude	47°	43°
Regression coefficient; x=SIA, y=$T_{850,\phi>70^\circ}$ $T_{anom,850\,hPa,\phi>70^\circ}$/SIA; I50	-0.21 ±0.01 -0.33	-0.16 ±0.01 -0.24
Regression coefficient; x=SIA, y= max(u_{anom}) max(u_{anom})/SIA; I50	0.10 ±0.01 0.26	0.08 ±0.01 0.19
Regression coefficient; x=$T_{850,\phi>70^\circ}$, y=max(u_{anom})	-0.50 ±0.02	-0.53 ±0.03

Table 5.2: A comparison of the control states and the magnitude of response to forcing between SST1 (column 2) and SST2 (column 3).
Top: EDJ latitude (defined below) in NOICE(_2) experiment. Rows 2,4,6: Regression coefficient b from linear model $y = a + bx$, for given variables; regression is performed across the experiments with WEAK or MODERATE forcing (NOICE–I60 and NOICE_2–I60_2). Rows 3,5; for the STRONG case I50(_2), the response scaled by the sea ice area. This can be compared to the WEAK/MODERATE scaling directly in rows 2 and 4.
Variable definitions are: **EDJ latitude**- the latitude of max($\overline{u}$, 850–500 hPa average); **SIA**- sea ice area, million km^2; $\mathbf{T}_{anom,850\,hPa,\phi>70^\circ}$- low-level temperature anomaly (in K) averaged, with area weighting, over the polar cap; and **max($\mathbf{u}_{anom}$)**- the maximum value of the zonal-mean zonal wind anomaly, ms^{-1}.
Errors on regression slopes are given in brackets, and calculated as the 1-sigma uncertainty estimates on the regression, neglecting uncertainties in x and y; various treatments of uncertainties did not affect the regression coefficients by more than 0.01.

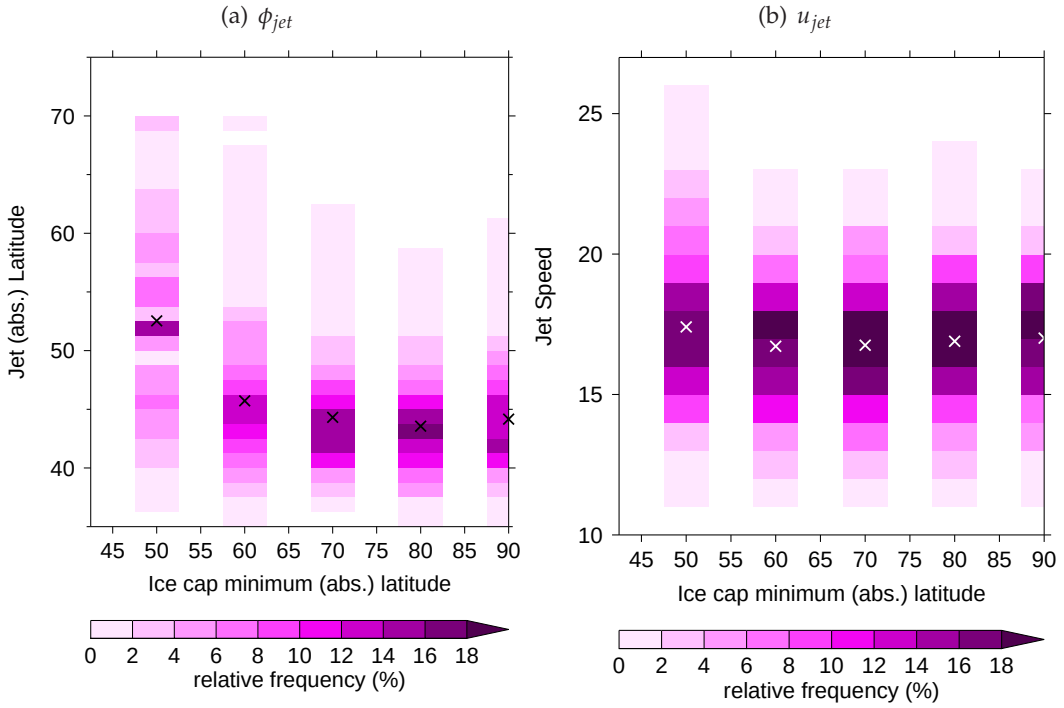

Figure 5.25: As Figure 5.25 but for SST2: The PDF of jet latitude ϕ_{jet} (a) and speed u_{jet} (b) as derived from daily-mean [u], vertically averaged over 925–700 hPa. Crosses denote mean ϕ_{jet} (a) and u_{jet} (b).

In SST1, the I50 JLI showed a jet which was already shifted poleward (increased ϕ_{jet}) and faster (increased u_{jet}) than in the NOICE case. In contrast I50_2 retains high variability in jet position ϕ_{jet} (Figure 5.25) and mean u_{jet} is not greatly increased (Figure 5.25); this is more similar to the I55 case in SST1. This is consistent with the hypothesis that the response is different in this different background state, and in particular, a more equatorward ice forcing is required to obtain a given response. This suggests a different interpretation of the weighting discussion above, namely that the triggering behaviour which causes the nonlinear jet response may require a stronger or more equatorward forcing for this second SST profile. However, an I55_2 experiment would be required to investigate this hypothesis fully.

5.5 Summary and Discussion

In this chapter, experiments performed with an aquaplanet AGCM were used to investigate the response to sea ice addition. The dominant, robust response is of an increase in zonal wind speeds poleward of the eddy driven jet. This response is linear for forcings which fall in the regime of recent or projected near-future climate, namely, ice restricted to poleward of 60°. However, for stronger cases the response is nonlinear. While the zonal wind anomalies in these cases are centred on the same latitudes, they constitute a poleward shift in the eddy driven jet, storm tracks and associated overturning circulation. There are associated changes in other features of the circulation, for example a strengthening of the subtropical jet.

5.5.1 Implications for 20^{th} and 21^{st} century climate

The majority of previous work on sea ice has focused on recent or projected near-future climate. As such, the result that more sea ice would force a poleward intensification of the eddy driven jet, or positive phase of the annular mode, is consistent with the findings from more realistic experimental configurations. For example, Magnusdottir *et al.* (2004), Honda *et al.* (2009), Seierstad and Bader (2009), Liu *et al.* (2012) and Peings and Magnusdottir (2013) all cite a negative annular mode in response to various negative sea ice anomalies in the North Atlantic. This finding is also consistent with results from simple models (Butler *et al.*, 2010) and multi-model ensemble studies (Harvey *et al.*, 2013;

Cattiaux and Cassou, 2013).

However, caution should be exercised when interpreting these results. It was noted in Section 5.1.3 that in terms of ice area forcing, it is the cases I70, I75 and I80 which are most relevant to the current climate state. The response in these cases has been shown to be weak and to not strongly project onto the annular mode. Indeed, there is some evidence that the I80-NOICE anomalies (e.g. EOF projection) are of opposite sign, although they are not statistically significant. This is in line with the results of Screen *et al.* (2013b) and Screen *et al.* (2013a), that sea ice anomalies are actually unlikely to be forcing large changes in our current climate. In addition, even where the response does project strongly onto the annular mode, there is a robust residual in the sense of increased zonal wind at high latitudes. The residual response has previously been interpreted by Deser *et al.* (2004) as a direct response to the ice addition which then triggers the annular mode; the fact that this 'residual' is present in all the experiments considered here could provide evidence for this hypothesis.

It has been concluded above that the response to current-day ice anomalies is likely to be small. However, an important caveat to this is as follows: evidence has been found in the above analysis that, while the response is qualitatively robust to a different background jet state, the magnitude of the response and the latitude at which a nonlinear response is triggered is sensitive to the background jet state. While these results are tentative at present, it can be speculated that a jet at 47° (as in SST1) was sensitive to forcing at equatorward of 55°, and a jet at 43° was perhaps sensitive to forcing equatorward of 50°. A jet at 60° might therefore be sensitive to forcing at 65°, which is within the realms of current climate.

Moreover these results are all for zonally symmetric anomalies in an aquaplanet. Such experiments have enabled investigation of the dynamical mechanisms relevant for the response to forcing. However there are naturally limitations to interpretation of results in an aquaplanet model. Firstly, the lack of seasonality and choice of SSTs mean that these experiments is not designed to exactly represent any one season or ocean basin. Secondly, the ocean cannot adjust in response to a forcing, producing unrealistic effects locally (for example an unrealistically large surface temperature front) and in terms of the global energy balance. Atmosphere-only modelling is however a common tool, so such limitations are common to most previous studies into the atmospheric response to ice anomalies. Fi-

nally, the lack of asymmetry means that the eddy-mean flow feedbacks are particularly large, and that stationary wave activity is small. Responses in a more realistic framework may be different due for example to interaction with existing stationary waves; this is the focus of the next chapter. This is of particular interest since many hypotheses regarding sea ice reduction include the triggering of Rossby waves and their remote impact (e.g. Alexander *et al.*, 2004; Honda *et al.*, 2009) or the propagation of Rossby waves (Francis and Vavrus, 2012; Strong and Magnusdottir, 2010b).

The discussion on sensitivity of the jet can be informed by considering the literature on the effect of SST fronts, since the addition of sea ice constitutes such a surface front as well as a thermal forcing at high latitudes. For example, Brayshaw *et al.* (2008) found that the storm tracks are most sensitive to SST anomalies which perturb the region of maximum baroclinicity. Such a result would imply that a background state with a different region of peak baroclinicity and therefore a different eddy driven jet latitude would be sensitive to forcing at a different latitude.

5.5.2 Implications for palaeoclimate

Another implication of these results is for simulations of palaeoclimate. For example, while the LGM was a higher ice state, it is also generally thought that the jet was further south, or equivalently, that warmer climates have more poleward jets (Toggweiler *et al.*, 2006). However, in the experiments in this chapter, the colder climate (with more sea ice) has a more poleward jet. These results are therefore consistent with the findings of Merz *et al.* (2015) that the position of the jet during the LGM was dominantly forced by mechanical forcing by the Laurentide ice sheet (over present day North America), rather than by the sea ice state.

Chapter 6

The Response to Sea Ice in HadGAM1 with Idealised Continents

6.1 Introduction

In this chapter, model experiments are performed with HadGAM1 using asymmetric northern hemisphere lower boundary forcings in the form of land and orography. The orographic and land-ocean forcing is designed to be representative of the North American continent, Rocky Mountains, and Eurasian continent. These elements have previously been shown to be important in forcing the observed North Atlantic jet and storm track (e.g. Brayshaw *et al.*, 2009). Therefore, these experiments are a step in the modelling hierarchy between aquaplanet lower boundary conditions (considered in chapter 5) and fully realistic boundary conditions.

Ice perturbation experiments are performed, firstly with ice at all longitudes and then in the 'North Atlantic' sector only. These experiments are designed to investigate the following questions:-

- Is the response to ice addition found in chapter 5 - increased wind speeds on the jet's poleward flank and nonlinearity at large ice extents - robust when asymmetric land and orographic lower boundary conditions are prescribed?
- Can any knowledge can be gained from idealised asymmetric experiments about the spatial distribution of responses to sea ice addition, given the simplified geography?
- What are the differences of the response to sea ice addition between this asymmetric case and the symmetric case in Chapter 5? Can these be understood as an example of a response to forcing (in this case sea ice) being sensitive to the background state of the jet and storm track (e.g. their strength and location)?

This chapter is structured as follows; the experimental design and naming conventions are detailed in Section 6.2. Section 6.3 describes the atmospheric state in the case with no sea ice, placing the work in the context of previous studies and providing a basis for comparison to Chapter 5. Section 6.4 looks at the effect of symmetric ice addition to 65°N. Section 6.5 considers the atmospheric response to ice addition and removal in the Atlantic sector, using the 65°N ice case as a control.

6.2 Model Formulation

HadGAM1 was described in Chapter 3. Insolation, ozone and aerosols used are identical to those in the zonally symmetric case (Section 5.1.1) and all the experiments in this chapter use SST1 (Section 5.1.2). A zonally symmetric SST forcing was chosen in order to isolate the effect of adding land and orography when comparing to the symmetric case. The other boundary conditions used in this chapter are described below. While the model configuration is based on that in Brayshaw *et al.* (2009) and companion studies, there are adjustments to the land, orography and SST as compared to these studies. The addition of sea ice is a new component in this framework.

While the zonally symmetric SST allows more direct comparison with the symmetric experiments than would otherwise be the case, it does constitute a substantial simplification of the real system. In the North Atlantic for example, meridional SST gradients are strong in the west (in the region of the Gulf Stream for example) but very slack in the east, so there are zonal gradients in SST. These features have been shown (e.g. Brayshaw *et al.*, 2011) to affect the North Atlantic atmospheric circulation. The reader may refer back to Figure 4.1a for a realistic climate model simulation of the winter surface temperature climatology which demonstrates these SST asymmetries.

6.2.1 Land masses

A flat 'Eurasian' continent and a 'North American' continent with a mountain range representing the Rocky mountains are specified. The configuration is based on those used in Brayshaw *et al.* (2009), Brayshaw *et al.* (2011) and Saulière *et al.* (2012). These studies demonstrated that this gives an adequate representation of the location and magnitude of the North Atlantic jet (Brayshaw *et al.*, 2011, Figure 3e), but is deficient in the North

Pacific with an equatorward jet bias (Saulière *et al.*, 2012, Figure 4). A description of this configuration, and justification for changes to the continents and orography used in these earlier papers, is given in the following paragraphs.

Figure 6.1 shows the land used in Saulière *et al.* (2012) (panel a) and in this study (e.g., panel b). As can be seen, two changes have been made for the purposes of this study:-

- The north coast of both continents is at 70°N rather than 60°N. This change is made for two reasons. Firstly, it is a more realistic representation of the real world. Secondly, the choice is partially motivated by the desired ice profiles (Section 6.2.4); if the coastline were further south, I65 for example would have an unrealistic latitudinal surface temperature profile between the very cold continental surface, the warm sea surface, and the cold ice surface.

- The south coast of Eurasia is at 30°N rather than 17.5°N. As noted in Brayshaw (2006), the configuration with land at lower latitudes has a strong positive surface temperature anomaly (relative to the SSTs at the same latitude) over the Eurasian land mass, and an associated easterly jet. These features are not realistic when considering long runs (rather than short seasonal events). The south coast is therefore moved northwards to remove this issue.

The tilted Eurasian coastline follows Saulière *et al.* (2012), and is used because it more accurately represents reality, but differs from the meridionally aligned coastline of Brayshaw *et al.* (2009). Saulière *et al.* (2012) noted that this tilt weakened the zonal-mean storm track and westerly zonal wind. However, they linked this in part to the strong heating over south Eurasia, which (as just discussed) has been removed for the following experiments.

Points in the model are specified to be either land or ocean, so that in each grid point the land fraction is specified as either 1.0 or 0.0. An important consequence of the addition of land is that, unlike the ocean surface which is set at fixed SST and so represents an infinite heat and moisture source, the land surface (e.g. surface and deep temperature, soil moisture, snow cover) will adjust to the atmospheric conditions.

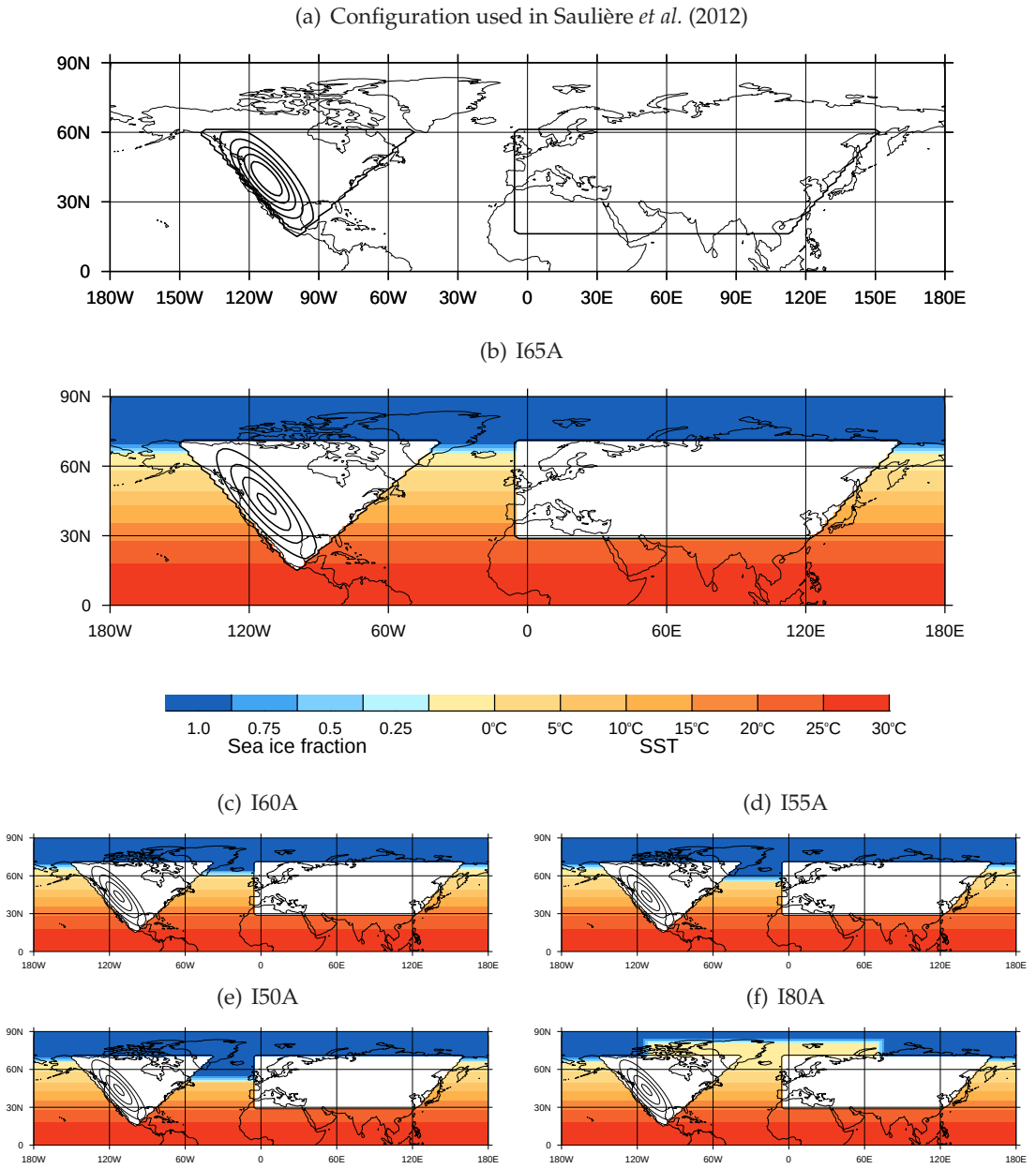

Figure 6.1: The surface forcings (land, orography, SST and SIC) applied in a) Saulière *et al.* (2012) (land and orography only), b) I65A, c) I60A, d) I55A, e) I50A, f) I80A. Shown are the orography (contours, every 500m); land (white mask); SST (reds, every 5K); and sea ice concentration (blue, every 25%). The faint contours show the coastlines in reality.

6.2.2 Land surface properties

Properties of the land surface, specifically soil and vegetation, use a representative point method as in the studies of Brayshaw *et al.* (2009) and Saulière *et al.* (2012). In this method all properties are set to mimic those of some specified point in the standard climatological boundary conditions, here chosen to be (52.5°N, 0.0°E) representing East Anglia in the UK. The land surface types at this point are a combination of grasses, urban cover

and bare soil. This choice of method and location is the same as that in Brayshaw *et al.* (2009), which chose this point as being representative of lowland areas in midlatitudes. Since there is no specific motivation for altering them, keeping the parameters the same enables the most direct comparison between this study and the earlier papers. Implicit in this method is that the perturbations made are to sea ice only, and not to land ice (since the specified land surface properties are homogeneous and are unchanged between experiments) .

6.2.3 Orography

Orography representative of the Rocky mountains is specified using a bump, essentially Gaussian in form, tilted to align with the west coastline of North America. Defining η as:-

$$\eta = \exp\left(-\left[\left(\frac{(\lambda')cos\gamma + (\phi')sin\gamma}{A} \right)^2 + \left(\frac{(\phi')cos\gamma - (\lambda')sin\gamma}{B} \right)^2 \right] \right) \tag{6.1}$$

then, given an orographic parameter ψ, the value of ψ over land is defined as

$$\psi = \begin{cases} C(\psi_{max}\eta + \psi_{flat}(1-\eta)) & \text{if } \eta \geq 0.05 \\ \psi_{flat} & \text{if } \eta < 0.05 \end{cases} \tag{6.2}$$

The formulation is almost exactly the same as that in Brayshaw *et al.* (2009) and Saulière *et al.* (2012) (Brayshaw, 2006, equations 3.5 and 3.6). Here, $\lambda' = \lambda - \lambda_0$, the zonal deviation from the centre of the mountain range λ_0, and similarly for ϕ' in the meridional direction. γ is the mountain's rotation anticlockwise from a North-South alignment and A and B are scaling factors. The values of all these factors and how they compare to Brayshaw *et al.* (2009) is given in Table 6.1. ψ_{max} is a first estimate of the parameter's maximum value and ψ_{flat} its value over flat land, sufficiently far from the mountain's centre. ψ_{flat} = 61 m for orographic height, again following the representative point method.

Finally, the scaling factor C is calculated such that the area integral of each orographic parameter within the idealised mountain range is equal to that in the standard boundary conditions; therefore the mountain has the same volume as the equivalent area in the standard boundary conditions. The orographic parameters include all those used in the standard configuration- including orographic height, roughness, and subgridscale gradients of orography. The orographic height for both Saulière *et al.* (2012) (equivalently

Brayshaw *et al.*, 2009)) and the current study is shown in Figure 6.1. The orography differs from that in Saulière *et al.* (2012) not only in range but in peak height, since the scaling (volume correction) when applied to the extended mountain range gives a lower maximum height, of 2120 m in the current study.

This is lower than the Rocky mountains' peak in the standard HadGAM1 boundary forcing files, of 2560 m, which is in turn lower that the true maximum height of the Rockies, which is 4400 m (at Mount Elbert). This may affect the representation of downstream atmospheric processes; for example, using low resolution orogaphy in a high resolution model has a detrimental effect on simulation of European blocking in one model (Berckmans *et al.*, 2013). This suggests that higher resolution of orography, one effect of which is to increase its maximum height, is crucial for accurate simulation of some atmospheric features. However, the approach used in this chapter has been demonstrated to be useful in several previous studies; as well as those mentioned above, a similar simplified Gaussian orography approach was used in Gerber and Vallis (2009) for the Rocky Mountains, with a height of 2000m, and in Cash *et al.* (2005) for the Tibetan plateau.

6.2.4 Sea ice perturbations

All experiment names in this chapter are suffixed with the letter 'A' (asymmetric) to distinguish them from those in Chapter 5. Table 6.2 describes how the sea ice conditions in these experiments relate to those of Chapter 5; Figure 6.1b–f shows the northern hemisphere sea ice profiles for all but the NOICEA case. Crucially, many of the perturbations are applied in the North Atlantic only, as discussed below.

NOICEA has the same ice profile as NOICE (Section 5.1.3) in both hemispheres and both ocean basins. The difference NOICEA-NOICE can be understood in the light of previous studies, providing a foundation for interpreting the rest of the runs. I65A (Figure 6.1b) has the same sea ice boundary conditions as I65 (Section 5.1.3) in both hemispheres and both ocean basins. I65A-NOICEA can be interpreted as the response to symmetric ice addition in an asymmetric background state.

Four further experiments investigate the response to further adding or removing ice in the North Atlantic sector only. The I65 ice profile is retained in the Pacific ocean and southern hemisphere. In the North Atlantic, the profiles from I80, I60, I55 and I50 are used, giving experiments I80A, I60A, I55A and I50A (Table 6.2, Figure 6.1c–f). The deci-

	Interpretation	B09 value	Present value	Change from B09
λ_0	Central longitude	247.5°	247.5°	None
ϕ_0	Central latitude	40.0°	43.75°	Moved north for consistency with greater meridional extent of continent
A	Scaling factor 'across mountain'	7.5°	7.5°	None
B	" " 'along mountain'	20°	25°	Edited for consistency with greater meridional extent of continent
γ	Anticlockwise rotation from N-S alignment	$\tan^{-1}\frac{40}{45}$	$\tan^{-1}\frac{40}{45}$	None

Table 6.1: Values used in this study and in Brayshaw *et al.* (2009) (B09) as input to equation 6.1.

Experiment name	SH ice	North Pacific ice	North Atlantic ice
NOICEA	pole only	pole only	pole only
I65A	as I65	as I65	as I65
I60A	as I65	as I65	as I60
I55A	as I65	as I65	as I55
I50A	as I65	as I65	as I50
I80A	as I65	as I65 (75°E–115°W)	as I80 (115°W–75°E)

Table 6.2: The ice profiles and experiment names used to investigate the effect of ice addition and removal in an asymmetric setting. For the details of symmetric profiles I80,...,I50 see Table 5.1. For maps, see Figure 6.1.

sion to focus on ice addition experiments was made after preliminary analysis of I80A, which showed only a small response. For the I80A profile (Table 6.1 bottom row, Figure 6.1f) there is asymmetry in the Arctic Ocean; however, it was designed such that the strong zonal temperature gradients associated with the ice edge are well away from the North Atlantic, the region of most interest (Figure 6.1f).

6.2.5 Spinup, run length and data processing

A spinup of ten years is performed with the boundary conditions specified in Sections 6.2.1 to 6.2.3 and the NOICEA sea ice profile. This spinup is initialised with an atmospheric start dump from the 2C (two continents and Rocky mountains) experiments of Saulière *et al.* (2012).

For this spinup run, the dynamic land surface variables (soil moisture, deep soil temperature, canopy water content) are initialised using the representative point method described in Section 6.2.2. After the spinup run they are strongly heterogeneous across the

land surface. Their relatively slow evolution is the reason such a long spinup is required. In particular, while near-surface soil moisture is spunup within a year, soil moisture at the deepest of four levels (depth 1–3 m; see Section 3.3.2) continues to decrease. It continues to drift, but after 5 years into the spinup run this drift is small and approximately linear, and therefore assumed not to affect the model results.

NOICEA, I80A, I65A, I60A, I55A and I50A are then initialised from the spinup run and run for ten years. The first year is treated as spin up, so the analysis in this chapter uses years 2–10. Unless specifically noted, only the Northern Hemisphere is considered.

Snow cover at high latitudes is unable to melt due to low insolation and the lack of seasonality, and so accumulates linearly throughout the runs. However, the snow accumulation is not associated with a drift in variables such as surface temperature, SLP or near-surface geopotential height, or snow covered area (not shown). Therefore the unrealistic snow cover does not affect the model results, although it precludes any analysis of deep snow.

Since the orography intersects the 850 hPa and 925 hPa surfaces, plots and zonal averages at these levels exclude the region of orography which exceeds some height threshold. The specified thresholds are 1000 m at 850 hPa and 62 m (i.e. all enhanced orography) at 925 hPa. These thresholds are based on the minimum height at which the geopotential surfaces intersect the orography in the NOICEA run.

6.3 NOICEA: The Effect of Continents

This section describes the atmospheric state in the NOICEA experiment and compares it to NOICE, in order to understand the effect of addition of continents and orography. (The theoretical response to orography, and previous modelling studies in which similar asymmetries have been introduced, was discussed in Section 2.3.4).

6.3.1 Temperature

Figure 6.2a (contours) shows the zonal-mean temperature in NOICEA. The lower troposphere is warmer in the subtropics and colder in mid-to-high latitudes than in the symmetric case (Figure 6.2a, shading). This can be linked to the effect of land on surface temperature (Figure 6.2b). There is strong asymmetry in the surface temperature. Pole-

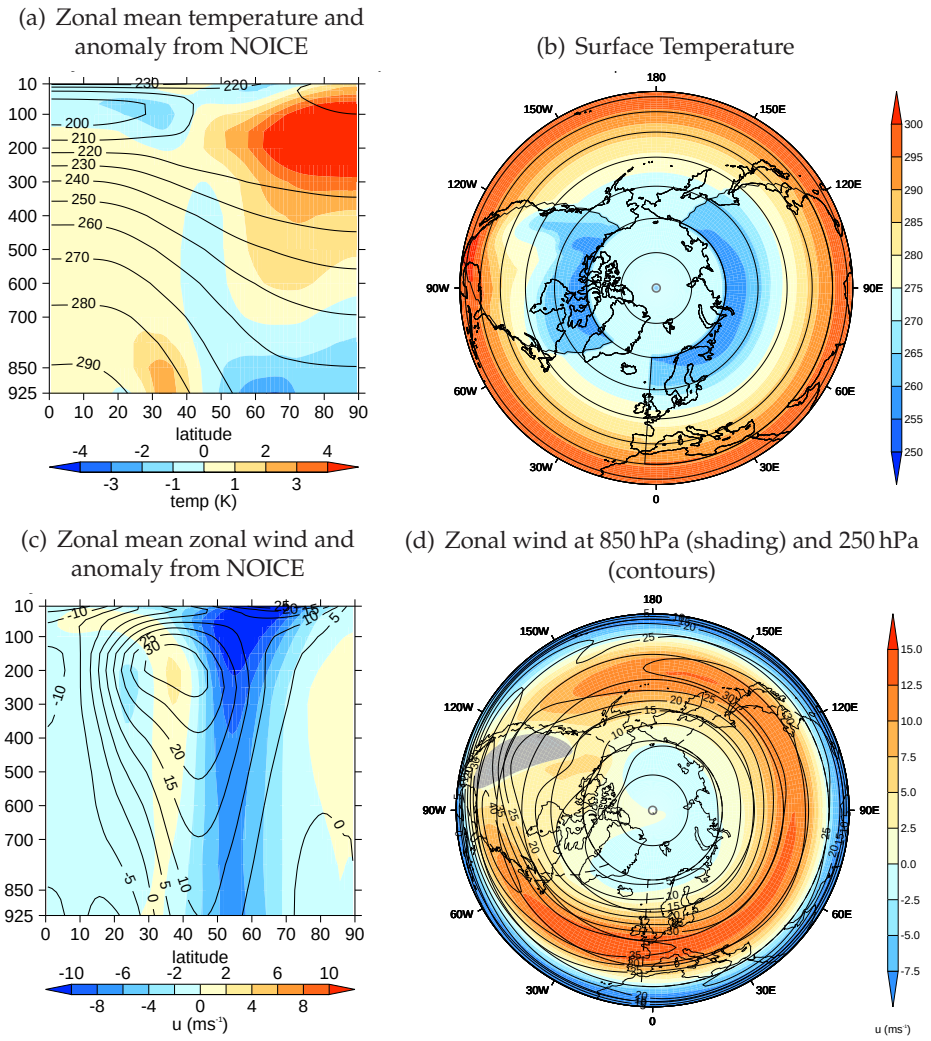

Figure 6.2: Temperature and zonal wind in NOICEA. a) Zonal mean temperature T (contours) and anomaly from symmetric experiment NOICE (shading). b) Surface temperature. c) as a) but for zonal wind. d) as b) but for zonal wind at 250 Pa and 850 hPa. Here and in all other figures using the polar projection, the minimum latitude is 15°N and gridlines, where plotted, are at 10° intervals from 30°N to 80°N.

ward of approximately 35°, the land surface is cooler than the ocean surface at the same latitude; equatorward of here, the land surface is warmer than the ocean surface at the same latitude (Figure 6.3a).

While it is not possible to evaluate the full radiative budget since not all the relevant model outputs were obtained, elements of the radiative budget provide insight into the temperature difference. The net downward shortwave radiation at the surface differs between land and ocean (Figure 6.3c). This is feasibly due to differing surface albedo (especially at high latitudes where snow is present) and planetary albedo, for example reduced cloud cover over most land relative to the ocean (Figure 6.3b), consistent with

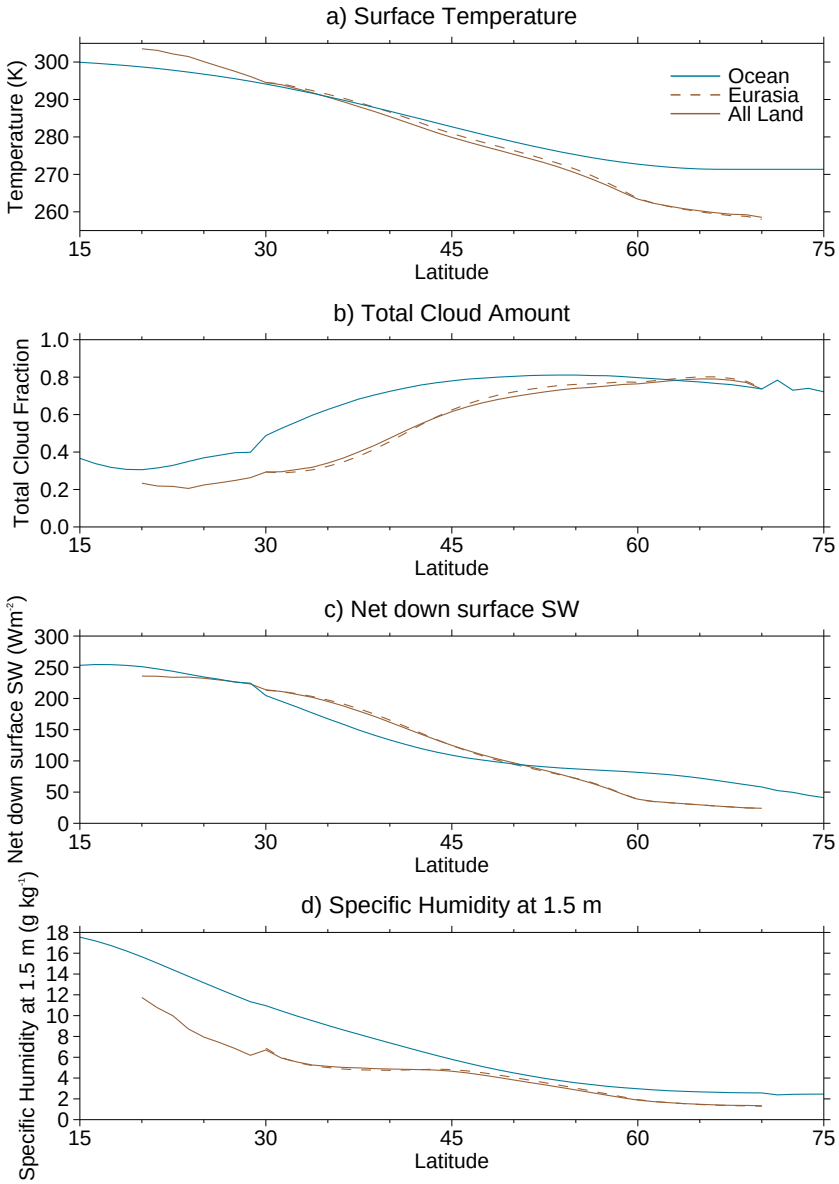

Figure 6.3: A comparison of variables over ocean and land in NOICEA. a) Surface temperature. b) Total cloud amount. c) Net down shortwave radiation at the surace. d) Specific humidity q at 1.5 m. Variables are zonally averaged over ocean (blue), all land (solid brown) and Eurasia only (dashed brown).

an expected reduction in moisture availability over land (Figure 6.3d). In addition, as discussed in Section 6.2.1, the land surface is able to radiatively adjust to the incoming shortwave radiation, unlike the (fixed) SSTs. This radiative adjustment would affect the surface temperature even in the absence of changes in incoming radiation.

Lower tropospheric temperature changes are not solely determined by local surface temperature changes; for example, the polar lower troposphere is colder than in the sym-

metric case, despite the fact that the polar surface temperature is unchanged. A plausible hypothesis for this cooling can be reached by considering the effect of the addition of land at lower latitudes on transport into high latitudes. Locally, the addition of land produces a relative cooling (Figure 6.3a) and cuts off the moisture source. At low levels (700 hPa and below) both $[\overline{vT}]$ and $[\overline{vq}]$ across 70°N decrease (not shown), and consistent with the reduced moisture flux into the polar region there is a decrease in low level specific humidity over the pole (not shown). The polar cooling is therefore consistent with the effects of both the reduction in warm advection and the decreased longwave optical depth associated with the decreased moisture content.

The polar stratosphere is also warmer than in the symmetric case. As discussed in Section 5.3.1.5, large changes in stratospheric temperature may arise in an aquaplanet due to changes in EP fluxes into the stratosphere. In NOICEA, asymmetries introduce stationary waves, which are not present in the symmetric case. Stationary eddy heat flux is therefore a possible driver of the increase in stratospheric temperature. A decomposition of the heat transport $[\overline{vT}]$ in the symmetric and asymmetric experiments was performed to address this possibility (not shown). While the upper level meridional heat flux into the polar stratosphere increases in the asymmetric experiment, the change due to the mean circulation $[\overline{v}][\overline{T}]$ exceeds the change due to stationary waves $[\overline{v^*T^*}]$ tenfold.

6.3.2 Circulation and dynamics

NOICEA zonal-mean zonal wind is shown in Figure 6.2. The jet is weaker and more subtropically dominated than in the symmetric case (Figure 6.2, shading). In particular the NOICEA low level (850 hPa) zonal wind maximum, associated with the eddy driven jet, is 11.5 ms^{-1}; this is over 30% weaker than in the symmetric case (the reader is referred to Figure 5.2a for the NOICE zonal wind structure). However, the jets are strongly localised (Figure 6.2d). Low level zonal wind is weakest over North America and strongest over the east Atlantic (30°W–0°W) with a local maximum of 15 ms^{-1}, which is close in magnitude to the symmetric NOICE maximum. Positive anomalies from the zonal mean are evident north and south of the Rockies (not shown) indicating flow deflection around the orography. Upper level zonal wind is strongest over the west Atlantic.

The key features of the zonal wind structure are similar to that in Brayshaw *et al.* (2009) and were discussed at length there. Surface frictional drag, orographic drag, and

land-ocean contrasts in temperature and moisture (see above) are important. (Other past literature on the role of land and orography in localising the jet and storm track and in forcing atmospheric stationary waves was discussed in Section 2.3.4.) The main points are mentioned below, with a discussion of other elements of the circulation in particular the transient heat and eddy fluxes and the asymmetric streamfunction (Figure 6.4).

The upper tropospheric asymmetric streamfunction ψ^* (Figure 6.4a) demonstrates the asymmetry generated by land and orography[1]. There is an anticyclonic anomaly to the north west of the mountain range, and an extended cyclonic anomaly over the Rockies themselves and extending into the Atlantic. There is also evidence of a downstream wavetrain. The local response differs somewhat from the theoretical linear response to orography (Hoskins and Karoly, 1981) which has an upstream anticyclone and downstream cyclone (Section 2.3.4). This was discussed in Brayshaw *et al.* (2009); the theory leading to the upstream-downstream pair assumes that the obstacle is sufficiently low that the flow is deflected over it. The southern side of the mountain range here blocks the flow causing horizontal deflection, resulting in a cyclonic feature over the southern flank of the mountain rather than downstream. The streamfunction anomalies in the current study also look similar to the nonlinear responses to the Rocky mountains in the dry GCM study of Chang (2009); in both cases, there is an underestimation of the tilt in the North Atlantic found in reality or in more realistically forced model simulations (e.g. Chang (2009) Figure 2c).

6.3.3 Storm tracks and precipitation

The Eady growth rate at 850 hPa (Figure 6.4b) has maxima over the continental interiors and on the tilted continental coasts, particularly the North American/West Atlantic coast around 40°N. This is consistent with the temperature gradation across the North American coast (Figure 6.2b) and strong vertical wind shear in this location (difference in upper and lower level winds in Figure 6.2d). These regions are therefore expected to be regions of maximum baroclinic growth. At 850 hPa, $\overline{v'T'}$ maxima are approximately colocated with the north of regions of maximum baroclinicity, in central Eurasia at about 45°N and off the East coast of North America (Figure 6.4c). However, the Eurasian maximum is shallow, and at 700 hPa the Atlantic maximum is 50% stronger than the Eurasian one

[1]The full streamfunction was calculated from time mean flow fields using the Met Office SFVP routine

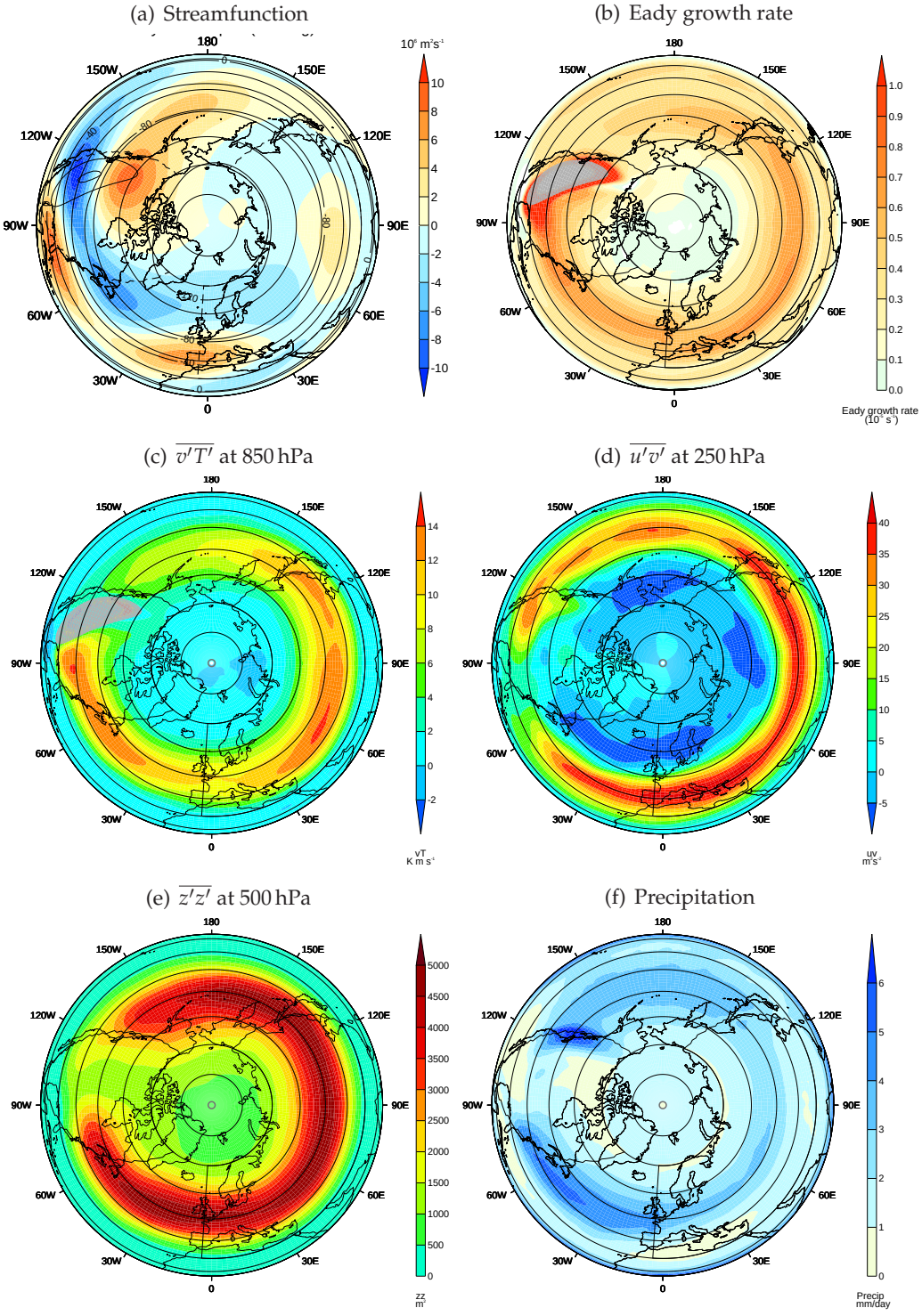

Figure 6.4: The asymmetric streamfunction and five measures related to the storm tracks (including precipitation) in NOICEA. (a) The streamfunction ψ (contours) and asymmetric component ψ^* (shading) at 250 hPa. (b) Eady growth rate σ_{BI} at 850 hPa. (c) Transient heat flux $\overline{v'T'}$ at 850 hPa. (d) Transient momentum flux $\overline{u'v'}$ at 250 hPa. (d) Geopotential height variance $\overline{z'z'}$ at 500 hPa. (f) Total precipitation. Transient fluxes (c)-(e) use a 2–6 day band pass filter, as in Chapter 5 (Duchon, 1979).

(not shown). $\overline{u'v'}$ (Figure 6.4d) also shows strong zonal asymmetry, but the maxima are generally downstream of those in $\overline{v'T'}$ and slightly to the south. This offset between the maxima of $\overline{u'v'}$ and $\overline{v'T'}$ is consistent with baroclinic lifecycle arguments whereby $\overline{v'T'}$ tends to dominate in the growth phase and $\overline{u'v'}$ in the decay phase, so that $\overline{v'T'}$ is more dominant upstream (Section 2.3.3).

The storm track (geopotential height variance $\overline{z'z'}$ at 500 hPa (Figure 6.3(e)) has a maxima at 45–50°N extending from approximately 60°W to 120°E, again with a tilt evident in the North Atlantic. This is consistent with the maximum storm growth implied by the baroclinicity, beginning slightly downstream and to the north of the baroclinicity maximum in the North Atlantic. Precipitation is centred in two bands, one zonally uniform band at 10°N (not shown) associated with the ITCZ and a second, zonally varying band in the midlatitudes (Figure 6.3(f)) associated with the storm tracks.

The zonal mean ITCZ precipitation has a maximum of 7.8 mm day^{-1} and is slightly enhanced relative to the symmetric case, implying that the tropics are perturbed by the addition of land. The midlatitude zonal mean precipitation maximum is 3.2 mm day^{-1}, a reduction relative to the symmetric case consistent with the reduced moisture availability over land, but there are local maxima of 7.8 mm day^{-1} on the upstream side of the Rockies, 4.0 mm day^{-1} in the upstream Pacific storm track and 5.3 mm day^{-1} in the Atlantic storm track. The Pacific storm track precipitation is approximately equal to that in the symmetric case (not shown).

The southern hemisphere is virtually indistinguishable from the NOICE symmetric case but the zonal wind speed is slightly increased (by less than 1 ms^{-1}) in the subtropical jet core (not shown). Given that there is evidence of change in the tropics, for example a small change in ICTZ precipitation in both hemispheres relative to the NOICE symmetric experiment (mentioned above for the Northern Hemisphere) it is possible that this is caused by the Northern hemisphere perturbations.

6.3.4 Realism of simulated circulation

In summary, the addition of continents and orography causes zonal localisation of the jet and storm tracks, weakens the zonal mean jet relative to the symmetric case, and forces upper level stationary waves. To see how this localised jet compares to the observed winter northern hemisphere state, Figure 6.5 shows the NOICEA zonal wind at 250 hPa

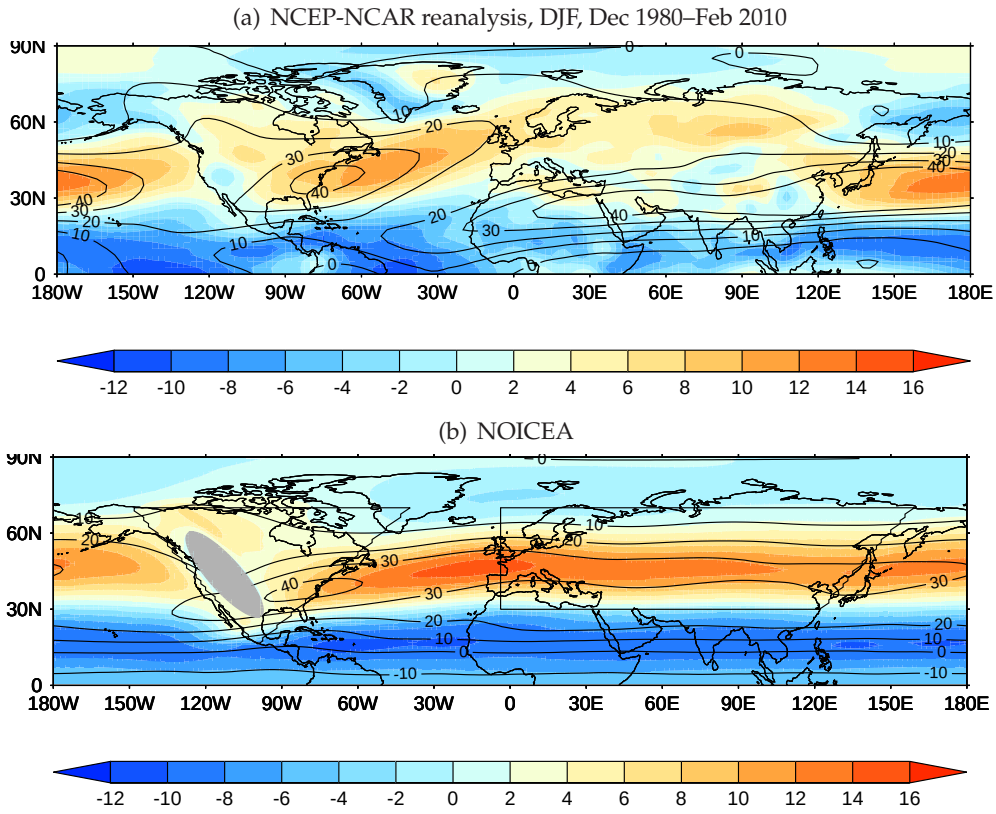

Figure 6.5: The zonal wind $\bar{u}$ a) in reanalysis data for the period 1981–2010 and b) in NOICEA; at 850 hPa (shading) and 250 hPa (contours, interval 10 ms^{-1}).

and 850 hPa alongside the NCEP reanalysis for 1981–2010 winter (DJF). It can be immediately seen that the model with these simple elements produces an upper tropospheric jet in the West Atlantic and lower tropospheric jet in the East Atlantic which resemble the reanalysis data.

However, there are unsurprisingly some notable deficiencies. These include

- substantial under-representation of the North Atlantic tilt
- insufficient suppression of the jet and storm track over Eurasia due to the simple representation of Eurasia in particular the lack of the Tibetan plateau (e.g. Saulière *et al.*, 2012)
- insufficient enhancement of the eady growth rate and other storm track measures in the western Atlantic basin at around 40°N.
- Pacific jet bias, which may be related to the use of equinoctial conditions since the jet here has a particularly sharp seasonal transition (Saulière *et al.*, 2012)

Other possible causes of these deficiencies are as follows: both extratropical and tropical SST anomalies and asymmetries have been shown to be important for forcing zonal asymmetries (Section 2.3.4) and neither are simulated here. Moreover, the model itself features biases such as the overly zonal North Atlantic jet even in its most realistic configuration and either coupled to a dynamic ocean or forced with fixed SSTs (Martin *et al.*, 2006).

However, the purpose of this study is to investigate the effects of ice addition on a state representative of the North Atlantic in winter, for which purposes the circulation simulated is adequate.

6.4 Symmetric Ice Addition

This section examines the effect of adding a symmetric polar ice cap to an asymmetric background state, by comparing experiment I65A to NOICEA. The similarities and differences between these results and those found in Chapter 5 for a symmetric background state are discussed.

Ice addition causes a reduction in local surface temperature relative to NOICEA (Figure 6.6b). This relative cooling reaches 25 K in magnitude near the pole. Unlike in the symmetric case, remote changes to the surface temperature are also possible, due to the presence of land in place of a fixed-temperature sea surface. As a result the surface meridional temperature gradient (not shown) is intensified across the ice edge, along the tilted eastern coastlines, and to a lesser extent throughout the continental interior. In NOICEA there was a sharp reverse temperature gradient across the land-sea boundary at 70°N due to the relatively warm ocean surface and cold land. This is reversed in I65A and the normal equator-to-pole temperature gradient is present across the boundary.

Figure 6.6c shows zonal mean temperature in I65A, and as an anomaly from NOICEA. Small but significant low level cooling relative to NOICEA extends south to 30° N, consistent with the cooling of the land surface. At the pole, the vertical structure of cooling in the troposphere is similar to that in I65-NOICE (symmetric; Figure 5.4d).

In the zonal mean, the addition of ice causes an increase in zonal wind speed on the poleward flank of the jet (Figure 6.7a, 50–80°N), and a smaller decrease on the equatorward flank, both through the depth of the troposphere. One consequence is that the low

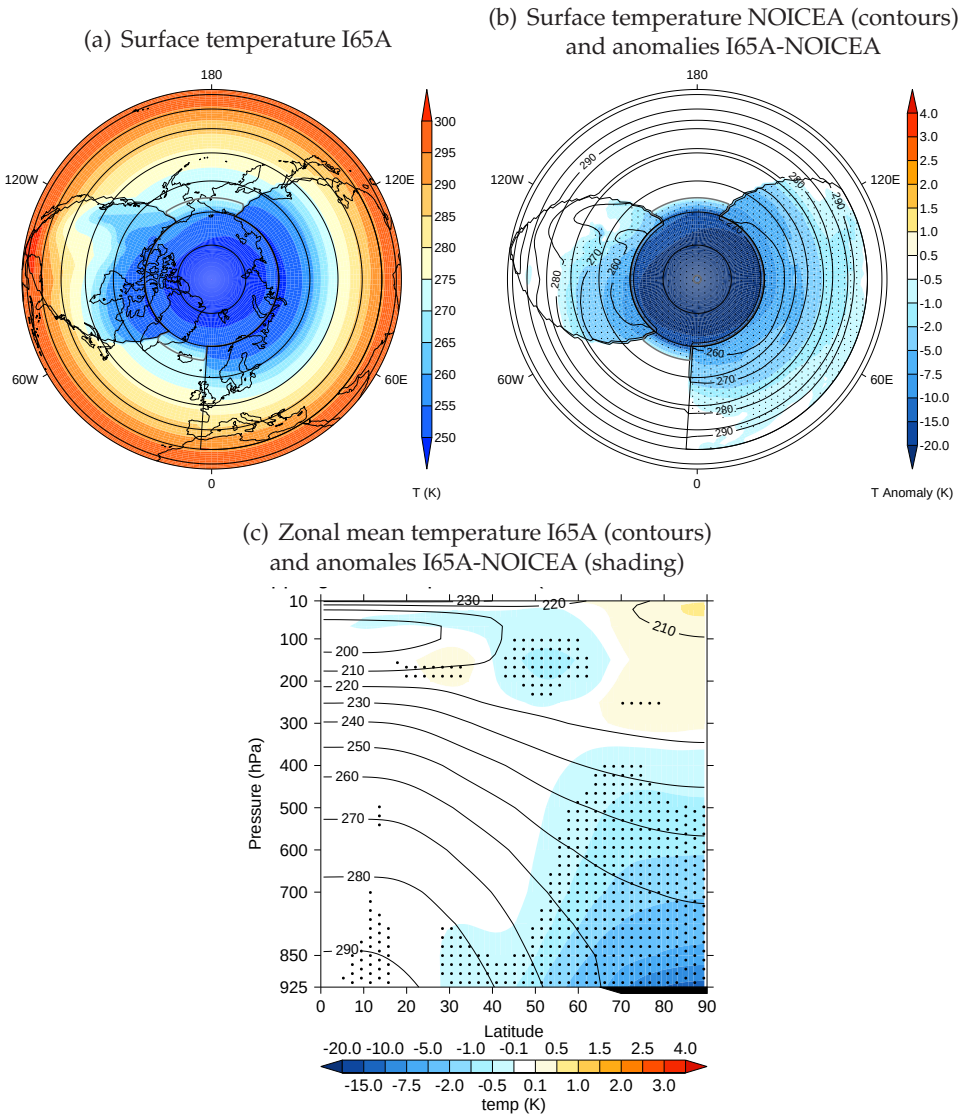

Figure 6.6: Temperature in I65A. a) Surface Temperature. b) Surface Temperature anomaly from NOICEA (shading), overlaid with the NOICEA surface temperature field (contours). c) Zonal mean temperature I65A full field (contours) and anomaly from NOICEA (shading). Stippling implies 95% significance in a student t-test.

level easterly region (72–90°N, below 700 hPa, Figure 6.7a) is contracted polewards and downwards. The increase in zonal wind is present at all longitudes but at both lower and upper levels it is strongest in the Atlantic sector between 65 and 70°N (Figure 6.7c,d; shading).

Given this asymmetry, Figure 6.7b) shows the I65A-NOICEA anomaly zonally averaged over the Atlantic sector only. The pattern is robust to different definition of the Atlantic sector. The greater high-latitude response magnitude in this sector, and the evidence of anomalies in the tropics, are even closer to what was seen in the aquaplanet

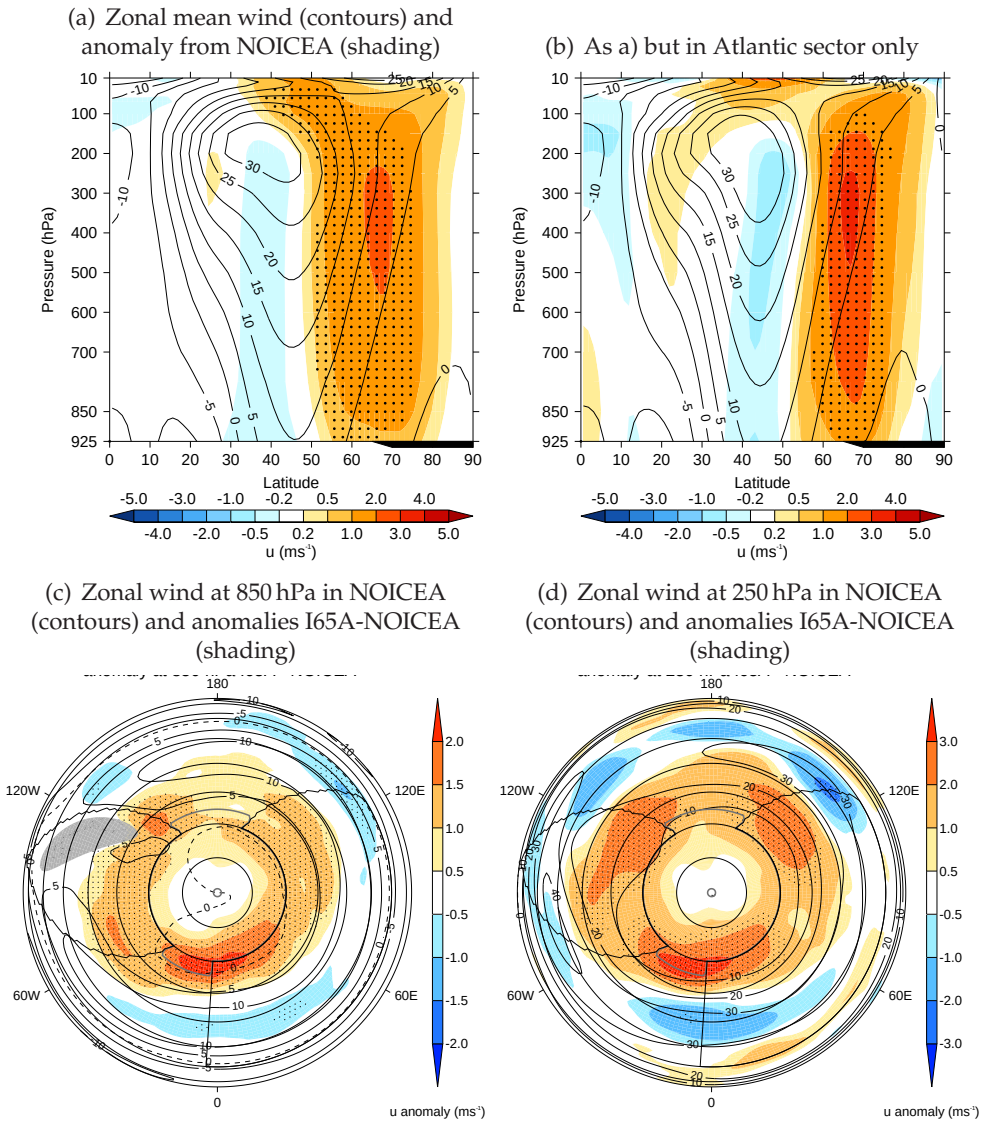

Figure 6.7: The response to symmetric ice addition; zonal wind in I65A. a) zonal-mean zonal wind in I65A (contours) and as an anomaly from NOICEA (shading); b) As a) but for Atlantic sector (60°W–0°E) only. c) Zonal wind at 850 in NOICEA (contours) and I65A-NOICEA anomaly (shading); d) as c) but at 250 hPa.

experiments (Figure 5.6d) than the full zonal-mean response in panel a. Further discussion of this comparison with the aquaplanet experiments is found in Section 6.4.3.

6.4.1 Storm tracks

Consistent with the surface forcing, the maximum meridional temperature gradient anomaly at 850 hPa is above the ice edge (Figure 6.8a). This gradient also strengthens between 50 and 60°N, especially over land. The low level (850 hPa) Eady growth rate is increased over most of the continents, and in particular over the ice edge (Figure 6.8b),

consistent with these gradient changes. Therefore it is likely that, as in the symmetric case, these are dominated by the temperature gradient rather than the static stability component which would act to decrease baroclinicity where the surface temperature is decreased.

The transient heat flux at 850 hPa (Figure 6.8c) is increased north of about 50°N at all longitudes. This is to the north of the NOICEA maximum. The largest increases are over the Atlantic ice edge at 65°N, near the Eurasian east coast at 60–65°N and over the North American east coast at 55–60°N although the significance of this last is uncertain. The 500 hPa geopotential height variance anomalies (Figure 6.8e) have the same structure. The upper level (250 hPa) transient momentum flux anomalies (Figure 6.8d) are again approximately a meridional dipole with increases on the poleward side of the NOICEA maximum and decreases in the core. The momentum flux anomalies however are weaker relative to the NOICEA variability as indicated by the low statistical significance of the results. Taken together, these variables give a consistent picture of increases poleward of the NOICEA maximum, consistent with the symmetric case. However, there is regional detail due to the storm track asymmetry and the response of the land surface, and the transient heat flux anomalies over the ice edge particularly in the Pacific are weaker than in the symmetric case (Figure 5.9e).

Over the ocean, the precipitation response is a decrease over the pole and an increase from approximately 50°N to the ice edge (Figure 6.8f). This is consistent with the response in the symmetric case, and again is due primarily to reduced convective precipitation over the ice, consistent with reduced moisture availability and increased stability, and increased large scale precipitation in midlatitudes. Over Eurasia, the I65A-NOICEA precipitation anomaly is negative. This is predominately large scale precipitation reduction, which is greatest around 60°E (not shown). Previous studies have linked exposure of the Arctic ocean moisture source to increased Eurasian snowfall (Liu *et al.*, 2012; Li and Wang, 2013; Deser *et al.*, 2010); the decrease in precipitation here in response to adding sea ice to the Arctic ocean is consistent with this hypothesis but is not investigated further.

6.4.2 Asymmetric streamfunction

The wave train generated by the Rocky mountains (ψ^* at 250 hPa) is weakened relative to NOICEA (Figure 6.9 a vs b). For example the anticyclone at 50°N 0°E is weakened.

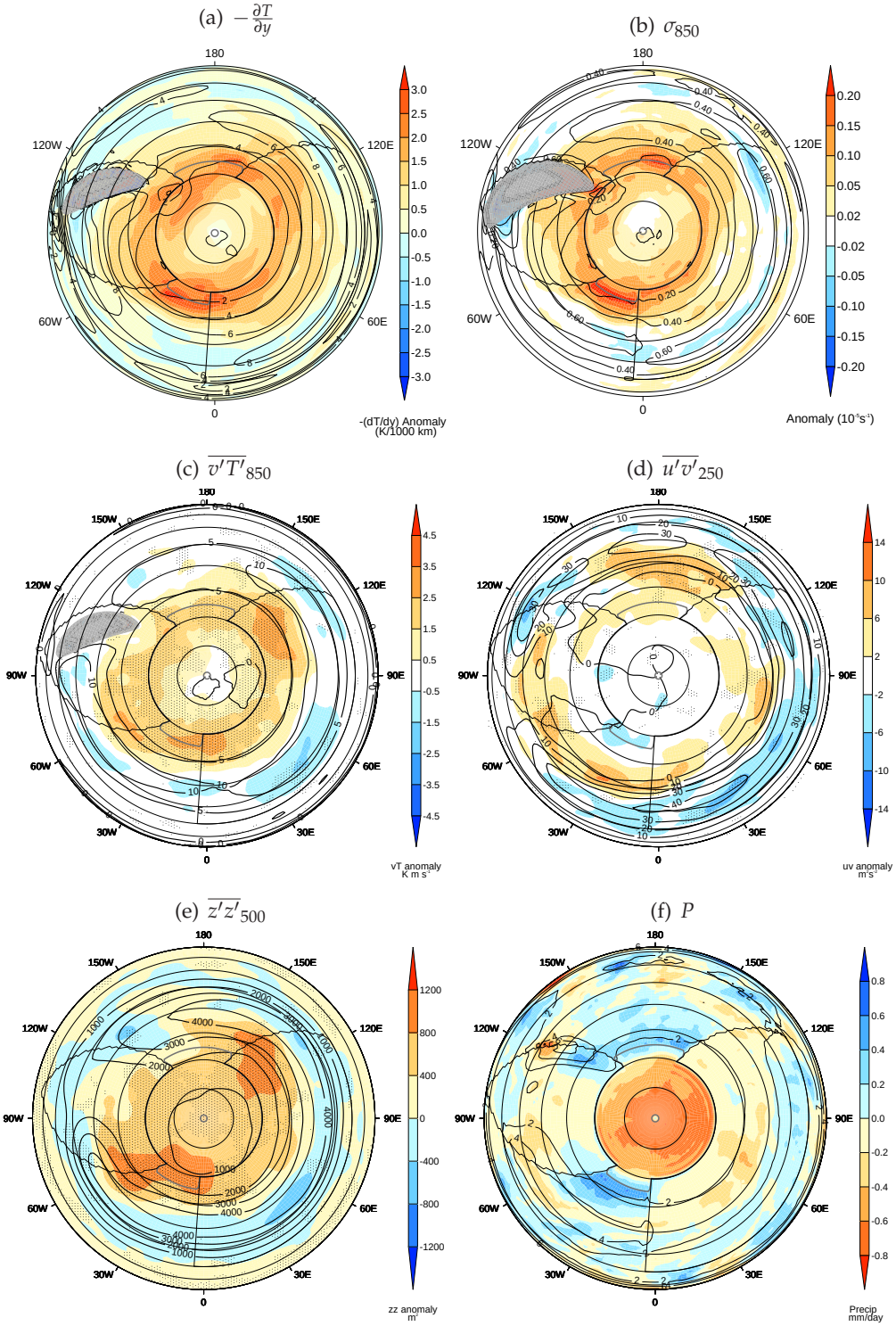

Figure 6.8: Anomalies, I65A-NOICEA. a) Minus the meridional temperature gradient (such that positive implies the normal equator-to-pole gradient) at 850 hPa b) Eady growth rate at 850 hPa c) Heat flux $\overline{v'T'}$, NOICEA (contours, interval 2 $K\,ms^{-1}$) and I65A-NOICEA (shading). d) Momentum flux $\overline{u'v'}$ at 250 hPa, NOICEA (contours, interval 10 m^2s^{-2}) and I65A-NOICEA (shading). e) Geopotential height variance at 500 hPa. f) Precipitation. In this and subsequent plots, the 'real world' continents are not shown.

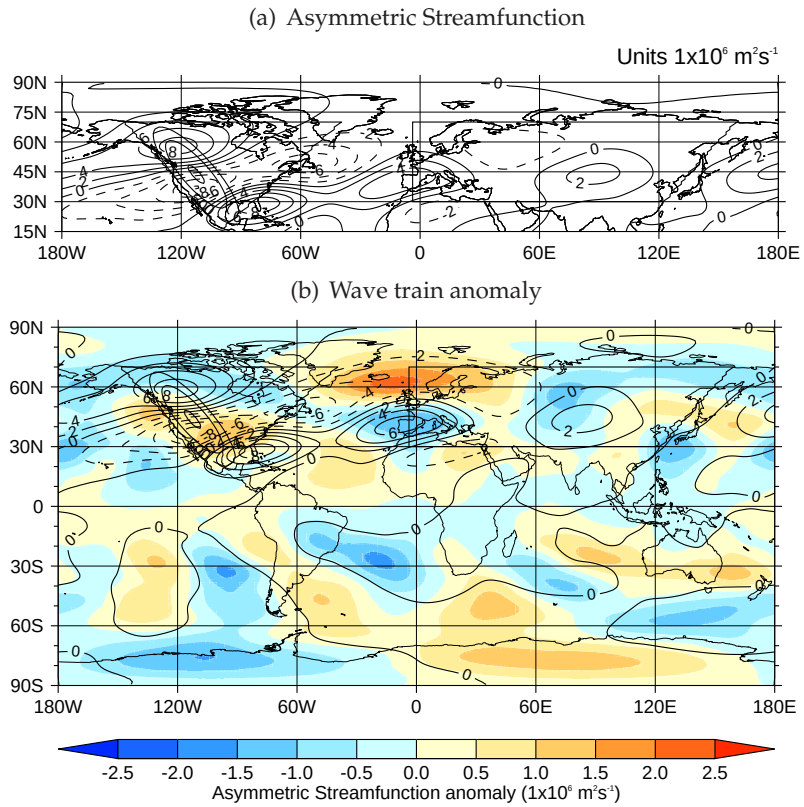

Figure 6.9: The upper level stationary waves in I65A. a) The asymmetric streamfunction ψ^* at 250 hPa in I65A; and b) in NOICEA (contours) and I65A-NOICEA (shading). All latitudes are shown in b) to demonstrate the magnitude of southern hemisphere anomalies and mean structure.

However the path of the waves appears to be unaltered. The reason for this is unclear. The incident Pacific jet north of 50°N is significantly increased by the ice addition (Figure 6.7b and c), a similar change to I65-NOICE, and for some longitudes the jet maximum is therefore shifted poleward. It is feasible that a more poleward jet would increase the importance of vertical deflection (over the poleward side of the Rockies) relative to horizontal deflection (over the equatorward side) but it is not clear how this would change the downstream magnitudes.

6.4.3 Comparison with symmetric case

In terms of forcing strength, I65A-NOICEA is most comparable to the I65-NOICE symmetric case. The ice area is slightly smaller in I65A than I65 because in the band 65–70°N there is land (not ocean/sea ice) at some longitudes. The maximum zonal mean zonal wind anomaly anywhere in the troposphere is 2.2 ms^{-1} (Figure 6.7a), which is slightly weaker than the maximum response in I65A-NOICEA (3 ms^{-1}; Figure 5.6d).

There is therefore not a large change in the magnitude of the response in I65A-NOICEA relative to I65-NOICE. However it is possible that this is the effect of competing factors, and so some possible hypotheses regarding influences of the background flow on the response are considered briefly.

Firstly, the I65A temperature response includes temperature reductions over the continents which are an indirect result of ice addition. For example, the surface temperature gradient across the North American-Atlantic coast is strengthened (not shown) and lower tropospheric temperature gradients are intensified over the continental interiors (Figure 6.8a), with corresponding increases in heat flux over the continents. Therefore the nature of the forcing is different in locality and magnitude (with more widespread cold anomalies) to that in the symmetric case.

As well as the different effective forcing, the atmospheric state into which the forcing is imposed differs. The zonal mean flow in the Atlantic is altered due to the upstream continent and orography, as discussed above. If either the latitude of the jet (in particular relative to the region where sea ice is added) or the level to which is it constrained are different in this experiment compared to the symmetric experiment one might expect a different response.

Figure 6.10 shows the jet latitude index in the Atlantic sector (60°W–0°E) and for an average over 60° longitude in the symmetric experiments. Focusing on the black lines (NOICE or NOICEA), it is clear that while the mean jet position in the symmetric case is further north, it also has a more symmetric distribution. The jet in the symmetric case has lower but non-zero frequency of occurence at high latitudes. Therefore there is not strong evidence that the jet is more constrained in the North Atlantic, although its variability is more confined to lower latitudes. The 'real world' north Atlantic jet has very different variability (Woollings *et al.*, 2010), with a northern regime where the jet in the eastern Atlantic is at around 60°N. It is possible that an ice edge at 65°N would have a different effect should such variability be present.

Therefore this experiment does not give a clear indication of the effect of the asymmetry on the response to ice, other than to localise the response in the region of the jet and storm tracks.

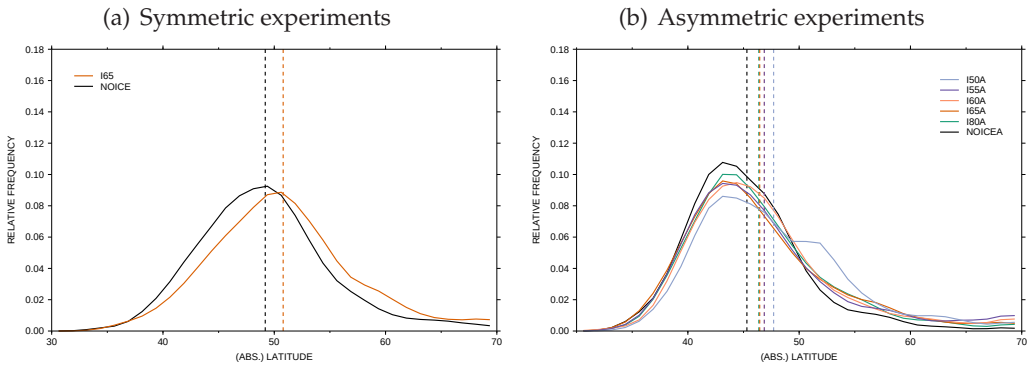

Figure 6.10: Jet Latitude Index, for levels 925–500 hPa, averaged over a 60° band in the symmetric SST1 experiments (a) and over the Atlantic 60–0°W in the asymmetric experiments. Other methodological details as in Chapters 3 and 5.

6.5 Response to Atlantic Ice Addition

In this section, further sea ice is added in the North Atlantic sector as far as 50°N (as was shown in Figure 6.1). The circulation response to this local ice addition is considered relative to I65A. The particular questions of interest are, is this response robust across the experiments and how does it compare with the results in chapter 5, what governs its magnitude and spatial extent, and is there any evidence of a Rossby wave response.

Since I65A is considered as the control case in these experiments it is helpful to recap its main features which, despite the anomalies introduced by symmetric ice addition, are similar to those of NOICEA. These are:-

- Large asymmetry in the surface temperature field, with strong meridional gradients across 65° N (a result of the ice edge) and the North America-Atlantic coast.
- Zonal localisation of the jet. The upper level maximum is in the West Atlantic, associated with a strong vertical wind shear, while the lower level maximum is in the East Atlantic.
- A stationary Rossby wave train emanating from the North American continent.

Figure 6.11 shows the zonal mean zonal wind averaged over the lower troposphere. As already discussed, the zonal mean zonal wind is weaker in the asymmetric than the symmetric experiments due in part to the effect of drag. The response to ice addition in midlatitudes (equatorward of 65°N) in the asymmetric experiments is qualitatively similar to that in the symmetric experiments, with an incremental increase in the zonal wind

as ice is added (Figure 6.11, a versus b). This is also true at 250 hPa (not shown). The response is much weaker in the asymmetric experiments. This is consistent with the weaker forcing, since ice is added in one sector only, such that the polar temperature anomalies are weaker; as shown in Chapter 5, a strong relationship exists in aquaplanet experiments between ice area, polar ice cap temperature and zonal wind anomalies. Examining the mean over the Atlantic only (Figure 6.11c) shows that this result does not hold universally; in particular the I55A-I65A response is weaker than the I60A-I65A response. This section examines the three responses I60A-I65A, I55A-I65A and I50A-I65A and seeks to understand this difference (including its statistical significance) and the spatial structure of the response.

(a) Zonal wind: symmetric experiments, all longitudes

(b) Zonal wind: asymmetric experiments, all longitudes

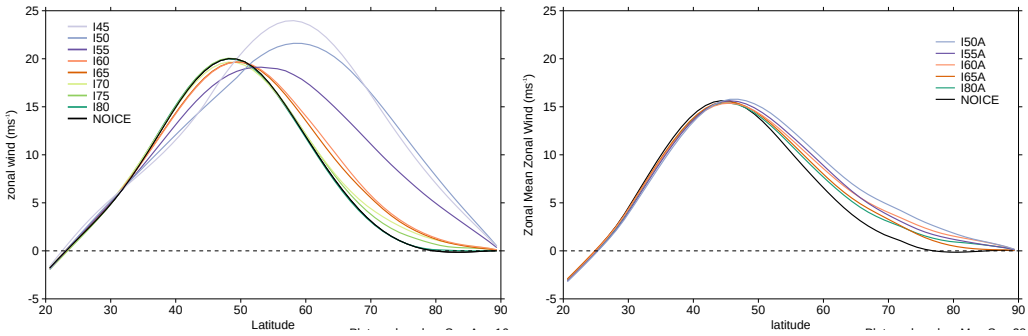

(c) Zonal wind: asymmetric experiments, Atlantic only

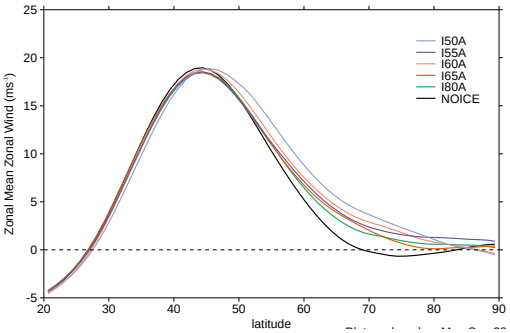

Figure 6.11: The low level (850–500 hPa average) zonal mean zonal wind. a) The symmetric experiments. b) The asymmetric experiments, all longitudes except those with orography. c) Asymmetric experiment, mean taken over Atlantic (60°W–0°E) only.

6.5.1 Spatial response

The surface temperature response to Atlantic sea ice addition (Figure 6.12a–c) is dominated in all cases by the local cold anomaly in the Atlantic ice-covered region. The magnitude of this anomaly reaches 17–20 K depending on the latitude to which ice is added.

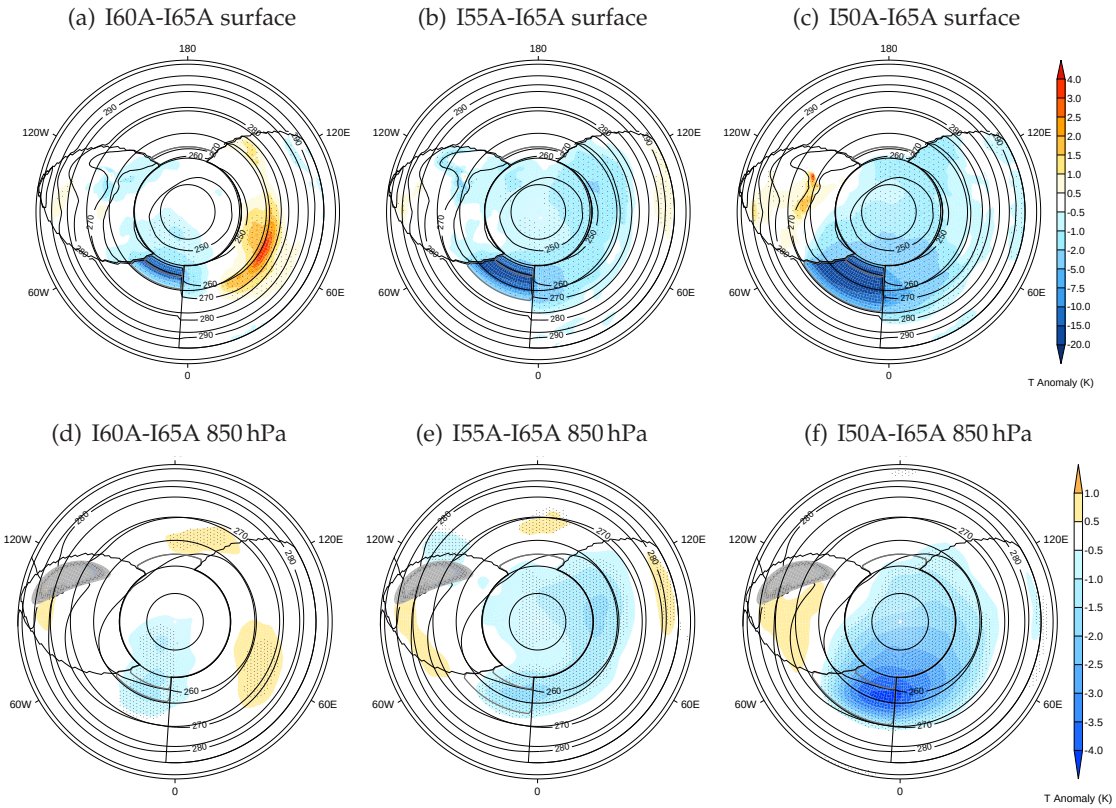

Figure 6.12: Surface (top) and 850 hPa (bottom) temperature anomalies from I65A for Atlantic ice addition experiments I60A, I55A and I50A. a) Surface temperature anomaly I60A-I65A (shading) and I65A temperature (contours). b) as a) but for I55A-I65A. c) as a) but for I50A-I60A. d)-f) as a)-c) but for 850 hPa.

This is accompanied by a small relative surface cooling over the whole sea ice area which, averaged over the polar cap, is less than 1.5 K (relative to I65A). The magnitude of this anomaly decreases across the Arctic basin away from the Atlantic (e.g. Figure 6.12a). In I60A-I65A the negative anomaly is significantly different from zero at the 95% level only in the Atlantic sector, in I55A it is significant across the Eurasian sector and in I50A it is significant across most of the Arctic ocean. The incremental polar cap cooling with increasing ice addition is consistent with the findings in Chapter 5, although it is much weaker here; the (symmetric) I50-I65 polar cap temperature anomaly was 10 K. Temperature anomalies at 850 hPa have the same structure as those at the surface (Figure 6.12d). However, the I55A-I60A temperature anomalies at 850 hPa are only locally significant, in a band around the Eurasian coast.

All three cases have reduced temperatures in north west Eurasia, immediately downstream of the region of ice addition. This is consistent with reduced warm advection due to the removal of the warm surface upstream. However, the response over the continents

otherwise differs between the cases. In I55A and I50A, there is significant cooling over all of Eurasia, which is largest at over 5 K in the north west and decreases away from this region (Figure 6.12b,c). In I60A, there is a statistically significant surface warming over Eurasia, centred on a band at 57°N and peaking at 4 K (Figure 6.12a).

The sharp northern bound of the Eurasian warm anomaly in I60A-I65A and the very low temperatures (e.g. for I65A, Figure 6.12 contours), suggest that this is related to snow cover. As discussed in section 6.2.5, there is a drift in deep snow depth through the experiments; however, at the latitudes being considered here, melt still occurs so there is no drift in ice depth or in the latitude of a given depth isoline (not shown). Because the thermal conductivity of snow is independent of depth once depth exceeds 0.5 m (Essery *et al.*, 2001), Figure 6.13 captures the temperature-relevant snow cover in I65A as the difference in the number of 'deep snow months' (where monthly-mean cover exceeds 0.5 m). As shown, the reduction in this value is directly aligned with the positive surface temperature anomaly shown by black contours.

Figure 6.13b shows that the precipitation increases here, so the process leading to less snow accumulation must be temperature rather than moisture dominated. As shown in 6.13c and consistent with expectation from the symmetric experiments, there is anomalously south westlerly flow here. Although the causality cannot be established in these experiments, these colocated anomalies suggests a mechanism whereby ice addition leads to anomalously southerly and westerly winds at approximately 55 to 60 °N. In I60A, the upstream region is still open ocean at these latitudes, so there is an increase in warm advection due to the wind anomaly. This leads to snow melt and since this is a region of little snow accumulation, there are more days with little or no lying snow. It is possible that this leads to a feedback since this lack of deep snow leads to a change in the surface heat fluxes, causing reinforcement of the temperature anomaly. Since the snow behaviour in general in these experiments is not very realistic, due in particular to the lack of seasonal cycle, this temperature anomaly is probably not a fundamental feature of the climate response to Atlantic sea ice anomalies, although aspects of these processes may be relevant.

At 500 hPa the temperature response is small ($<$1 K everywhere; not shown). In I60A, the anomalies have the same sign as those at 850 hPa. For I55A, there is a warm anomaly across the Atlantic, in contrast to low levels, but no anomalies at this level are significant

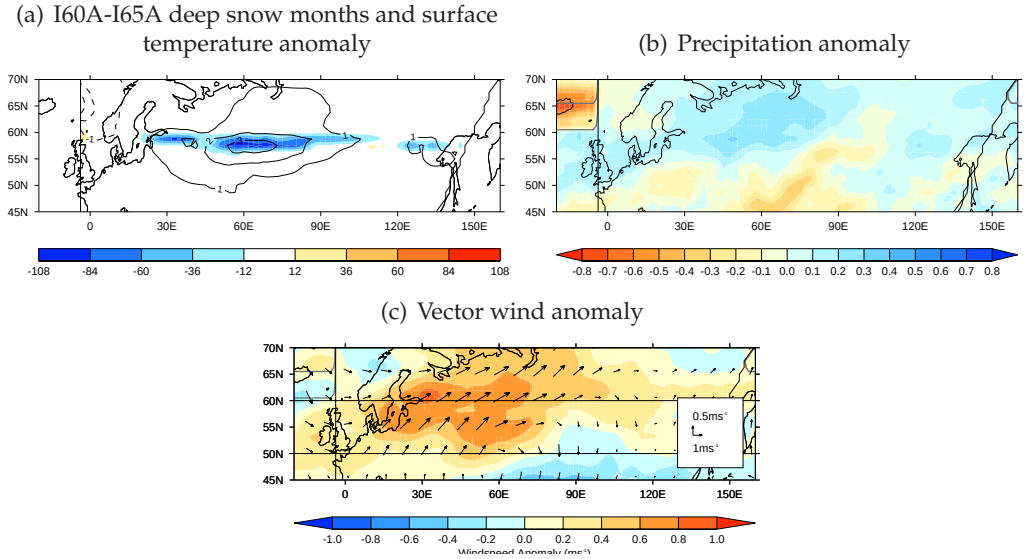

Figure 6.13: a) The difference in number of 'deep snow months' (monthly mean snow deeper than 0.5 m; shading) and the surface temperature anomaly (contours, dashed negative), I60A-I65A. b) The precipitation anomaly, mm day^{-1}. c) The vector wind and windspeed anomaly. u and v components of vector are differently scaled for arrow length.

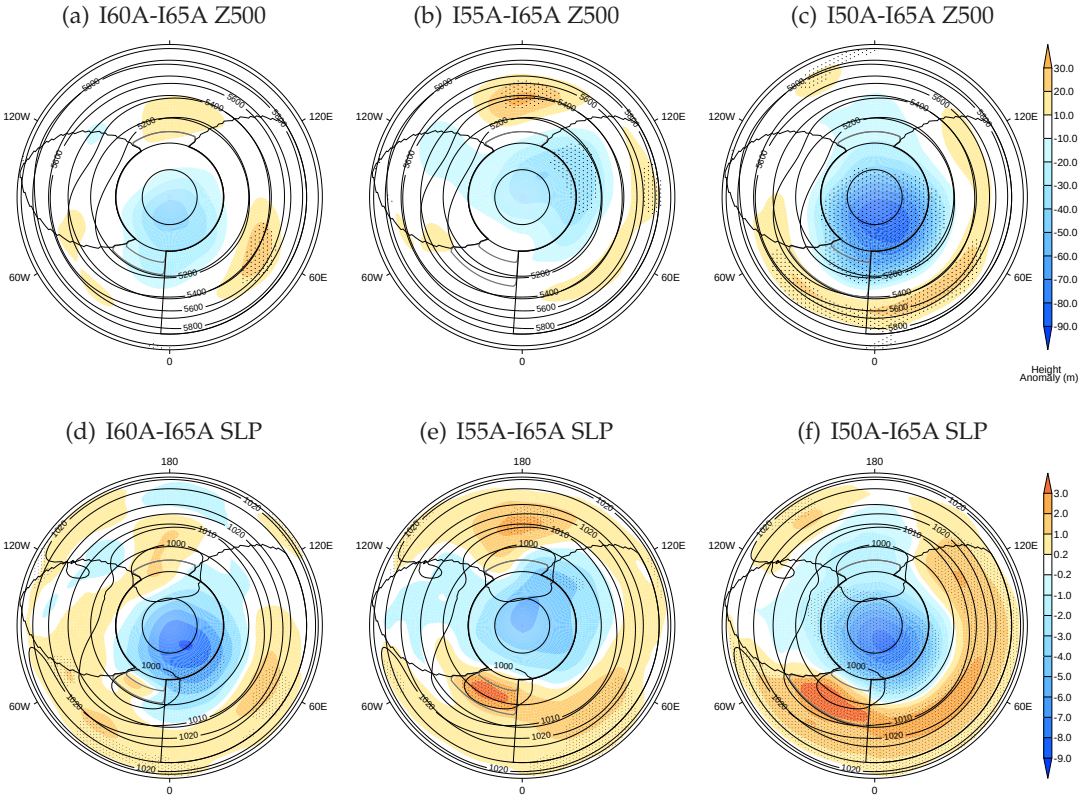

Figure 6.14: 500 hPa geopotential height Z500 (top) and sea level pressure SLP (bottom) anomalies from I65A for Atlantic ice addition experiments I60A, I55A and I50A. a) Z500 anomaly I60A-I65A (shading) and I65A Z500 (contours; m). b) as a) but for I55A-I65A. c) as a) but for I50A-I60A. d)-f) as a)-c) but for SLP (hPa).

at the 95% level. In I50A, on the other hand, the Atlantic response is of significant warming from 40–50°N and cooling from 60–70°N. This I50A behaviour is consistent with the response in the symmetric case, where for STRONG ice addition experiments there was a dome of cold anomalies over the pole, and warm anomalies in midlatitudes associated with changes in the Ferrel cell. The emerging picture is therefore that I50A fits the paradigm established for the MODERATE to STRONG responses in the symmetric case. On the other hand, I60A and I55A, while having elements of this response, are weaker (consistent with the weak forcing) and have local features particular to the configuration (e.g. the I60A Eurasian warm anomaly).

The geopotential height response at 500 hPa (Figure 6.14) has a very similar structure to that for 500 hPa temperature, with positive 500 hPa temperature anomalies in general being associated with positive geopotential anomalies. In both I60A and I55A, the anomaly is small and only significant in very localised regions (Figure 6.14 d and e) either in the Eurasian or Pacific sectors. In I50A on the other hand the geopotential response is a large scale dipole, with low pressure centred over the ice anomaly and Atlantic sector of the Arctic, and a high pressure between 30 and 50 °N.

The sea level pressure response (Figure 6.14) is a positive anomaly over the region of added sea ice. Elsewhere, the response is equivalent barotropic (i.e., has the same sign at the surface and in the mid troposphere). The classic linear response to surface *heating* is a downstream *low* and upper level *high*; since the sea ice addition is a surface cooling, the opposite might be expected. The sign of the anomalies is therefore consistent with this picture, although the anomaly in Figure 6.14 appears to be colocated with the ice edge.

The dominant feature in the zonal wind response (Figure 6.15) is a robust change in the zonal wind over Eurasia. The response is an increase north of approximately 50° and therefore an increase on the poleward jet flank, as expected from the zonal mean response in these experiments. In I60A, the anomaly is present over the Atlantic and as far as 90°E (Figure 6.15a,d); in I55A, it is present downstream only (Figure 6.15c,e). The local zonal wind responses in both these experiments are consistent with a thermal wind balance argument based on the low level temperature anomalies shown above, namely the warm anomaly at 57°N in I60A and the east Eurasian warming at 35°N in I55A. In I50A the zonal wind response is part of a mostly annular shift that is evident across the hemisphere (Figure 6.15c,f), but largest in the east Atlantic and western Eurasia. The

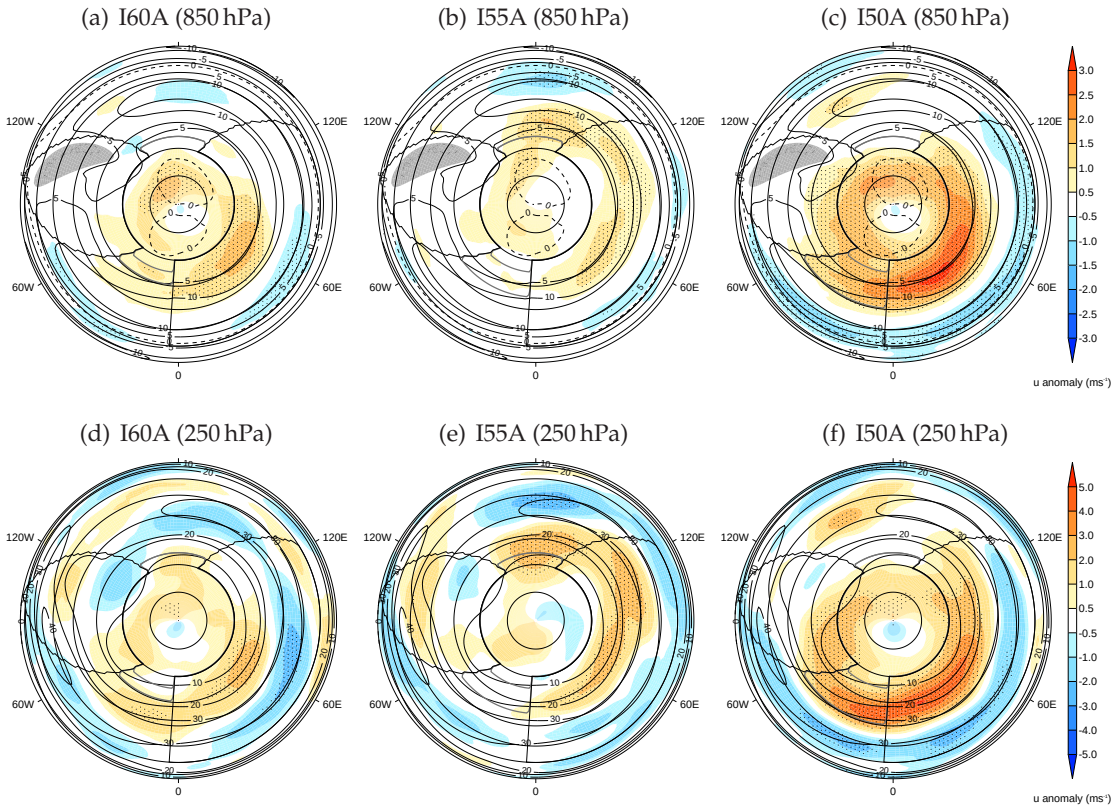

Figure 6.15: Zonal wind anomaly at 850 hPa (top, shading) and 250 hPa (bottom, shading) relative to I65A (contours) for the Atlantic ice addition experiments. Stippling indicates significance at the 95% level.

anomaly structure is equivalent barotropic. There is also an increase in zonal wind across the Arctic ocean.

The magnitude of the zonal wind responses is similar in I60A and I55A and much larger in I50A. Both the I60A and I50A experiments feature an anomaly at the longitudes of and immediately downstream of ice addition.

6.5.1.1 Storm tracks and transient fluxes

To shed light on the different responses, this section considers the storm track and eddy feedback anomalies in I60A, I55A and I50A.

The response of the near-surface baroclinicity σ_{850} is largest in the Atlantic sector, with maximum reductions and increases corresponding to the enforced change in ice edge (Figure 6.16). All three ice addition experiments also have an increase in baroclinicity in the Pacific between 60°N and 70°N. Although no ice has been added here this is consistent with the decrease in temperature of the polar cap, and therefore strength-

ened temperature gradients, at 850 hPa (as was shown in Figure 6.12). Over Eurasia, the I60A response is a reduction of the maximum baroclinicity, between 40 and 50°N (Figure 6.16a). This is consistent with a reduction of the temperature gradient due to the large low-level warm anomaly to the north. In I55A and I50A, in contrast, the response resembles a north-south dipole with increased baroclinicity to the north, consistent with the widespread cooling and strengthened temperature gradient at 850 hPa.

In all three experiments, there is an increase (statistically significant at the 95% level) in the transient heat fluxes near the location of the imposed ice edge and further increases downstream over Eurasia (Figure 6.17). There is also evidence of a small decrease at lower latitudes (around 40°N). In all cases the Atlantic anomaly corresponds to a poleward shift of the maximum relative to I65A, and in I50A this corresponds to an alignment of the heat flux along the ice edge.

All experiments also have an increase in the poleward momentum flux (Figure 6.18) from 50 to 60°N in the east Atlantic and over Eurasia, corresponding to an increase on the poleward flank of the control maximum. However, statistical significance of this measure at the 95% level is patchy and localised. The combined tendencies of the mean zonal wind suggested by the transient and momentum flux anomalies are shown by the E-vector (Figure 6.19). As already discussed, the heat flux anomaly is characterised by a band of increases from approximately 50°N to 70°N, although the southern limit of this bands varies between the experiments. I50A and I60A both have bands of increases in the upper level divergence (50–70°N, and 40–50°N in the Pacific) co-located with the zonal wind anomalies (Figure 6.15) at both levels. This is consistent with these anomalies forcing an anomalous deep acceleration of the flow.

In contrast, in I55A there is no increase in the upper level divergence between 30°W and 30°E (Figure 6.19c)- a fact which is consistent with the lack of zonal wind response in the Atlantic in I55A. Instead, the largest positive anomalies are off the North American coast at around 40°N, and from 90–150°E and over the Pacific. These differences in the anomalies are clear, yet there is not an equivalent obvious difference in the low level heat flux anomalies. This could suggest a hypothesis whereby, in the I55A case, there is interaction of the flow with the stationary wave in the Atlantic, resulting in a lack of response in the transients. However, again given the small forcing and response, such an explanation may not be needed to explain the differing responses; further investigation

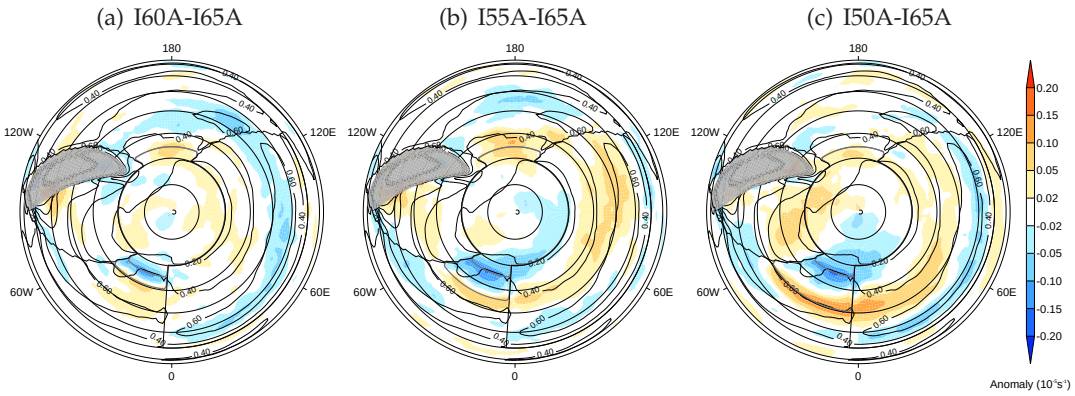

Figure 6.16: Eady growth rate σ_{BI} at 850 hPa. a) I65A (contours) and I60A-I65A (shading). b) As a, but I55A-I65A anomalies. c) As a, but I50A-I65A anomalies. Orography over 500 m is greyed out.

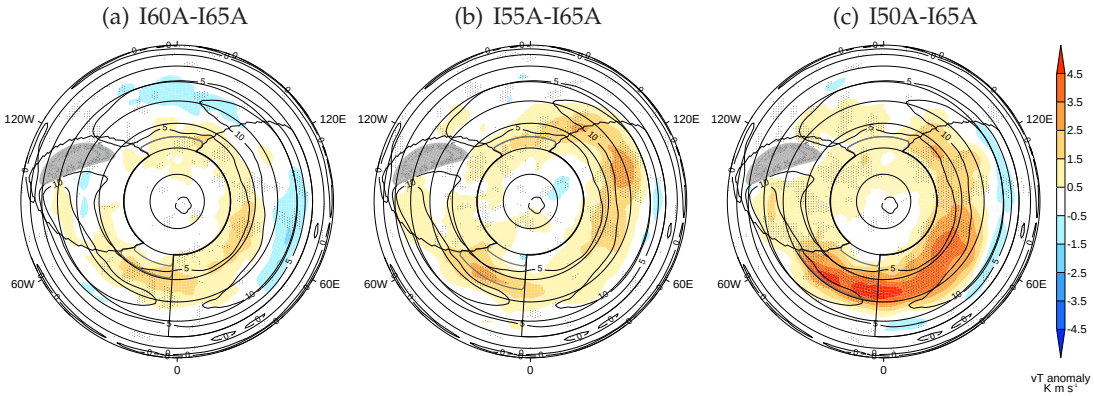

Figure 6.17: Transient heat flux $\overline{v'T'}$ (2–6 day band pass filter) at 850 hPa. a) I65A (contours) and I60A-I65A (shading). b) As a, but I55A-I65A anomalies. c) As a, but I50A-I65A anomalies. Stippling indicates significance at the 95% level according to the non parametric WMW rank-sum test for equivalence of location (details in Section 3.5).

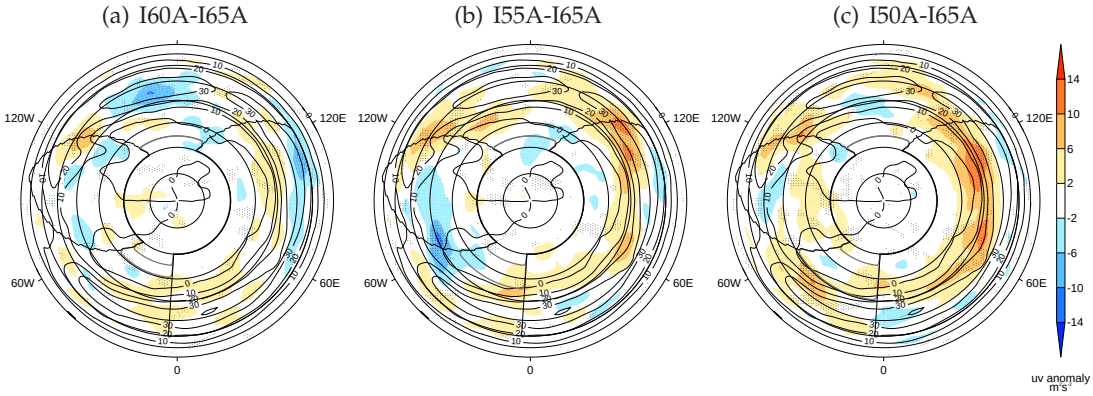

Figure 6.18: Transient momentum flux $\overline{u'v'}$ (2–6 day band pass filter) at 850 hPa. a) I65A (contours) and I60A-I65A (shading). b) As a, but I55A-I65A anomalies. c) As a, but I50A-I65A anomalies. Stippling as in 6.17.

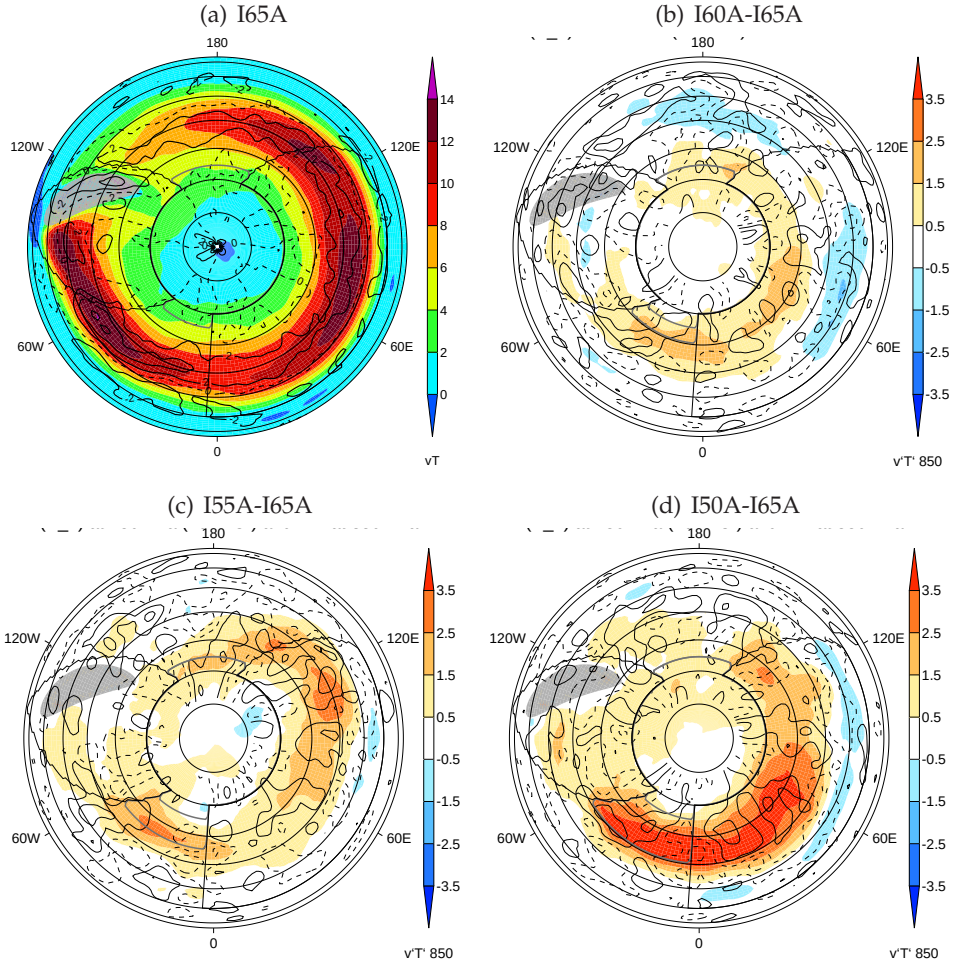

Figure 6.19: E-vector **E** due to synoptic (2–6 day band pass filter) fluxes. a) Low level (850 hPa) heat flux (shading) and upper-level (250 hPa) horizontal divergence (contours). The contour interval for upper level divergence is 2E-5 ms^{-2}; the zero contour is dashed. b) Anomalous heat flux (shading) and horizontal divergence (contours) I60A-I65A. Upper level contours are plotted at (-1.5),(-0.5) (0.5) and (1.5) x$10^{-5}ms^{-2}$ c) As b but for I55A-I65A. d) As b but for I50A-I65A. A boxcar filter is applied over three grid points in each direction (approximately 6°x4°) in order to smooth the plotted field for ease of legibility.

would be required to discover whether this were the case.

6.5.2 Stationary waves

The asymmetric streamfunction response (Figure 6.20) provides little evidence of a consistent response to the ice Atlantic addition, for the following reasons:-

- the peaks and troughs established by the Rocky mountains (e.g. 6.20a) do not move, suggesting the ice does not alter the path of existing stationary waves;
- the magnitudes of these wave peaks and troughs change in the opposite sense for

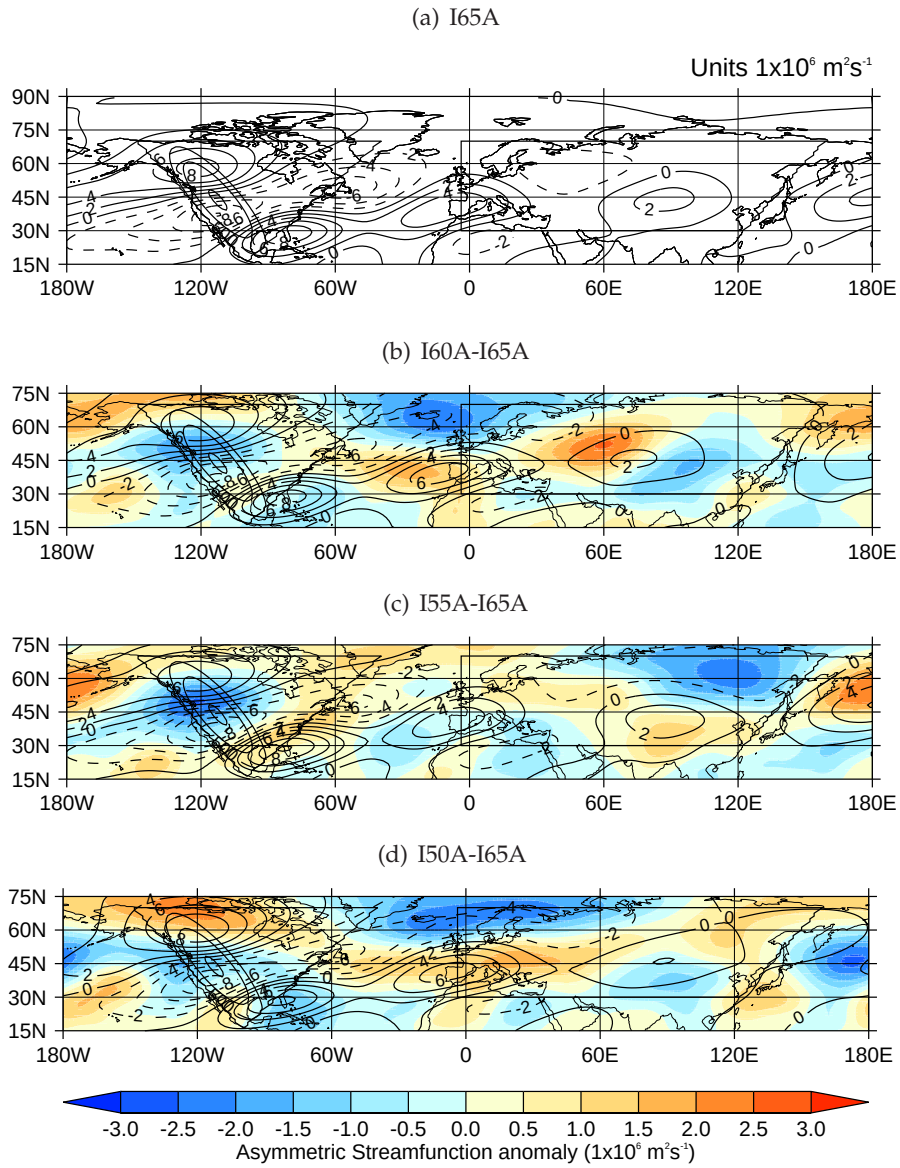

Figure 6.20: Asymmetric streamfunction ψ^* at 250 hPa. a) I65A. b) I60A-I65A anomaly (shading) and I60A (contours). b) as a but for I55A. c) as a but for I50A.

I55A to that in I50A and I60A (e.g. the East Atlantic);

- the anomaly magnitudes away from the orography itself are in general comparable to those in symmetric runs or in the SH (not shown) and lack spatial coherence; in particular there is no pattern indicative of propagation from the North Atlantic, where the ice addition has been imposed;

- the large anomalies over Eurasia in I60A are consistent with the deep warming at approximately 57°N which has been discussed above and is likely to be at least partially a remnant of the model configuration.

6.6 Synthesis and Comparison to Symmetric Case

The discussion of the previous section has established that, when local ice anomalies are imposed in the Atlantic in an asymmetric framework:-

- For the largest forcing considered (I50A-I65A), the response (positive zonal wind anomalies on the poleward jet flank) is qualitatively similar to the response to zonal mean ice addition in an aquaplanet.
- For weaker forcings, there are still elements of this response, but it is much weaker and there are regional variations.

One of the results established in Chapter 5 linked the polar cap (>70°N) temperature anomaly to the magnitude of the response. This large scale idea would imply a much smaller zonal wind response in these experiments given the much smaller polar temperature anomaly. If it were the magnitude of the temperature anomaly itself determining the response magnitude, then the I55A zonal wind response would still be expected to be larger than the I60A response, which it is not. However, neither is the I55A response significantly smaller than the I60A response over most of the region (not shown). There is therefore an outstanding question regarding the extent to which these responses are set by the large scale temperature structure, or by the local anomalies associated with the ice edge, and the relevance of interaction with the mean flow.

6.7 Response to Atlantic Ice Removal

While the above has focused on ice addition in the Atlantic, an ice removal experiment was also conducted where ice was removed to 80°N (Figure 6.1) in the Atlantic half of the Arctic basin. This section assesses the response to this perturbation; all anomalies are expressed relative to I65A.

As expected, the removal of ice causes local increases in surface temperature of over 20 K as the surface reverts to the specified SST value (Figure 6.21). The increases in surface T are also widespread across the continental areas. Significant warming at 850 hPa is similarly widespread with a maximum anomaly of 5 K over the ice removal area (not shown), and significant warming in more localised regions extends to the mid tropo-

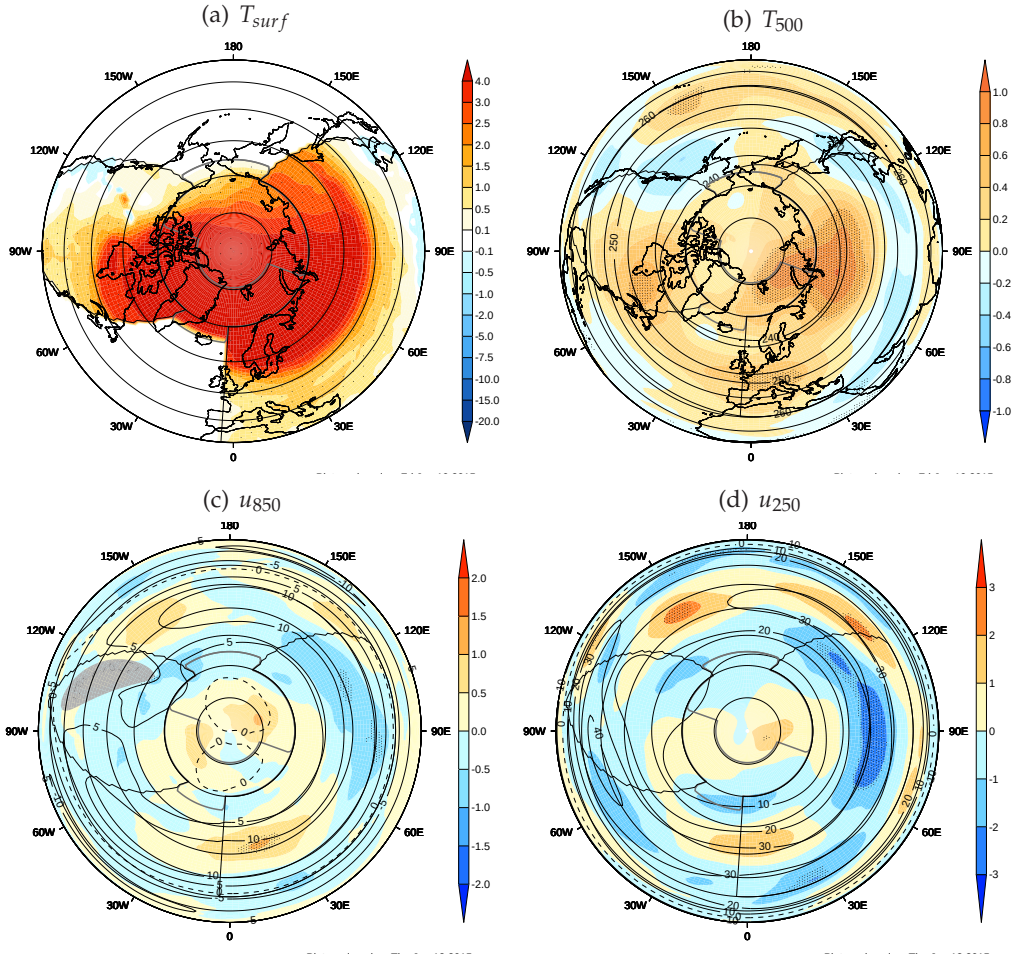

Figure 6.21: The response to ice removal in the Atlantic; anomalies I80A-I65A. (a) Surface temperature. (b) Temperature at 500 hPa. (c) zonal wind at 850 hPa. (d) zonal wind at 250 hPa.

sphere (Figure 6.21b). This mid level warming corresponds to a high pressure anomaly at 60–120 E and 50–70 N (not shown).

Figure 6.21c and d show the zonal wind response at both 850 hPa and 250 hPa. The response is roughly equivalent barotropic (the structure is the same at both levels). However, it is small everywhere and only significant at the 95% level in very localised regions in West Europe, East Eurasia and, at 250 hPa, the Pacific. In Western Europe the response is a poleward shift or contraction, which is perhaps surprising since the response to ice addition was also a poleward shift (e.g. Figure 6.15). This suggests that the response is nonlinear in the ice extent. However, given the small response magnitude and low statistical significance, it is likely that this response is dominated by noise and a longer run would be needed to establish if a robust response is present. Moreover, the spatial nature of the ice forcing and the temperature response to it is very different in I80A to that in the earlier experiments.

Due to the low significance discussed above, this experiment is not discussed in great detail. However, it should be noted that the strongest and most significant response is the weakening zonal wind in East Eurasia. This is consistent (via thermal wind balance) with the strong weakening of the meridional temperature gradient, which is a direct response to the ice removal. Moreover, this reduction in temperature gradient causes reduction in continental baroclinicity and transient heat flux, and a downstream reduction in transient momentum flux. However, while this is a self-consistent set of eddy feedbacks it should be noted that the strength of storm activity found here over the Eurasian continent seems highly unrealistic.

6.8 Summary and Conclusions

In this chapter, ice addition experiments have been performed in an AGCM with idealised lower boundary conditions representing two Northern Hemisphere continents and the Rocky mountains. These boundary conditions are very similar to those used in previous studies (Brayshaw *et al.*, 2009; Saulière *et al.*, 2012) where they were shown to reproduce features of the northern hemisphere circulation. In particular, this setup simulates zonal asymmetries of the storm track and jet, a small south west-north east tilt of the jet in the North Atlantic, and a Rossby wave train propagating from the orography.

In an experiment with zonally symmetric sea ice added to 65°N (except where restricted by continents) the jet stream response is to first order an increase on the its poleward flank, peaking between 60 and 70°N. This response is consistent with, but slightly weaker than, the closest equivalent symmetric experiment (I65-NOICE). Further experiments, with ice addition or removal in the Atlantic only, also give a robust response in the zonal mean, with experiments with more sea ice having greater wind speeds on the poleward flank of the jet. There is also an increase on the poleward flank of the jet immediately downstream of the Atlantic ice addition in all cases. There is a progression in the response and some evidence again of nonlinearity, with the response to ice addition to 50°N being much stronger than for weaker forcings.

However, the asymmetric component of the response to local Atlantic ice addition is harder to interpret. There are differences in sign in the temperature response over Eurasia, which may well be an artefact of details of the model configuration. For two

of the forcings considered, the main zonal wind response is downstream of ice addition over Eurasia, but is generally still on the poleward flank of the unperturbed jet. There is little evidence of a Rossby wave response to the Atlantic ice addition.

The responses to local ice addition either in the zonal or regional mean are smaller than in the symmetric case. It is possible that the forcing in the two weaker local ice addition cases (to 60° and 55°) is simply too weak to cause a large-scale response, and that the flow anomalies seen in these cases are primarily driven by secondary remote temperature anomalies.

On the other hand, elements of this configuration may limit its ability to represent the real world response to sea ice anomalies. In particular the jet in the East Atlantic is insufficiently far north; equivalently the jet is too zonal. If the storm track proximity to the ice edge is important, this would limit the ability of the model to respond. There is scope for careful design of future experiments using known elements which increase the jet realism in the Atlantic. For example, zonally symmetric SSTs have been used in this thesis which is not an accurate representation of the winter North Atlantic; either more realistic fixed SSTs or a 'slab' ocean in which SSTs are able to change would form the basis for appropriate future experiments.

In Chapter 5, the possible implications for palaeoclimate were discussed. The experiments in this chapter are arguably even more relevant since they feature a zonally localised storm track. The movement of the storm track (band-pass filtered $\overline{v'T'}$ at 850 hPa, Figure 6.17, and $\overline{z'z'}$ at 500 hPa, not shown) to along the ice edge in the I50A experiment is consistent with findings of Kageyama et al (1999) and Dong and Valdes (1999) for the last glacial maximum, in modelling experiments conducted under PMIP.

Chapter 7

Conclusions

7.1 Overview

There is rapid ongoing change in the Arctic, with large negative trends in sea ice and rapid warming of the surface and lower atmosphere observed in recent decades and projected to continue under greenhouse gas forcing (Stroeve *et al.*, 2012a). This raises the question of whether, how, and how much, sea ice loss or the amplified surface warming may affect the climate of midlatitudes. One particular question regards the effect of Arctic change on jet and storm track dynamics in the North Atlantic, with conflicting results having been found for example in AGCM modelling studies.

This thesis has examined mechanisms through which Arctic change has the potential to impact the climate of midlatitudes, addressing the following questions:-

1. To what extent does thermal advection contribute to projections of 21st century temperature variability in coupled climate models?
2. What is the atmospheric response to sea ice removal? In particular what is the response of the eddy-driven jet, including its mean, variability and spatial heterogeneity?
3. What determines the nature and magnitude of the jet response to sea ice forcing?

Question 1 has been addressed in state of the art coupled climate models (Chapter 4). For questions 2 and 3, experiments were conducted in idealised configurations of an AGCM.

7.2 Answers to research questions

1. To what extent does thermal advection contribute to projections of 21st century temperature variability in coupled climate models? (Chapter 4)

Analysis of monthly surface temperatures in a single model, initial condition ensemble (ESSENCE) and the CMIP5 archive demonstrates that there is a clear spatial pattern and

seasonality in the projected changes of the standard deviation of monthly surface air temperature. This can be summarised as, in winter, a decrease in temperature variability in midlatitudes and an increase in high latitudes and the tropics and, in summer, an increase over most land areas and the tropics and a decrease over high latitude oceans.

In a single model ensemble, a simple metric of atmospheric thermal advection was found to explain over 50% of 20^{th} century monthly temperature variability in widespread areas in winter. The following hypothesis was investigated: given future change in surface temperature gradients due to Arctic amplification and greater warming over land than ocean, unchanged circulation patterns would contribute to different temperature anomalies and therefore changed temperature variance. In support of this hypothesis a relatively simple regression model, taking account only of changes in mean meridional and zonal temperature gradients, was able to reproduce many aspects of the spatial pattern of change in both seasons. Crucially, these changes in variability, linked to the robust feature of heterogenous mean-state surface warming, can be treated with added confidence due to the underlying physical understanding.

Over large regions of Europe and North America in winter the advection could account for over half of the projected decrease in temperature variability. These results are consistent with results in the literature suggesting relationships between variability and zonal gradients (de Vries *et al.*, 2012, for Europe) or Arctic amplification (Screen, 2014; Schneider *et al.*, 2015). However, this study goes further than these previous studies in examining the whole globe and both zonal and meridional gradient changes, and in linking a projected change to this specific mechanism. The study explicitly recreates future changes in variability using changed temperature gradients, which no previous study has done. Thermal advection is found to be important for projected changes in Alaska, western Canada, Europe, south Australia, and subpolar oceans in winter.

The contribution of changing temperature gradients to variability change is weaker in summer than in winter. It still amounts to several tens of percent over large regions, such as parts of Australia, Europe, subtropical land areas, and off the Arctic coast. However, the change induced by the thermal advection mechanism is, in most areas, less than 50% of the whole. This smaller role is consistent with studies showing that land surface and radiative processes, for example, soil moisture changes, are dominant in summer (e.g. Fischer *et al.*, 2012, for Europe).

The importance of the thermal advection mechanism found above has important implications for understanding the impacts of circulation variability in the future: the results suggest there would be changes in the relationships between circulation and temperature anomalies, as found in Goubanova *et al.* (2010) and Masato *et al.* (2014). For example, the familiar temperature impacts of given circulation regimes such as the cold weather found in northern Europe in the negative phase of the North Atlantic Oscillation may become less severe in winter due to reduced temperature gradients (Cattiaux *et al.*, 2010; Osborn, 2011; Masato *et al.*, 2014; Dong *et al.*, 2011). The conclusion that temperature gradient changes are more important than circulation changes for future variability change are also consistent with the results of Cattiaux *et al.* (2012) that changes in circulation are not the dominant driver of projected future changes in interannual temperature variability.

Implications for extremes

The investigation of temperature variability is partly motivated by the possible effect of changes in variability on extremes (e.g. Schär *et al.*, 2004). This is particularly of interest for midlatitude land areas, where large populations may be exposed to temperature extremes and where the thermal advection mechanism is relevant. The consequences for extremes have not been explicitly discussed in this thesis. However, all other things being equal (i.e., the form and higher order statistical properties of the temperature distribution remaining the same):-

- A decrease in variance of winter monthly temperatures, combined with an increase in mean temperature, would reduce the frequency of cold extremes (the distribution shifts towards warmer temperatures, but narrows)
- The effect on mild winters is unclear since, independently, the increase in mean would increase their frequency and a decrease in variance would decrease their frequency; the changes therefore happen in the opposite sense
- An increase in variance of summer monthly temperatures, combined with an increase in mean temperature, would increase the frequency of warm extremes.

It is challenging to compare these results with existing literature on extremes, which generally focuses on shorter periods of days to weeks. An increase in extreme hot days Fischer and Schär (2009) and decreases in cold spells (de Vries *et al.*, 2012; Peings *et al.*, 2012)

has been projected, consistent with the bullet points above. Moreover, Screen (2014) have more explicitly investigated the relationship between reduced severity of extreme cold days in winter and thermal advection, in both the recent past and future; they found, for autumn and winter, that northerly wind days become less anomalously cold in future.

2. What is the atmospheric response to sea ice removal? In particular what is the response of the eddy driven jet, including its mean and variability, and what is the zonal structure of the response? (Chapter 5 and 6)

All the experiments presented here provide evidence for the hypothesis that increased sea ice over the pole and extending into midlatitudes causes an increase in wind speed on the poleward flank of the eddy driven jet. This adds to the growing body of evidence which suggests that sea ice can influence the jet (e.g. Barnes and Screen, 2015). However, a crucial finding in the context of recent and current sea ice and climate is the magnitude of the response. For sea ice extents in the range relevant to the 20^{th} and 21^{st} centuries, i.e., with a minimum ice latitude at or poleward of 70°N, the response does not cause the mean eddy driven jet to shift poleward.

In an aquaplanet model, the zonal wind response to ice addition projects onto the positive phase of the first zonal wind EOF, except in one experiment with ice to 80° where the zonal wind anomalies are not significant. This change is qualitatively consistent with the majority of model results to date which find a negative NAO response to ice removal (Budikova, 2009). Again however, for extents relevant to the present day, this projection is weak and most of the response is separate from the EOF structure. There is therefore some discrepancy with the oft-reported 'negative NAO' response to recent past or projected autumn and winter sea ice anomalies. In some of these cases, the explanation may be very simple; the projection onto the mode of variability is not quantified but simply used as a helpful description given the broad similarity between the response and the annular mode, whereas the projection strength may be weak.

There may be true physical differences between the response in the configuration here and more realistic models. For example, this configuration lacks the asymmetries which localise the annular mode (Cash *et al.*, 2005), and the anomalies are highly idealised. Moreover the use of experiments with fixed SST means that elements of the response which are likely to be strongly dependent on coupling will not be present. This is

discussed further below.

Jet variability, described by indices of its latitude and speed, also changes with ice addition. There is evidence that more ice leads to increased probability of a more poleward jet, even when the mean position does not change; the jet in experiments with ice extending to 50–55° latitude does not have a strongly favoured mean position, due to this behaviour. In the experiment with ice to 45° latitude, the forcing is sufficiently large that the modal jet position is much further poleward than in cases with little or no ice, suggesting the circulation has entered a new regime.

An asymmetric framework with simple northern hemisphere landmasses (following Brayshaw *et al.*, 2009) has been used to investigate more localised responses to ice loss. The addition of ice in only the Atlantic sector causes the same zonal-mean response, of increased wind speeds on the poleward flank of the eddy-driven jet. This is consistent with high latitude cooling at all longitudes even although the ice addition is localised. There are some contrasts in local details of the response, for example in lower tropospheric temperature and zonal wind, in these experiments, but in all cases there is a strong response downstream of the region of ice addition.

3. What determines the nature and magnitude of the jet response to sea ice forcing? (Chapter 5 and 6)

This study provides a valuable bridge between simpler models addressing the effect of high latitude heating (Butler *et al.*, 2010), aquaplanet or other idealised AGCM studies investigating the effect of local SST anomalies (e.g. Brayshaw *et al.*, 2011) or large scale SST change (Lu *et al.*, 2010; Chen *et al.*, 2010), and on the other hand, experiments in fully realistic AGCMs addressing specific questions of sea ice removal or addition (e.g. Deser *et al.*, 2007).

- **Is the response linear in the magnitude of the forcing?**

  In this study there is evidence that the response (the maximum zonal wind anomaly, or EOF projection strength) is linear with forcing (ice area) for ice restricted to polar latitudes of around 60° or more. The response appears nonlinear for larger forcings. While for weak forcings the response is confined to the jet's poleward flank, as found in most realistic experiments, for strong forcings there is a resulting shift in

the jet maximum. This larger response is found in studies such as Butler *et al.* (2010).

While this thesis is the first study to analyse sea ice addition in an aquaplanet or simplified GCM, aquaplanet models have been used to investigate the response to changes in the mean and gradient of SST (Caballero and Langen, 2005; Lu *et al.*, 2010). Lu *et al.* (2010) adjusted global mean SST T_m in the range 0–35°C and the equator-to-pole difference $\triangle T$ in the range 0–60°C. Aquaplanet experiments in this thesis have 11°C $< T_m <$17°C and 27°C $< \triangle T <$68°C, so $\triangle T$ varies much more than T_m. The poleward shift of the eddy driven jet with increasing $\triangle T$ in this thesis, within this range, is consistent with Lu *et al.* (2010), although they found a reversal of this relationship at smaller $\triangle T$. However, the location of maximum temperature gradient in Lu *et al.* (2010) is the same in all simulations, in contrast to the simulations in this thesis, in particular the cases with ice extending to 45–55° latitude.

- **What is the effect of the location of the temperature front associated with the ice edge?** The nonlinearity becomes apparent when the ice edge reaches 55° in a background state which has a maximum near surface baroclinicity, quantified by the Eady growth rate, just equatorward of 50°. This may suggest that it is this perturbation of the midlatitude baroclinic zone which triggers the nonlinearity, rather than just the large-scale thermal gradient exceeding some threshold. This is consistent with results from the SST front literature whereby perturbation of this baroclinic zone is crucial for causing a response (Brayshaw *et al.*, 2008).

  This is also consistent with the response to southern hemisphere sea ice anomalies corresponding to a 7° expansion or contraction relative to its climatological position (Kidston *et al.*, 2011b). In Kidston *et al.* (2011b) the warm season climatological ice edge was approximately 70°S at most longitudes, while in the cold season it was between 55 and 65°S. Kidston *et al.* (2011b) found a response in the cold season ice expansion case only and linked this to the necessity of perturbing the midlatitude baroclinic zone. The findings in this thesis that a large response is only caused equatorward of 60° are therefore consistent with the results of that study.

- **What is the effect of the state into which the forcing is imposed, including the jet latitude and variability?**

  This thesis has investigated ice addition into three background states; two aqua-

planet states with different SST profiles, and an asymmetric state. Comparing the response to a given sea ice anomaly between experiments with two different SST profiles, there is some evidence that experiments where the eddy driven jet is well equatorward of the anomaly respond more weakly to the anomaly than those in which the eddy driven jet is close to the anomaly. The responses are however qualitatively similar.

Previous studies have found qualitative differences between the response to asymmetric SST anomalies in different seasons (Ting and Peng, 1995), and therefore different background flows. Results from Chapter 6 suggest there may be such sensitivity present, although there was insufficient evidence to deduce whether the apparent sensitivity was merely a consequence of a small forcing.

These elements may be relevant to the interpretation of climate model responses to forcing. Harvey *et al.* (2013) and Barnes and Polvani (2015) both found that the magnitude of Arctic Amplification was correlated with the response of the jet or storm track; i.e., the size of the surface anomaly is related to the response of the jet. Secondly, if the response of the jet to sea ice forcing was sensitive to the location of the jet relative to the sea ice, as suggested above, it could manifest as a relationship between the climate model jet latitude bias and the projected change. No such relationship was found for North Atlantic storm tracks by Zappa *et al.* (2013a). This could be due to complicating factors such as different changes in sea ice between the models, or that the sea ice edge is too far away from the storm tracks in projections of the 21^{st} century for this effect to manifest.

7.3 Future Work

7.3.1 Thermal advection mechanism for temperature variability change

The analysis of thermal advection did not assess the role of meridional and zonal gradient change separately. Given the finding of Screen (2014) that a weakened cooling effect of northerly wind days leads to reduced daily temperature variability in autumn and winter in both the recent past and climate model projections, this separation may be informative. The regression model (Chapter 4) used a meridional temperature gradient scale of 11.25° so, for example, the effect of Arctic amplification in the East Atlantic/Western Europe

sector would be restricted to high latitudes only. Investigation of different lengthscales in both the meridional and zonal directions would therefore extend understanding of the latitudes affected.

The regression model accounted for mean temperature gradients and the variability of geostrophic wind. It did not, however, include the mean circulation, or variability (even a seasonal cycle) in temperature gradients. These components could be investigated for regions where they are known to be particularly important.

Finally, the thermal advection mechanism has not been examined in the CMIP5 ensemble. To apply the thermal advection regression in all CMIP5 models would be costly and the amount of data generated challenging to interpret. However, given the knowledge gained from the single model ensemble, the regression could be applied only in isolated regions where the thermal advection mechanism appears to be important for variability change. Alternatively, a cross-model regression of temperature variance change with gradient change could be performed (a direct extension of the methodology in de Vries *et al.* (2012)). Further analysis of the model spread in variance projections in CMIP5 could also help to evaluate the role of structural or model uncertainty in areas where variance changes are *not* robust, and possible causes. In this thesis, the analysis was conducted after removing the seasonal cycle. However, when preliminary analysis was performed on CMIP5 data without this processing, large differences in variance emerged between models in the late 21^{st} century, particularly in the Arctic. This suggests large discrepancies between models in their simulations of trends and seasonal cycles.

7.3.2 Atmospheric circulation response to sea ice addition

- **Further aquaplanet experiments**

  Some evidence was found, in comparison of experiments with two different SST profiles, that the response to a given sea ice forcing depended on the background state. However, fewer experiments were conducted with the second SST profile; completing the missing experiments in this profile would help to provide further evidence for, or against, this hypothesis. Other approaches could also be used to modify the background state, for example with different SST or insolation profiles. This could inform questions regarding the different responses found in different seasons and in subtly different configurations. Moreover, there is known to be some

spread in CMIP5 projections of the North Atlantic circulation. Therefore, if such experiments could be targeted to resemble different CMIP5 model biases, they could inform discussion of whether model circulation responses are related to their biases, thereby building understanding of model projections.

- **Advancement of the asymmetric setup**

  The experiments were designed to probe the sensitivity and mechanics of the system, more than they were designed to address a specific season. It would be beneficial to conduct future experiments more specifically representing the North Atlantic in early or late winter.

  Despite representing many Atlantic features well, the model setup used in Chapter 6 has insufficient tilt in the North Atlantic jet and storm track, such that it does not extend far enough North in the east Atlantic. Changes to the lower boundary conditions, including increased complexity, may improve the representation of the jet and equivalently stationary waves in the North Atlantic. For example, use of Eurasian topography would give a more realistic representation of the Pacific jet incident on the Rockies (Saulière *et al.*, 2012). Moreover, slightly lower Rocky mountains in this thesis than in Saulière *et al.* (2012) may have contributed to weaker stationary waves in the North Atlantic. It is feasible that changes to the stationary waves would alter the response; a jet which was further poleward in the East Atlantic might respond more strongly to sea ice forcing, although it is also possible that a jet constrained by strong stationary waves would be less responsive to forcing.

  On the other hand, decreasing the complexity of the model may be advantageous. There was, by intention, a large gap in complexity between the asymmetric and aquaplanet experiment; given previous work (Brayshaw *et al.*, 2009), using a recognised set of continents was an efficient route into conducting semi-realistic experiments. However, this leap in complexity leaves a gap in understanding. For example, the question considered in the previous paragraph regarding the effect of stationary waves from the Rocky mountains on the response is of great interest. However, the large Eurasian continent in the experiments in this thesis also introduced changes in the large scale temperature gradients which were not present in the aquaplanet, and sea ice anomalies were introduced in a smaller region. Adding

experiments with isolated forcing from the Rocky mountains and sea ice anomalies at all other latitudes could provide further insight into the drivers of the response in the asymmetric framework.

There are limitations in conducting atmosphere-only experiments into the response of sea ice (Peings and Magnusdottir, 2013), because the ocean cannot respond to atmospheric anomalies induced by sea ice anomalies. In reality, increased SIC and a colder atmosphere would be associated with anomalous fluxes at the ocean surface. This would be expected to reduce the severity of the surface front and magnitude of the surface anomalies (Peings and Magnusdottir, 2013). Recent studies have investigated the response to sea ice anomalies in coupled models using longwave nudging (Deser *et al.*, 2015) and sea ice thickness perturbations (Petrie *et al.*, 2015). At a global scale, the inclusion of ocean dynamics in the experiments of Deser *et al.* (2015) caused a change in the response to Arctic sea ice anomalies; the response changed from one confined to midlatitudes and the northern polar region in atmosphere only experiments to being a global response in the experiment with ocean dynamics.

- **Further analysis methodology**

  One hypothesis for the effect of sea ice on the atmosphere, particularly in the recent past, is that reduced sea ice in the recent past may have contributed to a slower, 'wavier' jet stream and more persistent weather as a result (Francis and Vavrus, 2012). This thesis has demonstrated that, in an aquaplanet, the zonal wind response for present-day-like sea ice extents is small, and generally on the jet flank rather than in the jet core. However, the hypothesis of jet 'waviness' has not been directly addressed. Analysis of wave activity in both the symmetric and asymmetric settings would be valuable.

  In addition, the mechanisms for the poleward shift could be further probed. For example, changes in wavebreaking behaviour (Barnes and Polvani, 2015; Rivière, 2011) or the length scale of the dominant eddies (Kidston *et al.*, 2011a) could be investigated. It would be of merit to explore this in both symmetric and asymmetric settings to investigate whether the presence of stationary waves affects the conclusions. However, equilibrium experiments such as those presented in this thesis would need to be complemented with ensemble spinup experiments (e.g. Deser

et al., 2007) in order to further understand these mechanisms and the processes by which they are initatiated.

7.4 Final Comments

This thesis has shed new light on understanding of polar sea ice impacts on the atmospheric circulation, with implications both for the present day and distant past. Further evidence has been found that increases in sea ice correspond to increased wind speeds on the poleward jet flank (and vice versa). However, the results also suggest that the common paradigms of jet shifts and annular mode responses may be over simplifications for recent and future sea ice extents.

Appendix A

Notation Conventions

Symbol	Definition/Value	Description
T		Temperature
u		Zonal Wind
θ		Potential temperature
f		Coriolis parameter
σ_{BI}	$0.31\frac{f}{N}\frac{\partial \overline{U}}{\partial z}$	Eady growth rate
E		Three-dimensional e-vector
F		Eliasson-Palm (EP) flux
ψ (Ch5)		Meridional mass streamfunction
ψ (Ch6)		Horizontal streamfunction
ϕ		Latitude
β		Gradient of planetary vorticity
g	9.81 ms$-$2	Acceleration due to gravity
a	6.371E6 m	Earth radius
N		Brunt-Vaisala frequency
Operators on a variable A		
[A]		Zonal mean
A*		Deviation from zonal mean
$\overline{\text{A}}$		Time mean
A$'$		Deviation from time mean

Appendix B

Abbreviations

AA	Arctic Amplification
AMIP	Atmospheric Model Intercomparison Project
(A)(O)GCM	(Atmosphere) (and Ocean) General Circulation Model
AO	Arctic Oscillation
CMIP	Coupled Model Intercomparison Project
EOF	Empirical Orthogonal Function
ESSENCE	Ensemble SimulationS of Extreme weather events under Nonlinear Climate change
HadGAM	Hadley centre Global Atmospheric Model
IPCC	Intergovernmental Panel on Climate Change
ITCZ	Inter Tropical Convergence Zone
JLI	Jet Latitude Index
LGM	Last Glacial Maximum
NAO	North Atlantic Oscillation
NSIDC	National Snow and Ice Data Center
NH	Northern Hemisphere
PMIP	Paleoclimate Modelling Intercomparison Project
PC	Principal Component
RCP	Representative Concentration Pathway
SAM	Southern Annular Mode

DJF	December, January and February
MAM	March, April and May
JJA	June, July and August
SON	September, October and November
Variables	
SIC	Sea Ice Concentration
SIE	Sea Ice Extent
SIA	Sea Ice Area
SLP	Sea Level Pressure
SST	Sea Surface Temperature
TAS	Surface Air Tempeature

References

Alexander, M. A., Bhatt, U. S., Walsh, J. E., Timlin, M. S., Miller, J. S., and Scott, J. D. (2004). The Atmospheric Response to Realistic Arctic Sea Ice Anomalies in an AGCM during Winter. *Journal of Climate*, **17**, 890–905.

Ambaum, M. H. (2010a). Statistical Tests in Climate Science. *Journal of Climate*, **23**, 5927–5932.

Ambaum, M. H. (2010b). *Thermal physics of the atmosphere*, volume 1. John Wiley & Sons.

Ambaum, M. H., Hoskins, B. J., and Stephenson, D. B. (2001). Arctic oscillation or North Atlantic oscillation? *Journal of Climate*, **14**(16), 3495–3507.

Bader, J., Mesquita, M. D. S., Hodges, K. I., Keenlyside, N., Osterhus, S., and Miles, M. (2011). A review on Northern Hemisphere sea-ice, storminess and the North Atlantic Oscillation: Observations and projected changes. *Atmospheric Research*, **101**, 809–834.

Bader, J., Flgge, M., Kvamst, N., Mesquita, M., and Voigt, A. (2013). Atmospheric winter response to a projected future Antarctic sea-ice reduction: a dynamical analysis. *Climate Dynamics*, **40**(11-12), 2707–2718.

Barlow, R. J. (1989). *Statistics. A Guide to the Use of Statistical Methods in the Physical Sciences*. John Wiley & Sons Ltd.

Barnes, E. A. (2013). Revisiting the evidence linking arctic amplification to extreme weather in midlatitudes. *Geophysical Research Letters*, **40**(17), 4734–4739.

Barnes, E. A. and Polvani, L. (2013). Response of the midlatitude jets, and of their variability, to increased greenhouse gases in the cmip5 models. *Journal of Climate*, **26**, 7117–7135.

Barnes, E. A. and Polvani, L. (2015). Cmip5 projections of arctic amplification, of the north american/north atlantic circulation, and of their relationship. *Journal of Climate*, **28**(13).

Barnes, E. A. and Screen, J. A. (2015). The impact of Arctic warming on the midlatitude jet-stream: Can it? Has it? Will it? *Wiley Interdisciplinary Reviews: Climate Change*, **6**(3),

277–286.

Barnes, E. A., Hartmann, D. L., Frierson, D. M. W., and Kidston, J. (2010). Effect of latitude on the persistence of eddy-driven jets. *Geophysical Research Letters*, **37**(11), n/a–n/a.

Bengtsson, L., Hodges, K. I., Koumoutsaris, S., Zahn, M., and Berrisford, P. (2013). The Changing Energy Balance of the Polar Regions in a Warmer Climate. *Journal of Climate*, **26**(10), 3112–3129.

Berckmans, J., Woollings, T., Demory, M.-E., Vidale, P.-L., and Roberts, M. (2013). Atmospheric blocking in a high resolution climate model; influences of mean state, orography and eddy forcing. *Atmospheric Science Letters*, **14**(1), 34–40.

Bindoff, N., Stott, P., AchutaRao, K., Allen, M., Gillett, N., Gutzler, D., Hansingo, K., Hegerl, G., Hu, Y., Jain, S., Mokhov, I. I., Overland, J., Perlwitz, J., Sebbari, R., and Zhang, X. (2013). Detection and Attribution of Climate Change: from Global to Regional. In T. F. Stocker, D. Qin, G.-K. Plattner, M. Tignor, S. K. Allen, J. Boschung, A. Nauels, Y. Xia, V. Bex, and P. M. Midgley, editors, *Climate Change 2013: The Physical Science Basis. Contribution of Working Group I to the Fifth Assessment Report of the Intergovernmental Panel on Climate Change*, pages 867–952. Cambridge University Press, Cambridge, United Kingdom and New York, NY, USA.

Blackmon, M. L. (1976). A climatological spectral study of the 500 mb geopotential height of the Northern Hemisphere. *Journal of the Atmospheric Sciences*, **33**(8), 1607–1623.

Blüthgen, J., Gerdes, R., and Werner, M. (2012). Atmospheric response to the extreme Arctic sea ice conditions in 2007. *Geophysical Research Letters*, **39**(2), n/a–n/a.

Boer, G. J. (2011). The ratio of land to ocean temperature change under global warming. *Climate Dynamics*, **37**, 2253–2270.

Branstator, G. and Selten, F. (2009). Modes of variability and climate change. *Journal of Climate*, **22**(10), 2639–2658.

Brayshaw, D. J. (2006). *Large scale forcing of the North Atlantic storm track*. Ph.D. thesis, University of Reading.

Brayshaw, D. J., Hoskins, B., and Blackburn, M. (2008). The Storm-Track Response to Idealized SST Perturbations in an Aquaplanet GCM. *Journal of the Atmospheric Sciences*, **65**, 2842–2860.

Brayshaw, D. J., Hoskins, B., and Blackburn, M. (2009). The Basic Ingredients of the North Atlantic Storm Track. Part I: LandSea Contrast and Orography. *Journal of the*

Atmospheric Sciences, **66**, 2539–2558.

Brayshaw, D. J., Hoskins, B., and Blackburn, M. (2011). The Basic Ingredients of the North Atlantic Storm Track. Part II: Sea Surface Temperatures. *Journal of the Atmospheric Sciences*, **68**, 1784–1805.

Broccoli, A. J., Lau, N.-C., and Nath, M. J. (1998). The cold ocean-warm land pattern: Model simulation and relevance to climate change detection. *Journal of Climate*, **11**(11), 2743–2763.

Budikova, D. (2009). Role of Arctic sea ice in global atmospheric circulation: A review. *Global and Planetary Change*, **68**, 149–163.

Butler, A. H., Thompson, D. W. J., and Heikes, R. (2010). The Steady-State Atmospheric Circulation Response to Climate Change-like Thermal Forcings in a Simple General Circulation Model. *Journal of Climate*, **23**, 3474–3672.

Caballero, R. and Langen, P. L. (2005). The dynamic range of poleward energy transport in an atmospheric general circulation model. *Geophysical Research Letters*, **32**, n/–n/a.

Cash, B. A., Kushner, P. J., and Vallis, G. K. (2002). The structure and composition of the annular modes in an aquaplanet general circulation model. *Journal of the Atmospheric Sciences*, **59**(23), 3399–3414.

Cash, B. A., Kushner, P. J., and Vallis, G. K. (2005). Zonal asymmetries, teleconnections, and annular patterns in a GCM. *Journal of the Atmospheric Sciences*, **62**(1), 207–219.

Cattiaux, J. and Cassou, C. (2013). Opposite CMIP3/CMIP5 trends in the wintertime Northern Annular Mode explained by combined local sea ice and remote tropical influences. *Geophysical Research Letters*, **40**(14), 3682–3687.

Cattiaux, J., Yiou, P., and Vautard, R. (2012). Dynamics of future seasonal temperature trends and extremes in Europe: a multi-model analysis from CMIP3. *Climate Dynamics*, **38**(9-10), 1949–1964.

Cattiaux, J. a. R. V., Cassou, C., Yiou, P., Masson-Delmotte, V., and Codron, F. (2010). Winter 2010 in Europe: A cold extreme in a warming climate. *Geophysical Research Letters*, **37**, L20704.

Chang, E. K. (2009). Diabatic and orographic forcing of northern winter stationary waves and storm tracks. *Journal of Climate*, **22**(3), 670–688.

Chang, E. K., Lee, S., and Swanson, K. L. (2002). Storm Track Dynamics. *Journal of Climate*, **15**(16), 2163–2183.

Chang, E. K., Guo, Y., and Xia, X. (2012). Cmip5 multimodel ensemble projection of

storm track change under global warming. *Journal of Geophysical Research: Atmospheres (1984–2012)*, **117**(D23).

Chen, G., Plumb, R. A., and Lu, J. (2010). Sensitivities of zonal mean atmospheric circulation to SST warming in an aqua-planet model. *Geophysical Research Letters*, **37**(12).

Cohen, J., Screen, J. A., Furtado, J. C., Barlow, M., Whittleston, D., Coumou, D., Francis, J., Dethloff, K., Entekhabi, D., Overland, J., *et al.* (2014). Recent Arctic amplification and extreme mid-latitude weather. *Nature Geoscience*, **7**(9), 627–637.

Collins, M., Knutti, R., Arblaster, J., Dufresne, J. L., Fichefet, T., Friedlingstein, P., Gao, X., Gutowski, W. J., Johns, T., Krinner, G., Shongwe, M., Tebaldi, C., Weaver, A. J., and Wehner, M. (2013). Long-term Climate Change: Projections, Commitments and Irreversibility. In T. F. Stocker, D. Qin, G.-K. Plattner, M. Tignor, S. K. Allen, J. Boschung, A. Nauels, Y. Xia, V. Bex, and P. M. Midgley, editors, *Climate Change 2013: The Physical Science Basis. Contribution of Working Group I to the Fifth Assessment Report of the Intergovernmental Panel on Climate Change*, pages 1029–1136. Cambridge University Press, Cambridge, United Kingdom and New York, NY, USA.

Comiso, J. C. and Nishio, F. (2008). Trends in the sea ice cover using enhanced and compatible AMSR-E, SSM/I, and SMMR data. *Journal of Geophysical Research: Oceans (1978–2012)*, **113**(C2).

Comiso, J. C., Parkinson, C. L., Gersten, R., and Stock, L. (2008). Accelerated decline in the Arctic sea ice cover. *Geophysical Research Letters*, **35**(1).

Cox, P., Betts, R., Bunton, C., Essery, R., Rowntree, P., and Smith, J. (1999). The impact of new land surface physics on the GCM simulation of climate and climate sensitivity. *Climate Dynamics*, **15**(3), 183–203.

Davies, T., Cullen, M., Malcolm, A., Mawson, M., Staniforth, A., White, A., and Wood, N. (2005). A new dynamical core for the Met Office's global and regional modelling of the atmosphere. *Quarterly Journal of the Royal Meteorological Society*, **131**(608), 1759–1782.

Day, J. J., Hargreaves, J. C., Annan, J. D., and Abe-Ouchi, A. (2012). Sources of multi-decadal variability in Arctic sea ice extent. *Environmental Research Letters*, **7**, 034011.

de Vries, H., Haarsma, R. J., and Hazeleger, W. (2012). Western European Cold Spells in Current and Future Climate. *Geophysical Research Letters*, **39**(4), n/a–n/a. L04706.

Deser, C., Walsh, J. E., and Timlin, M. S. (2000). Arctic sea ice variability in the context of recent atmospheric circulation trends. *Journal of Climate*, **13**, 617–633.

Deser, C., Magnusdottir, G., Saravanan, R., and Phillips, A. (2004). The Effects of North

Atlantic SST and Sea Ice Anomalies on the Winter Circulation in CCM3. Part II: Direct and Indirect Components of the Response. *Journal of Climate*, **17**, 877–889.

Deser, C., Tomas, R. A., and Peng, S. (2007). The Transient Atmospheric Circulation Response to North Atlantic SST and Sea Ice Anomalies. *Journal of Climate*, **20**, 4751–4767.

Deser, C., Tomas, R., Alexander, M., and Lawrence, D. (2010). The seasonal atmospheric response to projected Arctic sea ice loss in the late twenty-first century. *Journal of Climate*, **23**(2), 333–351.

Deser, C., Phillips, A., Bourdette, V., and Teng, H. (2012). Uncertainty in climate change projections: the role of internal variability. *Climate Dynamics*, **38**(3–4), 527–546.

Deser, C., Phillips, A. S., Alexander, M. A., and Smoliak, B. V. (2014). Projecting north american climate over the next 50 years: Uncertainty due to internal variability. *Journal of Climate*, **27**(6), 2271–2296.

Deser, C., R., Tomas, A., and Sun, L. (2015). The role of ocean-atmosphere coupling in the zonal-mean atmospheric response to Arctic sea ice loss. *Journal of Climate*, **28**(6), 2168–2186.

Ding, Q., Wallace, J. M., Battisti, D. S., Steig, E. J., Gallant, A. J., Kim, H.-J., and Geng, L. (2014). Tropical forcing of the recent rapid Arctic warming in northeastern Canada and Greenland. *Nature*, **509**(7499), 209–212.

Dong, B. and Valdes, P. J. (1998). Simulations of the Last Glacial Maximum climates using a general circulation model: prescribed versus computed sea surface temperatures. *Climate Dynamics*, **14**, 571–591.

Dong, B. and Valdes, P. J. (2000). Climates at the Last Glacial Maximum: Influence of model horizontal resolution. *Journal of Climate*, **13**(9), 1554–1573.

Dong, B., Sutton, R., and Woollings, T. (2011). Changes of interannual NAO variability in response to greenhouse gases forcing. *Climate Dynamics*, **37**(7-8), 1621–1641.

Duchon, C. E. (1979). Lanczos filtering in one and two dimensions. *Journal of Applied Meteorology*, **18**(8), 1016–1022.

Eady, E. (1949). Long waves and cyclone waves. *Tellus*, **1**(3), 33–52.

Edmon, H., Hoskins, B. J., and Mcintyre, M. E. (1980). Eliassen-Palm cross-sections for the troposphere. *Journal of the Atmospheric Sciences*, **37**(12), 2600–2616.

Edwards, J. and Slingo, A. (1996). Studies with a flexible new radiation code. i: Choosing a configuration for a large-scale model. *Quarterly Journal of the Royal Meteorological*

Society, **122**(531), 689–719.

Ely, C. R., Brayshaw, D. J., Methven, J., Cox, J., and Pearce, O. (2013). Implications of the North Atlantic Oscillation for a UK-Norway renewable power system. *Energy Policy*, **62**, 1420–1427.

Essery, R., Best, M., and Cox, P. (2001). MOSES 2.2 technical documentation. Technical report, Hadley Centre Technical Note.

Fetterer, F., Knowles, K., Meier, W., and Savoie, M. (2002). Sea Ice Index. Boulder, Colorado USA: National Snow and Ice Data Center. http://nsidc.org/data/docs/noaa/g02135_seaice_index/.

Fischer, E. M. and Schär, C. (2009). Future changes in daily summer temperature variability: driving processes and role for temperature extremes. *Climate Dynamics*, **33**, 917–935.

Fischer, E. M., Rajczak, J., and Schär, C. (2012). Changes in European summer temperature variability revisited. *Geophysical Research Letters*, **39**, L19702.

Flato, G., Marotzke, J., Abiodun, B., Braconnot, P., Chou, S. C., Collins, W., Cox, P., Driouech, F., Emori, S., Eyring, V., Forest, C., Gleckler, P., Guilyardi, E., Jakob, C., Kattsov, V., Reason, C., and Rummukainen, M. (2013). Evaluation of Climate Models. In T. F. Stocker, D. Qin, G.-K. Plattner, M. Tignor, S. K. Allen, J. Boschung, A. Nauels, Y. Xia, V. Bex, and P. M. Midgley, editors, *Climate Change 2013: The Physical Science Basis. Contribution of Working Group I to the Fifth Assessment Report of the Intergovernmental Panel on Climate Change*, pages 741–866. Cambridge University Press, Cambridge, United Kingdom and New York, NY, USA.

Francis, J. A. and Vavrus, S. J. (2012). Evidence linking Arctic amplification to extreme weather in mid-latitudes. *Geophysical Research Letters*, **39**, L06801.

Frierson, D. M., Lu, J., and Chen, G. (2007). Width of the Hadley cell in simple and comprehensive general circulation models. *Geophysical Research Letters*, **34**(18).

Fyfe, J. C., von Salzen, K., Gillett, N. P., Arora, V. K., Flato, G. M., and McConnell, J. R. (2013). One hundred years of Arctic surface temperature variation due to anthropogenic influence. *Scientific reports*, **3**.

Gerber, E. P. and Vallis, G. K. (2009). On the zonal structure of the North Atlantic Oscillation and annular modes. *Journal of the Atmospheric Sciences*, **66**(2), 332–352.

Gerdes, R. (2006). Atmospheric response to changes in Arctic sea ice thickness. *Geophysical Research Letters*, **33**(18), n/a–n/a.

Goubanova, K., Li, L., Yiou, P., and F.Codron (2010). Relation between Large-Scale Circulation and European Winter Temperature: Does It Hold under Warmer Climate? *Journal of Climate*, **23**, 37523760.

Graff, L. S. and LaCasce, J. H. (2011). Changes in the Extratropical Storm Tracks in Response to Changes in SST in an AGCM. *Journal of Climate*, **25**, 1854–1870.

Graham, T. and Vellinga, M. (2013). Heat budget of the upper Arctic Ocean under a warming climate. *Climate Dynamics*, **40**(1-2), 143–153.

Greeves, C., Pope, V., Stratton, R., and Martin, G. (2007). Representation of Northern Hemisphere winter storm tracks in climate models. *Climate Dynamics*, **28**(7-8), 683–702.

Gregory, J. M. and Mitchell, J. F. B. (1995). Simulation of daily variability of surface temperature and precipitation over Europe in the current and 2 x COz climates using the UKMO climate model. *Quarterly Journal of the Royal Meteorological Society*, **121**, 1451–1476.

Hall, A. (2004). The Role of Surface Albedo Feedback in Climate. *Journal of Climate*, **17**, 1550–1568.

Hansen, J., Ruedy, R., Sato, M., and Lo, K. (2010). Global surface temperature change. *Reviews of Geophysics*, **48**(4).

Hartmann, D. L., Tank, A. M. G. K., Rusticucci, M., Alexander, L. V., Brnnimann, S., Charabi, Y., Dentener, F. J., Dlugokencky, E. J., Easterling, D. R., Kaplan, A., Soden, B. J., Thorne, P. W., Wild, M., and Zhai, P. M. (2013). Observations: Atmosphere and Surface. In T. F. Stocker, D. Qin, G.-K. Plattner, M. Tignor, S. K. Allen, J. Boschung, A. Nauels, Y. Xia, V. Bex, and P. M. Midgley, editors, *Climate Change 2013: The Physical Science Basis. Contribution of Working Group I to the Fifth Assessment Report of the Intergovernmental Panel on Climate Change*, pages 159–254. Cambridge University Press, Cambridge, United Kingdom and New York, NY, USA.

Harvey, B. J., Shaffrey, L. C., Woollings, T. J., Zappa, G., and Hodges, K. I. (2012). How large are projected 21st century storm track changes? *Geophysical Research Letters*, **39**(18), n/a–n/a.

Harvey, B. J., Sharey, L. C., and Woollings, T. J. (2013). Equator-to-pole temperature differences and the extra-tropical storm track responses of the CMIP5 climate models. *Climate Dynamics*, pages 1–12.

Hassanzadeh, P., Kuang, Z., and Farrell, B. F. (2014). Responses of midlatitude blocks and

wave amplitude to changes in the meridional temperature gradient in an idealized dry gcm. *Geophysical Research Letters*, **41**(14), 5223–5232.

Hawkins, E. and Sutton, R. (2012). Time of emergence of climate signals. *Geophysical Research Letters*, **39**, L01702.

Held, I. M. (1975). Momentum transport by quasi-geostrophic eddies. *Journal of the Atmospheric Sciences*, **32**(7), 1494–1497.

Held, I. M. (1993). Large-Scale Dynamics and Global Warming. *Bulletin of the American Meteorological Society*, **74**, 228–241.

Held, I. M. (2005). The Gap between Simulation and Understanding in Climate Modeling, B. Am. Meteorol. Soc., 86, 1609–1614, doi: 10.1175. *Bulletin of the American Meteorological Society*, **86**, 1609–1614.

Held, I. M. and Hou, A. Y. (1980). Nonlinear axially symmetric circulations in a nearly inviscid atmosphere. *Journal of the Atmospheric Sciences*, **37**(3), 515–533.

Held, I. M., Ting, M., and Wang, H. (2002). Northern winter stationary waves: theory and modeling. *Journal of Climate*, **15**(16), 2125–2144.

Henderson, G., Barrett, B., and M. Lafleur, D. (2014). Arctic sea ice and the MaddenJulian Oscillation (MJO). *Climate Dynamics*, **43**(7-8), 2185–2196.

Holmes, C. R., Woollings, T., Hawkins, E., and de Vries, H. (2016). Robust Future Changes in Temperature Variability under Greenhouse Gas Forcing and the Relationship with Thermal Advection. *Journal of Climate*, **29**(6), 2221–2236.

Holton, J. R. (2004). *An introduction to dynamic meteorology*, volume 88. Academic Press Inc., 4 edition.

Honda, M., Inoue, J., and Yamane, S. (2009). Influence of low Arctic sea-ice minima on anomalously cold Eurasian winters. *Geophysical Research Letters*, **36**(8), n/a–n/a.

Hoskins, B. J. and Karoly, D. J. (1981). The Steady Linear Response of a Spherical Atmosphere to Thermal and Orographic Forcing. *Journal of the Atmospheric Sciences*, **38**, 1179–1196.

Hoskins, B. J. and Valdes, P. J. (1990). On the existence of storm-tracks. *Journal of the Atmospheric Sciences*, **47**(15), 1854–1864.

Hoskins, B. J., James, I. N., and White, G. H. (1983). The Shape, Propagation and Mean-Flow Interaction of Large-Scale Weather Systems. *Journal of the Atmospheric Sciences*, **40**(7), 1595–1612.

Hunke, E. C., Lipscomb, W. H., Turner, A. K., *et al.* (2010). CICE: the Los Alamos Sea

Ice Model Documentation and Software Users Manual Version 4.1 LA-CC-06-012. *T-3 Fluid Dynamics Group, Los Alamos National Laboratory*.

Hurrell, J. W. (2015). The Climate Data Guide: Hurrell North Atlantic Oscillation (NAO) Index (PC-based). Retrieved from https://climatedataguide.ucar.edu/climate-data/hurrell-north-atlantic-oscillation-nao-index-pc-based. Accessed 05 July 2015.

Hurrell, J. W., Kushnir, Y., Ottersen, G., and Visbeck, M. (2003). An Overview of the North Atlantic Oscillation. *The North Atlantic Oscillation: Climatic Significance and Environmental Impact. Geophys. Monogr.* Vol. 134, Amer. Geophys. Union, 1-35.

Inatsu, M., Mukougawa, H., and Xie, S.-P. (2000). Formation of subtropical westerly jet core in an idealized GCMwithout mountains. *Geophysical Research Letters*, **27**(4), 529–532.

Inatsu, M., Mukougawa, H., and Xie, S.-P. (2002a). Stationary Eddy Response to Surface Boundary Forcing: Idealized GCM Experiments. *Journal of the Atmospheric Sciences*, **59**(11), 1898–1915.

Inatsu, M., Mukougawa, H., and Xie, S.-P. (2002b). Tropical and extratropical SSTeffects on the midlatitude storm track. *JOURNAL-METEOROLOGICAL SOCIETY OF JAPAN SERIES 2*, **80**(4B), 1069–1076.

Inatsu, M., Mukougawa, H., and Xie, S.-P. (2003). Atmospheric Response to Zonal Variations in Midlatitude SST: Transient and Stationary Eddies and Their Feedback. *Journal of Climate*, **16**, 3314–3329.

IPCC (2013). *Climate Change 2013: The Physical Science Basis. Contribution of Working Group I to the Fifth Assessment Report of the Intergovernmental Panel on Climate Change*. Cambridge University Press, Cambridge, United Kingdom and New York, NY, USA.

Jaiser, R., Dethloff, K., Handorf, D., Rinke, A., and Cohen, J. (2012). Impact of sea ice cover changes on the orthern Hemisphereatmospheric winter circulation. *Tellus A*, **64**(0).

James, I. N. (1995). *Introduction to Circulating Atmospheres*. Cambridge University Press.

Jones, C. P. (1993). Unified Model Documentation Paper No. 71: Specification of sea-ice concentration in the operational global model. Technical Report No. 71, National Centre for Atmospheric Science.

Joshi, M. M., Gregory, J. M., Webb, M. J., Sexton, D. M. H., and Johns, T. C. (2008). Mechanisms for the land/sea warming contrast exhibited by simulations of climate change. *Climate Dynamics*, **30**, 455–465.

Joshi, M. M., Lambert, F. H., and Webb, M. J. (2013). An explanation for the difference between twentieth and twenty-first century land-sea warming ratio in climate models. *Climate Dynamics*, **41**, 1853–1869.

Kageyama, M., Valdes, P., Ramstein, G., Hewitt, C., and Wyputta, U. (1999). Northern hemisphere storm tracks in present day and last glacial maximum climate simulations: A comparison of the european pmip models*. *Journal of Climate*, **12**(3), 742–760.

Kalnay, E., Kanamitsu, M., Kistler, R., Collins, W., Deaven, D., Gandin, L., Iredell, M., Saha, S., White, G., Woollen, J., Zhu, Y., Leetmaa, A., Reynolds, R., Jenne, R., and Joseph, D. (1996). The NCEP/NCAR 40-Year Reanalysis Project. *Bulletin of the American Meteorological Society*, **77**, 437–471.

Kang, S. M., Seager, R., Frierson, D. M., and Liu, X. (2015). Croll revisited: Why is the northern hemisphere warmer than the southern hemisphere? *Climate Dynamics*, **44**(5–6), 1457–1472.

Kaspi, Y. and Schneider, T. (2013). The role of stationary eddies in shaping midlatitude storm tracks. *Journal of the Atmospheric Sciences*, **70**(8), 2596–2613.

Katz, R. W. and Brown, B. G. (1992). Extreme events in a changing climate: variability is more important than averages. *Climatic Change*, **21**(3), 289–302.

Kay, J. E., Holland, M. M., and Jahn, A. (2011). Inter-annual to multi-decadal Arctic sea ice extent trends in a warming world. *Geophysical Research Letters*, **38**(15).

Kidston, J. and Gerber, E. P. (2010). Intermodel variability of the poleward shift of the austral jet stream in the CMIP3 integrations linked to biases in 20th century climatology. *Geophysical Research Letters*, **37**(9), n/a–n/a.

Kidston, J., Vallis, G., Dean, S., and Renwick, J. (2011a). Can the increase in the eddy length scale under global warming cause the poleward shift of the jet streams? *Journal of Climate*, **24**(14), 3764–3780.

Kidston, J., Taschetto, A. S., Thompson, D. W. J., and England, M. H. (2011b). The influence of Southern Hemisphere seaice extent on the latitude of the midlatitude jet stream. *Geophysical Research Letters*, **38**.

Kinnard, C., Zdanowicz, C. M., Fisher, D. A., Isaksson, E., de Vernal, A., and Thompson, L. G. (2011). Reconstructed changes in Arctic sea ice over the past 1,450 years. *Nature*, **479**(7374), 509–512.

Korty, R. L. and Schneider, T. (2008). Extent of Hadley circulations in dry atmospheres. *Geophysical Research Letters*, **35**(23).

Kushnir, Y., Robinson, W., Bladé, I., Hall, N., Peng, S., and Sutton, R. (2002). Atmospheric GCM response to extratropical SST anomalies: Synthesis and evaluation. *Journal of Climate*, **15**(16), 2233–2256.

Kwok, R. (2010). Satellite remote sensing of sea-ice thickness and kinematics: a review. *Journal of Glaciology*, **56**(200), 1129–1140.

Kwok, R., Cunningham, G., Wensnahan, M., Rigor, I., Zwally, H., and Yi, D. (2009). Thinning and volume loss of the Arctic Ocean sea ice cover: 2003–2008. *Journal of Geophysical Research: Oceans (1978–2012)*, **114**(C7).

Laxon, S. W., Giles, K. A., Ridout, A. L., Wingham, D. J., Willatt, R., Cullen, R., Kwok, R., Schweiger, A., Zhang, J., Haas, C., Hendricks, S., Krishfield, R., Kurtz, N., Farrell, S., and Davidson, M. (2013). CryoSat-2 estimates of Arctic sea ice thickness and volume. *Geophysical Research Letters*, **40**(4), 732–737.

Lee, S. and Kim, H.-k. (2003). The dynamical relationship between subtropical and eddy-driven jets. *Journal of the Atmospheric Sciences*, **60**(12), 1490–1503.

Lee, S., Gong, T., Johnson, N., Feldstein, S. B., and Pollard, D. (2011). On the possible link between tropical convection and the Northern Hemisphere Arctic surface air temperature change between 1958 and 2001. *Journal of Climate*, **24**(16), 4350–4367.

Lenderink, G., Van Ulden, A., Van den Hurk, B., and Van Meijgaard, E. (2007). Summertime inter-annual temperature variability in an ensemble of regional model simulations: analysis of the surface energy budget. *Climatic Change*, **81**(1), 233–247.

Lesins, G., Duck, T. J., and Drummond, J. R. (2012). Surface energy balance framework for Arctic amplification of climate change. *Journal of Climate*, **25**(23), 8277–8288.

Li, C. and Wettstein, J. J. (2012). Thermally driven and eddy-driven jet variability in reanalysis. *Journal of Climate*, **25**(5), 1587–1596.

Li, F. and Wang, H. (2013). Autumn Sea Ice Cover, Winter Northern Hemisphere Annular Mode, and Winter Precipitation in Eurasia. *Journal of Climate*, **26**, 39683981.

Lindsay, R., Zhang, J., Schweiger, A., Steele, M., and Stern, H. (2009). Arctic sea ice retreat in 2007 follows thinning trend. *Journal of Climate*, **22**(1), 165–176.

Liptak, J. and Strong, C. (2014). The Winter Atmospheric Response to Sea Ice Anomalies in the Barents Sea. *Journal of Climate*, **27**, 914–924.

Liu, J., Curry, J. A., Wong, H., Song, M., and Horton, R. M. (2012). Impact of declining Arctic sea ice on winter snowfall. *PNAS*, **109**, 4074–4079.

Lock, A., Brown, A., Bush, M., Martin, G., and Smith, R. (2000). A new boundary layer

mixing scheme. part i: Scheme description and single-column model tests. *Monthly Weather Review*, **128**(9), 3187–3199.

Lorenz, D. J. and DeWeaver, E. T. (2007). Tropopause height and zonal wind response to global warming in the IPCC scenario integrations. *Journal of Geophysical Research: Atmospheres*, **112**(D10), n/a–n/a.

Lu, J., Chen, G., and Frierson, D. M. (2010). The position of the midlatitude storm track and eddy-driven westerlies in aquaplanet AGCMs. *Journal of the Atmospheric Sciences*, **67**(12), 3984–4000.

Magnusdottir, G., Deser, C., and Saravanan, R. (2004). The Effects of North Atlantic SST and Sea Ice Anomalies on the Winter Circulation in CCM3. Part I: Main Features and Storm Track Characteristics of the Response. *Journal of Climate*, **17**, 857–876.

Manabe, S. and Wetherald, R. T. (1975). The Effects of Doubling the CO2 Concentration on the climate of a General Circulation Model. *Journal of the Atmospheric Sciences*, **32**(1), 3–15.

Marsland, S. J., Haak, H., Jungclaus, J. H., Latif, M., and Röske, F. (2003). The Max-Planck-Institute global ocean/sea ice model with orthogonal curvilinear coordinates. *Ocean Modelling*, **5**, 91–127.

Martin, G., Ringer, M., Pope, V., Jones, A., Dearden, C., and Hinton, T. (2006). The physical properties of the atmosphere in the new Hadley Centre Global Environmental Model (HadGEM1). Part I: Model description and global climatology. *Journal of Climate*, **19**(7), 1274–1301.

Masato, G., Woollings, T., and Hoskins, B. J. (2014). Structure and impact of atmospheric blocking over the Euro-Atlantic region in present-day and future simulations. *Geophysical Research Letters*, **41**(3), 1051–1058.

McLaren, A., Banks, H., Durman, C., Gregory, J., Johns, T., Keen, A., Ridley, J., Roberts, M., Lipscomb, W., Connolley, W., *et al.* (2006). Evaluation of the sea ice simulation in a new coupled atmosphere-ocean climate model (HadGEM1). *Journal of Geophysical Research: Oceans (1978–2012)*, **111**(C12).

Menendez, C. G., Serafini, V., and Treut, H. L. (1999). The effect of sea-ice on the transient atmospheric eddies of the Southern Hemisphere. *Climate Dynamics*, **15**, 659–671.

Merz, N., Raible, C. C., and Woollings, T. (2015). North Atlantic eddy-driven jet in interglacial and glacial winter climates. *Journal of Climate*, **28**, 3977–3997.

Mesquita, M. D. S., Hodges, K. I., Atkinson, D. E., and Bader, J. (2011). Sea-ice anomalies

in the Sea of Okhotsk and the relationship with storm tracks in the Northern Hemisphere during winter. *Tellus A*, **63a**, 312–323.

Min, S.-K., Zhang, X., Zwiers, F. W., and Agnew, T. (2008). Human influence on Arctic sea ice detectable from early 1990s onwards. *Geophysical Research Letters*, **35**(21).

Minobe, S., Kuwano-Yoshida, A., Komori, N., Xie, S.-P., and Small, R. J. (2008). Influence of the gulf stream on the troposphere. *Nature*, **452**(7184), 206–209.

Monahan, A. H. and Fyfe, J. C. (2006). On the nature of zonal jet EOFs. *Journal of Climate*, **19**(24), 6409–6424.

Mori, M., Watanabe, M., Shiogama, H., Inoue, J., and Kimoto, M. (2014). Robust arctic sea-ice influence on the frequent eurasian cold winters in past decades. *Nature Geoscience*.

Nakicenovic, N. and Swart, R. e. (2000). *Special Report on Emissions Scenarios. A Special Report of Working Group III of the Intergovernmental Panel on Climate Change*. Cambridge University Press, Cambridge, United Kingdom and New York, NY, USA.

Neale, R. B. and Hoskins, B. (2000a). A standard test for AGCMs including their physical parametrizations. II: Results for the Met Office Model. *Atmospheric Science Letters*, **1**(2), 108–114.

Neale, R. B. and Hoskins, B. J. (2000b). A standard test for AGCMs including their physical parametrizations: I: The proposal. *Atmospheric Science Letters*, **1**, 101–107.

North, G. R., Bell, T. L., Cahalan, R. F., and Moeng, F. J. (1982). Sampling errors in the estimation of empirical orthogonal functions. *Monthly Weather Review*, **110**(7), 699–706.

Notz, D. and Marotzke, J. (2012). Observations reveal external driver for Arctic sea-ice retreat. *Geophysical Research Letters*, **39**(8).

Novak, L., Ambaum, M. H., and Tailleux, R. (2015). The Life Cycle of the North Atlantic Storm Track. *Journal of the Atmospheric Sciences*, **72**(2), 821–833.

O'Gorman, P. A. (2011). The effective static stability experienced by eddies in a moist atmosphere. *Journal of the Atmospheric Sciences*, **68**(1), 75–90.

Osborn, T. J. (2011). Winter 2009/2010 temperatures and a record-breaking North Atlantic Oscillation index. *Weather*, **66**, 19–21.

Osborn, T. J., Conway, D., Hulme, M., Gregory, J. M., and Jones, P. D. (1999). Air flow influences on local climate: observed and simulated mean relationships for the United Kingdom. *Climate Res.*, **13**, 173–191.

Palmer, T. N. (1999). A nonlinear dynamical perspective on climate prediction. *Journal of*

Climate, **12**(2), 575–591.

Parker, D. E. (2009). Anomalies of Central England Temperature Classified by Air Source. *Journal of Climate*, **22**, 1069–1081.

Parker, D. E., Legg, T. P., and Folland, C. K. (1992). A new daily Central England temperature series, 1772-1991. *International Journal of Climatology*, **12**, 585–596.

Parkinson, C. and Cavalieri, D. (2012). Antarctic sea ice variability and trends, 1979–2010. *The Cryosphere Discussions*, **6**(2), 931–956.

Parkinson, C. L. and Comiso, J. C. (2013). On the 2012 record low Arctic sea ice cover: Combined impact of preconditioning and an August storm. *Geophysical Research Letters*, **40**(7), 1356–1361.

Pausata, F., Li, C., Wettstein, J. J., Kageyama, M., and Nisancioglu, K. H. (2011). The key role of topography in altering North Atlantic atmospheric circulation during the last glacial period. *Climate of the Past*, **7**, 1089–1101.

Peings, Y. and Magnusdottir, G. (2013). Response of the Wintertime Northern Hemisphere Atmospheric Circulation to Current and Projected Arctic Sea Ice Decline: A Numerical Study with CAM5. *Journal of Climate*, **17**, 244–264.

Peings, Y., Cattiaux, J., and Douville, H. (2012). Evaluation and response of winter cold spells over western europe in cmip5 models. *Climate Dynamics*, pages 1–13.

Petoukhov, V., Rahmstorf, S., Petri, S., and Schellnhuber, H. J. (2013). Quasiresonant amplification of planetary waves and recent Northern Hemisphere weather extremes. *Proceedings of the National Academy of Sciences of the United States of America*.

Petrie, R., Shaffrey, L., and Sutton, R. (2015). Atmospheric impact of arctic sea ice loss in a coupled atmosphere-ocean simulation. *Journal of Climate*.

Pfahl, S. and Wernli, H. (2012a). Quantifying the relevance of atmospheric blocking for co-located temperature extremes in the northern hemisphere on (sub-)daily time scales. *Geophysical Research Letters*, **39**(12), n/a–n/a.

Pfahl, S. and Wernli, H. (2012b). Quantifying the relevance of cyclones for precipitation extremes. *Journal of Climate*, **25**(19), 6770–6780.

Pinto, J., Ulbrich, U., Leckebusch, G., Spangehl, T., Reyers, M., and Zacharias, S. (2007). Changes in storm track and cyclone activity in three SRES ensemble experiments with the ECHAM5/MPI-OM1 GCM. *Climate Dynamics*, **29**(2-3), 195–210.

Pithan, F. and Mauritsen, T. (2014). Arctic amplification dominated by temperature feedbacks in contemporary climate models. *Nature Geoscience*.

Pope, V. and Stratton, R. (2002). The processes governing horizontal resolution sensitivity in a climate model. *Climate Dynamics*, **19**(3-4), 211–236.

Randall, D., Wood, R., Bony, S., Colman, R., Fichefet, T., Fyfe, J., Kattsov, V., Pitman, A., Shukla, J., Srinivasan, J., Stouffer, R., Sumi, A., and Taylor, K. (2007). Climate Models and Their Evaluation. In S. Solomon, D. Qin, M. Manning, Z. Chen, M. Marquis, K. B. Averyt, M. Tignor, and H. L. Miller, editors, *Climate Change 2007: The Physical Science Basis. Contribution of Working Group I to the Fourth Assessment Report of the Intergovernmental Panel on Climate Change*, pages 0–1. Cambridge University Press, Cambridge, United Kingdom and New York, NY, USA.

Rayner, N., Parker, D. E., Horton, E., Folland, C., Alexander, L., Rowell, D., Kent, E., and Kaplan, A. (2003). Global analyses of sea surface temperature, sea ice, and night marine air temperature since the late nineteenth century. *Journal of Geophysical Research: Atmospheres (1984–2012)*, **108**(D14).

Rigor, I., Wallace, J., and Colony, R. (2002). Response of sea ice to the arctic oscillation. *Journal of Climate*, **15**, 2648–2663.

Ring, M. J. and Plumb, R. A. (2007). Forced annular mode patterns in a simple atmospheric general circulation model. *Journal of the Atmospheric Sciences*, **64**(10), 3611–3626.

Ring, M. J. and Plumb, R. A. (2008). The response of a simplified GCM to axisymmetric forcings: Applicability of the fluctuation-dissipation theorem. *Journal of the Atmospheric Sciences*, **65**(12), 3880–3898.

Ringer, M., Martin, G., Greeves, C., Hinton, T., James, P., Pope, V., Scaife, A., Stratton, R., Inness, P., Slingo, J., *et al.* (2006). The physical properties of the atmosphere in the new Hadley Centre Global Environmental Model (HadGEM1). Part II: Aspects of variability and regional climate. *Journal of Climate*, **19**(7), 1302–1326.

Rivière, G. (2011). A dynamical interpretation of the poleward shift of the jet streams in global warming scenarios. *Journal of the Atmospheric Sciences*, **68**(6), 1253–1272.

Roeckner, E., Bäuml, G., Bonaventura, L., Brokopf, R., Esch, M., Giorgetta, M., Hagemann, S., Kirchner, I., Kornblueh, L., Manzini, E., *et al.* (2003). The atmospheric general circulation model ECHAM5. Part I: Model Description. *Max Planck Institute for Meteorology Report*, **349**, 127.

Rowell, D. P. (2005). A scenario of European climate change for the late twenty-first century: seasonal means and interannual variability. *Climate Dynamics*, **25**, 837–849.

Sampe, T., Nakamura, H., Goto, A., and Ohfuchi, W. (2010). Significance of a Midlatitude

SST Frontal Zone in the Formation of a Storm Track and an Eddy-Driven Westerly Jet. *Journal of Climate*, **23**, 1793–1815.

Sato, K., Inoue, J., and Watanabe, M. (2014). Influence of the Gulf Stream on the Barents Sea ice retreat and Eurasian coldness during early winter. *Environmental Research Letters*, **9**(8), 084009.

Saulière, J., Brayshaw, D. J., Hoskins, B., and Blackburn, M. (2012). Further Investigation of the Impact of Idealized Continents and SST Distributions on the Northern Hemisphere Storm Tracks. *Journal of the Atmospheric Sciences*, **69**, 840–856.

Schär, C., Vidale, P. L., Lüthi, D., Frei, C., Häberli, C., Liniger, M. A., and Appenzeller, C. (2004). The role of increasing temperature variability in European summer heatwaves. *Nature*, **427**, 332–336.

Scherrer, S. C., Appenzeller, C., Liniger, M. A., and Schär, C. (2005). European temperature distribution changes in observations and climate change scenarios. *Geophysical Research Letters*, **32**.

Schneider, T., Bischoff, T., and Płotka, H. (2015). Physics of changes in synoptic midlatitude temperature variability. *Journal of Climate*, **28**, 2312–2331.

Schröder, D., Feltham, D. L., Flocco, D., and Tsamados, M. (2014). September Arctic sea-ice minimum predicted by spring melt-pond fraction. *Nature Climate Change*, **4**(5), 353–357.

Schweiger, A., Zhang, J., Lindsay, R., and Steele, M. (2008). Did unusually sunny skies help drive the record sea ice minimum of 2007? *Geophysical Research Letters*, **35**(10).

Screen, J. A. (2014). Arctic amplification decreases temperature variance in northern mid- to high-latitudes. *Nature Climate Change*.

Screen, J. A. and Simmonds, I. (2010). The central role of diminishing sea ice in recent Arctic temperature amplification. *Nature*, **464**, 1334–1337.

Screen, J. A. and Simmonds, I. (2013). Exploring links between Arctic amplification and mid-latitude weather. *Geophysical Research Letters*, **40**(5), 959–964.

Screen, J. A., Deser, C., and Simmonds, I. (2012). Local and Remote Controls on observed Arctic Warming. *Geophysical Research Letters*, **39**, n/a–n/a.

Screen, J. A., C.Deser, Simmonds, I., and Tomas, R. (2013a). Atmospheric impacts of Arctic sea-ice loss, 1979-2009: separating forced change from atmospheric internal variability. *Climate Dynamics*, pages 1–12.

Screen, J. A., Simmonds, I., C.Deser, and Tomas, R. (2013b). The Atmospheric Response

to Three Decades of Observed Arctic Sea Ice Loss. *Journal of Climate*, **26**, 1230–1248.

Sedlàček, J., Knutti, R., Martius, O., and Beyerle, U. (2012). Impact of a Reduced Arctic Sea Ice Cover on Ocean and Atmospheric Properties. *Journal of Climate*, **25**, 307–319.

Seierstad, A. S. and Bader, J. (2009). Impact of a projected future Arctic Sea Ice reduction on extratropical storminess and the NAO. *Climate Dynamics*, **33**, 937–943.

Sellers, W. D. (1969). A global climatic model based on the energy balance of the earth-atmosphere system. *Journal of Applied Meteorology*, **8**(3), 392–400.

Semmler, T., McGrath, R., and Wang, S. (2012). The impact of Arctic sea ice on the Arctic energy budget and on the climate of the Northern mid-latitudes. *Climate Dynamics*, **39**, 2675–2694.

Semtner Jr, A. J. (1976). A model for the thermodynamic growth of sea ice in numerical investigations of climate. *Journal of Physical Oceanography*, **6**(3), 379–389.

Seneviratne, S. I., Lüthi, D., Litschi, M., and Schär, C. (2006). Land–atmosphere coupling and climate change in Europe. *Nature*, **443**(7108), 205–209.

Serreze, M., Barrett, A., Stroeve, J., Kindig, D., and Holland, M. (2009). The emergence of surface-based Arctic amplification. *The Cryosphere*, **3**(1), 11–19.

Serreze, M. C. and Barry, R. G. (2005). *The Arctic Climate System*. Cambridge University Press.

Serreze, M. C. and Barry, R. G. (2011). Processes and impacts of Arctic amplification: A research synthesis. *Global and Planetary Change*, **77**(1), 85–96.

Serreze, M. C. and Francis, J. A. (2006). The Arctic amplification debate. *Climatic Change*, **76**(3-4), 241–264.

Simmonds, I. and Rudeva, I. (2012). The great arctic cyclone of august 2012. *Geophysical Research Letters*, **39**(23).

Simmons, A. J. and Hoskins, B. J. (1978). The life cycles of some nonlinear baroclinic waves. *Journal of the Atmospheric Sciences*, **35**(3), 414–432.

Slingo, J., Belcher, S., Scaife, A., McCarthy, M., Saulter, A., McBeath, K., Jenkins, A., Huntingford, C., Marsh, T., Hannaford, J., and Parry, S. (2014). The recent storms and floods in the UK. http://www.metoffice.gov.uk/media/pdf/1/2/Recent_Storms_Briefing_Final_SLR_20140211.pdf.

Sokolova, E., Dethloff, K., Rinke, A., and Benkel, A. (2007). Planetary and synoptic scale adjustment of the arctic atmosphere to sea ice cover changes. *Geophysical Research Let-*

ters, **34**(17), n/a–n/a.

Sterl, A., Severijns, C., Dijkstra, H., Hazeleger, W., van Oldenborgh, G. J., van den Broeke, M., Burgers, G., van den Hurk, B., van Leeuwen, P. J., and van Velthoven, P. (2008). When can we expect extremely high surface temperatures? *Geophysical Research Letters*, **35**.

Stott, P. A., Stone, D. A., and Allen, M. R. (2004). Human contribution to the European heatwave of 2003. *Nature*, **432**, 610–614.

Stouffer, R. J. and Wetherald, R. T. (2007). Changes of Variability in Response to Increasing Greenhouse Gases. Part I: Temperature. *Journal of Climate*, **21**, 5455–5467.

Stroeve, J., Serreze, M., Drobot, S., Gearheard, S., Holland, M., Maslanik, J., Meier, W., and Scambos, T. (2008). Arctic sea ice extent plummets in 2007. *Eos, Transactions American Geophysical Union*, **89**(2), 13–14.

Stroeve, J. C., Serreze, M. C., Holland, M. M., Kay, J. E., Malanik, J., and Barrett, A. P. (2012a). The Arctics rapidly shrinking sea ice cover: a research synthesis. *Climatic Change*, **110**(3-4), 1005–1027.

Stroeve, J. C., Kattsov, V., Barrett, A., Serreze, M., Pavlova, T., Holland, M., and Meier, W. N. (2012b). Trends in Arctic sea ice extent from CMIP5, CMIP3 and observations. *Geophysical Research Letters*, **39**, L16502.

Strong, C. and Magnusdottir, G. (2010a). Modeled winter sea ice variability and the North Atlantic Oscillation: a multi-century perspective. *Climate Dynamics*, **34**(4), 515–525.

Strong, C. and Magnusdottir, G. (2010b). The Role of Rossby Wave Breaking in Shaping the Equilibrium Atmospheric Circulation Response to North Atlantic Boundary Forcing. *Journal of Climate*, **23**, 1269–1276.

Strong, C. and Magnusdottir, G. (2011). Dependence of NAO variability on coupling with sea ice. *Climate Dynamics*, **36**, ??–??

Taylor, K. E., Stouffer, R. J., and Meehl, G. A. (2011). A summary of the CMIP5 experiment design. cited 2011.

Taylor, K. E., Stouffer, R. J., and Meehl, G. A. (2012). An overview of CMIP5 and the experiment design. *Bulletin of the American Meteorological Society*, **93**(4), 485–498.

Thompson, D. W. and Wallace, J. M. (2000). Annular modes in the extratropical circulation. Part I: month-to-month variability. *Journal of Climate*, **13**(5), 1000–1016.

Ting, M. and Peng, S. (1995). Dynamics of the Early and Middle Winter Atmospheric

Responses to the Northwest Atlantic SST anomalies. *Journal of Climate*, **8**, 2239–2254.

Toggweiler, J. R. (2009). Shifting Westerlies. *Science*.

Toggweiler, J. R. and Russell, J. L. (2008). Ocean Circulation in a Warming Climate. *Nature*, **451**.

Toggweiler, J. R., Russell, J. L., and Carson, S. R. (2006). Dynamics of the Early and Middle Winter Atmospheric Responses to the Northwest Atlantic SST anomalies. *Paleocoeanography*, **21**.

Turner, J., Bracegirdle, T. J., Phillips, T., Marshall, G. J., and Hosking, J. S. (2013). An initial assessment of Antarctic sea ice extent in the CMIP5 models. *Journal of Climate*, **26**(5), 1473–1484.

Ulbrich, U., Pinto, J. G., Kupfer, H., Leckebusch, G., Spangehl, T., and Reyers, M. (2008). Changing Northern Hemisphere storm tracks in an ensemble of IPCC climate change simulations. *Journal of Climate*, **21**(8), 1669–1679.

Uppala, S. M., Kållberg, P., Simmons, A., Andrae, U., Bechtold, V., Fiorino, M., Gibson, J., Haseler, J., Hernandez, A., Kelly, G., *et al.* (2005). The era-40 re-analysis. *Quarterly Journal of the Royal Meteorological Society*, **131**(612), 2961–3012.

van Oldenborgh, G. J., Collins, M., Arblaster, J., J.H.Christensen, Marotzke, J., Power, S., Rummukainen, M., and Zhou, T. (2013). Annex I: Atlas of Global and Regional Climate Projections. In T. F. Stocker, D. Qin, G.-K. Plattner, M. Tignor, S. K. Allen, J. Boschung, A. Nauels, Y. Xia, V. Bex, and P. M. Midgley, editors, *Climate Change 2013: The Physical Science Basis. Contribution of Working Group I to the Fifth Assessment Report of the Intergovernmental Panel on Climate Change*, pages 1311–1394. Cambridge University Press, Cambridge, United Kingdom and New York, NY, USA.

van Ulden, A. P. and van Oldenborgh, G. J. (2006). Large-Scale atmospheric circulation biases and changes in global climate model simulations and their importance for climate change in Central Europe. *Atmospheric Chemistry and Physics*, **6**, 863–881.

van Vuuren, D. P., Edmonds, J., Kainuma, M., Riahi, K., Thomson, A., Hibbard, K., Hurtt, G. C., Kram, T., Krey, V., Lamarque, J.-F., Masui, T., Meinshausen, M., Nakicenovic, N., Smith, S. J., and Rose, S. J. (2011). The representative concentration pathways: an overview. *Climatic Change*, **109**, 5–31.

Vaughan, D., Comiso, J., Allison, I., Carrasco, J., Kaser, G., Kwok, R., Mote, P., Murray, T., Paul, F., Ren, J., Rignot, E., Solomina, O., Steffen, K., and Zhang, T. (2013). Observations: Cryosphere. In T. F. Stocker, D. Qin, G.-K. Plattner, M. Tignor, S. K. Allen,

J. Boschung, A. Nauels, Y. Xia, V. Bex, and P. M. Midgley, editors, *Climate Change 2013: The Physical Science Basis. Contribution of Working Group I to the Fifth Assessment Report of the Intergovernmental Panel on Climate Change*, pages 317–382. Cambridge University Press, Cambridge, United Kingdom and New York, NY, USA.

Vidale, P., Lüthi, D., Wegmann, R., and Schär, C. (2007). European summer climate variability in a heterogeneous multi-model ensemble. *Climatic Change*, **81**(1), 209–232.

Wang, M. and Overland, J. E. (2012). A sea ice free summer Arctic within 30 years: An update from CMIP5 models. *Geophysical Research Letters*, **39**(18).

Watterson, I. G., McGregor, J. L., and Nguyen, K. C. (2008). Changes in extreme temperatures of Australasian summer simulated by CCAM under global warming, and the roles of winds and land-sea contrasts. *Aust. Meteorol. Mag*, **57**, 195–212.

Webster, S., Brown, A., Cameron, D., and Jones, C. (2003). Improvements to the representation of orography in the met office unified model. *Quarterly Journal of the Royal Meteorological Society*, **129**(591), 1989–2010.

Wilcox, L. J., Charlton-Perez, A. J., and Gray, L. J. (2012). Trends in Austral jet position in ensembles of high-and low-top CMIP5 models. *Journal of Geophysical Research: Atmospheres (1984–2012)*, **117**(D13).

Wilks, D. S. (2005). *Statistical Methods in the Atmospheric Sciences: An Introduction*. Academic Press, London.

Wilson, C., Sinha, B., and Williams, R. G. (2009). The effect of ocean dynamics and orography on atmospheric storm tracks. *Journal of Climate*, **22**(13), 3689–3702.

Woollings, T. and Blackburn, M. (2012). The North Atlantic Jet Stream under Climate Change and Its Relation to the NAO and EA Patterns. *Journal of Climate*, **25**, 886–902.

Woollings, T., Hannachi, A., and Hoskins, B. (2010). Variability of the North Atlantic eddy-driven jet stream. *Quarterly Journal of the Royal Meteorological Society*, **136**, 856–868.

Woollings, T., Czuchnicki, C., and Franzke, C. (2014). Twentieth century North Atlantic jet variability. *Quarterly Journal of the Royal Meteorological Society*, **140**(680), 783–791.

Yin, J. H. (2005). A consistent poleward shift of the storm tracks in simulations of 21st century climate. *Geophysical Research Letters*, **32**(18), n/a–n/a.

Ylhäisi, J. S. and Räisänen, J. (2014). Twenty-first century changes in daily temperature variability in CMIP3 climate models. *International Journal of Climatology*, **34**(5), 1414–1428.

Zappa, G., Shaffrey, L. C., Hodges, K. I., Sansom, P. G., and Stephenson, D. B. (2013a). A Multimodel Assessment of Future Projections of North Atlantic and European Extratropical Cyclones in the CMIP Climate Models. *Journal of Climate*, **26**(16), 5846–5862.

Zappa, G., Shaffrey, L. C., and Hodges, K. I. (2013b). The Ability of CMIP5 Models to Simulate North Atlantic Extratropical Cyclones. *Journal of Climate*, **26**(15), 5379–5396.

Zhang, J. and Rothrock, D. (2003). Modeling global sea ice with a thickness and enthalpy distribution model in generalized curvilinear coordinates. *Monthly Weather Review*, **131**(5), 845–861.

Zhang, J., Rothrock, D., and Steele, M. (2000). Recent Changes in Arctic Sea Ice: The Interplay between Ice Dynamics and Thermodynamics. *Journal of Climate*, **13**, 3099–3114.

Zhang, J., Lindsay, R., Steele, M., and Schweiger, A. (2008). What drove the dramatic retreat of Arctic sea ice during summer 2007? *Geophysical Research Letters*, **35**(11).

Zhang, J., Lindsay, R., Schweiger, A., and Steele, M. (2013). The impact of an intense summer cyclone on 2012 Arctic sea ice retreat. *Geophysical Research Letters*, **40**(4), 720–726.